Imperial College London
Department of Physics

On the effect of climate change on European summer blocking

Carl Magnus Thomas

Submitted in part fulfilment of the requirements
for the degree of Doctor of Philosophy at

Imperial College London, July 2022

I hereby declare that this thesis and the work reported herein was composed by and originated entirely from me. Information derived from the published and unpublished work of others has been acknowledged in the text and references are given in the list of sources.

Carl Magnus Thomas (2022)

Abstract

Atmospheric blocking events are regularly observed mid-latitude weather patterns, which obstruct the usual path of the jet streams. However, there is no well-defined historical dataset of blocking events and the effect of climate change on atmospheric blocking is uncertain. In this thesis, I explore how climate change influences European summer blocking (ESB). I develop a new algorithm to identify regional blocking events (the SOM-BI index), combining supervised and unsupervised learning. This is compared to other methods and a new ground truth dataset. I find the SOM-BI has an improved detection skill over other methods, particularly for climate models. I apply the SOM-BI to study ESB in the abrupt-4xCO2 experiments from phases 5 and 6 of the Coupled Model Intercomparison Project. These runs maximise the forcing and have not previously been used to study atmospheric blocking. I identify a strong negative correlation between the historical occurrence of ESB and the change in occurrence of ESB. This enables a prediction of the ESB climate response from the historical model bias. Further, I identify the two main physical mechanisms which affect the ESB climate response: the poleward shift of the North Atlantic jet; and the propagation of Rossby waves across the North Pacific from diabatic heating in the tropical Pacific. I develop an informed physical understanding of these mechanisms, which have not been discussed in the literature as positive influences on the ESB climate response. I then define two metrics as proxies for these physical mechanisms and estimate a positive climate feedback on ESB: 0.22 ± 0.35 days / °C. My thesis demonstrates the potential for machine learning in studying atmospheric blocking, highlights the importance of tropical forcing in influencing the climate feedback on ESB, and identifies new mechanisms that can be further explored to develop our understanding of how climate change will influence atmospheric blocking.

Acknowledgements

I am deeply indebted to the support and hard work of my supervisors, Peer and Apostolos. They have both been incredibly supportive at guiding my research efforts, providing very helpful feedback across the process and have enabled me to develop in my confidence as a researcher. Thank you!

I am deeply indebted to my parents, without whom I would not exist; they have also provided needed support and encouragement, particularly over the lockdown period. My brothers Philip and Robin have also been very supportive. Neil Grant was an excellent office mate who continued encouragement has sustained me through challenging periods.

Main thanks go to the Lord. He is my shepherd, anchor, Saviour and guide. The mighty hand of God is sufficient to carry the weight of all my anxieties and fears, for He cares for me.

Soli deo gloria.

Can anyone understand the spreading of the clouds, the thunderings of his pavilion? Behold, he scatters his lightning about him and covers the roots of the sea.

- Job 36:29-30

Contents

List of Tables

List of Figures

Nomenclature

Z	Geopotential height [m]
Z_{500}	Geopotential height at 500 hPa [m]

Greek Symbols

η	Absolute vorticity [s^{-1}]
μ	Mean
ω	Vorticity [s^{-1}]
p	Pressure [Pa]
ψ	Streamfunction [$m^2\,s^{-1}$]
σ	Standard deviation
θ	Potential temperature [K]
θ-PV	Potential temperature on the PV = 2 PVU surface [K]
ξ	Potential vorticity [s^{-1}]
ζ	Relative vorticity [s^{-1}]

List of Abbreviations

AGP	Absolute geopotential
BI	Blocking index
BMU	Best matching unit
CMIP5	Coupled Model Intercomparison Project Phase 5
CMIP6	Coupled Model Intercomparison Project Phase 6
CMIP	Coupled Model Intercomparison Project
DJF	December-January-February

EKE Eddy kinetic energy per unit mass [$\mathrm{J\,kg^{-1}}$]

GMST Global mean surface temperature

JJA June-July-August

LTDM Long term daily mean

MSLP Mean sea level pressure [Pa]

PCA Principal component analysis

PV Potential Vorticity [$10^{-6}\ \mathrm{K\,m^2\,kg^{-1}\,s^{-1}}$]

VPV Vertically averaged Potential Vorticity [$10^{-6}\ \mathrm{K\,m^2\,kg^{-1}\,s^{-1}}$]

IPV Isentropic Potential Vorticity [$10^{-6}\ \mathrm{K\,m^2\,kg^{-1}\,s^{-1}}$]

SOM-BI Self-organizing map blocking index

SOM Self-organizing map

T Temperature [K]

Chapter 1

Introduction

1.1 Thermodynamic and dynamic climate change

Climate change is a global phenomenon with far reaching implications for society. Among the most important effects of climate change are the increased frequency of extreme weather events such as heatwaves, droughts and floods (Cutter et al. 2012; King et al. 2015). These events occur on regional scales across cities, countries and continents, and our confidence in projections of extreme events varies significantly depending on the region and extreme event under consideration (Madsen et al. 2017). This uncertainty has several causes, including a finite observational record, constraints in model capability, internal variability in the regional climate and a limited understanding of the physical processes contributing to changes in extreme event patterns (Hawkins and Sutton 2009; Knutti et al. 2010). In particular, in the extratropics the internal variability is enhanced due to persistent large-scale weather patterns, causing greater uncertainty in extreme event projections (Xie et al. 2015).

A common approach to constraining and understanding regional projections in extreme events is to separate thermodynamic and dynamic mechanisms driven by climate change (Shepherd 2014; Horton et al. 2015; Oueslati et al. 2019; Cloutier-Bisbee et al. 2019; Norris et al. 2019; Ali and Mishra 2018; Suarez-Gutierrez et al. 2020). Investigating how these two classes of mechanisms have changed patterns of extreme events has proved useful in understanding the causes of extreme events and in further constraining their trends (Chen et al. 2018; Vautard et al. 2016).

Thermodynamic climate change can be understood as corresponding to an average change in the global energy budget, reflected in an average change in mean surface temperature. This leads to a mean shift in the surface air temperature distribution globally, which is then correlated with regional increases in air temperature. This increase in the global mean surface temperature therefore has a direct effect on the frequency and intensity of regional persistence of hot extremes, since even a small shift in the mean can have a large relative effect on the extremes of a temperature distribution (Coumou et al. 2013; Fischer and Knutti 2015). Such increases in regional surface air temperature also lead to increased precipitation extremes, since warmer air can store more water vapour (Trenberth et al. 2003; Stephens and Ellis 2008). Whilst the mechanisms of thermodynamic climate change are relatively well understood, uncertainty remains surrounding the magnitude of future regional and global warming (Hawkins and Sutton 2009; Qu et al. 2018).

Dynamic climate change involves changes in atmospheric circulation regimes, which could have significant regional effects on the occurrence and persistence on phenomena such as heatwaves. This is particularly true for mid-latitude regions such as Europe, where large-scale weather patterns significantly enhance regional uncertainty in future projections (Xie et al. 2015). Changes in the occurrence and persistence of weather regimes are currently poorly understood and constrained relative to the thermodynamic mechanism, but could have significant effects on the surface temperature extremes, affecting not just the mean but also the variance of the temperature distribution (Shepherd 2014; Tamarin-Brodsky et al. 2020). Atmospheric dynamics has therefore been identified as a significant source of uncertainty in climate model projections, and there has been considerable interest into the effect of anthropogenic climate change on atmospheric circulation (Vecchi and Soden 2007; Horton et al. 2015; Fereday et al. 2018; Ma et al. 2018).

The dynamic mechanisms of climate change are more difficult to constrain (Held 1993), since atmospheric dynamics are nonlinear (Palmer 1999) and are governed by a wide range of regional phenomena and possible feedbacks (Shepherd 2014), such as Arctic Amplification (Barnes and Screen 2015), land-surface feedbacks (Miralles et al. 2014), and SSTs and sea ice anomalies (Deser et al. 2004). There is also a significant uncertainty arising from the problem of distinguishing trends in atmospheric dynamics from internal variability (Deser et al. 2004; Simpson et al. 2009; Deser et al. 2012).

The dynamic component of climate change is particularly relevant for extreme events, which typically occur under exceptional weather regimes. Of particular relevance to mid-latitude heatwaves is atmospheric blocking, where a persistent high pressure system blocks the zonal flow over a region for several days to weeks (Rex 1950; Nakamura and Huang 2018). Both the prominent 2003 and 2019 European summer heatwaves were associated with a blocking system centered over Western Europe (Black et al. 2004; Mitchell et al. 2019), and the 2010 Euro-Russian heatwave was caused by strong persistent blocking over Russia and Eastern Europe (Matsueda 2011; Quandt et al. 2017).

It should be noted that in the physical atmosphere, dynamic and thermodynamic processes are often closely coupled. One example of a process occurring under climate change in the atmosphere that responds both to thermodynamic and dynamic mechanisms is the expansion of the Hadley cell, a common feature across all global climate models (Chou et al. 2013). As the tropical atmosphere warms, the tropospheric column-integrated water vapour increases at the Clausius-Claperyon rate (7% K^{-1}), whereas the rate of increase in global mean precipitation is much smaller (2% K^{-1}) as it is limited by changes in net surface radiative flux and the increase of Bowen's ratio (Allen and Ingram 2002). This increases moist convection, leading to enhanced upper-tropospheric warming and a reduced magnitude of the moist adiabatic lapse rate (Held and Soden 2006). This increases dry static stability, stabilizing the subtropical jet streams at the poleward extent of the Hadley Cell. This shifts the baroclinic eddies poleward and thus the Hadley cell expands (Chou et al. 2013; Levine and Schneider 2015). In short, the thermodynamic effects resulting from increased heating and water vapour in the tropics lead to dynamic changes in the Hadley cell expansion. It is therefore misleading in this case to try to separate the thermodynamic and dynamic effects. However, since in general the changes in circulation are more poorly constrained than changes in the average global mean energy budget, the separation of dynamic and thermodynamic climate change mechanisms is a useful heuristic to better understand the sources of uncertainties in model projections (Shepherd 2014).

1.2 Physical overview of atmospheric dynamics

This section discusses the key physical concepts that are needed to discuss atmospheric blocking and the influence of climate change on atmospheric blocking events.

1.2.1 The momentum equation

The momentum equation is a partial differential equation that describes how the velocity or momentum of a fluid responds to internal and imposed forces. For an incompressible inviscid fluid in a rotating frame of reference, the momentum equation can be written as (Vallis 2006a)

$$\frac{\mathrm{D}\mathbf{v}}{\mathrm{D}t} + \mathbf{2\Omega} \times \mathbf{v} = -\frac{\mathbf{1}}{\boldsymbol{\rho}}\boldsymbol{\nabla} \boldsymbol{p} - \boldsymbol{\nabla}\boldsymbol{\Phi}, \tag{1.1}$$

where $\mathbf{v}$ is the wind vector (relative to the rotating frame), t is time, $\mathbf{\Omega}$ is the angular velocity of the rotating frame, ρ is the density of the fluid parcel and p is pressure of the fluid parcel. Φ is the geopotential of the effective gravitation force $\mathbf{g}$ which includes the centrifugal force and Newtonian gravity such that $\mathbf{g} = -\nabla\Phi$. Since the Earth has developed a slight bulge to make the centrifugal force zero at the surface, the geopotential Φ can simply be taken as $\Phi = gz$, where g is the acceleration due to gravity and z is the height of the fluid parcel above the surface.

Equation (1.1) is frequently simplified to create the primitive equations, using three related assumptions:

1. *Hydrostatic balance.* This assumes that the pressure gradient force acting of the fluid parcel is balanced by the gravitational force such that:

$$\frac{\partial p}{\partial z} = -\rho g, \tag{1.2}$$

   where z is the height of the fluid parcel above the surface and g is the acceleration due to gravity. This means that in the vertical direction the Coriolis terms and advection of vertical velocity are neglected.

2. *The shallow-fluid approximation.* This approximation replaces the coordinate r in spherical coordinates with the radius of the Earth a (except where it is used as a differentiating argument), noting that $r = a + z$ and $a >> z$.

3. *The traditional approximation.* Following the above assumption of a small aspect ratio of motion, the Coriolis terms and metric terms in the horizontal momentum equations involving the vertical velocity are neglected.

These approximations are all very accurate for large-scale flow in the atmosphere. By considering the above approximation for an inviscid fluid on the Earth, the horizontal momentum equation can be written as (Vallis 2006a)

$$\frac{\partial \mathbf{u}}{\partial t} + (\mathbf{u} \cdot \nabla)\mathbf{u} + \mathbf{f} \times \mathbf{u} = -\frac{1}{\rho}\nabla_z p, \tag{1.3}$$

where $\mathbf{u}$ is horizontal wind vector, t is time. $\mathbf{f}$ is the vertical component to the Coriolis term, defined as $\mathbf{f} = f\mathbf{k} = 2\Omega \sin \phi \mathbf{k}$, where Ω is the Earth's rotation rate at the equator, ϕ is the angle of the air parcel with respect to the equator and $\mathbf{k}$ is the unit vector in the vertical direction.

1.2.2 Geostrophic balance

The ratio of the advection term ($(\mathbf{u} \cdot \nabla)\mathbf{u}$) to the Coriolis term ($\mathbf{f} \times \mathbf{u}$) in equation (1.3) is defined to be the Rossby number (Ro), which scales as (Vallis 2006a)

$$Ro = \frac{U}{fL}, \tag{1.4}$$

where U and L are the horizontal wind and length scales of the flow, and f is the magnitude of the Coriolis term. This follows from the fact that $(\mathbf{u} \cdot \nabla)\mathbf{u}$ scales as U^2/L and $\mathbf{f} \times \mathbf{u}$ scales as fU.

If the Rossby number is small then the rotation effects are important, which is the case for large-scale flow in the atmosphere (Vallis 2006b). In this case the rotation term dominates the advection term, so equation (1.3) can be simplified as (Vallis 2006a):

$$\mathbf{f} \times \mathbf{u} \approx -\frac{1}{\rho}\nabla_z p. \tag{1.5}$$

Equation (1.5) can be written in component form as (Vallis 2006a)

$$fu \approx -\frac{1}{\rho}\frac{\partial p}{\partial y}, \tag{1.6a}$$
$$fv \approx \frac{1}{\rho}\frac{\partial p}{\partial x}, \tag{1.6b}$$

where x and y are the zonal and meridional distance components respectively. The above situation is known as **geostrophic balance**, and it has significant consequences for large-scale flow in the atmosphere. The geostrophic wind is defined as $\mathbf{u}_g = (u_g, v_g, 0)$, where

$$fu_g = -\frac{1}{\rho}\frac{\partial p}{\partial y}, \tag{1.7a}$$
$$fv_g = \frac{1}{\rho}\frac{\partial p}{\partial x}. \tag{1.7b}$$

1.2.3 Thermal wind balance

Thermal wind balance is obtained from combining the geostrophic and hydrostatic approximations. In pressure coordinates geostrophic balance can be expressed as (Vallis 2006a)

$$\mathbf{f} \times \mathbf{u}_g = -\nabla_p \Phi, \tag{1.8}$$

where Φ is the geopotential and ∇_p is the gradient operator taken at constant pressure. Hydrostatic balance can be expressed as

$$\frac{\partial \Phi}{\partial p} = -\alpha, \tag{1.9}$$

where $\alpha = 1/\rho$ is the specific volume of the flow. Using the ideal gas equation ($p = \rho RT$, where R is the gas constant and T is temperature), α can be expressed as $\alpha = RT/p$. Taking the vertical derivative of equation (1.8) and using equation (1.9) gives the thermal wind equation:

$$\mathbf{f} \times \frac{\partial \mathbf{u}_g}{\partial p} = -\nabla_p \alpha = \frac{R}{p} \nabla_p T. \tag{1.10}$$

In component form this is

$$-f \frac{\partial v_g}{\partial p} = \frac{R}{p} \frac{\partial T}{\partial x}, \tag{1.11a}$$

$$f \frac{\partial u_g}{\partial p} = \frac{R}{p} \frac{\partial T}{\partial y}. \tag{1.11b}$$

This creates an important effect: **a horizontal temperature gradient is accompanied by a vertical shear of the horizontal wind**. Since temperatures decrease poleward from the equator in the atmosphere, the thermal wind relation is one reason why there is fast-flowing westerly wind in the upper troposphere known as the *jet stream*. There are two prominent jet streams in each hemisphere: the polar jet stream, which is situated in the midlatitudes; and the subtropical jet stream, situated at the poleward edge of the tropics. The thermal wind relation is also important for understanding the response of European summer blocking (ESB) to climate change; this will be explained in detail in section 3.4.3.

1.2.4 Vorticity and streamfunction

Two important dynamical quantities that relate to atmospheric flow are vorticity and streamfunction. The vorticity $\boldsymbol{\omega}$ is defined as (Vallis 2006c)

$$\boldsymbol{\omega} = \boldsymbol{\nabla} \times \mathbf{u}. \tag{1.12}$$

In a rotating frame of reference, the vorticity induced by the air velocity relative to the Earth's surface (called the *relative vorticity* and labelled $\boldsymbol{\zeta}$) is distinct from the *absolute vorticity* $\boldsymbol{\eta}$, which is computed from the air velocity relative to an inertial frame and therefore includes the

Coriolis parameter:

$$\boldsymbol{\eta} = \boldsymbol{\zeta} + \mathbf{f}. \tag{1.13}$$

The streamfunction ψ is defined as the vector potential such that

$$\mathbf{u} = \nabla \times \psi, \tag{1.14}$$

with the horizontal components of the flow

$$u = \frac{\partial \psi}{\partial y}, v = -\frac{\partial \psi}{\partial x}. \tag{1.15}$$

These quantities are both discussed in later sections and are applied to the analysis of the ESB response to climate change in chapter 3.

1.2.5 Potential temperature

Following from the first law of thermodynamics for an ideal gas, if a fluid parcel changes pressure adiabatically it will change its temperature. However, an important temperature-like quantity can be constructed which only changes when diabatic effects are present. This quantity is called *potential temperature* (labelled θ), and it is defined to be the temperature that a fluid parcel would have if moved adiabatically with no change in composition to a reference pressure (typically 1000 hPa). It can be written as (Vallis 2006c)

$$\theta = T \left(\frac{p_{ref}}{p} \right)^{\frac{R}{c_p}}, \tag{1.16}$$

where T is temperature, p_{ref} is the reference pressure, p is the pressure of the air parcel, R is the molar gas constant and c_p is the heat capacity at constant pressure. Since θ does not change adiabatically, it is constant on surfaces of constant entropy, which enables θ to be a useful quantity for tracing the motion of fluid parcels in the atmosphere (Vallis 2006c).

1.2.6 Potential vorticity

An important perspective on the atmosphere can be obtained through potential vorticity, which is "a primary concept in modern dynamical meteorology" (Hoskins and James 2014b).

A prerequisite for understanding potential vorticity is Kelvin's circulation theorem, which was first discussed in the context of meteorology by Bjerknes (1898). Kelvin's circulation theorem states that in a barotropic ideal fluid with conservative body forces, the circulation around a closed curve (which encloses the same fluid elements) moving with the fluid remains constant with time. The circulation (Γ) around a closed contour is a function of time (t) and is defined as (Hoskins and James 2014b)

$$\Gamma(t) = \oint_C \mathbf{u} \cdot d\mathbf{l}, \tag{1.17}$$

where u is the wind vector and l is a line element along the closed contour. The total derivative of circulation with respect to time can be written as

$$\frac{\mathrm{D}\Gamma}{\mathrm{D}t} = \oint_C \frac{\mathrm{D}\mathbf{u}}{\mathrm{D}t} \cdot d\mathbf{l} + \oint_C \mathbf{u} \cdot \frac{\mathrm{D}d\mathbf{l}}{\mathrm{D}t} \tag{1.18}$$

The second term on the right hand side of equation (1.18) can be shown (using gradient theorem) to be equal to 0. Using the governing equation for an inviscid fluid (a fluid with no viscosity) with a conservative body force and applying Stokes' theorem means that the first term on the right hand side of equation (1.18) can be written as (Hoskins and James 2014b)

$$\oint_C \frac{\mathrm{D}\mathbf{u}}{\mathrm{D}t} \cdot d\mathbf{l} = \oiint_s \nabla \times \left(\frac{-1}{\rho} \nabla p + \nabla \Phi \right) \cdot \mathbf{n} dS = \oiint_s \frac{1}{\rho^2} (\nabla \rho \times \nabla p) \cdot \mathbf{n} dS. \tag{1.19}$$

where ρ is the density and p is the pressure of the fluid parcel, Φ is the body force applying on the fluid parcel, S is the surface and $\mathbf{n}$ is the unit vector normal to the surface S. If the fluid is **barotropic** (that is, the density of the fluid is a function only of pressure, $\rho = \rho(p)$), then equation (1.19) is also zero, resulting in

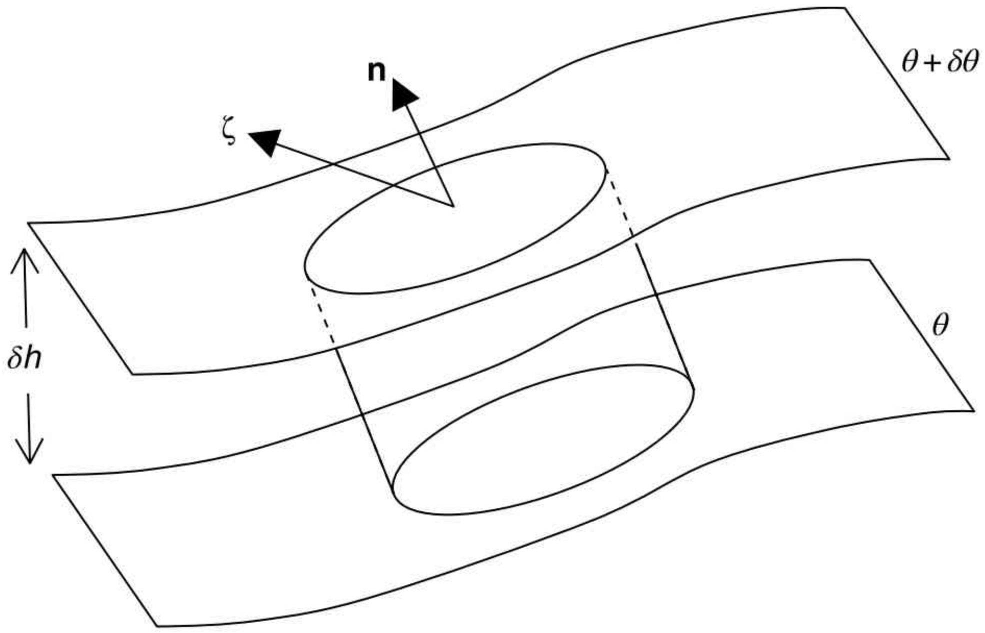

Figure 1.1: A parcel of fluid moves between two nearby surfaces of constant potential temperature, conserving its mass and the circulation around it. Reproduced from Fig. 10.1 of Hoskins and James (2014b).

$$\frac{\mathrm{D}\Gamma}{\mathrm{D}t} = 0 \tag{1.20}$$

for a barotropic fluid.

Kelvin's circulation theorem means that the circulation around a fluid parcel is constant if the integral of the pressure gradient force around it is zero (Hoskins and James 2014b). In a situation where the motion is adiabatic (and potential temperature is conserved), the mass is constant (no change in the vapour pressure of the air parcel) and where there is no friction between the air parcel and the surface (above the boundary layer), a conservation relation can be written for a fluid parcel enclosed between two isentropes:

$$\frac{\boldsymbol{\zeta} \cdot \mathbf{n}}{\rho \delta h} = \text{constant}. \tag{1.21}$$

where $\boldsymbol{\zeta}$ is relative vorticity (see equation (1.13)), ρ is the density and h is the height of the fluid parcel. Such a cylindrical fluid parcel is shown in Fig. 1.1. $\mathbf{n}$ in equation 1.21 is a unit vector normal to the isentropes, which can be expressed as

$$\mathbf{n} = \frac{\nabla\theta}{|\nabla\theta|}. \tag{1.22}$$

Noting that in the limit of a small cylinder (see Fig. 1.1)

$$|\nabla\theta| = \frac{\nabla\theta}{\nabla h}, \tag{1.23}$$

equation (1.21) can be written as

$$\frac{\mathrm{D}P}{\mathrm{D}t} = 0, \text{ where } P = \frac{\boldsymbol{\zeta}\cdot\nabla\theta}{\rho}. \tag{1.24}$$

P is called Ertel-Rossby potential vorticity (commonly potential vorticity or PV), first introduced by Rossby (1940) and Ertel (1942). P is nearly conserved where there is no friction (outside of the boundary layer) and negligible latent heat release (outside of weather fronts and regions of intense precipitation); as a result, P is conserved for much of the flow in the mid- and upper-troposphere. In addition, if friction or heating occur within a region, P will be altered, but outside of the region of heating or friction P will adjust such that the mass-weighted P integrated over a given volume remains constant. Potential vorticity (hereafter PV) therefore provides a strong constraint on atmospheric motion.

When advective processes dominate frictional and diabatic processes, PV on an isentropic surface acts as a Lagrangian tracer of air parcels (Starr and Neiburger 1940). An additional feature of PV is that (given certain boundary conditions) the PV field can be inverted to derive all other dynamical fields, including winds, temperatures, geopotential heights, static stability and vertical velocity (Hoskins et al. 1985). This arises because the potential vorticity field (ξ) is related to the streamfunction field (ψ) by a Poisson equation (Thorpe 1985):

$$\nabla^2\psi = \xi. \tag{1.25}$$

Because of its conservation properties and relationship to other meteorological variables, PV is useful in operational forecasting (Mansfield 2007). PV has also been used in the study of atmospheric blocking (Pelly and Hoskins 2003; Schwierz et al. 2004), and is applied to understanding blocking events in chapter 2.

1.2.7 The quasi-geostrophic potential vorticity equation

Using hydrostatic balance, geostrophic balance and assuming the appropriate horizontal scale of flow for large-scale synoptic activity, a set of equations that simplify the Navier-Stokes relation is obtained called the **quasi-geostrophic equations** (Vallis 2006d). The specific assumptions made are:

- there is a small Rossby number;
- there are small variations in the Coriolis parameter;
- the time scale of the motion T scales advectively (such that $T = L/U$); and
- the scale of motion is not significantly larger than the deformation radius.

The deformation radius L_d is defined as the length scale at which rotational effects become as important as gravity wave effects, and is written as:

$$L_d = \frac{NH}{f_0}. \tag{1.26}$$

$H = RT/g$ is the scale height of the atmosphere - that is, the change in altitude over which the atmospheric pressure decreases by a factor of e. $f_0 = 2\Omega \sin\vartheta_0$, where ϑ_0 is the latitude of a plane tangent to the Earth's surface and ϑ is the latitude of an air parcel. f_0 relates to the Coriolis parameter f through the *beta-plane approximation*, which is that for small variations in latitude:

$$f = 2\Omega \sin\vartheta \approx 2\Omega \sin\vartheta_0 + 2\Omega(\vartheta - \vartheta_0)\cos\vartheta_0 \approx f_0 + \beta y, \tag{1.27}$$

where

$$\beta = \partial f / \partial y = (2\Omega \cos\vartheta_0)/a. \tag{1.28}$$

N from equation (1.26) is the Brunt-Väisälä frequency, which is the frequency at which a vertically displaced parcel will oscillate in a statically stable atmosphere:

$$N = \sqrt{\frac{g}{\theta}\frac{d\theta}{dz}}, \tag{1.29}$$

where z is height, g is the acceleration due to gravity and θ is potential temperature defined in equation (1.16).

To make the quasi-geostrophic assumption, the ratio of the length scale of the motion L to the deformation must satisfy

$$\left(\frac{L}{L_d}\right)^2 \gg 1. \tag{1.30}$$

From applying the above assumptions, expressing the dynamic terms to order Rossby number and cross differentiating the momentum equation (Vallis 2006d), one obtains the quasi-geostrophic potential vorticity equation for a stratified fluid:

$$\frac{\mathrm{D}q}{\mathrm{D}t} = 0, \text{where } q = \nabla^2\psi + f + \frac{f_0^2}{\tilde{\rho}}\frac{\partial}{\partial z}\left(\frac{\tilde{\rho}}{N^2}\frac{\partial\psi}{\partial z}\right). \tag{1.31}$$

$\tilde{\rho}$ is the reference density profile for a stratified fluid. q is called the quasi-geostrophic potential vorticity, and is analogous to the Ertel potential vorticity (see equation (1.24)). q is conserved when advected by the horizontal geostrophic flow. Equation (1.31) is "one of the most important equations in dynamical meteorology" (Vallis 2006d) and can be used to explain many synoptic-scale processes in the atmosphere.

1.2.8 Rossby waves

Rossby waves are the most important large-scale waves in the atmosphere. They can be derived from considering the equation of motion for adiabatic quasi-geostrophic potential vorticity, which from equation (1.31) can be written as

$$\frac{\partial q}{\partial t} + \mathbf{u}\cdot\nabla q = 0. \tag{1.32}$$

Equation (1.32) can be linearized by expressing $q(x, y, z, t)$ and $\mathbf{u}(x, y, z, t)$ as a function of a time-independent base state ($\bar{q}$ and $\bar{u}$) and a small perturbation (q' and u'):

$$q = \bar{q}(y, z) + q'(x, y, t), \mathbf{u} = \bar{\mathbf{u}}(y, z) + \mathbf{u}'(x, y, t). \tag{1.33}$$

Substituting (1.33) into equation (1.32) and neglecting small quantities yields the common equation of motion for Rossby waves:

$$\frac{\partial q'}{\partial t} + \bar{u}\frac{\partial q'}{\partial x} + v'\frac{\partial \bar{q}}{\partial y} = 0. \tag{1.34}$$

Rossby waves therefore arise from gradients in potential vorticity in the atmosphere. These gradients commonly arise from the differential rotation of the atmosphere arising from the meridional gradient of the Coriolis parameter; this is called the β effect (see equation (1.28)). If a barotropic fluid parcel is displaced it conserves its potential vorticity, which means that the relative vorticity will change. This change in relative vorticity creates a velocity field that displaces adjacent fluid parcels, thus leading to further changes in relative vorticity and therefore a propagating displacement in the fluid (Vallis 2006e).

For a non-zero β the ambient potential vorticity increases northward, and in general Rossby waves propagate westward in the direction of increasing potential vorticity (Vallis 2006e).

These Rossby waves form large meanders in the polar jet stream, creating *ridges* and *troughs* in the midlatitude flow which form anticyclones and cyclones in the atmosphere. Atmospheric blocking events can be understood as times when the Rossby wave breaks, forming a persistent anticyclone over a region (Hoskins and James 2014a).

1.2.8.1 Rossby waves and diabatic heating

Whilst a key ingredient for the existence of Rossby waves is a potential vorticity gradient, this potential vorticity does not have to be produced by the β effect. Another source of potential vorticity gradients in the atmosphere which produces Rossby waves is diabatic heating. This is a particularly prominent source in the tropics (Hoskins and Karoly 1981). Such Rossby waves have relevance for understanding the European summer blocking response to climate change, as discussed in section 3.4.5. Such Rossby wave perturbations can be understood by considering a simple model of the atmosphere with the following assumptions:

- The background easterly flow $\bar{u}$ is considered to be only a function of altitude and increasing with height z

$$\bar{u}(z) = \bar{u}_z z, \tag{1.35}$$

where $\bar{u}_z$ is the vertical derivative of $\bar{u}$.

- The background flow is in geostrophic and hydrostatic balance (see sections 1.2.1 and 1.2.2).
- the equation of state is of the form

$$\rho = \rho_0(1 - \gamma\theta) \tag{1.36}$$

where ρ is density, ρ_0 is the reference density for the fluid, γ is a constant and θ is potential temperature.

If the atmosphere is heated or cooled, then the entropy will increase or decrease. This creates density perturbations arising from the equation of state, and pressure perturbations arising from hydrostatic balance.

By considering a perturbation that is much smaller than the mean state, one can rewrite the wind $\mathbf{u}$, density and pressure p fields in the same fashion as in section 1.2.8 (with a time independent base state and a time dependent perturbation). This means that geostrophic balance (see equation (1.7)) can be expressed as

$$\bar{u}\frac{\partial u'}{\partial x} - fv' = -\frac{1}{\rho_0}\frac{\partial p'}{\partial x}, \tag{1.37}$$

$$\bar{u}\frac{\partial v'}{\partial x} + fu' = -\frac{1}{\rho_0}\frac{\partial p'}{\partial y}, \tag{1.38}$$

where p' is the pressure perturbation and u' and v' are the zonal and meridional wind perturbations respectively. By manipulating equations equation (1.37) and equation (1.38) (taking the x-derivative of equation (1.38) and subtracting the y-derivative of equation (1.37)); considering volume conservation ($u_x + v_y + w_z = 0$) and simplifying the notation for derivatives (such that $u_y = \partial u/\partial y$ and similar) we obtain equation 3.1 of Hoskins and Karoly (1981):

$$\bar{u}\zeta'_x + \beta v' = fw'_z, \tag{1.39}$$

where ζ is the relative vorticity ($\zeta \equiv v_x - u_y$), β is the change of the Coriolis parameter with latitude ($\beta \equiv f_y = 2\Omega\cos\phi/R$, where ϕ is the angle with respect to the vertical). The first term on the left hand side of equation (1.39) is a local increase of spin when the flow brings high vorticity fluid. The second term is the local increase of spin when a fluid parcel shifts towards the equator (the β-effect).

Equation 3.2 of Hoskins and Karoly (1981) is obtained from the second law of thermodynamics: $Ds/Dt = \dot{Q}/T$, where s is entropy, $\dot{Q}$ is the heating rate and T is temperature. Re-writing D/Dt in terms of an air parcel ($D/Dt = \partial/\partial t + u\partial/\partial x + v\partial/\partial y + w\partial/\partial z$), substituting potential temperature for entropy and employing the thermal wind relationship ($fv'_z = g\alpha\theta'_x$) gives equation 3.2b of Hoskins and Karoly (1981):

$$f(\bar{u}v'_z - v'\bar{u}_z) + w'N^2 = Q. \tag{1.40}$$

N is the Brunt-Väisälä frequency of the atmosphere, defined in equation (1.29). The three terms on the left hand side of equation (1.40) reflect the zonal, meridional and vertical advection of entropy respectively. By assuming synoptic scale diabatic heating in the upper troposphere and considering the situations when each term on the left hand side of equation (1.40) dominates, two different physical situations can be obtained:

- The diabatic heating is opposed by cooling due to expansion of a rising air parcel. From equation (1.39) this results in poleward motion at low-levels, and implies a low pressure west of the heating anomaly.
- The diabatic heating is opposed by cooling due to the advection of cold air from the pole. From equation (1.39), this results in downward motion in the mid-troposphere, and due to geostrophic balance a low-pressure cell east of the heating.

These two situations occur in the tropics and midlatitudes, and are depicted in Fig. 1.2a and Fig. 1.2b respectively. A third situation involving shallow heating in the midlatitudes is also shown in Fig. 2c, where low-level heating is balanced by the advection of zonal flow, leading to a temperature gradient in the direction of flow.

The situation depicted in Fig. 1.2a leads to Rossby wave perturbations that extend poleward and east of the source of the heating (Hoskins and Karoly 1981; Hoskins and Ambrizzi 1993; Ting and Sardeshmukh 1993). This mechanism is relevant for the understanding of the ESB response to climate change, discussed in section 3.4.5.

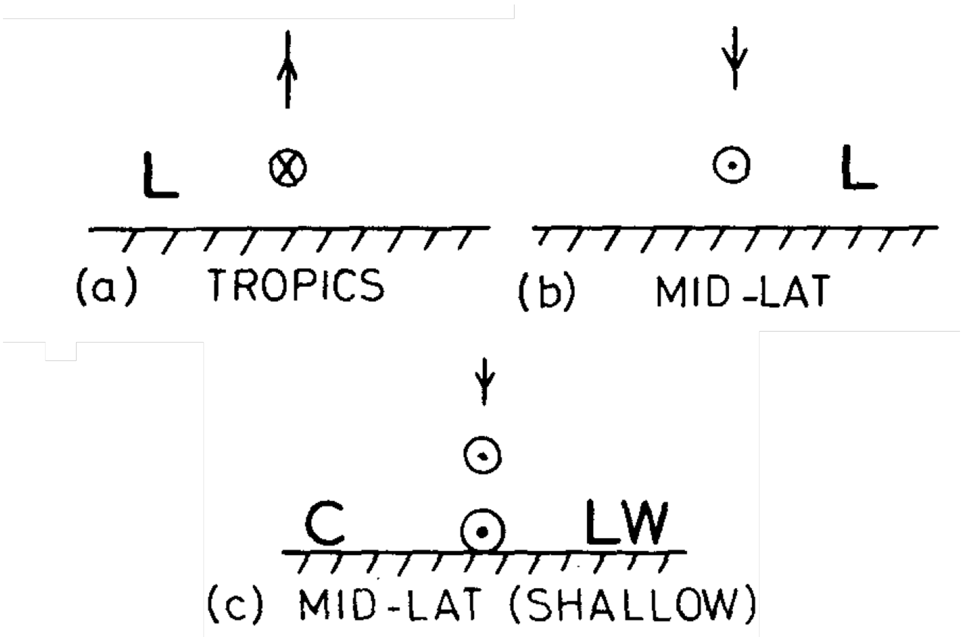

Figure 1.2: Longitude-height sections showing the different responses to thermal forcing in (a) tropics, (b) midlatitudes, and (c) the midlatitudes for shallow forcing. The arrow depicts vertical motion. Circled crosses and dots show motion into and out of the section, respectively. L is the pressure trough. C and W is cold and warm air respectively. Reproduced from Fig. 2 of Hoskins and Karoly (1981).

1.2.9 Barotropic and baroclinic instability

There are two broad characteristics of the flow in the atmosphere that separate the tropical atmosphere from the midlatitude atmosphere. In the tropics a common assumption made to describe the flow is that of a *barotropic atmosphere*. In a barotropic atmosphere pressure is only a function of height ($\rho = \rho(p)$). This means that surfaces of constant pressure are also surfaces of constant density. There is no horizontal gradient of temperature and no vertical wind shear, so the geostrophic wind is independent of height.

A *baroclinic atmosphere* is one in which the density is a function both of pressure and temperature (from the ideal gas equation $\rho = \rho(p, T) = p/RT$). Surfaces of constant pressure cut across surfaces of constant density at a constant angle. and a horizontal temperature gradient exists, along with a vertical wind shear. This is a useful way to describe midlatitude flow.

These two assumptions have associated hydrodynamic instabilities which describe much of the synoptic-scale flow in the atmosphere. *Barotropic instability* occurs when flow is unstable because of horizontal wind shear. Disturbances to the flow grow by extracting kinetic energy from the background flow. This describes short-waves in the jet stream and vortices in tornadoes

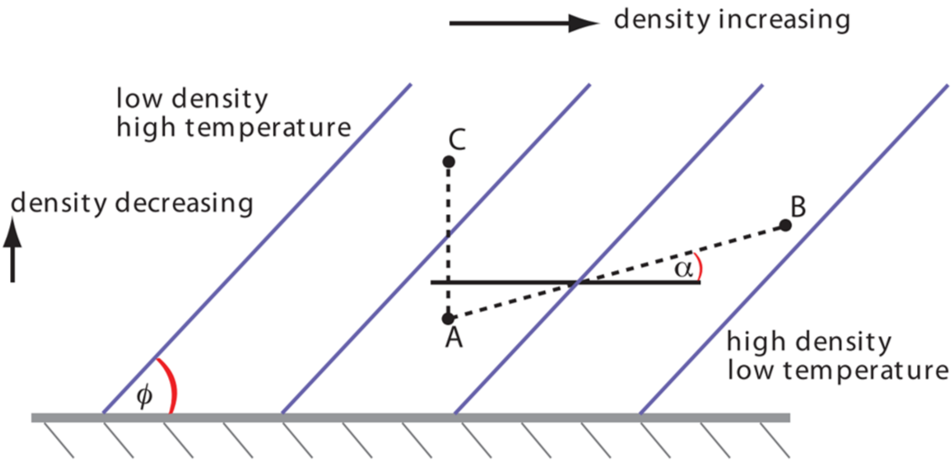

Figure 1.3: A steady basic state giving rise to baroclinic instability. Potential density decreases upwards and equatorwards, and the associated horizontal pressure gradient is balanced by the Coriolis force. Parcel 'A' is heavier than 'C', and so statically stable, but it is lighter than 'B'. Hence, if 'A' and 'B' are interchanged there is a release of potential energy. Reproduced from Fig. 9.9 of Vallis (2006b).

and tropical cyclones.

Baroclinic instability occurs in a rotating stably stratified fluid that is subject to a horizontal temperature gradient. From the thermal wind relationship this creates unstable vertical wind shear. Disturbances to the flow grow by extracting potential energy from the background flow, which is converted to potential and kinetic energy of flow perturbations. Baroclinic instability is the main instability which causes weather systems in the atmosphere (Vallis 2006b).

Given a basic state of a baroclinic atmosphere where there is stable baroclinic flow, layers of the atmosphere with decreasing potential density are at a constant angle with the surface. Each layer has some available potential energy, which could be converted to kinetic energy by adjacent air parcels shifting such that lower density air shifts to a higher altitude. A disturbance to the atmosphere introduces baroclinic instability where such movements of air parcels take place. This converts potential energy to kinetic energy, which feeds the instability. This process is shown in Fig. 1.3.

1.2.9.1 Baroclinic eddies

These disturbances form baroclinic eddies which extract energy from the mean midlatitude flow. In addition to this effect, the available energy of the mean flow is replenished by external radiative forcing, which maintains an equator-to-pole temperature gradient.

The scale of baroclinic eddies in the atmosphere is determined by the deformation radius (approximately 1000 km), the mean equator-to-pole temperature gradient (approximately 40 K), and the strength of the zonal flow and the β effect. The lifecycle and phenomenology of baroclinic eddies is also determined by the effect of geostrophic turbulence (Vallis 2006f). Baroclinic eddies can be cyclonic or anticyclonic. Regions where eddy activity is strongest determine the location of the storm tracks (Orlanski and Gross 2000), where extratropical cyclones most frequently occur. Baroclinic eddies interact with atmospheric blocking events by becoming less baroclinic close to the blocking high; anticyclonic eddies can reinforce atmospheric blocking events through advection of low potential vorticity air from lower latitudes (Nakamura and Wallace 1993).

1.3 Atmospheric blocking

1.3.1 Atmospheric blocking events

One important feature of extratropical circulation are persistent anti-cyclones which are known as atmospheric blocking events. These synoptic-scale events are characterised by a persistent reversal of the usual westerly flow over a region, which diverges weather systems to the North or South (Berggren et al. 1949; Rex 1950). They usually exhibit a large anticyclonic anomaly and often a dipole with a low-pressure system equatorward of the blocking high (Hoskins and James 2014a; Woollings et al. 2018).

Blocking events were first noted in the context of long-range forecasting by Garriott (1904). However, whilst blocking events have been extensively studied, the onset and longevity of blocking events is still not well forecast or completely understood (Lupo 2021). The American Meteorological Society (AMS) (Glickman and Zenk 2000) specifies three criteria to classify a flow pattern as blocked (Pinheiro et al. 2019):

1. persistent obstruction of the usual westerly flow,

2. pronounced meridional flow in the upper levels, and

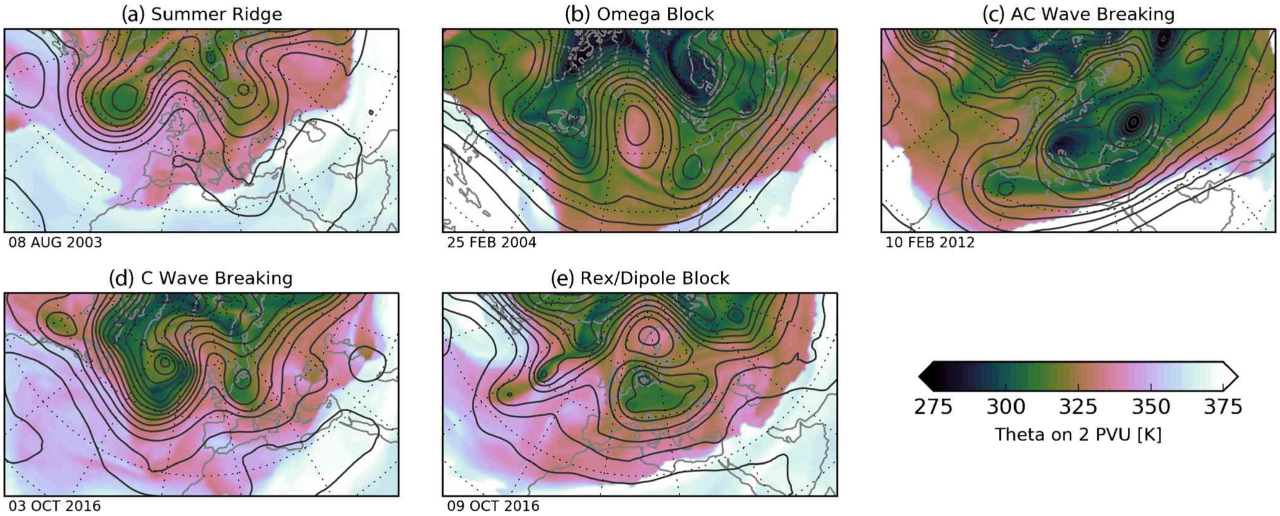

Figure 1.4: Example North Atlantic blocks. Snapshots of (colour shading) potential temperature (θ) on the dynamical tropopause (PV = 2 PVU) and (contour lines) geopotential height at 500 hPa (contour spacing 60 m) for the dates indicated. Data is from ERA-Interim. Caption and figure adapted from Fig. 1 of Woollings et al. (2018).

3. anticyclonic circulation at high latitudes accompanying cyclonic circulation at low latitudes.

A range of circulation patterns have been referred to as blocking events; the most important categories of atmospheric blocking are shown in Fig. 1.4. These include ridges in large amplitude Rossby waves with low phase speed, where low potential vorticity (PV) air is advected from the subtropics resulting in a large stationary anticyclone (Hoskins et al. 1985). The "omega block" is described as such since the geopotential height contours around the anticyclone resemble the letter Omega (Sousa et al. 2021). Blocking has also been characterised by Rossby wave-breaking, where PV on specific isentropes are folded over and the meridional PV gradient is reversed (Gabriel and Peters 2008). Other blocking events can be associated with a bifurcation of the jet stream (Sumner 1954).

Blocking events with a dipole characteristic are typically formed through the poleward motion of warm air and equatorward and eastward movement of cooler air. The two air masses develop anticyclonic and cyclonic motion and are cut off from their source. This Rossby wave-breaking sets up a blocking anticyclone (Hoskins and James 2014a). Furthermore, Nakamura and Huang (2018) has recently compared the onset of a blocking event to traffic congestion, where as a highway has a limit to the number of vehicles before congestion, the jet stream has a limited capacity for meandering wave activity, beyond which a blocking pattern forms.

Blocking events can often persist for several weeks. Their persistence is due to the fact that a dipole cut-off structure can only be returned back to westerly flow if the cyclone and anticyclone are advected back to their source positions (which can occur only through a strong incoming weather system), or through frictional and heating processes (which have a timescale of weeks) (Hoskins and James 2014a). Furthermore, synoptic-scale eddies can reinforce the blocking structure. Eddies propagating into a split jet stream develop a meridionally stretched vorticity field, which reinforces the vorticity fields in the block (Shutts 1983; Mullen 1987; Swanson et al. 1997; Altenhoff et al. 2008).

1.3.2 Atmospheric blocking and extreme weather

Blocking systems are often associated with regional extreme weather events, particularly heatwaves in summer and cold snaps in winter. A widely studied example was the record-breaking 2003 European heatwave. This event exhibited a range of significant societal impacts such as increased mortality, reduced crop yields and reduced labour productivity (Ciais et al. 2005; Robine et al. 2008; García-Herrera et al. 2010; García-León et al. 2021).

The 2003 heatwave was shown to have been made at least twice as likely due to anthropogenic climate change (Stott et al. 2004). According to climate change projections, such heatwaves will become commonplace by the 2040s irrespective of future emissions scenarios (Christidis et al. 2014). The most extreme temperatures during this heatwave were recorded from the 6-12 August, where the peak temperature recorded was in Southern France at 41°C. Black et al. (2004) reports that atmospheric flow anomalies were recorded in early August, although there was a relatively weak signature of blocking. The 2003 heatwave remained the European temperature record until 2019, when surface temperatures of 46°C were observed in central France. The 2019 heatwave was concurrent with persistent hot air that originated in North Africa (the so-called "Saharan heat bubble"), which was sustained by an omega block centered on Western Europe (Mitchell et al. 2019).

Other extreme weather events associated with blocking include the 2010 Russian heatwave (Schneidereit et al. 2012) and the 2018 European heatwave (Kueh and Lin 2020). The recent 2021 Pacific Northwest heatwave was also associated with an omega block (Philip et al. 2021). Persistent ridges over the North-Eastern Pacific have led to several recent periods of drought in California (Swain et al. 2016), and the 2009/10 winter cold events in Europe were associated with atmospheric blocking (Cattiaux et al. 2010).

1.3.3 The effect of climate change on atmospheric blocking

The influence of climate change on atmospheric blocking remains an open question (Francis and Vavrus 2012; Barnes 2013; Francis and Vavrus 2015; Barnes and Polvani 2015; Barnes and Screen 2015; Mann et al. 2018; Coumou et al. 2018a; Fabiano et al. 2021). As a complex dynaical feature of the atmosphere, the underlying physics involved in developing atmospheric blocking events is nonlinear (Palmer 1999) and not fully understood (Nakamura and Huang 2018; Woollings et al. 2018; Hauser et al. 2022). Furthermore, there is a large seasonal, inter-annual and decadal variability (Kennedy et al. 2016; Brunner et al. 2017), which compounds the problem of separating forced changes in blocking occurrence from unforced variability (Barnes et al. 2014; Shepherd 2014). There are two prominent mechanisms that have been discussed as possible mechanisms which can affect summer atmospheric blocking under climate change: Arctic Amplification (AA) and increased upper-tropospheric warming (UTW). These two mechanisms have competing influences and have been described as in a "tug-of-war" (Barnes and Screen 2015) of effects which work to increase and decrease atmospheric blocking occurrence respectively.

Arctic amplification (AA) is the the increased surface warming over the Arctic compared to the rest of the Earth surface (Manabe and Wetherald 1975), associated with rapid sea ice loss (Dai et al. 2019). It has been hypothesised that this impacts the Northern Hemisphere polar jet stream (Francis and Vavrus 2012), since by reducing the meridional temperature gradient the speed of the jet stream may also decrease. It has been proposed that this slows down Rossby waves and increases their amplitude (Francis and Vavrus 2015; Francis et al. 2018), increasing the likelihood of blocking events.

This hypothesis has received criticism, with several studies claiming that there is no convincing evidence that a link between AA and midlatitude extreme weather exists (Barnes 2013; Barnes and Screen 2015; Blackport and Screen 2020; Dai and Song 2020). Cohen et al. (2020) noted that whilst there is significant observational evidence to link AA to winter midlatitude extreme weather including atmospheric blocking, particularly in the Barents-Kara sea region, there is limited evidence from modelling studies to associate AA and severe midlatitude weather. One example of a modelling study investigating this relationship is McCusker et al. (2016), who found that from 600 years of GCM simulations with multiple ensembles, the unusually cold winters reported over the Barents-Kara sea region relate to a pattern of anticyclonic activity that is independent of AA. Whilst there are several studies which propose a connection between Arctic sea ice loss and midlatitude weather extremes (Honda et al. 2009; Petoukhov and Semenov 2010; E. et al. 2011; Inoue et al. 2012; Liu et al. 2012), the role of Arctic Amplification in this link between sea ice loss and midlatitude extremes is not clear (Hopsch et al. 2012). Screen and Simmonds (2013) found that the link between Arctic warming and midlatitude wave amplitude is sensitive to the definition of wave. Additional proposed hypotheses to connect AA to midlatitude extreme weather include the weakening of the Arctic stratospheric polar vortex (Cohen and Barlow 2005; Kim et al. 2014; Garfinkel et al. 2017), and the favourable occurrence of splits in the jet stream (Petoukhov et al. 2013; Coumou et al. 2014). This divergence of conclusions leads to a lack of clarity about the role AA plays in midlatitude weather extremes.

A second and competing mechanism that is frequently discussed in the literature which may have an impact on ESB under climate change is enhanced tropical upper-tropospheric warming (UTW). The temperature gradient between the tropics and mid-latitudes at higher altitudes is strengthening under anthropogenic greenhouse gas forcing (Allen and Sherwood 2008), which would work to increase jet stream-level winds through the thermal wind relationship (see section 1.2.3). An increased upper-level temperature gradient is expected to shift the jet stream poleward and increase storm track activity (Held 1993). This may work to decrease the persistence and frequency of atmospheric blocking events by reducing the stationarity of circulation patterns (Vries et al. 2013). This process competes with AA which is expected to shift the jet stream equatorward, weaken the jet stream and decrease storm track activity, leading to more blocking events (Barnes and Polvani 2015).

Further discussion of the role of these mechanisms in influencing the ESB response to climate change events is discussed in chapter 3.

1.3.4 The representation of atmospheric blocking in global climate models

Global climate models are known to generally underestimate the occurrence of atmospheric blocking (Berckmans et al. 2013a). Newer generations of complexity of models have led to sizeable improvements in the simulation of atmospheric blocking events (Davini and D'Andrea 2016; Schiemann et al. 2020). Fernandez-Granja et al. (2021) note that whilst there is a general (although not without exceptions) improvement in the CMIP6 models, the latest generation of CMIP6 models still shows significant biases in the representation of atmospheric blocking events.

A commonly cited reason for the bias is the lack of horizontal atmospheric resolution in the models (Scaife et al. 2010; Schiemann et al. 2020). Higher horizontal resolution can improve transient eddy activity and therefore enable the blocking highs to be sustained (Berckmans et al. 2013b). Mean state biases have also been identified as a reason for the low occurrence of atmospheric blocking in models, since blocking occurrence has been shown to be sensitive to the climatological mean state (Scaife and Knight 2008; Matsueda et al. 2009; Woollings et al. 2010). Improving the horizontal resolution of orography can also decrease the blocking bias, since the mean state of planetary waves is better described (Brayshaw et al. 2009). Improved convection over the Pacific can also reduce the atmospheric blocking bias (Jung 2012), which suggests a physical connection between convection in the Pacific and atmospheric blocking. This last point will be particularly important for a mechanistic discussion of potential future ESB changes in section 3.4.5.

1.3.5 Future trends in atmospheric blocking in global climate models

In general, most models show a small decrease in atmospheric blocking under climate change, but with significant differences regionally and seasonally (Woollings et al. 2018). The CMIP3, CMIP5 and CMIP6 model ensembles all predict a multi-model mean reduction in blocking occurrence in the future (Barnes et al. 2012a; Masato et al. 2013; Davini and D'Andrea 2020). Davini and D'Andrea (2020) found statistically significant decreases in the atmospheric blocking in both JJAS and DJFM across most of the NH (with some positive trend over the Barents-Kara sea area). Stronger trends were found in winter than in summer, but for European summer the trend in atmospheric blocking decreased. Woollings et al. (2018) also generally found decreases in NH atmospheric blocking as a result of climate change, although for the most part not statistically significant. The Greenland blocking index, which uses geopotential height anomaly over Greenland as a proxy for atmospheric blocking over the region (scaled by the NH geopotential height increase to account for thermodynamic climate change) has also been observed to be generally stationary or to decrease in the CMIP6 runs (Delhasse et al. 2021). High-resolution models similarly predict a decline (Matsueda et al. 2009).

This decrease in atmospheric blocking across climate models can be explained by the change in the mean state and variance of the westerly winds (Vries et al. 2013). This suggests that the change in atmospheric blocking events under climate change in the climate models is a passive change in response to changes in the mean flow rather than an active component acting on atmospheric blocking events specifically. However, although changes in blocking occurrence are generally small, the impact of blocking events under climate change on surface temperature extremes can be modified by climate change. This is because changes to the land-sea temperature contrast under climate change (Sejas et al. 2014) modify thermal advection associated with atmospheric blocking patterns (Masato et al. 2014).

In addition, given the challenges that climate models have in representing atmospheric blocking (see section 1.3.4), the fact that most climate models show a general decrease in the future occurrence of atmospheric blocking has not led to a consensus view in the literature of the role of atmospheric blocking (Woollings et al. 2018). Furthermore, other mechanisms (in addition to those discussed in section 1.3.3) have been suggested that could lead to increases in the occurrence of atmospheric blocking with climate change. These include quasi-resonant amplification (Petoukhov et al. 2013) and the formation of double jets (Petoukhov et al. 2013; Coumou et al. 2014). Mann et al. (2018) found that quasi-resonant amplification is increasing with climate change in the CMIP5 model archive, which could be associated with atmospheric blocking, and Rousi et al. (2022) found that increased persistence in heatwaves is associated with increases in double jet formation. Therefore, whilst climate models show a general decrease in atmospheric blocking in the future, the response of atmospheric blocking to climate change remains an open question.

1.4 Data

The data that I use in this thesis includes data from Global Circulation Models and from global reanalysis data.

1.4.1 Global climate models (GCMs)

Global circulation models are mathematical-physical models of radiative transfer and the circulations of the atmosphere and oceans. They use the equations discussed in sections 1.2.1-1.2.7 with the energy sources of radiation and latent heat to simulate the Earth's atmosphere and oceans. They include several components, which with the recent generations of GCMs often extends them to 'Earth System Models (ESMs)', such as interactive atmospheric chemistry, land-surface and sea ice components. Different GCMs have different levels of complexity and resolution, and coupled GCMs include feedbacks between the atmosphere and ocean. In this thesis, I use data from the two latest generations of inter-comparisons between GCMs: The Coupled Model Intercomparison Project Phase 5 (CMIP5) (Taylor et al. 2012) and the Coupled Model Intercomparison Project Phase 6 (CMIP6) (Eyring et al. 2016). In each of these intercomparison projects, several experiments are run, where the models are forced in different scenarios. In this thesis I show data from three different experiments:

- the pre-industrial control (piControl) scenario, where models can be run for centuries using a constant pre-industrial climate forcing (e.g., pre-industrial levels of CO_2);
- the historical scenario, where models are run across the historic period (from 1850-2005 in CMIP5 and 1850-2012 in CMIP6) using the historic prescribed emissions for this period of CO_2 and atmospheric components such as aerosols and CFCs;
- the 4xCO_2 scenario, where the models are forced with a sudden quadrupling of CO_2 in the atmosphere starting from pre-industrial baseline simulations.

Several such modelling experiments are available for each climate model. Each model is run with a number of ensemble members in order to estimate the effects of internal variability.

1.4.1.1 Sources of uncertainty in GCMs

There are three sources of uncertainty in climate projections from GCMs (Hawkins and Sutton 2009; Wu et al. 2022):

1. **Natural variability**. This refers to the natural fluctuations in the Earth's climate that are produced without radiative forcing. The dominant source of this uncertainty in the midlatitudes is internal atmospheric variability associated with (Deser et al. 2012) annular modes of circulation variability such as the North Atlantic Oscillation (Visbeck et al. 2001) and the Southern Annular Mode (Fogt and Marshall 2020). The use of different ensemble members for a given GCM can quantify this uncertainty.

2. **Model uncertainty**: this is the uncertainty associated with the fact that different models have different responses in their climates under the same radiative forcing. These differences arise from varied implementation of numerical methods, different parameterisations of mathematical expressions, and different integrations between small-scale and large-scale processes (Wang et al. 2022). Using an ensemble of models can quantify this uncertainty. The increased integration of complex biological, chemical and physical processes in the CMIP6 model ensemble compared to CMIP5 leads to greater complexity in the investigation of model uncertainty (Eyring et al. 2016).

3. **Scenario uncertainty**. Scenario uncertainty arises from the uncertain changes in future emissions of greenhouse gases and other pollutants. This uncertainty arises from different projections of population and social and economic development (Yu et al. 2018). The use of different pathways of future development (labelled the SSP scenarios in CMIP6 (Eyring et al. 2016)) can quantify this uncertainty.

1.4.2 Reanalysis data

A climate reanalysis project is a global data assimilation of historic weather measurements, that is assimilated across an extended period on homogeneous spatial grids at various time resolutions. In this thesis, I use the ERA5 global reanalysis from 1979-2019 (Hersbach et al. 2020), produced by ECMWF. The ERA5 reanalysis uses data from several sources including satellite observations, weather stations and radiosondes. The data is assimilated and a weather prediction model is combined with the data assimilation algorithm to produce a gridded dataset of historic atmospheric, oceanic and land surface variables at a horizontal resolution of 30 km grid and a time resolution of 3 hours. The atmospheric variables are produced across 137 vertical levels, which extend up to 80 km from the surface. I take the ERA5 reanalysis to be a broadly reliable reconstruction of the historic synoptic-scale weather across the Euro-Atlantic region which I am interested in.

1.5 Methods

1.5.1 Blocking indices

Whilst much significant work has been undertaken to understand blocking events, there is no complete theory that can capture all of the processes across the life cycle of a blocking event (onset, maintenance, decay) (Woollings et al. 2018). The different ways of understanding blocking events has led to a wide variety of blocking indices (BIs) to automatically detect blocking events (Lejenäs and Økland 1983; Dole and Gordon 1983; Tibaldi and Molteni 1990; Pelly and Hoskins 2003; Schwierz et al. 2004; Small et al. 2013; Chen et al. 2015; Thomas et al. 2021). The uncertainty around the definition and categorisation of blocking events complicates the task of comparing scientific results (Liu 1994).

The first blocking climatology defined blocking as a persistent surface high pressure anomaly that exceeded a certain climatological threshold for a long period (Elliot and Smith 1949). Lejenäs and Økland (1983) adapted the criterea from Rex (1950) to develop a one-dimensional index based on the geopotential height differences between 60° N and 40° N, computed across longitudes. This method was adapted by Tibaldi and Molteni (1990), who added a further condition between 80° N and 60° N to remove instances of a southward displacement of the westerly jet that would not be recognised as blocked. The Tibaldi and Molteni (1990) index has been widely adopted in the literature, with a range of modifications employed to improve blocking detection (Barriopedro et al. 2006; Barriopedro et al. 2010; Schalge et al. 2011; Davini et al. 2012; Barnes et al. 2012b). In particular, Scherrer et al. (2006) extended the one-dimensional method of Tibaldi and Molteni (1990) across latitudes to develop a two-dimensional climatology of blocking.

An alternative development of a blocking index involves using geopotential height anomalies over an extended area for a period of time (Dole and Gordon 1983; Shukla and Mo 1983; Knox and Hay 1984). Subsequent literature has developed thresholds used for the amplitude, persistence, areal extent and contour overlap (the extent to which blocked regions overlap on adjacent days) of the blocked region (Pinheiro et al. 2019). Hybrid indices have also been developed that combine thresholds for the anomaly of the field and the meridional gradient of geopotential height (Barriopedro et al. 2010; Dunn-Sigouin et al. 2013). In addition, motivated by the potential vorticity perspective (Hoskins et al. 1985), Pelly and Hoskins (2003) developed a blocking index using the overturning of potential temperature on the PV = 2 PVU surface. Schwierz et al. (2004) adapted the method of Dole and Gordon (1983) but used mid-tropospheric potential vorticity anomalies as the field to identify blocking instead of geopotential height anomaly.

The multiplicity of these BIs, with a variety of thresholds for defining the area, persistence and magnitude of blocked features on different atmospheric dynamical variables, mean that these methods necessarily carry the burden of somewhat subjective definitions. Notably, while previous intercomparisons of BIs show similar global climatologies, and while all indices capture many of the basic features of atmospheric blocking within their definitions, there are known regional and seasonal differences (Croci-Maspoli et al. 2007; Barriopedro et al. 2010; Pinheiro et al. 2019). For example, Pinheiro et al. (2019) found that the Scherrer et al. (2006) adaptation of the Tibaldi and Molteni (1990) method identified anomalous features in the low latitudes in NH summer and an approximately 10% blocking frequency over most of Northern Europe for JJA. However, the Dole and Gordon (1983) approach did not exhibit such anomalous low latitude features, and also had a higher blocking frequency (15%) in the JJA Euro-Atlantic region, with a distinct maximum South of the Icelandic low.

In addition, whilst spatial climatologies obtained from these BIs have been compared extensively, to the best of my knowledge there has been no direct *time series* comparison of the BIs beyond case study analyses such as those in Scherrer et al. (2006) and Pinheiro et al. (2019). A time series comparison forms part of chapter 2.

One important consideration is that the Tibaldi and Molteni (1990) index has been most frequently used to identify DJF blocking events in the NH, which is the most commonly studied period for blocking. This thesis focuses on studying blocking events in summer, as these are associated with extreme heat, which has significant societal impacts. However, in the NH summer the eddy-driven jet stream shifts poleward and the subtropical jet, which is usually confined to the upper troposphere, exerts a stronger influence on midlatitude circulation anomalies (Illari 1984; Woollings et al. 2010). This suggests that the thresholds and variables that are commonly used in a winter context may not be valid in summer (Small et al. 2013).

In chapter 2, I use three blocking indices to compare to a new blocking index that I have developed. These three are:

- **AGP** - the geopotential height gradient method, which is the Tibaldi and Molteni (1990) index as adapted by Scherrer et al. (2006) to construct a two-dimensional field of geopotential height gradients
- **DG83** - the Dole and Gordon (1983) method of investigating positive geopotential height anomalies
- **S04** - the Schwierz et al. (2004) method of identifying persistent anomalies in the potential vorticity field (VPV) averaged over 150-500 hPa (VPV).

These methods were developed from previous work by Pinheiro et al. (2019) who applied four thresholds for each blocking index: the magnitude of the anomaly, the persistence of the blocking event (minimum five days), a minimum area over which the anomaly takes place and an overlap criterion which measures if there is continuity across the blocked region between different days (an overlap of the blocked contours). Pinheiro et al. (2019) standardised the thresholds used for these different methods to develop an intercomparison. For my application of these methods in chapter 2 I apply further modifications, which will be discussed in section 2.2.3.

1.5.2 Machine learning

In my thesis, I apply machine learning (ML) techniques to develop a new blocking index. ML involves the use of predictive models which iteratively use data to improve performance on specific tasks ("learning"). ML has been frequently employed in several atmospheric science applications (e.g. Skific and Francis (2012), Lary et al. (2016), Gil et al. (2018) and Karpatne et al. (2018)), including the study of regional atmospheric circulation patterns (Horton et al. 2015; Schlef et al. 2019; Juliano and Lebo 2020).

There are two broad categories of ML algorithms: supervised learning and unsupervised learning algorithms. Both of these are used in this thesis. Supervised learning is a set of methods in which predictive models are trained on a labelled dataset (i.e. there are predictors and predictands). This can be either a regression or classification task. For the latter, the goal is to identify the difference between different classifications (where the classes are the predictands, and features characterising the classes are the predictors) of data, such that it can from a new set of data create accurate classifications. In the case of binary labelled datasets where each data point can be one of two types (such as a picture being of a dog or a cat), the skill of a model can be quantified using the classification skill measures described in section 1.5.3.

Unsupervised learning involves training a consistently associative model from an unlabelled dataset (such as a series of daily geopotential height anomalies over a region). An algorithm is used to infer consistent patterns from the unlabelled dataset. Common unsupervised learning techniques are clustering algorithms, where a specified number of distinct patterns is provided as input, and the algorithm produces that number of distinct clusters by iteratively adjusting the patterns to states representative of the training data. The input patterns can initially be randomly defined, randomly selected from data samples or initialised using other dimension reduction methods such as principal component analysis. In the case of regional daily geopotential height anomalies, the output clusters could be types of circulation patterns over the region. There are two clustering algorithms that are used in this thesis: K-means clustering and self-organizing maps. K-means is introduced in section 1.5.4, self-organizing maps (SOMs) are introduced in section 1.5.5. The use of these clustering approaches in identifying blocking events is discussed in section 1.5.6.

1.5.3 Classification skill measures

There are several skill measures that can be used to identify how skillful a classification algorithm is; the three classification skill measures used in this thesis are precision, recall and F_1 score. **Precision** (P) is defined as the ratio of true positives to total detected positives. For example, a precision of 0.8 indicates that 80% of the events identified by a method are true positives and the remaining 20% are false positives. Note that in meteorological forecasting literature, the equivalent metric to precision is called the *success ratio* (Roebber 2009). **Recall** (R) is the number of true positives divided by the total number of actual events. A recall of 0.8 indicates that 80% of all total blocking events are captured by the classification method, but 20% are false negatives. Note that in meteorological forecasting literature, the equivalent metric to recall is called the *probability of detection* (Roebber 2009). A higher recall is typically associated with a loss in precision, as identifying more events also means that one typically identifies more false positive events. Therefore, a careful balance between precision and recall is usually sought after. One widely used skill metric to achieve this balance is the **$\mathbf{F_1}$ score**, which is the harmonic mean of precision and recall:

$$\mathrm{F}_1 = \frac{2 \cdot \mathrm{P} \cdot \mathrm{R}}{\mathrm{P} + \mathrm{R}} \tag{1.41}$$

which can vary between 0 (worst case, low detection skill) and 1 (best score). If either P or R are low, the F_1 score tends towards 0, thus indicating low detection skill in at least one of the two measures. For example, if a given classification algorithm identifies a small number of events correctly, the precision is very high but the recall is very low - a small number of events are well described but many events are missed by the classification. When a larger number of events are identified, then typically precision decreases and recall increases; more events are described but there is also a higher proportion of false positives.

1.5.4 K-means clustering analysis

K-means clustering analysis (Lloyd 1982) has been used extensively in atmospheric science to classify weather patterns (e.g. Vautard 1990; Michelangeli et al. 1995; Kageyama et al. 1999; Cassou 2008; Hannachi et al. 2017; Fabiano et al. 2021). As input to the algorithm, a specified number of clusters to produce is chosen and applied to an unlabelled dataset. In classifying atmospheric weather patterns this will often involve classifying daily geopotential height anomalies over a region. Each cluster is characterized by a data vector or matrix called the "centroid", which represents the center of a set of data points associated with the cluster. Here, this could for example be the mean pattern of daily geopotential height data for those samples, representing a typical circulation pattern. Each data entry (e.g. each daily geopotential height pattern) has one centroid which it is closest to in Euclidean distance. The purpose of the algorithm is to identify the optimal location in the data for each centroid, such that the location of each centroid is such that the total sum of squared errors across all clusters is at a minimum.

Once the k number of clusters is specified, the algorithm assigns the location of each within the space of all data points. This can be done by randomly setting a location within each dataset, sampling k random points within the dataset, or by using principal component analysis. Then each data sample is assigned to its nearest centroid, specified by the one with the smallest Euclidean distance between them. Next, the new center for each cluster is specified by shifting the location of each centroid to be the mean position across all the data samples that are - at the current iteration - assigned to it. This process is then repeated: by shifting the position of each cluster (or, its centroid), a different set of data samples will be assigned to each, leading to updated centroid positions. This process repeats until a new iteration of each centroid does not re-assign any of the data samples to a new centroid. At this point the algorithm has converged, and the mean position of each centroid/cluster is considered to be the final position for the given number of clusters (Hartigan and Wong 1979). In the case of daily geopotential height data patterns, this is often considered to be a set of typical atmospheric circulation patterns.

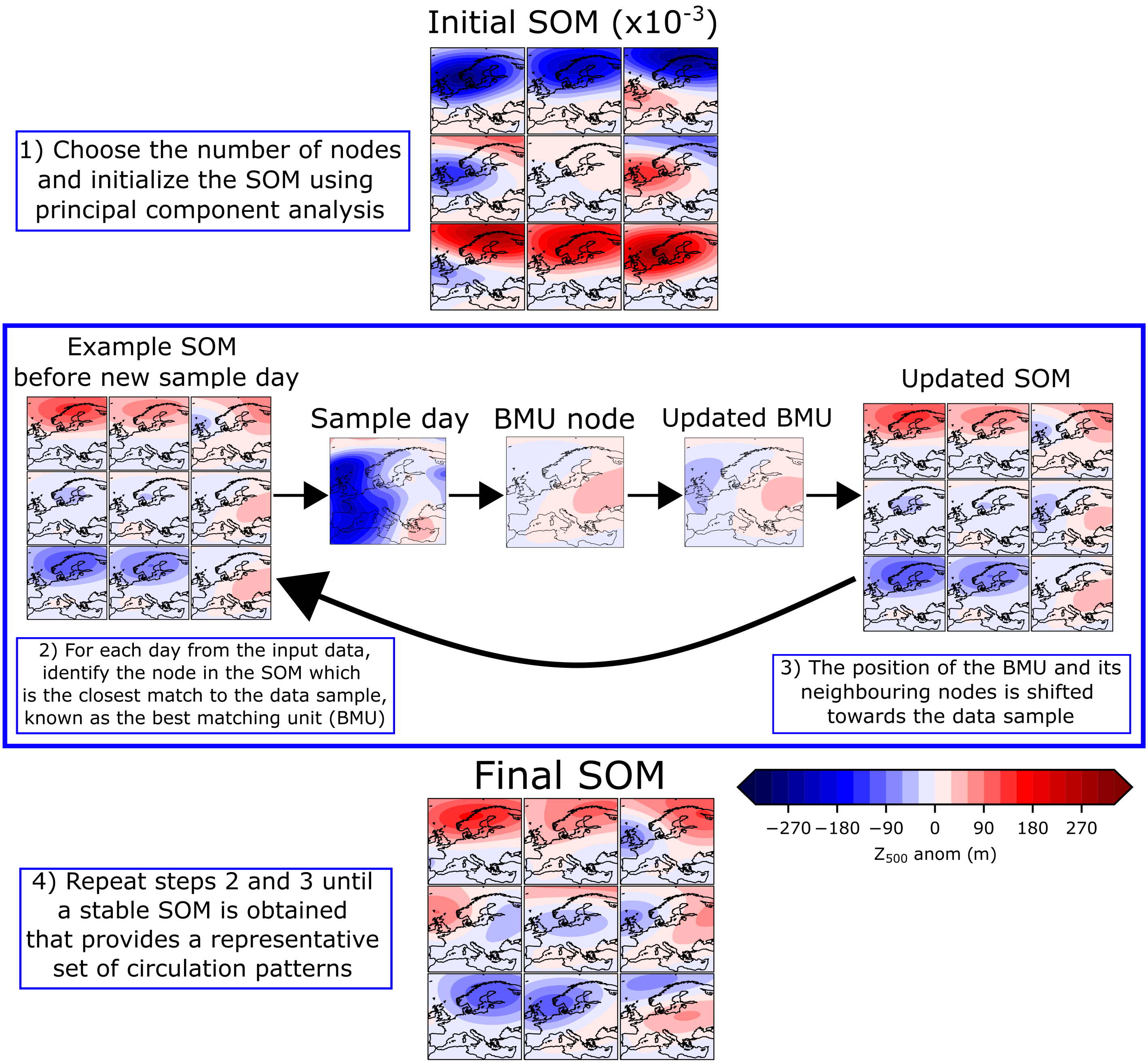

Figure 1.5: The self-organizing map algorithm. Illustrated using a 3x3 node SOM with ERA5 Z_{500} JJA 1979-2019. The PCA-initialised SOM pattern (step 1) has a much larger amplitude so has been multiplied by 10^{-3} for visualisation purposes. The BMU refers to the best-matching unit, the SOM node which most closely matches the sample day.

1.5.5 Self-organizing maps (SOMs)

Self-organizing map cluster analysis (SOM; Kohonen 1982) is an increasingly popular unsupervised machine learning technique in synoptic meteorology to learn representative patterns of weather regimes and to investigate their trends (Hewitson and Crane 2002; Liu and Weisberg 2005; Huth et al. 2008; Sheridan and Lee 2011; Johnson 2013; Horton et al. 2015; Xu et al. 2016; Singh et al. 2016; Diffenbaugh et al. 2017; Sánchez-Benítez et al. 2019). In the context of this thesis, the SOM algorithm is trained with daily spatial maps of dynamical states of the atmosphere above Europe, as for example characterized by maps of geopotential height anomalies, potential vorticity or sea level pressure. By iteratively cycling through all samples of such meteorological maps, the algorithm learns representative patterns of atmospheric dynamical states, which are referred to as "SOM nodes". Note that across this thesis, I use the term **centroid** to refer to each map in the optimised K-means cluster (there are K number of centroids in each K means analysis), and the term **node** to refer to each optimised map in the SOM grid in the SOM. An infographic to show the application of the SOM algorithm to classifying European circulation patterns is shown in Fig. 1.5.

First, the number of nodes is specified and the SOM is initialised either with random values or with principal component analysis patterns. Then for each day from the input field, the Euclidean distance between that daily meteorological pattern and each node pattern is calculated. The node with the smallest Euclidean distance to the sample day is known as the best matching unit (BMU) for that day. Then the BMU pattern is updated to shift towards the pattern of the sample day. The neighbouring SOM nodes (on the grid of SOM nodes) are also updated to shift towards the sample day according to a Gaussian neighbourhood function. The Gaussian neighbourhood function ensures that the updates for the neighbouring nodes are smaller than the update for the BMU. For each cycle of iterations through all training samples, the updates tend to become smaller as the SOM nodes converge towards a representative pattern of atmospheric dynamical states. A decay function on the updates is additionally applied, which ensures convergence. Finally, a stable SOM is obtained with a set of nodes that each provide a representative composite of circulation patterns, arranged according to their similarity on a row-column grid (i.e. the map). A diagram of the training procedure is shown in Fig. 1.5. The number of nodes to be learned by the algorithm, or in other words the number of representative weather patterns one aims to learn for a particular meteorological problem, is chosen by the user.

SOMs are of particular relevance in atmospheric science because they maintain the topological properties of the input space. Once optimised, each node pattern represents a possible state of the atmosphere, and the nodes are arranged in order of similarity, thus representing a continuum of atmospheric states. This contrasts with other methods of dimension reduction such as principal component analysis, where the identified patterns are orthogonal. Such purely mathematical representations are typically less meaningful from a physical point of view, whilst each SOM node maintains physical significance as it can closely resemble actual atmospheric states found in meteorological data, with the nodes on the row-column grid representing smooth transitions across those possible atmospheric states (see the similarity of neighbouring nodes in the final SOM grid in Fig. 1.5). I have implemented the SOM algorithm using the somoclu Python package (Wittek et al. 2017).

This property of SOMs is also a significant distinguishing feature between SOMs and K-means clustering. In the case of K-means clustering, each centroid is updated at each iteration independently and no neighbourhood function is applied. As a result, K-means maximizes differences between the nodes such that it does not learn a smooth topology of possible atmospheric states. This difference between K-means and SOMs is minor for low node numbers, since the sharp differences in spatial patterns are effectively imposed on the SOMs as to be able to represent the range of atmospheric states with only a small number of nodes, thus making the effect of the neighbourhood function negligible. For larger node numbers, the SOM topology becomes smoother and the K-means centroids remain distinct rather than representing a continuum of states, whereas a continuum is a more realistic reflection of the actual atmosphere (Skific and Francis 2012). A comparison between SOMs and K-means analysis for 4 and 20 node/cluster numbers is shown in Fig. A.5 in Appendix section A.3.

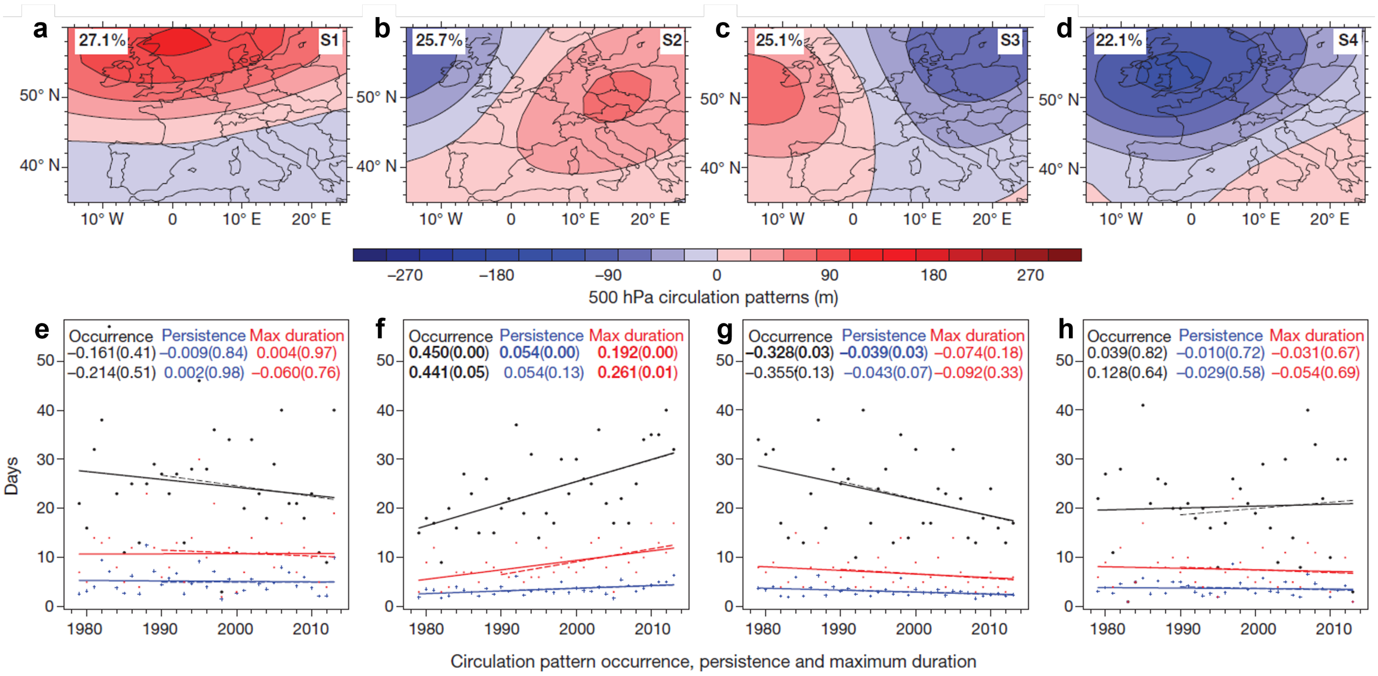

Figure 1.6: Adapted from Figure 3 of Horton et al. (2015). Trends in JJA circulation patterns over Europe. Identified by a four node SOM using daily 500 hPa geopotential height data from the 1979-2013 NCEP-DOE-R2 reanalysis (Kanamitsu et al. 2002). **(a-d)** shows SOM-derived atmospheric circulation patterns if the number of nodes is set to four. White boxed percentages in the top left show the frequencies of each pattern. The SOM node numbers are labelled in the top right. **(e-h)** shows the seasonally averaged time series of SOM circulation patterns across four metrics from 1979 to 2013: the total number of daily occurrences of patterns in each year (labelled "occurrence" and in black), the average length of circulation pattern occurrence (labelled "persistence" and in blue); and the maximum duration of each circulation pattern in each year (labelled "max duration" and in red). Each panel has a straight line showing the trend across 1979-2013, and a dashed line showing the trend from 1990-2013. At the top of each panel in **(e-h)** the colour-coded slopes of the trends are shown, with the 1979-2013 trend displayed above the 1990-2013 trend. The p-value of each trend is displayed in parentheses after the trend, and where the p-value is less than 0.05 the slope and p-value is in bold font.

1.5.6 A comment on previous use cases of clustering approaches to identifying blocking events

1.5.6.1 Self-organizing maps

In this section, I discuss some of the previous uses of clustering approaches in analysing circulation patterns, highlighting some of their benefits and limitations. This motivates my development of a new approach to analysing atmospheric blocking events using machine learning, which is introduced in chapter 2.

An approach to studying atmospheric circulation patterns through self-organizing maps was developed by Horton et al. (2015). They used SOM cluster analysis to track the occurrence and duration of circulation patterns over Europe and correlate these patterns with surface temperature extremes. By using the Cassano et al. (2007) method of correlating the surface temperature trends with the trends in the circulation patterns, they were able to quantify the thermodynamic and dynamic contributions to the increasing surface temperature extremes over Europe. They concluded that the "observed increase in extreme summer heat over Europe is attributable to both increasing frequency of blocking circulations and changes in the surface energy balance".

In their analysis, they explicitly associated an increase of atmospheric blocking events with the increased occurrence and persistence of the SOM pattern involving a dipole showing ridging across central Europe. This patterns and its trend are shown in Fig. 1.6b and Fig. 1.6f respectively. However, using the increased occurrence and persistence of this node to identify blocking patterns is unconvincing for several reasons:

- Most blocking events over Europe are centered over Scandinavia (see Fig. A.4 in section A). If one of the four SOM nodes used in Horton et al. (2015)'s analysis was to be associated with blocking events, it would then more naturally fit with Fig. 1.6a. Fig. 1.6c will be associated with some blocking events, but certainly not all of them.
- Fig. 1.6c with the ridge shifted across to Western Europe may actually be a better fit for the blocking anticyclones associated with some prominent Western European heatwaves such as the 2003 and 2019 heatwaves, where the anticyclone was centered on continental Western Europe (see Fig. 2.4 and 2.5 for a discussion of these case studies).
- As the occurrence and persistence of the Fig. 1.6b pattern increases, the occurrence and persistence of the opposite pattern in Fig. 1.6c decreases. This could mean that the number of blocking events is constant but that the center of the blocking anticyclone shifts to the Eastern part of the domain from the Western part. Therefore, it is not clear from the trend in Fig. 1.6f alone that there is a significant increase in the occurrence of atmospheric blocking events.
- Since blocking events are identified as **persistent anticyclones**, it is inaccurate to use daily circulation patterns to categorise a pattern as a circulation pattern. There will be several days in the period studied by Horton et al. (2015) which reflect circulation patterns

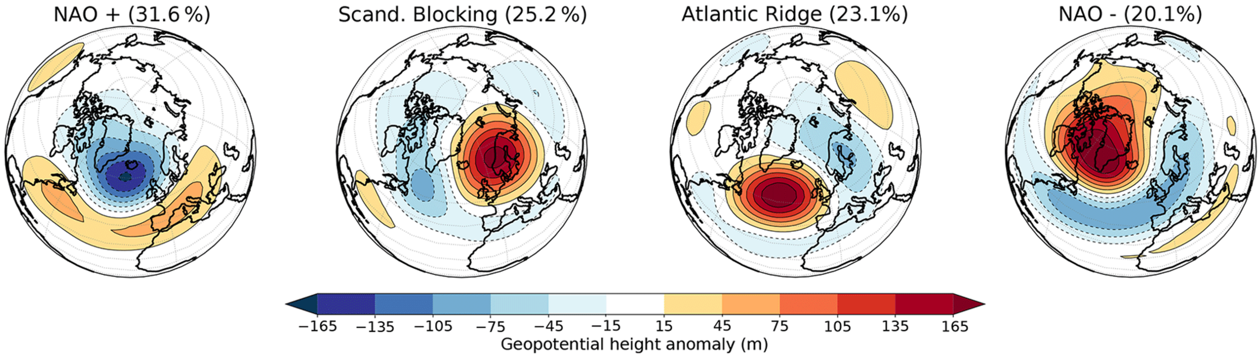

Figure 1.7: Regime patterns for the Euro–Atlantic regimes using 500 hPa geopotential height anomalies. Obtained from the ERA-40 and ERA-Interim reanalysis datasets (1964–2014, NDJFM). The observed regime frequencies are indicated in the subplot titles. Caption and figure taken from Fig. 1 of Fabiano et al. (2021).

that closely approximate Fig. 1.6c that will reflect non-stationary weather patterns such as the movement of weather fronts. If the occurrence of the ridging pattern increases, this does not necessarily mean that blocking across this part of the domain is increasing.

A further issue with the analysis of Horton et al. (2015) was noted by Jézéquel et al. (2018), namely that they failed to effectively detrend geopotential height to remove the thermodynamic effect. Since geopotential height at a given pressure level increases with a warming troposphere by the hypsometric equation, if geopotential height is to be used in analysis as a dynamical variable it needs to be detrended in some way to approximately account for this effect. This was not done by Horton et al. (2015) and therefore in their analysis they overstate their quantification for a dynamic shift already seen in the historical data. Therefore Horton et al. (2015) overstate the importance of the dynamic contribution to increasing surface temperature extremes. A new method in which I show how SOMs can be more accurately used to identify blocking events is described and applied in section 2.

1.5.6.2 K-means analysis

K-means cluster analysis has been used since the 1990s to identify distinct weather regimes in Winter in the Euro-Atlantic region (Vautard 1990; Michelangeli et al. 1995; Kageyama et al. 1999; Cassou 2008; Hannachi et al. 2017; Fabiano et al. 2021).

Four regimes are commonly identified: NAO+, NAO-, Atlantic Ridge and Scandinavian blocking. A typical pattern of these is shown in Fig. 1.7, using 500 hPa geopotential height

ERA-40 and ERA-Interim reanalysis data across 1964-2014 in NDJFM. Figure 1.7 accords with many similar analyses over the Euro-Atlantic region using both reanalysis data and climate model output (Dawson et al. 2012; Ferranti et al. 2015; Hannachi et al. 2017; Fabiano et al. 2020).

These patterns are robust, and it is clear that the Scandinavian blocking weather regime is commonly associated with Scandinavian blocking events; Day et al. (2019) used the Scandinavian blocking pattern as a continuous index to identify Scandinavian blocking events by pattern correlation with the daily geopotential height anomaly. Whilst this approach can yield physically meaningful results relevant to atmospheric blocking events, it also lacks the persistence criteria necessary for identifying individual blocking events.

1.5.7 The emergent constraint approach

One recent technique for using ESMs in reducing uncertainty on future climate change is through emergent constraints (ECs). These rely on strong statistical relationships between aspects of the current climate and future change across an ESM ensemble. If a relationship is identified between past and future states of the climate across a model ensemble, the historic observational record can be used to make an estimate for the future change in the climate system (Hall et al. 2019).

One example of the emergent constraint approach can be found in Hall and Qu (2006), who found that the variations in the strength of the snow albedo feedback with climate change across models were strongly correlated with variations in the feedback strength of snow albedo in the seasonal cycle. Therefore, in principle the current seasonal cycle can be used to constrain the snow albedo feedback under climate change.

The EC approach has received criticism. Cox et al. (2018) used the EC approach to provide an estimate of equilibrum climate sensitivity, which was critiqued by Rypdal et al. (2018), who argued that the work of Cox et al. (2018) is “derived from incorrect physics” and “sensitive to arbitrary methodological choices”. Hall et al. (2019) have developed a framework for assessing the viability of emergent constraints involving out-of-sample testing and verified mechanisms for where these approaches are valid.

An approach involving an emergent constraint in the relationship between the historic occurrence of ESB and the future trend of ESB is discussed in 4, and applied to provide an estimate for the ESB climate feedback.

1.6 Aim and research questions

The aim of this thesis is to produce an estimate for the ESB climate response using information from climate models.

The research questions are:

- What is the optimal blocking index for studying atmospheric blocking events?
- What is the optimal method for comparing the skill of blocking indices?
- What physical mechanisms are involved in influencing the ESB climate response?
- Can a comparison between the CMIP5/6 model ensemble and the ERA5 climatology of the model skill be used to obtain an estimate for the ESB response?

Chapter 2

An unsupervised learning approach to identifying blocking events: the case of European summer

2.1 Introduction

This chapter is based on a paper published in Weather and Climate Dynamics (Thomas et al. 2021).

In order to better understand blocking and to investigate the influence of climate change, there have been significant efforts to develop blocking indices (BIs) that can automatically detect blocking in long meteorological records (Lejenäs and Økland 1983; Dole and Gordon 1983; Tibaldi and Molteni 1990; Pelly and Hoskins 2003). However, the multiplicity of these BIs, with a variety of thresholds for defining the area, persistence and magnitude of blocked features on different atmospheric dynamical variables (Barnes et al. 2012b; Pinheiro et al. 2019), means that these methods necessarily carry the burden of somewhat subjective definitions. Whilst previous intercomparisons of BIs show similar global climatologies, and all indices capture many of the basic features of atmospheric blocking within their definitions, there are known regional and seasonal differences (Croci-Maspoli et al. 2007; Barriopedro et al. 2010; Pinheiro et al. 2019). In addition, whilst spatial climatologies obtained from these BIs have been compared extensively, to the best of my knowledge there has been no direct time series comparison of the BIs beyond case study analyses such as those in (Scherrer et al. 2006) and (Pinheiro et al. 2019).

The utility of machine learning in pattern recognition has led to several applications of clustering algorithms to study circulation patterns. In particular, self-organizing maps are frequently used to classify midlatitude circulation patterns (Cassano et al. 2007; Skific and Francis 2012; Horton et al. 2015; Loikith et al. 2017; Gibson et al. 2017a; Agel et al. 2021). These studies often categorise daily data of fields such as geopotential height to identify different circulation patterns and investigate how these are linked to changes in other variables such as temperature or precipitation. In doing so, certain weather regimes can be understood to be causally connected to temperature and precipitation extremes, which has several applications, including in attributing climate changes to dynamic and thermodynamic mechanisms (Cassano et al. 2007; Higgins and Cassano 2009; Skific et al. 2009; Horton et al. 2015; Mioduszewski et al. 2016). However, since atmospheric blocking events by definition are persistent across several days, individual SOM circulation patterns categorising daily weather patterns are not sufficient to classify blocking events as the blocking index since they lack the necessary persistence threshold for study of atmospheric blocking events.

K-means analysis, a clustering algorithm similar to SOMs, is also frequently used to study atmospheric circulation patterns (Vautard 1990; Michelangeli et al. 1995; Cassou 2008; Ullmann et al. 2014; Strommen et al. 2019; Fabiano et al. 2021). It is common in K-means clustering analyses over the Euro-Atlantic sector to identify four circulation regimes, including one that describes the typical conditions for Scandinavian blocking (Ferranti et al. 2015). This can also be used as a continuous index to identify Scandinavian blocking events (Day et al. 2019). However, as with the SOM analysis, this K-means approach lacks the persistence criterion which is a necessary requirement for any blocking index. A further discussion of these methods can be seen in section 1.5.6.

There are therefore two broad categories of approaches to studying blocking patterns and their connection to weather extremes - clustering algorithms and blocking indices. It has been highlighted that consistency across various methods in detecting long-term changes is a fundamental requirement to confidently identify trends (Barnes et al. 2014; Woollings et al.

2018). To the best of my knowledge, there has been no previous study that directly compared a clustering approach to other BIs.

In this chapter, I define a new binary ground truth dataset (GTD) of European blocking events across June–July–August (JJA) 1979-2019, based on a five-day persistence threshold, reanalysis data and expert judgement. Such a GTD is the first of its kind. As part of the process of labelling the GTD, my understanding (cf. expert judgement) of blocking events has been informed by the BIs and the various definitions that have been proposed, but as a key advance my event interpretations do not merely rely on labels obtained by using individual BIs. This enables an independent time series comparison with the BIs. I also compare my results to a K-means clustering approach to describing the weather regimes of the mid-latitude atmosphere. I present case studies of the prominent 2003 and 2019 European heatwaves, and show how well K-means, the BIs and self-organizing maps (SOMs) describe the blocking events.

I then use SOMs to develop a new blocking index (SOM-BI). This is a unique approach that combines both the persistence threshold of the blocking indices and the pattern recognition of the SOM. This SOM-BI method has advantages over previous BIs because it exploits all the spatial information provided in the input data and reduces the dependence on arbitrary thresholds. It also provides a new way of studying blocking events that can more intuitively distinguish between different regimes and locations of blocking events, which the other indices are lacking. I identify the skill of different BIs by developing a binary time series identification of European blocking patterns and comparing this to my GTD using standard skill metrics discussed in section 2.2.6. This study is the first to define such a GTD and I use it as a benchmark to compare the skill of different BIs over a region.

A key result introduced in this chapter is that the SOM-BI method has an improved skill at detecting European summer blocking events to other BIs, particularly in climate models. Since the SOM-BI method is not bound to a specific meteorological variable, I also quantify how its detection skill varies with the variable used, from geopotential height anomaly fields to potential vorticity maps. While there have been theoretical discussions on the importance of the meteorological variable used to define and identify blocking (Pelly and Hoskins 2003; Chen et al. 2015), the variable-dependence of skill of blocking detection methods has not been quantified before. Finally, I evaluate the performance of the SOM-BI on 41 years from the ERA5 reanalysis and 101 years of a pre-industrial control run carried out with the UK Earth System model (UKESM1-0-LL, hereafter UKESM). I identify a moderate improvement in blocking identification over the BIs for the reanalysis period and a significant improvement for the UKESM data. A key advantage is that the longer climate model simulation allows us to test the robustness of my method compared to other BIs over longer timescales, and to study the dependence of the SOM-BI detection skill on the number of years included in the algorithm's training dataset.

This chapter is structured as follows. In section 2.2 and its subsections, I introduce the meteorological reanalysis and climate model data, the new GTD, the BIs, K-means, SOMs, and my new SOM-BI. In section 2.3, I present the main results of my analysis. I first compare the various blocking identification methods by means of the 2003 and 2019 European heatwave case studies (section 2.3.1), followed by an evaluation and intercomparison of the methods on ERA5 reanalysis and UKESM climate model data (sections 2.3.2 and 2.3.3). In section 2.3.4, I discuss how the performance of the SOM-BI depends on the length of the data record used to train the algorithm. In section 2.3.5, I test the feasibility to train SOM-BI on ERA5 data to then reliably identify blocking in climate model data, and vice versa. In section 2.3.6, I briefly discuss the effect of other hyperparameters on the SOM-BI skill. In section 2.3.7, I demonstrate how the SOM-BI can be used to study trends in regional blocking patterns by applying it to ERA5 data. In section 2.4, I summarise and discuss my key results, and motivate the analyses of the subsequent result chapters on the detection of blocking in climate change simulations.

2.2 Methods

2.2.1 Meteorological data

As a proxy for observed dynamical states over Europe, I used ERA5 reanalysis data from the European Centre for Medium Range Weather Forecasts (ECMWF, Hersbach et al. 2020). The pre-industrial climate model data was obtained from simulations carried out with the UK Earth System Model UKESM1-0-LL (UKESM), as part of Coupled Model Intercomparison

Project Phase 6 (CMIP6, Eyring et al. 2016; Sellar et al. 2019). For ERA5, I used gridded data at a spatial resolution of 1° x 1° across 1979-2019, and created daily averages derived from 3-hourly intervals. In UKESM, I used 101 years of daily data from the pre-industrial run of the r1i1p1f2 ensemble member, across the 1960-2060 period (arbitrarily defined due to the absence of additional climate forcings). I used the UKESM data at the native resolution of 1.25° x 1.875° to develop the GTD plots and regridded to a 2° x 2° grid for the SOM analysis. When training and testing between the ERA5 and UKESM data (section 2.3.5), I also regridded the ERA5 data to a 2° x 2° grid.

For both types of datasets, I used the following common meteorological variables to characterize the dynamical state of the atmosphere at any given time: geopotential height at 500 hPa (Z_{500}), mean sea level pressure (MSLP), relative vorticity at 500 hPa (ζ_{500}). For ERA5, I also used vertically integrated potential vorticity across 150-500 hPa (VPV), isentropic potential vorticity on 350 K and 330 K (IPV_{350} and IPV_{330}) and potential temperature on the PV= 2 PVU surface (θ-PV). These PV-based variables have all been used in the context of understanding atmospheric blocking (Hoskins et al. 1985; Crum and Stevens 1988; Pelly and Hoskins 2003) but are not available from the CMIP6 archive. The 350 K and 330 K isentropes were chosen because these intersect with the tropopause in the mid-latitude summer, as shown in Fig. 1 of Liniger and Davies (2004), and therefore represent upper-level dynamics. For the case study analyses, I have also used the surface horizontal wind fields and surface temperature (T_{surf}).

Following Grotjahn and Zhang (2017) and Pinheiro et al. (2019), I define the anomaly fields that I study by subtracting a long-term daily mean (LTDM) from the data instead of subtracting the daily average. This is a smoothed function of the 365-day seasonal cycle across Z_{500}, VPV and T_{surf} using the first six harmonics of their Fourier series, where the first harmonic corresponds to the mean and the fifth to a 73 day span. The purpose of this is to smooth out the daily mean fields, which can otherwise show excessive variation between neighbouring days across the seasonal cycle calculated from the available observational record.

The T_{surf} and Z_{500} anomaly fields in ERA5 have been detrended linearly across time to approximately remove the effect of thermodynamic warming. Following Jézéquel et al. (2017), I subtract a spatially uniform trend, so that the horizontal gradients of the field are not altered. I depart from the Jézéquel et al. (2017) method by subtracting a linear Z_{500} anomaly trend instead of a cubic spline interpolation, since I assume that in the 1979-2019 time period the thermodynamic dilation of the troposphere can be approximated as linear, so removing nonlinear trends could risk removing the dynamical variability in the atmosphere that I am interested in. This assumption is based on the approximately linear increase in surface temperature over Europe across this period (Folland et al. 2018; Twardosz et al. 2021). I also apply the same detrending approach to the pre-industrial UKESM data, to remove any minor remaining trends in the data, e.g. due to the finite spin-up time of the control simulations (Gregory et al. 2004; Nowack et al. 2017; Mansfield et al. 2020).

2.2.2 Creating the ground truth dataset (GTD)

In order to objectively compare the blocking indices, I develop a ground truth dataset (GTD) of blocking events in JJA Europe, here defined as 30–75 °N, 10 °W–40 °E, following IPCC AR5 definitions (Stocker et al. 2013). The northern latitude is extended to 76 °N when using data on a 2° x 2° grid. JJA Europe was chosen because of my interest in the role of atmospheric dynamics in the development of mid-latitude land heatwaves. Europe is a region which has seen many recent significant heat extremes (Christidis et al. 2014), and the role of changes in atmospheric dynamics has been a significant area of interest (Cattiaux et al. 2013; Horton et al. 2015; Saffioti et al. 2017; Huguenin et al. 2020).

The size of the domain has been motivated by my purpose in developing a dataset that can be used to train an algorithm to identify blocking patterns over a region. Using a region much smaller or larger than this would lead to a significant difference between the number of days labelled as blocked and not blocked. Such a difference between the two sets of elements is described as a “biased dataset”, and would limit my ability to train and validate a blocking identification method.

The GTD has been derived by studying every successive five-day period from 28 May to 4 September within the years 1979 to 2019, and manually identifying whether or not a blocking high persisted across any such five-day period. By including the last four days at the end of

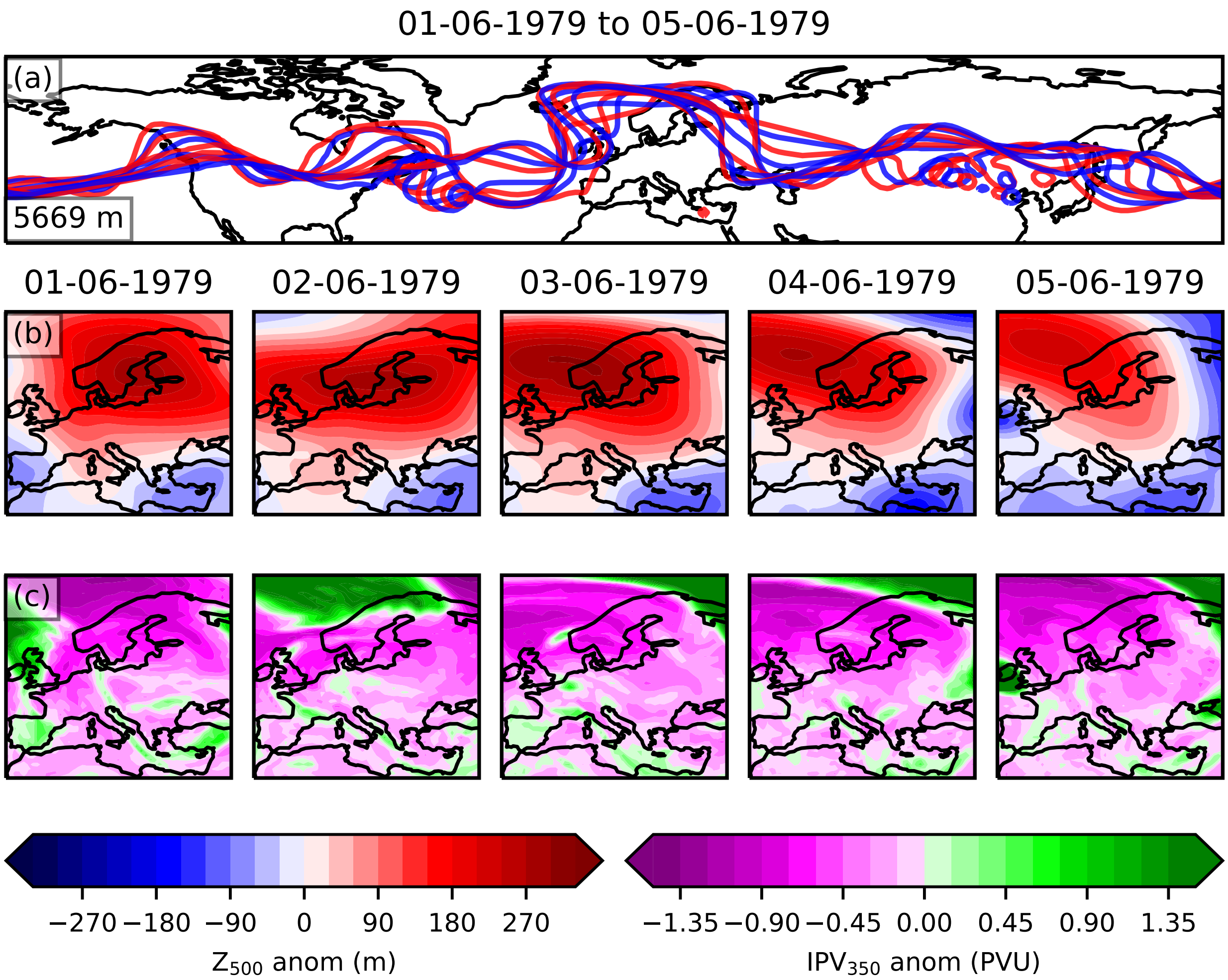

Figure 2.1: The information used to classify blocks in the ERA5 ground truth dataset (GTD). (a) shows the Z_{500} contour for the averaged value across 30-70 °N, indicated in the bottom left of the panel. The red and blue colours highlight the contours at midnight and midday, respectively. (b) and (c) show the Z_{500} time detrended anomaly and IPV_{350} anomaly for each day.

May and the first four days of September, I ensure that all blocking events within the JJA period are detected. Five days was chosen since this a typical persistence threshold for blocking indices (Verdecchia et al. 1996; Schwierz et al. 2004; Scherrer et al. 2006; Pinheiro et al. 2019), although a persistence of 7-10 days with weaker BI thresholds for amplitude and area has also been used (Rex 1950; Lejenäs and Økland 1983).

A diagram of the type of information analysed to label each individual day is shown in Fig. 2.1, for the example period 1-5 June 1979. This period was labelled as blocked, since Fig. 2.1a clearly shows a continuous northward shift in the Z_{500} contours over Europe and Fig. 2.1b shows a substantial positive Z_{500} anomaly which persists across Northern Europe. The

IPV_{350} maps in Fig. 2.1c highlight filaments and regions where there is fast moving air. Once the total set of all 4001 consecutive five-day periods across JJA 1979-2019 has been classified, persistent *blocking events* are reconstructed to form a time series where each day is labelled as blocked or not. If a day belongs to any one of the consecutive blocked five-day periods, it is individually labelled as blocked (1), and if a given day does not belong to any of the blocked five-day periods it is labelled as not blocked (0). This creates a classification of blocking patterns for each day where each blocking event has a minimum length of five days. Blocking events longer than five days are also identified through this approach, since days that are part of any consecutive five-day blocked period are labelled as blocked. Blocking events longer than five days are then identified through a series of adjacent five-day blocked periods.

A similar approach was adopted to classify 9494 five-day periods from 101 years of JJA data in the UKESM pre-industrial control run, with an example blocked period shown in Fig. A.1. As in Fig. 2.1, there is a clear quasi-stationary high centered on a region slightly north of the UK. This is indicated by the Z_{500} contours which show a significant northward protrusion over this region, and by the substantial Z_{500} anomaly across all panels in Fig. 2.1b. Since PV is not available in CMIP6 data and the physical variables used to derive PV are not available at sufficiently high vertical resolution, I instead show the MSLP anomaly field in Fig. A.1c, which also indicates a high pressure region consistent with Figs. A.1a and A.1b.

2.2.3 Blocking Indices (BIs)

One way of describing atmospheric flow and investigating trends in atmospheric dynamics is by using proxy indices such as those used to classify if a blocking event is occurring. There are many blocking indices (BIs) that have been used to create a blocking climatology, and these have been rigorously compared (Barriopedro et al. 2010; Pinheiro et al. 2019). A detailed discussion of the different BIs is included in section 1.5.1.

In this chapter, I use the three indices compared in Pinheiro et al. (2019) including their modifications:

- **AGP** - the geopotential height gradient method, which is the Tibaldi and Molteni (1990) index as adapted by Scherrer et al. (2006) to construct a two-dimensional field of geopotential height gradients.

- **DG83** - the Dole and Gordon (1983) method of investigating positive geopotential height anomalies.
- **S04** - the Schwierz et al. (2004) method of identifying persistent anomalies in the potential vorticity field (VPV) averaged over 150-500 hPa (VPV).

I refer the reader to section 2.2 in Pinheiro et al. (2019) for a detailed discussion of these methods and their associated thresholds. However, my analysis differs from the methodology outlined by Pinheiro et al. (2019) in three ways, reflecting the fact that my study is regional and seasonal instead of global. Firstly, I apply all thresholds defined by Pinheiro et al. (2019) only to those grid cells within the region of study to exclude events that are on the edges of the domain. Such events would be considered blocking events if the domain studied was extended. Secondly, Pinheiro et al. (2019) applied a spatial smoothing to their global threshold field, which defines the minimum threshold for each grid cell to be blocked. Although I have applied the LTDM smoothing of the seasonal cycle (which I subtract from variables to calculate field anomalies, section 2.2.1) and I also use a spatially varying threshold field, I have not applied this spatial smoothing to my threshold field. I found that the resulting blocking climatologies shown in Fig. A.4 are broadly consistent with those presented in Fig. 6 of Pinheiro et al. (2019), underlining that this regional use of the BIs is still valid. Finally, to remove the well-known problem of the AGP index identifying anomalous blocking events associated with the subtropical high in summer (Davini et al. 2012), I adopt the extra threshold of the AGP index from Woollings et al. (2018). The subtropical high feature was not observed in UKESM over Europe, since the meridional geopotential height gradients have a smaller magnitude. I use the standard AGP index for UKESM, but similar results are observed for UKESM with the modified index (not shown).

I note that more indices have been proposed, including hybrid approaches combining the AGP and DG83 indices (Barriopedro et al. 2010; Dunn-Sigouin et al. 2013; Woollings et al. 2018), the PV-θ approach developed by Pelly and Hoskins (2003) and the finite amplitude wave activity method (Huang and Nakamura 2015). K-means clustering analysis (Diday and Simon 1980) has also been extensively used to study the Euro-Atlantic midlatitude variability and to

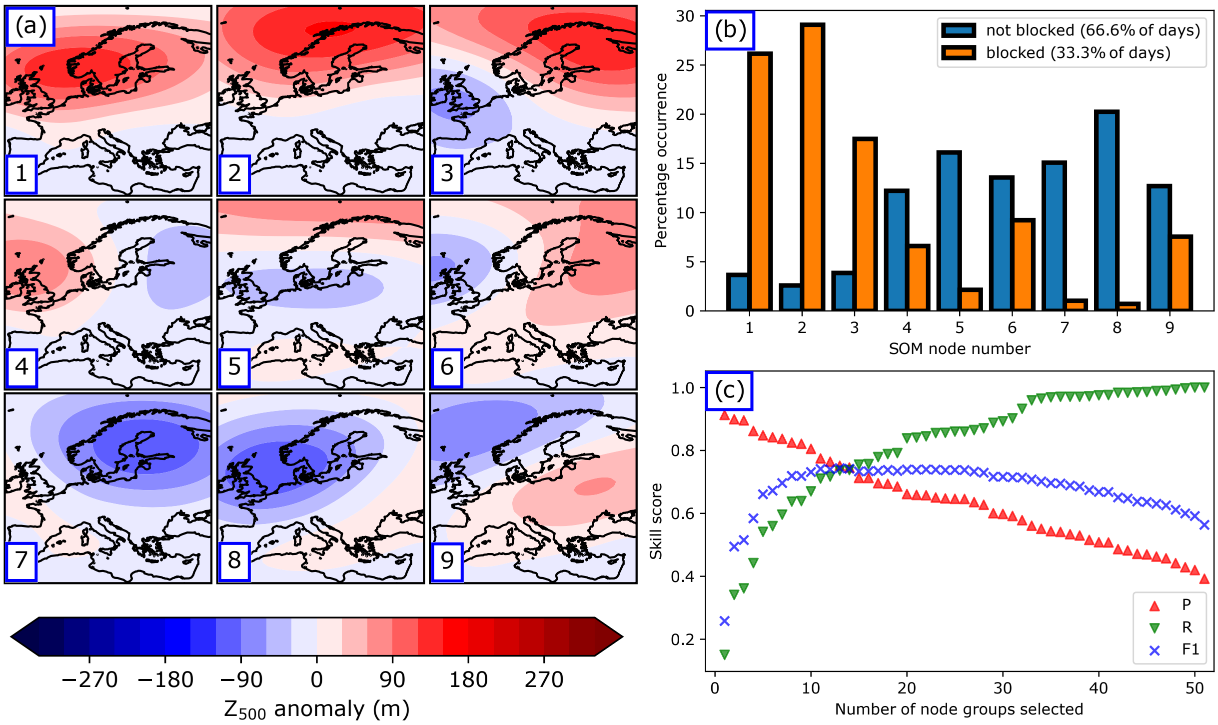

Figure 2.2: The SOM blocking index (SOM-BI). (a) The trained 3x3 SOM for Z_{500} time-detrended anomaly. (b) Normalised histograms showing the distributions of occurrence of BMUs for the days identified as blocked or non-blocked within the GTD. (c) The SOM-BI optimisation of the set of node groups against three different skill scores (precision (P), recall (R) and F_1 score) that are associated with the GTD blocking events.

identify weather regimes (Vautard 1990; Michelangeli et al. 1995; Cassou 2008; Ullmann et al. 2014; Strommen et al. 2019; Fabiano et al. 2021). However, with the three BI methods included here in addition to the SOM-BI and K-means comparison in the case studies, I expect to see results that are sufficiently representative of the range of blocking detection methods available, and to be able to highlight their most important similarities and discrepancies.

2.2.4 Self-organizing map (SOM)

The fourth method I used to investigate trends in atmospheric circulation regimes in European summer is self-organizing map cluster analysis (SOM; Kohonen 1982). I refer the reader to section 1.5.5 where SOMs are introduced and discussed in the context of this thesis. I have implemented the SOM algorithm using the somoclu Python package (Wittek et al. 2017).

2.2.5 The self-organizing map blocking index (SOM-BI)

Once I have created the GTD, this can be used to develop a new BI using SOM analysis. For a given variable from the ERA5 dataset, I can specify a node number and arrangement of nodes (number of rows and columns, Fig. 1.5) and then learn the corresponding SOM nodes from that data. Figure 2.2a shows the trained pattern for Z_{500} anomalies in ERA5 28 May-4 Sep 1979-2019 for 9 nodes arranged in a 3x3 grid. Since each day in the dataset has been matched to a BMU, I can identify which nodes are associated with blocked days according to my GTD. Figure 2.2b compares the histograms of those nodes which are and are not associated with the GTD blocking events. As expected, the three nodes with large positive Z_{500} anomalies (nodes 1, 2 and 3) are most closely associated with blocking events, and the nodes with large negative Z_{500} anomalies (nodes 7 and 8) are rarely associated with blocking events. However, nodes 1, 2 and 3 still occur on 15% of non-blocked days, and 28% of the blocked days are also matched with one of the other six nodes, including 3% of blocked days matched with nodes 7 and 8. This tells us that while the SOM nodes can indicate the occurrence of blocked events, there is no node or single combination of nodes that can be consistently identified with blocking events with high skill.

However, from every five-day period within the GTD, I can identify an associated "group" of nodes. For example, a five-day period can be associated with nodes 1 and 4 (any arrangement of nodes 1 and 4 across five days), and this would mean that [1,4] is the associated group of nodes for that five-day period. Since each five-day period has been classified either as blocked or not blocked, it raises the possibility that a set of such groups can be more specifically associated with blocking. In the following, I will identify the optimal set of node groups associated with blocking by ordering the list of all possible node groups (e.g. [1,2,3], [1,4], [1], [1,2,3,4,6] etc) from the node groups that have the highest to lowest precision (P) at identifying blocking events.

2.2.6 Classification skill measures

Fig. 2.2 (c) shows the binary classification skill according to the measures of precision, recall and F_1 score when applying the 9-node SOM-BI to ERA5 data. These three skill measures

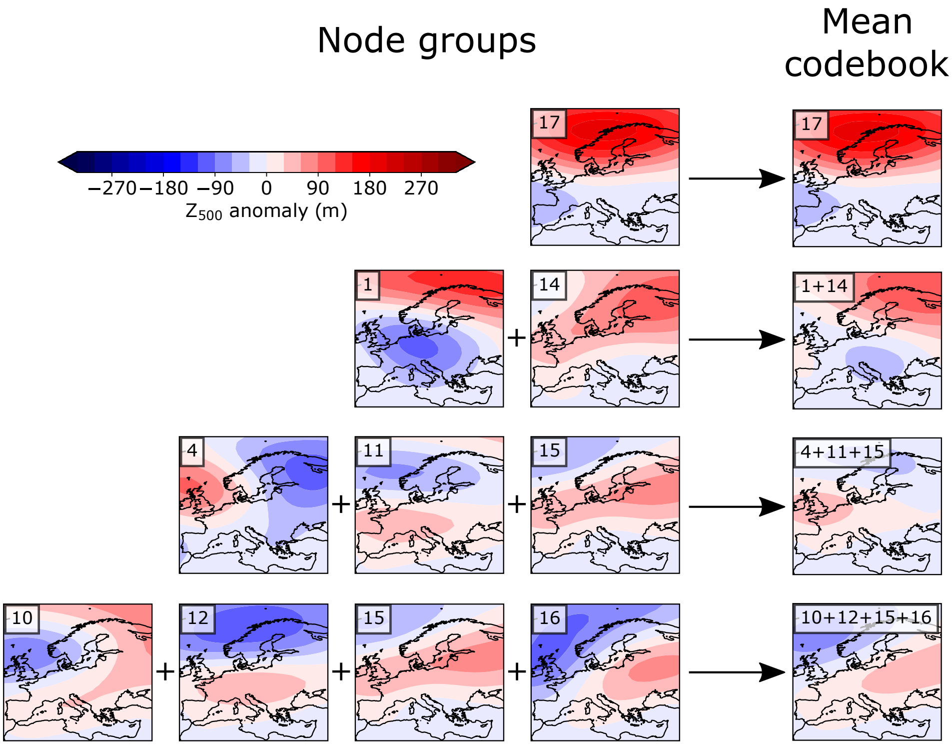

Figure 2.3: Examples of four blocked node groups identified by the SOM-BI described in section 2.2.5 averaged to form mean codebooks. Shown here for Z_{500} in the optimised case of 20 nodes. In this case, there are 114 blocked node groups in total.

are defined in section 1.5.3. The three skill measures are shown for consecutive cases where I successively add node groups as described above in order from highest to lower precision to the set of groups that are associated with blocking. In other words, once a new group has been added to the set of groups, this new group will define a series of blocked periods within my SOM-BI approach. For the 3x3 SOM learned from ERA5 data, the node group with the highest precision is [1], with P = 0.91 and R = 0.15, followed by [2] with P = 0.89 and R = 0.19 and [1, 2, 6] with P = 0.87 and R = 0.03. If only one node group is included in the set (e.g. [1] or [1, 2, 6]), there is a high P and low R, but as more node groups are added to the set of node groups (e.g. [1], [2]; then [1], [2], [1, 2, 6]), P decreases but R increases. The optimal set of node groups is identified by the value which maximises the F_1 score (Fig. 2.2c). I perform this classification for a range of node numbers and meteorological variables to identify an optimal performance in section 2.3.3.

2.2.7 SOM-BI application

Once an optimal set of node groups has been identified, these can be used to classify days as blocked or not blocked. This creates a time series of blocking events but it does not produce a spatial climatology. To develop a spatial climatology for the SOM-BI, I use the BIs described in 2.2.3 across the days that are identified as blocked by the SOM-BI.

A key advantage of the SOM-BI is that it identifies distinct types of regional blocking events, since each blocked node group within the set of node groups is associated with a set of blocking events. In the example shown in Fig. 2.2, 14 node groups are associated with blocking at the intersection of precision and recall, which therefore identifies 14 possible distinct types of blocking. For example, the node group [1] describes broad NW European events, [2] describes Scandinavian blocking, and [1, 2, 6] describes a more variable set of blocking patterns that are broadly associated with NE Europe.

To aid in my interpretation of these node groups, I calculate the mean of their node codebooks, i.e. the mean of the spatial patterns of the nodes in each node group, which in turn also characterize the corresponding blocking patterns. This forms "mean codebooks" for each node group. Figure 2.3 shows four examples of such node groups associated with blocking from ERA5 Z_{500} for the case of 20 nodes - the optimum number of nodes for this case (cf. Fig. 2.6a). These four node groups are chosen since they illustrate the variety of nodes and numbers of nodes present across the set of blocked node groups, and also represent a variety of spatial patterns in blocking (N, NW, W and E). In section 2.3.7, these mean codebooks are applied to identify distinct categories of blocking and to study their historical trends in ERA5.

As shown later in Fig. 2.8 (a), the optimised case of 20 nodes for Z_{500} yields a total set of 114 blocked node groups. This large number of different blocking patterns with subtly different characteristics creates a challenge for easy interpretation of results. Furthermore, several of these node groups occur very infrequently, perhaps only once in the 1979-2019 period, so a meaningful study of their trends is not possible. To address these challenges and to study the characteristics of different types of blocking events, I suggest a post-processing approach using K-means clustering analysis (Diday and Simon 1980) applied to the 114 mean codebooks from each node group. Each resulting K-means cluster will identify a sub-set of pattern-wise similar blocked node groups from the total set of blocked node groups. I will show in detail in section 2.3.7 and in Fig. 2.10 how this process can be used to identify distinct categories of blocking over Europe, which are straightforward to interpret, and which allow us to study trends in such blocking regimes.

2.3 Results

2.3.1 Case study analyses

Case studies of major past summer blocking events are useful to illustrate and understand differences among BIs. I thus first compare the blocking identification methods (i.e. SOMs/SOM-BI, the three conventional BIs, and K-means) for two examples of well-known 2003 and 2019 European heatwaves that were linked to blocking states of the atmosphere (Figs. 2.4 and 2.5). In addition, I study two blocking events from UKESM, to investigate how blocking events are described in the climate model. From the 101 years investigated in the pre-industrial control run I have found the largest extent of heat extremes to occur in an extended heatwave shown in Appendix Fig. A.2. This is contrasted with Fig. A.3, which shows the end of a blocking event and a weaker transitory anticyclone. Both UKESM events are discussed further in Appendix A.1.

The 2003 European heatwave was record-breaking and had significant societal impacts (Robine et al. 2008). It was shown to have been made at least twice as likely due to anthropogenic climate change (Stott et al. 2004). According to climate change projections, such heatwaves will become commonplace by the 2040s irrespective of future emissions scenarios (Christidis et al. 2014). The most extreme temperatures during this heatwave were recorded from the 6-12 August, where the peak temperature recorded was in Southern France at 41°C. Black et al. (2004) reports that atmospheric flow anomalies were recorded in early August, although there was a relatively weak signature of blocking. The 2003 heatwave remained the European temperature record until 2019, when surface temperatures of 46°C were observed in central France. The 2019 heatwave was concurrent with persistent hot air that originated in North Africa (the so-called "Saharan heat bubble"), which was sustained by an omega block centered on Western Europe (Mitchell et al. 2019).

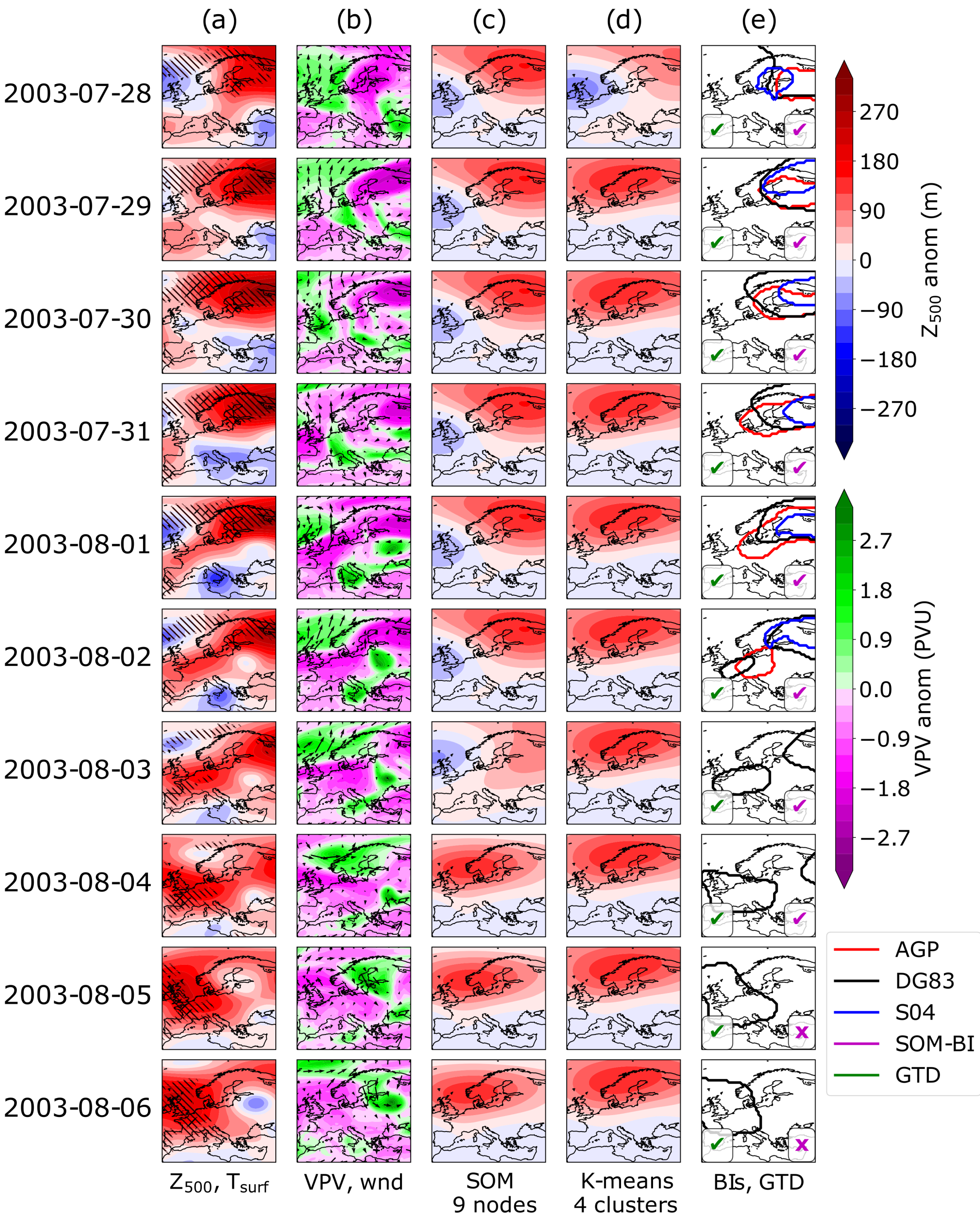

Figure 2.4: The 2003 European heatwave. (a) shows the detrended 500 hPa geopotential height anomaly for each day. Left (right) hatching indicates where the local surface temperature exceeds the 90th (99th) percentile for the detrended 2 m temperature. (b) shows the potential vorticity anomaly vertically averaged across 150-500 hPa, with arrows showing the 10-m wind field. (c) shows the corresponding SOM pattern for Z_{500} anomalies from 9 nodes. (d) similarly shows the corresponding K-means centroid for 4 clusters. (e) shows the contours identified as blocked in this region in the AGP (red), DG83 (black) and S04 (blue) indices. A green (magenta) tick or cross indicates if the GTD (SOM-BI) identifies the day as blocked or not.

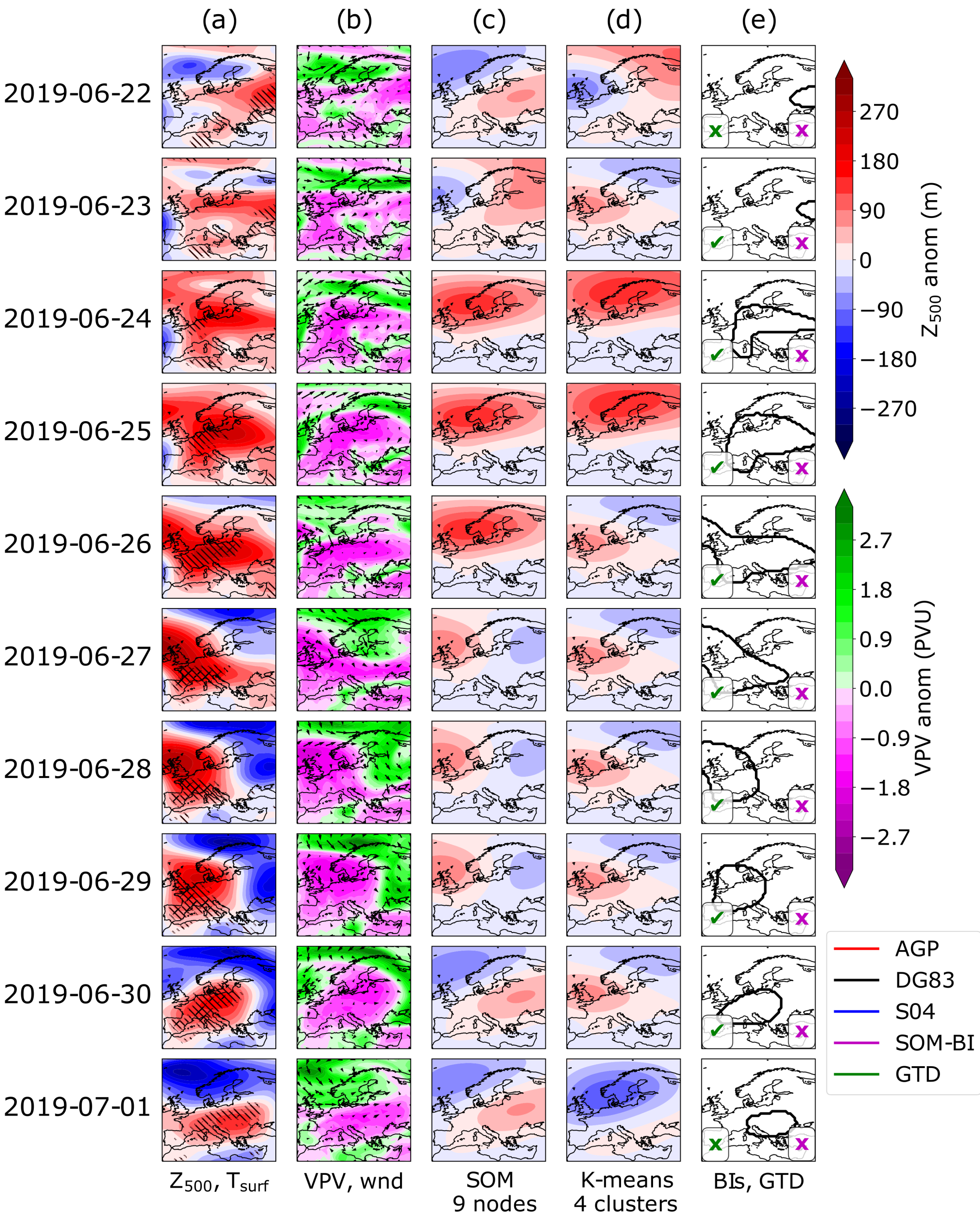

Figure 2.5: As in Fig. 2.4 but for the 2019 European heatwave.

Figs. 2.4a and 2.5a show daily maps of detrended Z_{500} anomalies for the two events, the field used by the DG83 index to identify blocking events. The hatching indicates detrended surface temperature extremes at the 90th and 99th percentile. It can be seen that across all cases there are significant positive Z_{500} anomalies which are associated with temperature extremes. Figures 2.4b and 2.5b show the vertically averaged potential vorticity (VPV) field, used by the S04 index to identify blocking, and also the 10 m winds. The VPV field is consistently anti-correlated with the Z_{500} field, and significant negative anomalies in the VPV field tend to be associated with stationary surface winds, particularly across 26-29 June 2019. Figures 2.4c and 2.5c show the BMU SOM pattern for the case of 9 nodes for detrended Z_{500} anomaly fields. Whilst the SOM nodes clearly track the features shown in the Z_{500} maps, a range of BMUs are identified in both case studies even though there is a consistent extreme weather event across these time periods. In the 2003 case study in ERA5, three SOM BMUs and four transitions between BMUs are shown in Fig. 2.4c. These all show positive Z_{500} anomalies in the Northern part of the domain, even though the meteorological situation varies meridionally more than zonally, particularly across 4-9 August 2003. An even greater variety of BMUs is observed in the 2019 case, where four nodes and four transitions between SOM nodes are shown in Fig. 2.5c.

This creates a difficulty of interpretation - whilst the SOM can identify the best matching spatial pattern of Z_{500} anomalies, these particular SOM patterns do not correspond to circulation regimes as conventionally understood, since even minor shifts in the domain (such as the change from the 2-3 August 2003) can cause the corresponding pattern to shift. The frequency of these shifts and sensitivity of the SOM is dependent both on the number of nodes chosen and the domain size. Smaller domains with fewer SOMs show more consistency in the synoptic weather patterns, but when these are sufficiently reduced (such as for four SOMs over the Mediterranean), the SOMs become less distinguishable and lose even more of their explanatory power to represent meaningful pattern variations across the domain (not shown). Overall, the fact that several SOM nodes occur during the case study blocking events shows that individual SOM patterns will not be able to consistently identify blocking events with high precision or recall, contrary to how SOMs are typically used in many applications in the literature. However, well-defined groups of nodes, as I will show below, can indeed achieve this task and can thus be used for the purpose of my new SOM-BI.

Figures 2.4d and 2.5d show a K-means clustering analysis using Z_{500} anomaly fields for the case of 4 centroids. As described in section 1.5.5, the case of K-means with 4 centroids produces a similar set of weather regimes to SOMs with 4 nodes. Consequently, the K-means analysis exhibits a similar behaviour to the SOMs discussed above but distinguishing between fewer weather regimes. One weather regime indicating Scandinavian blocking consistently represents the 2003 European heatwave across Fig. 2.4d, but the westward shift of the high pressure centre from Scandinavia on 31 July to the UK on 8 August 2003 is not described by 4 centroids. For the 2019 heatwave in Fig. 2.5d, all four weather regimes are represented, and the blocked period is primarily associated with a mixed weather regime. This shows that the 2019 case is also not described well by K-means clustering.

Figs. 2.4e and 2.5e show the contours demarking blocked regions as identified by the three different BIs. A tick or cross in the bottom left and right corners indicates whether the day was identified as blocked or not in the GTD and the SOM-BI, respectively. For the SOM-BI labelling, Z_{500} 20 SOM nodes are chosen on the basis of the optimisation of the SOM-BI in Fig. 2.6a. Across all case studies the DG83 index clearly tracks regions of positive Z_{500} anomalies. The S04 and AGP indices also track the same feature in the 2003 heatwave until 3 August 2003, but does not identify any blocking associated with the 2019 heatwave. The SOM-BI describes the initial period of the 2003 heatwave well, although it does not capture the Western European blocking event during the peak period of extreme temperature across 6-12 August. The SOM-BI also does not capture the 2019 blocking pattern coincident with the 2019 heatwave. This is because the SOM nodes are too variable over the 2019 event such that the set of nodes which best match the Z_{500} anomaly fields are not generally associated with blocking. For example, the SOM nodes across 27-30 June 2019 indicate mixed patterns which do not obviously correspond to blocking over a consistent area (the positive maxima shift from the British Isles to Eastern Europe within a day). This lack of pattern consistency is mostly the result of an unfortunate balance between the positive and negative Z_{500} anomalies on these days, where the latter play a major role in the allocation of the BMU during this period. I discuss the possibility of ignoring negative anomalies in my assignments of the BMUs in section 2.3.6, but

Table 2.1: A comparison of skill scores of the original BIs and the new SOM-BI against the GTD for ERA5 1979-2018 and UKESM for JJA over the European domain. Where not indicated the skill scores are measured with respect to the relevant GTD. "BLO" indicates the skill score for the trivial case of every day labelled as blocked, and "RND" where a random allocation of blocked days has occurred with the same proportion of blocked days as the GTD.

Dataset	**Method**	**Days blocked**	**Precision**	**Recall**	$\mathbf{F_1}$	$\mathbf{F_1}$ **wrt AGP**	$\mathbf{F_1}$ **wrt DG83**	$\mathbf{F_1}$ **wrt S04**	$\mathbf{F_1}$ **wrt SOM-BI**
ERA5	GTD	33.4%	1	1	1	**0.56**	**0.73**	**0.19**	**0.74**
ERA5	AGP	19.5%	0.76	0.44	0.56	1	0.55	0.22	0.51
ERA5	DG83	34.3%	0.72	0.75	0.73	0.55	1	0.19	0.69
ERA5	S04	5.3%	0.69	0.11	0.19	0.22	0.19	1	0.15
ERA5	SOM-BI	34.6%	0.73	0.75	0.74	0.51	0.69	0.15	1
ERA5	BLO	100%	0.33	1	0.50	0.33	0.51	0.10	0.51
ERA5	RND	33.4%	0.33	0.33	0.33	0.25	0.34	0.09	0.34
UKESM	GTD	29.0%	1	1	1	**0.34**	**0.60**	-	**0.71**
UKESM	AGP	20.8%	0.41	0.29	0.34	1	0.29	-	0.28
UKESM	DG83	14.5%	0.90	0.45	0.60	0.29	1	-	0.55
UKESM	SOM-BI	29.6%	0.70	0.72	0.71	0.28	0.55	-	1
UKESM	BLO	100%	0.29	1	0.45	0.34	0.25	-	0.46
UKESM	RND	29.0%	0.29	0.29	0.29	0.24	0.19	-	0.29

found that this modification does not improve the SOM-BI performance overall. In summary, there are blocking events such as these that will also not be described well by the new SOM-BI, but as I show below the SOM-BI performs as good as or better than conventional BIs in most cases.

2.3.2 Blocking index comparison in ERA5 and UKESM with GTD

A climatological comparison of the BIs over JJA Europe confirms what has been discussed in the case study analyses above, and is consistent with the results of Pinheiro et al. (2019), which are broadly consistent with other BI climatologies. I show the spatial distribution of blocking climatologies according to three conventional blocking indices in Fig. A.4. Where my analysis substantially differs from the literature is in the regional approach and consideration of direct time series comparisons across the BIs including the SOM-BI. I do not explicitly consider the time-averaged climatological distributions of blocking events over Europe (as shown in Fig. A.4), which can only emphasize a time-averaged picture instead of the series of individual events. For my comparison, I first apply all BIs to the historical ERA5 data over the European domain. Each day for each BI is labelled as blocked if a blocking event has been identified within the

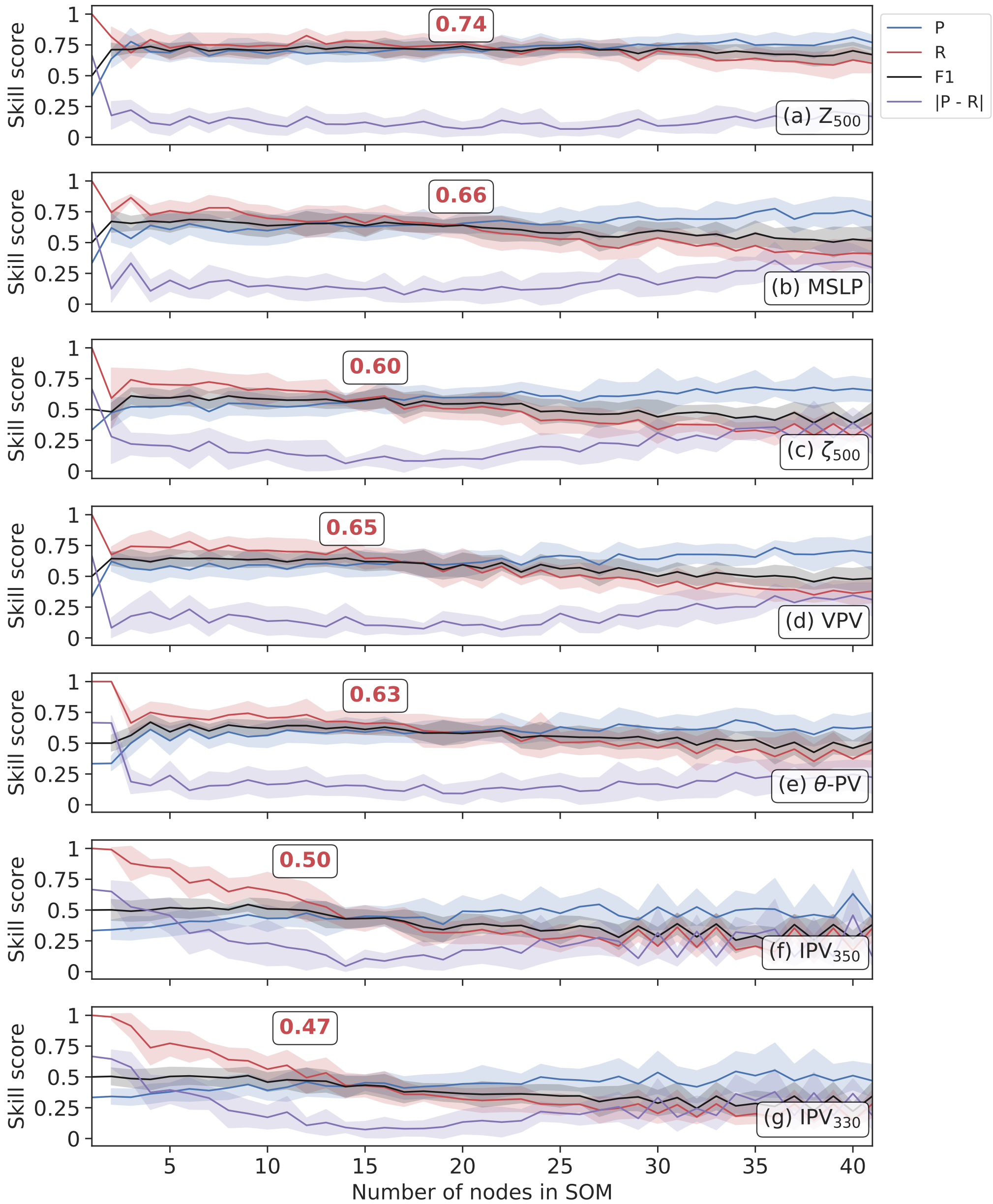

Figure 2.6: A comparison of the performance of the SOM blocking index for seven variables in the ERA5 1979-2019 historical period with a varying number of nodes in the SOM. Precision (P), recall (R) and F_1 scores are calculated, and the absolute difference between precision and recall is also shown. Error bands show the standard deviation ($\pm 1\sigma$) for 10-fold cross-validation. The red number inset into each panel shows the optimal F_1 score and the position of the box indicates the corresponding optimal node number. The optimal value is defined by the node number where the F_1 score is close to its maximum value and the difference between precision and recall is close to the minimum value.

European sector and persists for at least five days. A blocking event is not identified if the thresholds for amplitude, persistence, area and overlap discussed in section 2.2.3 are not met within the European domain. This results in a binary dataset for each BI that identifies periods of at least five consecutive days where blocking patterns exist within the European sector. These binary BI data sets I then compare to my manually labelled GTD.

Table 2.1 compares the precision, recall and F_1 scores of these BIs and the SOM-BI against the GTD for this domain-based comparison in both ERA5 and UKESM. I further compare the time series of blocking classifications among the BIs themselves to quantify how consistent the BIs are with each other. The key results are underlined. In both ERA5 and UKESM, the best blocking index is the SOM-BI, with a F_1 score of 0.74 in ERA5 and 0.71 in UKESM. All of the indices consistently perform worse in UKESM than in ERA5. This is because blocking is less frequent in the model and several of those blocking patterns identified in UKESM are less distinct (Fig. A.3). This is probably associated with mean biases in the representation of Z_{500} that have been observed across several climate models (Scaife et al. 2010; Schaller et al. 2018). The DG83 index performs almost as well as the SOM-BI in ERA5 with an F_1 score of 0.73, but there is a significant reduction in performance to 0.60 when applied to UKESM data. The AGP index in turn shows an even weaker skill than DG83 in both reanalysis and model, with a larger drop in skill from 0.56 to 0.34 in ERA5 and UKESM, respectively. The fact that SOM-BI still shows a relatively good score for UKESM of 0.71 suggests that the SOM-BI can be particularly useful in studying regional blocking in climate models. In particular, since a model ensemble may exhibit a variety of intensities of blocking, the SOM-BI would be able to overcome the limitations of BIs, where (particularly in the case of AGP) thresholds are defined with respect to the observational record. Since the anomalous flow patterns associated with blocking will be more consistent across datasets, the SOM-BI can identify blocking events across a model ensemble with greater accuracy. The consistent skill of the SOM-BI across both ERA5 and UKESM has been further verified by swapping the training and test datasets between each dataset, as described in section 2.3.5.

A case where every day in Europe is labelled as blocked ("BLO") is also compared, which represents the case of perfect recall (=1) but a low precision. This case gives an F_1 score of 0.53 for the GTD for ERA5 and 0.45 for the GTD of UKESM, and provides a useful benchmark of basic performance. Surprisingly, the AGP index only performs marginally better than BLO for ERA5, and performs worse in the UKESM case. Whilst S04 has a higher precision than BLO, because the recall is so low the total F_1 score is much lower (0.19). Finally, I compare a random labelling of blocked and non-blocked days, where the proportion of blocked days is equal to that of the GTD ("RND"). This gives an equal precision and recall because the number of true positives is equal to the number of false negatives. The F_1 score of RND still exceeds that of S04, with 0.33 for ERA5 and 0.29 for UKESM, and is comparable to the F_1 score of AGP in UKESM.

2.3.3 SOM-BI skill dependence on the choice of SOM node number and the meteorological variable

The key hyperparameter in the SOM-BI is the number of nodes (k), which here is similar to identifying the optimal number of circulation patterns required to effectively classify European summer weather regimes. In addition, there are a number of meteorological variables from which I could learn the SOM patterns, which in turn will also influence the skill of the SOM-BI method. The dependency of the skill of my BI on these two factors is quantified in the following. Figures 2.6 and 2.7 show how precision (P), recall (R) and F_1 score depend on k and the meteorological variable in ERA5 and UKESM, respectively. Specifically, I compare the skill metrics for cases where I learn the SOM nodes from Z_{500}, MSLP and ζ_{500} anomalies. For ERA5, I additionally consider four PV-related variables (VPV, θ-PV, IPV_{350} and IPV_{330}) shown in Fig. 2.6d-g.

Another hyperparameter related to the number of nodes is the row $\times$ column ($n \times m$) arrangement of nodes. For example, 16 nodes can be arranged as 16×1, 4×4, 8×2, 2×8 or 1×16. These different arrangements affect the topology of the SOM, the initialization of the nodes and which nodes are counted in the neighbourhood of other nodes during the update process of the SOM (Fig. 1.5). For each k in Figs. 2.6-2.8, I have used the arrangement of nodes that maximises the average number of nearest neighbours between each node (e.g. using 4×4 nodes for $k = 16$). This approach maximally exploits the SOM topology. I have also used $n \geq m$ (for example using a 9×2 arrangement instead of a 2×9 arrangement of nodes for $k = 18$) to preferentially arrange the SOM topology zonally across the domain rather than meridionally. This is done because there is greater variability in the occurrence of blocking patterns zonally

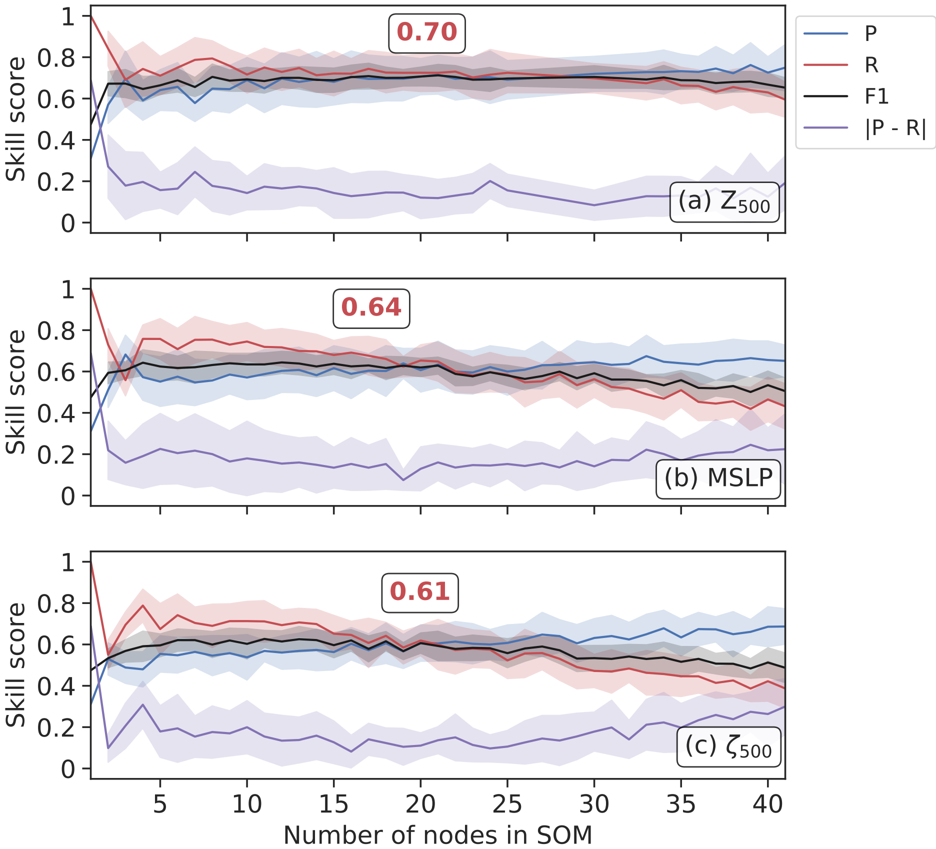

Figure 2.7: A comparison of the SOM blocking index performance for three variables in 101 years from the UKESM pre-industrial control period with a varying number of nodes in the SOM. Precision (P), recall (R) and F_1 scores are calculated, and the absolute difference between precision and recall is also shown. Error bands show the standard deviation ($\pm 1\sigma$). The red number inset into each panel shows the optimal F_1 score and the position of the box indicates the corresponding node number. As above, the largest F_1 score is for Z_{500}, indicating that Z_{500} is the best variable tested for analysing blocking patterns using the SOM-BI in UKESM.

than meridionally across Europe (Fig. A.4).

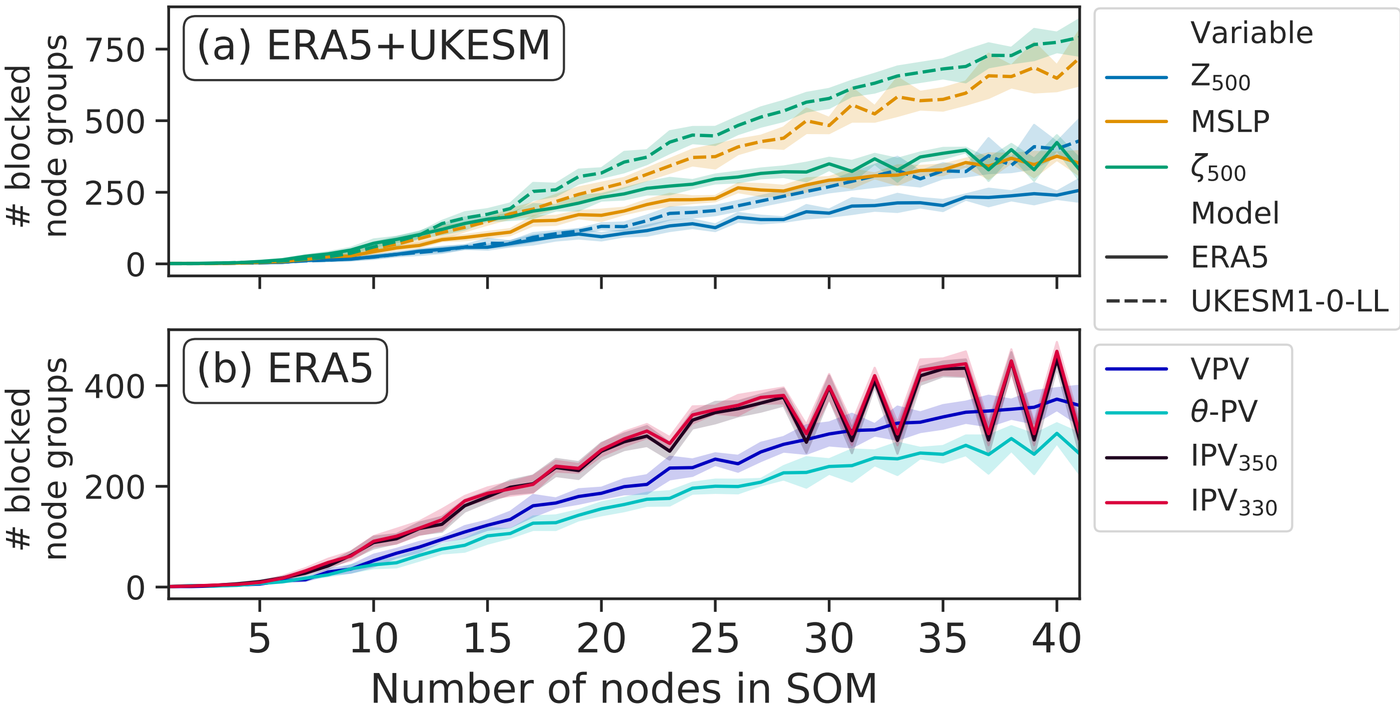

Figure 2.8: The number of node groups that are identified as blocked in the SOM-BI for ERA5 and UKESM for a range of node numbers and variables. The panels separate the variables available in both models from those only available in ERA5. Error bands show the standard deviation over cross-validation scores ($\pm 1\sigma$).

The results are shown for $1 < k < 41$. To measure out-of-sample skill, I used 10-fold cross-validation, where the GTD was split into 10 separate sections for testing the SOM-BI. The SOM-BI is trained on nine of the ten data sections and its skill is evaluated on the remaining section. The skill scores shown only indicate how well the SOM-BI is able to predict the test period in question, which was not used for training. This ensures that the SOM-BI has not been tuned to the data I measure its skill against, which could give it an unfair advantage compared to the other BIs. For ERA5 I used 4 year periods (1980-1984, ... , 2015-2019 inclusive) to test on and trained on the remaining 37 years, with each 4-year period once serving as the independent test set. In UKESM 10-year periods (1960-1959, ... , 2050-2059 inclusive) were used for testing the SOM-BI and it was trained on the remaining 91 year period. This 10-fold cross-validation procedure produces a range of precision, recall and F_1 scores for each node number. Figures 2.6 and 2.7 show the mean values for precision, recall, F_1 and the absolute difference between precision and recall. Figure 2.8 compares the number of groups of nodes identified as blocked for each variable. Error bands indicate the standard deviation of each skill metric ($\pm 1\sigma$).

Common features are observed for each variable for a very small or large number of SOM nodes. For small k the SOM-BI identifies more days as blocked, such that R >> P. This indicates that the SOM is under-fitting the data for European circulation patterns across the domain and so the algorithm lacks a precise delineation of blocking events. In other words, it could be beneficial to increase k to be able to represent a larger number of dynamical states and thus to detect and describe blocking events more precisely. For large k, $R << P$, showing that the SOM-BI is trending towards overfitting the training data. I deduce that the optimal k occurs when the difference between P and R is small and the F_1 score is close to its maximum value.

From Figs. 2.6 and 2.7, I find that for both ERA5 and UKESM the Z_{500} anomaly is the best variable to use with the SOM-BI, with a mean F_1 score of 0.74 and 0.71 for $k = 20$ and 21 in ERA5 and UKESM, respectively. From Fig. 2.8a, Z_{500} also shows the lowest number of blocked node groups for a given k, which shows that the blocked node groups are physically more explanatory in Z_{500} than the blocked node groups associated with other for other variables, making the SOM-BI results easier to interpret physically. MSLP is the second most effective variable, with an optimum F_1 score of 0.66 and 0.64 for ERA5 and UKESM respectively. This lower peak performance is because the MSLP field has a lower signal-to-noise ratio as it is influenced by effects within the boundary layer such as heat lows. The PV-related variables exhibit a variety of lower skills, where the VPV field performing at a similar level to MSLP, since the vertical integration of the VPV variable enables it to capture the pattern of blocking better than other PV-based variables (Schwierz et al. 2004).

2.3.4 SOM-BI skill dependence on number of training years

One important verification for the SOM-BI is to ensure its robustness over long timescales. Contrary to the other BIs, the SOMs learn from training data. Therefore, the SOM-BI skill on test data will also be a function of how representative the training samples are of general states of the atmosphere. Here I investigate if the observational record, for example, is long enough to indeed ensure the same performance of the SOM-BI described above over longer timescales. For

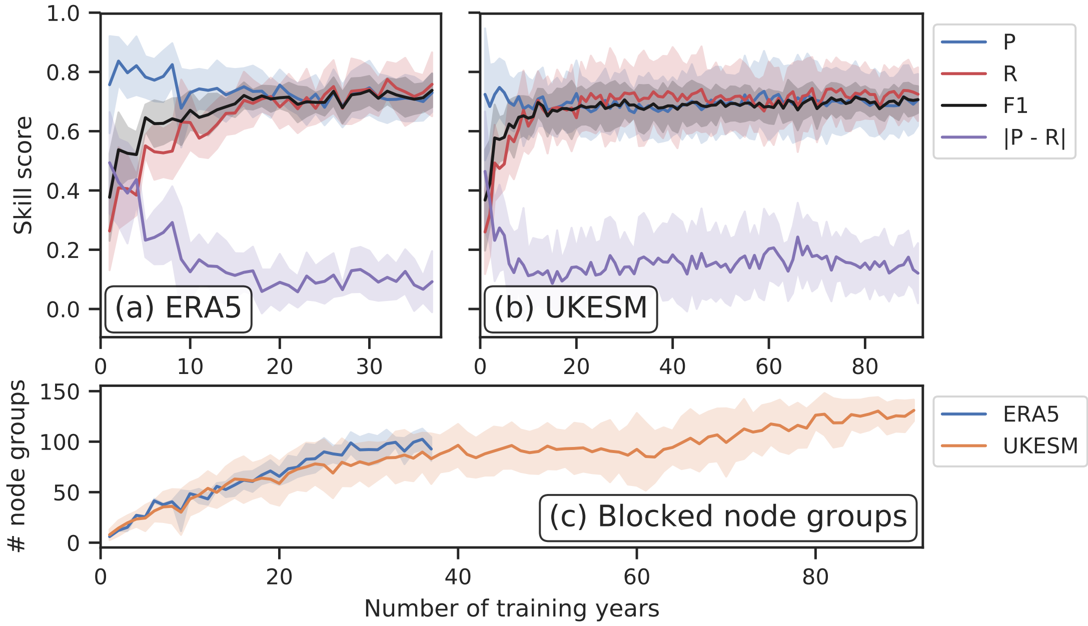

Figure 2.9: SOM-BI skill depending on the number of training years. (a) and (b) show the skill scores for ERA5 and UKESM, and (c) shows how the number of node groups associated with blocking varies with the length of the training record. 10-fold cross-validation is used, with 4 and 10 years used to test the SOM-BI for ERA5 and UKESM respectively. In both models Z_{500} is the variable tested with 20 (5x4) nodes in the SOM. Error bands indicate standard deviation ($\pm 1\sigma$) in the skill scores depending on the training/test set combination.

this purpose, I train the SOM-BI algorithm on a range of different numbers of training years, while keeping the number of years to test the algorithm performance consistent. Importantly, there is no overlap between the training and test data to ensure that the skill evaluation is truly independent, following the idea of statistical cross-validation (see e.g. Nowack et al. 2018b; Mansfield et al. 2020). Figure 2.9 shows the results of this analysis for Z_{500} and 20 nodes across both (a) ERA5 and (b) UKESM datasets, which is the best performing case according to my analysis above. Since the datasets have different lengths (41 years vs. 101 years), I tested the model on 4 and 10 years for each dataset respectively. For a small number of years, the algorithm only sees a few blocking events and so only identifies the particular node groups that are associated with these blocking events rather than identifying node groups that are in general associated with blocking events. This leads to a high precision for a small number of training years, particularly in the ERA5 data, since the SOM-BI is effectively over-fitting on a few events, but the recall and overall F_1 score are low. This behaviour is confirmed by Fig. 2.9 (c), which shows that there is a small set of node groups associated with blocking for a small number of training years.

Figs. 2.9 (a) and (b) both show that the recall and F_1 scores increase asymptotically for a larger number of training years, and the precision decreases asymptotically. These variations become very small after 20 years for both ERA5 and UKESM, which indicates that after around 20 years the SOM-BI seems to approximate optimal performance. Figure 2.8 (c) shows that the number of node groups associated with blocking continues to increase in both ERA5 and UKESM even after this point, with 120 node groups identified with blocking for UKESM over 91 years compared to 95 node groups over 37 years. However, these extra node groups occur rarely in the blocking datasets since they do not significantly affect either the precision or recall of the algorithm, and are therefore less important for the detection of blocking from meteorological data.

2.3.5 Cross-comparison of SOM-BI skill

For the SOM-BI to be effectively applied to understand future trends in atmospheric blocking, I need to verify that the training of the SOM-BI on the observational record is consistent with CMIP6 models. This step is necessary to ensure that the SOM-BI can identify blocking patterns in the models. If it is possible for the SOM-BI to identify blocking patterns in a CMIP6 model from training on the observations, then this shows potential for the SOM-BI to be applied consistently across a model ensemble. Furthermore, if the SOM-BI can be trained on a CMIP6 model and tested on the observations, differences in the skill of the SOM-BI would highlight limitations in that model's ability to represent blocking patterns. This could be applied across a model ensemble to compare the skill of different models at representing blocking patterns.

To investigate the feasibility of such studies, I test the skill of the SOM-BI algorithm by training Z_{500} data on the 41 years from the ERA5 dataset and testing on the UKESM dataset and vice versa. Table 2.2 shows the differences in the optimal performance for Z_{500} across the different datasets. In all cases several node numbers were tested, and I identified an optimal node number of 20 or 21 across all the configurations of training and testing data. There was also a good performance of the SOM-BI for other node numbers that is consistent with Fig. 2.6a (not shown). The stable performance of the SOM-BI shows that there is a consistent range of synoptic weather patterns between the ERA5 and UKESM for European summer.

Table 2.2: A comparison of the optimal F_1 score for when Z_{500} ERA5 and UKESM datasets are trained and tested on themselves and each other respectively. The corresponding node number and number of blocked node groups is shown. When the dataset is tested on itself, 10-fold cross-validation is used and the mean value is shown. The optimal F_1 score is identified by finding the node number with the smallest difference between precision and recall whilst maintaining a relatively high F_1 score.

Training data	**Test data**	**F_1 score**	**No of nodes**	**No of blocked node groups**
ERA5	ERA5	0.74	20	95
UKESM	ERA5	0.74	21	134
UKESM	UKESM	0.71	20	131
ERA5	UKESM	0.71	19	99

It also indicates a consistency between the labeling that occurred in the GTD across ERA5 and UKESM, despite the reduced performance in the blocking indices to label the GTD. This further shows that UKESM describes blocking patterns in a similar enough way to the historical observations for useful study of blocking events, which in turn reinforces the validity of studies in blocking trends from the CMIP6 archive (Davini and D'Andrea 2020). Finally, this underscores the potential for the SOM-BI to be used in understanding future trends and diagnosing model skill across the CMIP model ensemble.

2.3.6 Dependence of SOM-BI skill on other parameters

Apart from the number of SOM nodes, the number of years trained over and the choice of training dataset, there are several other parameters that could be modulated within the SOM-BI framework. First, I investigated 5-fold cross-validation on the ERA5 dataset, which involves testing the SOM-BI on 8 years of data five times. This was found to have a marginally lower performance than 10-fold cross-validation. Furthermore, I tested an alternative approach to identifying the corresponding best matching unit for the SOM pattern, where I only used positive anomalies to define the BMU. Since I am only interested in positive anomalies it is possible that such an approach would increase the skill score, particularly for events such as the 2019 European heatwave (Fig. 2.5). However, this modification was found to have a negligible effect on the overall SOM-BI skill.

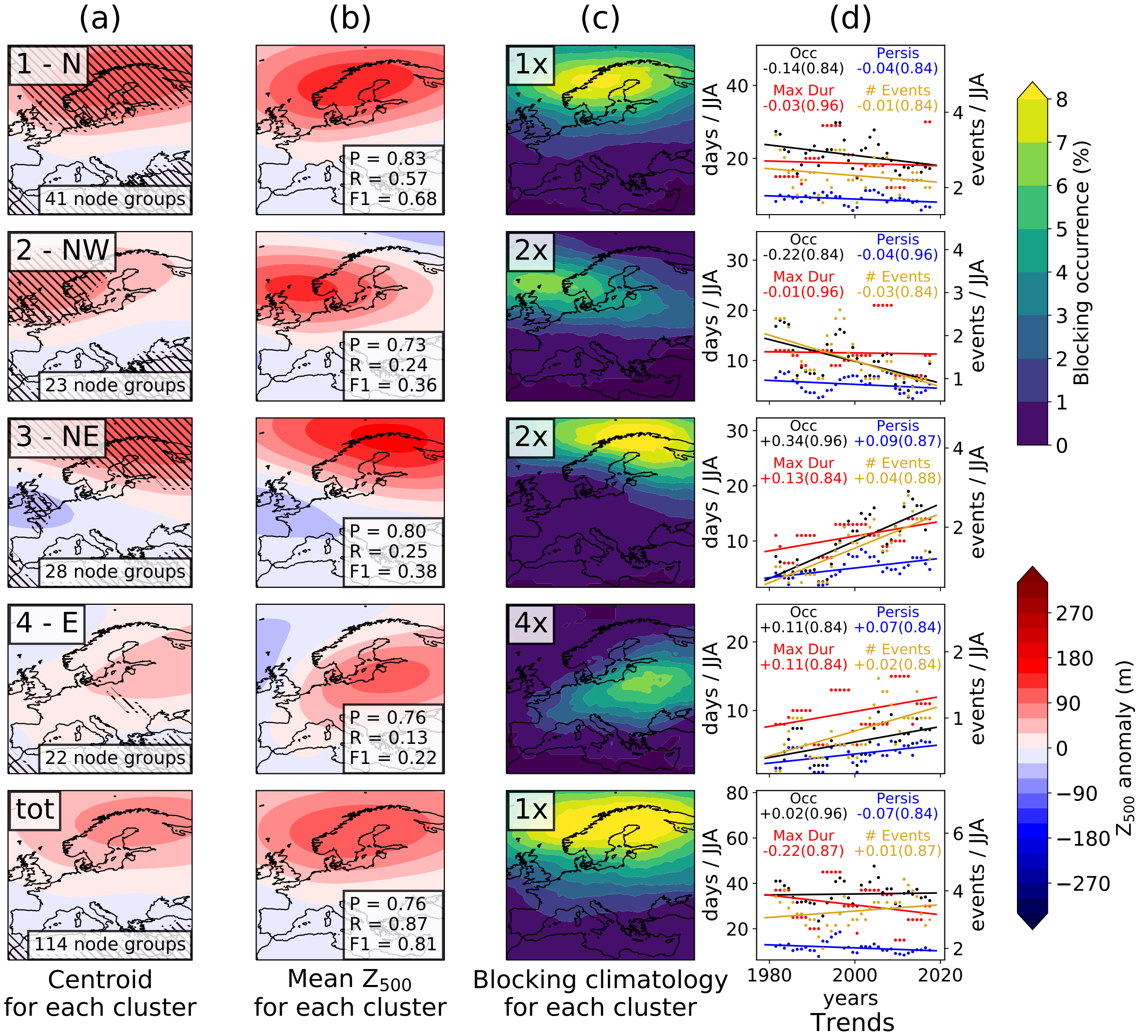

Figure 2.10: Application of the SOM-BI to ERA5 Z_{500} 1979-2019 JJA, using the method outlined in section 2.2.7. (a) The K-means centroids of the mean codebooks. Hatching indicates regions where the mean codebooks for contributing node groups agree on the sign. The number of node groups associated with each cluster is indicated in the bottom right of each panel. The labels in the top right of each panel reflect the main region with a positive anomaly. “tot” is the total combination across all blocked node groups. To show that the four clusters are consistent with the fields they represent, I show in (b) the average Z_{500} field across all days belonging to each cluster of blocked node groups. At the bottom right of each panel in (b) the precision, recall and F_1 scores are shown for each cluster. (c) The blocking climatology for each set of node groups, derived using the DG83 index for each blocked day identified by SOM-BI for the given K-means cluster. Since the frequency of blocked events varies strongly between each cluster, the climatologies have been scaled by the numbers in the top left of each panel. (d) Historical trends as characterized by four different metrics for each cluster, using five-year moving average data: black - occurrence of pattern; blue - persistence (average duration) of pattern; red - maximum duration of block; gold - average number of blocked events (uses the right hand y-axis scale). The numbers (numbers in brackets) show the gradients (p-values) for each trend, which are all insignificant after correcting for multiple testing and autocorrelation.

2.3.7 Application of the SOM-BI to ERA5

A central question of current research is how the characteristics of regional blocking events are affected by climate change (Woollings et al. 2018; Drouard and Woollings 2018; Kornhuber et al. 2019; Kornhuber et al. 2020). Here, I briefly demonstrate how the SOM-BI can be used to study such effects. For this purpose, I apply SOM-BI to ERA5 data (Fig. 2.8a), where my optimization yields the best performance for 20 SOM nodes (using Z_{500}), and a total set of 114 blocked nodes (section 2.6). Clearly, this large number of different blocking patterns with subtly different characteristics creates a challenge for easy interpretation of the results. In addition, because several of these node groups occur very infrequently, perhaps only once in the 1979-2019 period, a meaningful study of their trends is not always possible. To achieve this, I suggest a post-processing approach using the aforementioned K-means clustering analysis (Diday and Simon 1980), but now applied to the 114 mean codebooks (section 2.2.7) identified for each node group. The goal of this post-processing step is to identify distinct *K-means* clusters of SOM node groups, where each K-means cluster summarizes a pattern-wise similar set of blocked SOM node groups. In Fig. 2.8 (a), $k = 4$ is chosen since it is a common choice for identifying weather regimes (Michelangeli et al. 1995; Cassou 2008; Ullmann et al. 2014; Strommen et al. 2019; Fabiano et al. 2021), but I note that a larger value of k yields a more detailed classification of blocking patterns. Hierarchical clustering was also tested as an alternative to K-means, and similar patterns were produced (not shown).

To illustrate the method, Figure 2.10 (a) shows the cluster centroids for each set of mean codebooks for this case of $k = 4$. The bottom panel shows the mean pattern across all centroids. Regions of hatching show where all of the mean codebooks in each centroid agree on the sign. The number of node groups included in each cluster has been labelled in the bottom right of Fig. 2.10 (a). The different clusters show distinct regions of positive anomalies, with generally strong agreement across all mean codebooks included in each cluster. This underlines that the clustering approach is effective at identifying distinct types of blocking events. The clusters have been labelled in the top right of Fig. 2.10 (a) reflecting in each case the main region of positive anomaly. Fig. 2.10 (b) shows the mean Z_{500} field across all blocked days identified for each cluster, which are highly consistent with Fig. 2.10 (a). Consequently, the subsets of node groups are as expected physically consistent with the circulation patterns across these blocked days so that the K-means clusters can indeed be used to study specific types of regional blocking. In Fig. 2.10 (c), I show the blocking climatology associated with each cluster derived using the DG83 index across the days identified as blocked in each cluster. The climatology again matches well the patterns identified in (a) and (b). The bottom panel of Fig. 2.10 (c) shows the total blocking climatology from the SOM-BI. It is similar to the corresponding DG83 blocking climatology in Fig. A.4 (b), with a slightly reduced number of blocking events around the Scandinavian high. This suggests that the SOM-BI is reducing the identification of events on the edge of the domain.

Having established that SOM-BI, following by K-means post-processing, identifies clusters representing distinct regional blocking events, I turn my attention to studying potential trends in such blocking patterns. Such trends are given in Fig. 2.10 (d), using four different metrics to characterize the events. These are the rate of occurrence of events ("Occ"; the number of days in JJA that are associated with the pattern each year) and their persistence ("Persis"; the average persistence of a blocking pattern in days), maximum duration ("Max Dur"; the longest event for each year), and the number of events ("# Events"; the total number of continuous blocked events per year). These quantities are calculated for each cluster and I average all metrics using a five-year centred moving window, which is necessary to ensure that at least one event for each of the four blocking patterns occurs within a given period.

The numbers (numbers in brackets) show the gradients (p-values) for each trend. The p-values have been corrected for autocorrelation using the Zwiers and Storch (1995) two-tailed Student's t-test, and the multiple hypothesis testing has been corrected for using the false discovery rate (Benjamini and Hochberg 1995; Horton et al. 2015). Since all of the p-values are large, none of the trends are significant. However, I note that the number of E and NE European blocking events doubles whilst the number of W European events halves across the 1979-2019 period. Whilst none of these trends are statistically significant, it highlights how the SOM-BI method could be used to study changes in the characteristics of European blocking over time, e.g. in longer climate change simulations. The SOM-BI can provide information that is not directly available in the other BIs discussed here, since it can be used to study long-term trends across several types of automatically identified European blocking patterns.

2.4 Discussion and Conclusions

Using self-organizing maps (SOMs), I have developed a new blocking index (SOM-BI). This has involved the creation of a new time series dataset (GTD) to describe when blocking events have historically occurred over a region. I have described my approach as unsupervised through its use of the SOM algorithm, but I note that the SOM-BI also employs supervised learning through its blocking classification using the GTD. By studying the case of European summer, I have identified a similar or better skill score for SOM-BI compared to several other blocking indices (BIs) using ERA5 reanalysis data from 1979-2019. I further applied my new approach to a pre-industrial control run from UKESM, and find that my method shows consistent skill for this model dataset, whereas the other BIs substantially lose performance in this case. Whilst no individual SOM node directly corresponds to a weather regime such as blocking, with an optimal node number I can develop a set of node groups which are associated with blocking. I have also found that 20 years are needed to train the SOM-BI, which underlines that the SOM-BI has a robust level of performance if trained on standard reanalyses or on typical lengths of climate model simulations. The performance of the SOM-BI is also robust to the dataset used to train it, since it shows good performance when it is trained on the ERA5 data and tested on UKESM and vice versa. These results show that unsupervised learning can be usefully applied to understand regional blocking events, both historically and in the future.

I have further compared the performance of SOM-BI for a range of variables in both ERA5 and UKESM that have been classically used to study blocking (Figs. 2.6 and 2.7). I find that the best skill is obtained when applying SOM-BI to the Z_{500} field because it exhibits the best signal-to-noise ratio in blocking identification. This is reflected in Fig. 2.8, which shows that for a given node number the Z_{500} SOM-BI identifies blocking patterns with a smaller number of node groups than for other variables.

I have confirmed that individual SOM nodes do not represent weather patterns perfectly so that care needs to be taken in using SOM patterns as a means of diagnosing weather patterns

(Gibson et al. 2017b). If individual SOM nodes were used to create a blocking index, or if a small node number was used (3-6 nodes) there would be a high recall and low precision in detecting blocking using this approach, which would be the equivalent to some of the approaches applied elsewhere (e.g. Horton et al. 2015). If a higher node number (12+) was used and only one node was associated with blocking, then there would be a high precision and low recall, and overall a lower F_1 score than for a low node number. However, by using a large number of nodes and studying groups of nodes across periods of five days, I have developed an algorithm that can regionally identify blocking patterns with optimal precision and recall, and which outperforms several conventional blocking indices for this task.

Using this algorithm has involved the creation of a GTD, a binary dataset that identifies regional blocking events. There are several limitations to this approach. Firstly, the choice of domain is somewhat arbitrary and here primarily motivated by a specific scientific question (summer heatwaves in Europe), and events which are on the edges of the domain are excluded, even though a large region within the domain could be considered blocked. In addition, the task of assigning a binary label to each day can be further complicated, since there is subjectivity in assigning a binary label to the onset and decay of blocking events. However, by focusing on events which are centered within the domain, a broad agreement with the identification of blocked events was achieved, despite the somewhat subjective labelling nature of this approach. The fact that the SOM-BI exhibits consistently good skill across ERA5 and UKESM even when the SOM is trained on the other dataset underscores the consistency of my labelling as applied both to the climate model and reanalysis data.

The use of SOMs as a blocking index provides opportunities for regional study that are not directly available in the other BIs. Through an additional post-processing step involving K-means clustering on blocked node groups (sections 2.2.7 and 2.3.7), I have shown that the SOM-BI can identify specific types of blocking events and provide detailed information about the changing nature of blocked events over a European subdomain (Fig. 2.10). The case of $k = 4$ has been shown in Fig. 2.10, but larger values of k can also be chosen to identify more distinct types of blocking pattern. Whilst the SOM-BI does not directly produce a gridded climatology of blocking patterns, I have shown that the SOM-BI can be integrated with the other BIs to develop a climatology that only considers days detected as blocking by the SOM-BI. This results in a SOM-BI climatology with a higher precision than the DG83 index. The identification of distinct blocking patterns from node groups enables a detailed study of blocking characteristics over European subdomains as shown in Fig. 2.10.

This SOM-BI method has been applied to future trends in chapter 3 across CMIP5 and CMIP6 models to study the ESB response, and different mechanisms for understanding this response are proposed. In chapter 4 the SOM-BI method is used to provide an observational constraint for the response on European summer blocking.

Chapter 3

Model predictions and proposed physical mechanisms for the European summer blocking (ESB) response to climate change

3.1 Introduction

One reason for the current uncertainty in the response of atmospheric blocking to climate change is the large inter-annual and decadal variability in the blocking climatology (Kennedy et al. 2016; Brunner et al. 2017). This creates a challenge in separating forced changes in blocking occurrence from unforced variability (Barnes et al. 2014; Shepherd 2014). One way to address this is to study the response of atmospheric blocking in climate models in a high forcing scenario. The self-organizing maps blocking index (SOM-BI) introduced in chapter 2 (Thomas et al. 2021) provides an opportunity to study atmospheric blocking in high forcing scenarios, since it can be used on a wide variety of datasets with a comparable skill to alternative BIs.

The atmospheric blocking response to climate change has been discussed in light of two competing mechanisms: Arctic Amplification (AA) and increased upper-tropospheric warming (UTW). These mechanisms work to increase and decrease atmospheric blocking occurrence respectively (Barnes and Screen 2015). In studying the ESB response under high forcing across the CMIP5/6 model ensemble, I can investigate how other meteorological variables change under high forcing. This enables me to identify the importance of AA and UTW and propose other possible physical mechanisms which may have a role in influencing the ESB response.

The models and scenarios used for this analysis are introduced in section 3.2, and the application of the SOM-BI method is discussed in section 3.3. The results section is divided into five subsections. Section 3.4.1 presents the trends and relationship between past and future blocking change. Sections 3.4.2 present a discussion of four physical mechanisms which could affect the ESB response across the model ensemble:

1. Arctic amplification (AA) (section 3.4.2);
2. increased tropical upper-tropospheric warming (UTW) (section 3.4.3);
3. changes in the midlatitude meridional temperature gradient (section 3.4.4); and
4. the propagation of Rossby waves from diabatic heating in the equatorial Pacific (section 3.4.5).

Discussion and conclusions are presented in section 3.5.

3.2 Data

The climate model data used in this chapter comes from the Coupled Model Intercomparison Project Phases 5 and 6 (CMIP5 and CMIP6). I am studying JJA across 22 models (listed on the x-axis of Fig. 3.2). To maximise the effect of climate forcing and to improve the signal-to-noise ratio, I have studied blocking in the 4xCO_2 runs and compared to the historical period (note throughout this chapter I define “historical” as referring to the 1979-2005 period inclusive of all years). The 1979-2005 historical period is used to provide a comparison to reanalysis data from ERA5 and to maximise the number of models that can be used in this analysis, since more daily data was available for the historical scenarios than for the pre-industrial control runs. Since most models have only one ensemble member across the 4xCO_2 and historical runs, one ensemble member has been used in each model for consistency. The 22 models used in the analysis include all models across CMIP5 and CMIP6 which have provided monthly data output for wind fields and surface air temperature, with concurrent daily data for mean sea level pressure in both the studied 4xCO_2 and historical periods.

I have taken daily mean sea level pressure (MSLP) data for the 4xCO_2 and historical runs, and have studied the JJA period with 5 days before and after to ensure that all blocking events captured by the SOM-BI within JJA are included. To allow for the climate to adjust after the significant 4xCO_2 forcing, I have selected the period 120-150 years after the start of the 4xCO_2 run, since this period is available across all models (note throughout this chapter that the 4xCO_2 period refers to the 120-150 year period after the start of the 4xCO_2 run). Note that 120-150 years after the abrupt change is not long enough for the model to have reached an equilibrium with stationary global mean surface temperature (GMST). For example, Li et al. (2013) found that it takes 1,200 years for the surface to equilibriate after a 4xCO_2 step change in the ECHAM5 coupled climate model, and Rugenstein et al. (2019) found that the CESM104 coupled climate model needs 4,000 years to achieve radiative balance at the top of the atmosphere after a 4xCO_2 step change. However, across the 120-150 year period the rate of change of GMST is approximately the same as the rate of change of GMST across the 1979-2005 period (+0.1 ° C per decade) and much smaller than the first 100 years after the abrupt 4xCO_2 change (see e.g. Fig. 1a in Nowack et al. (2018a)). Therefore, I argue that it is legitimate to treat the 120-150 year period as a new state of the climate which can be compared to the 1979-2005 period.

To compare the change in ESB with the changes in other variables across the 22 models, I have studied monthly-mean data from the 4xCO_2 and historical runs across JJA and taken seasonal averages. The variables I have studied include zonal and meridional wind (U and V) at 200 hPa, which have been used to derive the dynamical variables of relative vorticity and streamfunction. Additionally, I have derived the vertical U gradient ($\partial U/\partial z$) by calculating a cubic spline interpolation across the pressure axis at every latitude and longitude and calculating the first derivative.

At the surface, I have also used surface air temperature (T_{surf}) to calculate the GMST. To account for differences in model climate sensitivity, in this chapter the inter-model changes in blocking occurrence between the historical and 4xCO_2 periods of each model have all been scaled by the change in GMST of each model, respectively. Similar correlations between the change in the synoptic variables considered and the change in ESB have been found without applying a GMST scaling (not shown).

3.3 Methods

3.3.1 Use of SOM-BI with MSLP

Since there is limited availability of daily geopotential height data in the 4xCO_2 runs, in this study I use daily MSLP fields to identify blocking events. MSLP is not frequently used as a variable for blocking studies, because it has a much lower signal-to-noise ratio than geopotential height or potential vorticity, partially because of the interaction with boundary layer effects such as surface lows. However, I have previously found in section 2.3.3 that the MSLP-based version of the SOM-BI provides more skill in identifying blocking events than other indices in climate models. A further benefit of MSLP is that it is a (mostly) stationary variable with respect to climate change, compared to geopotential height which linearly increases under warming according to the hypsometric equation. Whilst this effect can be detrended, such detrending relies on assuming that the thermodynamic effect is linear over time (see the discussion in section 2.2.1). However, in a sudden forcing scenario, the assumption of linearity in the response to the time following the forcing is clearly invalid, and it is therefore impossible to clearly separate out thermodynamic climate change effects on geopotential height from the dynamic effects (see discussion in 2.2.1 on detrending geopotential height and section 1.1 on dynamic and thermodynamic climate change). Therefore, MSLP appears to be the optimal choice of variable if one wants to study the response of atmospheric blocking to climate change in a scenario with abrupt forcing.

Note that global warming will thermodynamically impact the MSLP level by increasing the mass of the atmosphere through the increased capacity for the air to store water vapour (Trenberth and Guillemot 1994). The increase in the partial pressure of water vapour at typical temperatures in the atmosphere will lead to maximum increases in atmospheric pressure of approximately 3 hPa $^\circ$ C^{-1}, assuming the air is saturated (Lester et al. 1984). This thermodynamic effect is observable in the global mean in the 4xCO_2 simulations, where increasing the GMST increases the global MSLP by approximately 0.1 hPa $^\circ$ C^{-1}. However, whilst this thermodynamic effect is dominant in the global MSLP average, the regional change in MSLP over e.g. Europe is not in general correlated with changes in GMST. These differences are shown for the UKESM 4xCO_2 run in Appendix B.3. The lack of correlation demonstrates that when studying how MSLP patterns change under climate change, the effects of climate dynamics dominate on regional scales. I therefore assume that changes in MSLP reflect dynamic mechanisms of climate change, and that MSLP is a valid variable to track changes in the occurrence of atmospheric blocking in forced scenarios.

3.3.2 MSLP bias and normalization

To study blocking events in the 4xCO_2 runs, I use the SOM-BI as described in chapter 2 to classify days over Europe as blocked or not (Thomas et al. 2021). This is calculated from MSLP anomaly data over Europe for both the historical (1979-2005) and 4xCO_2 (120-150 years after start of 4xCO_2 run) periods.

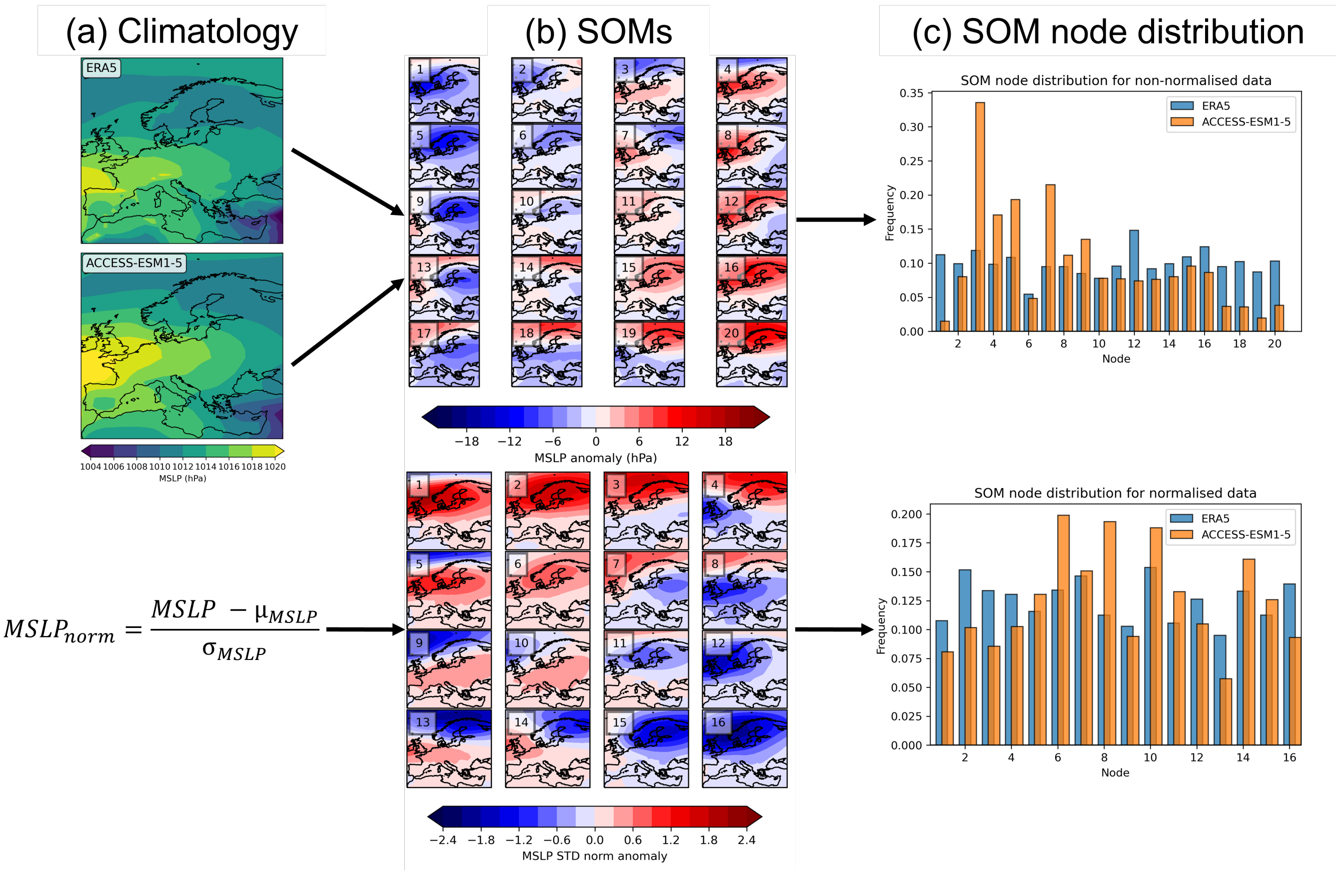

Figure 3.1: A diagram to show how model bias arises in the application of the SOM-BI (top half) and how the normalised MSLP (defined in lower right) addresses the issue of model bias (lower panel). (a) shows the MSLP climatology across JJA for the historic period (1979-2005) in both ERA5 and ACCESS-ESM-1-5. (b) shows the optimised self-organizing maps (SOMs, see section 1.5.5) for the MSLP (top) and $\mathrm{MSLP}_{\mathrm{norm}}$ (bottom) data. In both cases the JJA historic period of the ERA5 reanalysis was used to train the SOM. (c) shows the SOM node distribution for ACCESS-ESM1-5 and ERA5 for the MSLP (top) and $\mathrm{MSLP}_{\mathrm{norm}}$ data. The difference between the model and reanalysis data SOM node histograms is significantly reduced by applying the normalisation. This demonstrates that the normalisation is effective in removing the SOM node bias. See discussion below and in Appendix B.1.

3.3.2.1 MSLP bias and implications for SOM-BI skill

I have found that using the MSLP SOM-BI trained on ERA5 data for climate models introduces a significant bias in the results that is correlated with the future changes in the blocking of the model, particularly over Scandinavia (see Fig. B.4 in Appendix B). This is due to the fact that the bias of the historical MSLP climatology and variability of CMIP models is sufficiently different to the ERA5 MSLP climatology so as to create biases in the occurrence of certain SOM nodes. Such biases in the occurrence of certain SOM nodes will then lead to biases in the detection of blocked SOM node groups, and therefore biases in the occurrence of blocking events from using the SOM-BI method. Such biases are based on differences in the statistics of the SOM node occurrence, and therefore do not represent physical differences between ERA5 and a given climate model, so need to be addressed in some way.

This problem is illustrated in the top half of Fig. 3.1, which shows a comparison between the ERA5 reanalysis and the ACCESS-ESM1-5 model (a model which shows a particularly strong bias) for the historic period (1979-2006). In Fig. 3.1a the two MSLP climatologies are shown, and whilst they exhibit the same general features, the MSLP climatology shows significantly higher values (4 hPa) over much of the Western part of the domain, particularly the UK. Here, I use the optimised SOM trained on ERA5 data to assign the best-matching units for each day (see the discussion of SOMs in section 1.5.5 and the blocking index derived from SOMs in section 2.2.5). This SOM is shown in the top panel of Fig. 3.1b.

The difference in the MSLP climatology leads to an over-representation and under-representation of certain SOM nodes in the ACCESS-ESM1-5 model. These differences are shown in the top panel of Fig. 3.1c. In particular, node 1 is over six times as likely to occur in the ERA5 reanalysis than in ACCESS-ESM1-5, and node 3 is over twice as likely to occur in the ACCESS-ESM1-5 model than in the ERA5 reanalysis. The higher occurrence of node 3, which (from Fig. 3.1b) shows an SOM node with a dipole centered across Western Europe and the Norwegian Sea), and lower occurrence of node 1 (which has a node with low pressure centered on the UK) in ACCESS-ESM1-5 can be explained by the bias in the MSLP climatology in Fig. 3.1a over the UK and Western Europe.

This bias in the occurrence of certain SOM nodes will then lead to significant differences when occurrences of blocking events are detected, which from the SOM-BI are defined by using blocked node groups (see section 2.2.5). Since there are significant changes in the occurrence of certain blocked node groups historically, changes in the MSLP climatology and variability under 4xCO_2 will lead to more/less significant changes in the occurrence of the SOM node groups than are warranted. I have found across models that a higher historic MSLP climatology over Scandinavia leads to a decrease in the future occurrence of blocking (see Fig. B.4 in Appendix B). Such a relationship occurs because such models have an over-abundance historically of the SOM nodes with low pressure over Scandinavia (see Fig. B.3 in Appendix B). Therefore, any positive increases or pattern shifts over Scandinavia will lead to a disproportionate change in the occurrence of such SOM nodes, resulting in biased future changes in the number of blocking events from the SOM-BI.

Note that this issue of reduced model skill arising from applying the ERA5 SOM to CMIP data was already partially considered in section 2.3.5 for the UKESM model. However, for the UKESM model there was not a significant change in the skill score using the SOM derived from ERA5 or from UKESM across either model and vice versa (see Table 2.2). The need to use normalised MSLP data emerges from considering the CMIP5 and CMIP6 model ensemble, which has a wide range of skill in representing the European MSLP climatology.

3.3.2.2 MSLP normalisation and implications for SOM-BI skill

One means of addressing this issue of model bias is to define the SOM-BI using MSLP anomalies which are normalised by subtracting the mean and dividing by the standard deviation in each grid cell:

$$\mathrm{MSLP}_{norm} = \frac{\mathrm{MSLP} - \mu_{\mathrm{MSLP}}}{\sigma_{\mathrm{MSLP}}}, \tag{3.1}$$

where μ_{MSLP} and σ_{MSLP} are the mean and standard deviation of JJA-averaged MSLP in each grid cell respectively. If done for all ERA5 and CMIP model datasets separately, this approximately removes the model bias in the occurrence of certain SOM nodes. The resulting SOMs found for ERA5 using the $\mathrm{MSLP}_{\mathrm{norm}}$ data is shown in the bottom panel of Fig. 3.1b.

Note that using the SOM-BI with a new variable requires a redefinition of the set of blocked node groups and the optimal SOM node number. This could lead to a different skill in identifying blocking events, as shown in Fig. 2.8 in section 2.3.2 in the previous chapter. However, Fig. B.5 in Appendix B.2 shows that the SOM-BI using normalised MSLP anomalies has a similar skill in identifying blocking events to the SOM-BI using non-normalised MSLP anomalies.

The lower panel of Fig. 3.1c shows the SOM node histograms for ACCESS-ESM1-5 and ERA5 for the normalised SOM case, which more closely approximate each other than in the upper panel in Fig. 3.1c. This demonstrates that the model bias issue has been significantly reduced by using the normalised MSLP variable instead of the MSLP variable. The largest bias between ERA5 and ACCESS-ESM1-5 is for node 8, which is 1.5x more likely to occur in the ACCESS model than in the ERA5 reanalysis. However, these differences could of course equally be caused by internal variability (limited sample size) as well as model structure leading to different frequencies of event occurrence, i.e. the distributions are not expected to be exactly the same in any case.

Note that under 4xCO_2 the MSLP climatology shifts, and therefore the MSLP anomalies in the 4xCO_2 run are projected onto a different background climatology. Since atmospheric blocking events are deviations from the climatological background of MSLP, I separately define the MSLP anomaly field in the 4xCO_2 run with respect to the 4xCO_2 climatology, and separately apply the SOM-BI normalisation for the 4xCO_2 period. Note that in separately defining the anomalies for the historic and 4xCO_2 periods I remove any direct dependence of trends in atmospheric blocking on changes in the mean state of MSLP. This is a necessary step to apply in the normalisation process of the SOM-BI to remove the dependence between the historic MSLP climatology and the ERA5 climatology in a model. However, in separately defining the anomalies and applying the normalisation for the historic and 4xCO_2 periods I reduce the magnitude of the dynamic climate change signal. This means that the ESB response obtained from the normalised SOM-BI will tend to be an under-estimate of the actual ESB response. Figure B.1 in Appendix B.1 shows that when the normalisation is not applied, the magnitude of the ESB response is significantly larger. The implications of this under-estimate are discussed in section 4.4 and future work to address this challenge in defining/normalising for background climatologies is suggested in section 5.2.3.

The difference between the trends in the MSLP anomaly data using anomalies defined by the historic period, the normalised MSLP anomaly in each period, using anomalies defined by each period, is shown in Fig. B.1 in Appendix B.1. Since the model dependence on the differences in the model's historic MSLP climatology are significantly reduced when using the normalised SOM-BI, I use the normalised SOM-BI across chapters 3 - 4.

3.3.3 Comparison of meteorological variables to the ESB response across the model ensemble

The relationships across the CMIP5/6 model ensemble between a given variable and the blocking occurrence are analysed for both the historical and 4xCO_2 periods. These are averaged over the whole historical and 4xCO_2 time periods for each model in the CMIP5/6 ensemble, such that 22 data points are used in the regressions for each of the plots shown in sections 3.4.2 - 3.4.5. Note that in section C.1 in Appendix C the historical (1979-2005) relationship between U and blocking is presented for ERA5 and compared to individual relationships between historical U and blocking occurrence in the CMIP models. These regressions are all averaged across JJA for each year, such that 27 data points are used in the regressions for each latitude/level point in Figs. C.1, C.2 and C.3.

Fourteen pressure levels and seven longitude bands are used in this analysis. The pressure levels extend from 1000 hPa to 30 hPa: 1000 hPa, 925 hPa, 850 hPa, 700 hPa, 600 hPa, 500 hPa, 400 hPa, 300 hPa, 250 hPa, 200 hPa, 150 hPa, 100 hPa, 70 hPa, 50 hPa and 30 hPa. The seven longitude bands (defined as regions) in order are:

a) all longitudes;

b) Pacific (PAC): 140° E - 236° E;

c) Maritime Continent (MC): 100° E - 140° E;

d) Indian Ocean + Maritime Continent (IO+MC): 50° E - 140° E;

e) Indian Ocean + Pacific (IO+PAC): 50° E - 236° E;

f) Atlantic (ATL): 80° W - 14° W; and

g) Europe (EUR): 10° W - 40° E.

These regions are chosen since these longitude bands roughly delineate the major differences in the U climatology arising from the world's land masses and ocean basins.

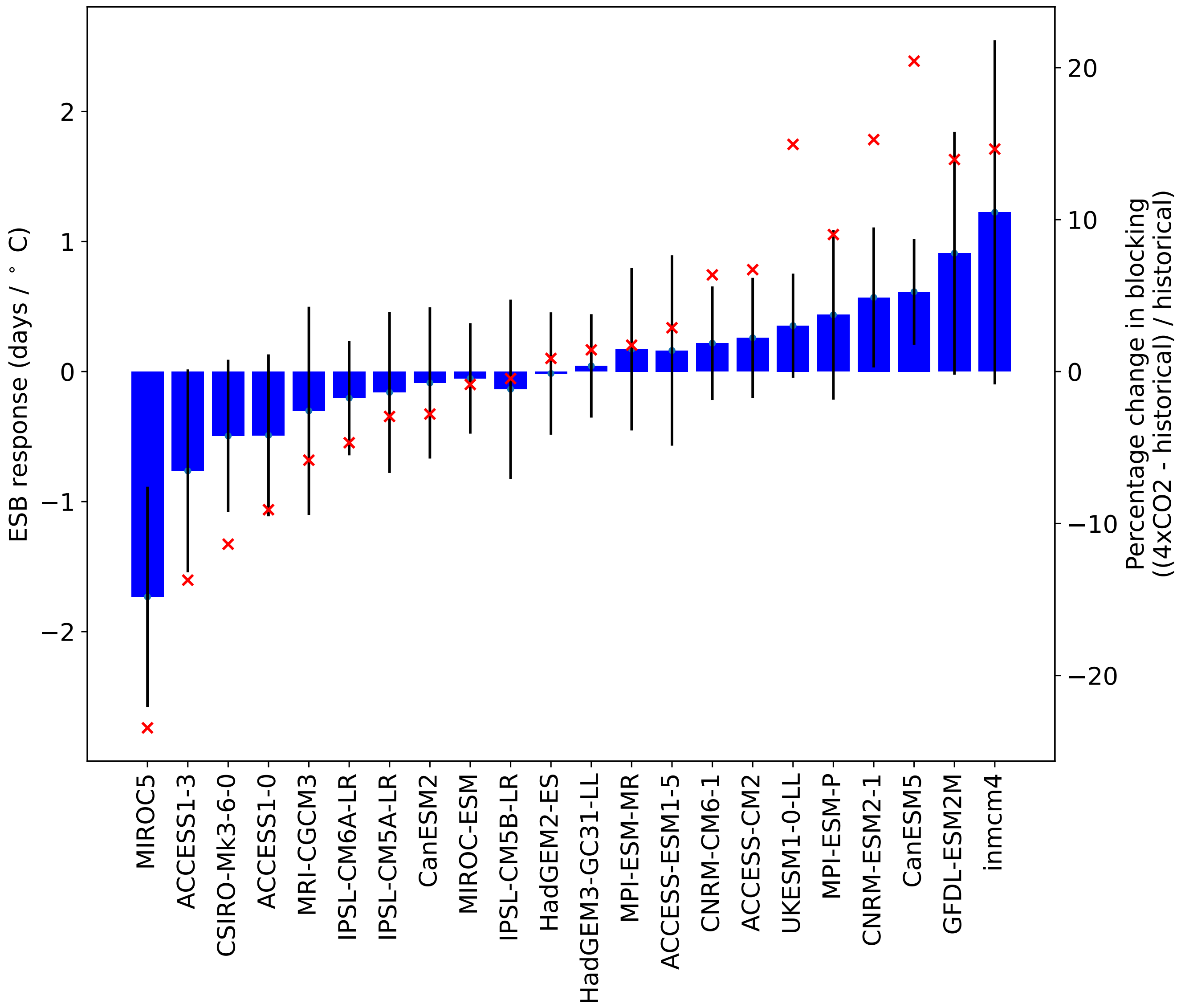

Figure 3.2: The ESB response across 22 global climate models. Derived by combining the 4xCO_2 and historical periods of JJA global mean surface temperature and mean JJA blocking over Europe and calculating a linear regression. The lines show the error bars on the trend, defined by the standard error of the slope. Blocking occurrence is calculated using the SOM-BI for the MSLP normalised anomaly discussed in section 3.3.2. Crosses indicate the percentage change in blocking occurrences.

3.4 Results

3.4.1 Response of European summer blocking to climate change

Figure 3.2 shows the ESB response across 22 global CMIP5 and CMIP6 climate models. These values are derived by combining the 4xCO_2 and historical periods of JJA global mean surface temperature and mean JJA blocking over Europe and calculating a linear regression over annual averages (using the 27 years across 1979-2005 and 30 years in the 4xCO_2 run, 120-150 years after the start of the 4xCO_2 run). A linear regression is calculated instead of defining the ESB response as the difference between the mean blocking occurrence divided by the difference between the mean GMST of the 4xCO_2 and historical runs. In subsequent figures the ESB response is defined as the difference between the mean blocking occurrence divided by the difference between the mean GMST of the 4xCO_2 and historical runs. Figure 3.2 uses a linear regression since this yields an error bar from the standard deviation of the slope. Both definitions have been found to yield almost identical results.

Most studies concerned with trends in future blocking consider proportional changes in blocking across models - reporting a percentage change in blocking under climate change instead of a ESB response (e.g. Woollings et al. (2018), Davini and D'Andrea (2020)). I am not aware of any study that presents the change in atmospheric blocking under climate change normalized by GMST. In principle, normalizing by GMST enables a better comparison across a model ensemble with a wide variation in climate sensitivity. Such an approach is common in studies using high forcing scenarios, where the effect of a large forcing on a certain physical feedback (e.g. cloud feedbacks) is often scaled by the change in GMST (e.g. Bacmeister et al. (2020), Ceppi and Nowack (2021) and Thornhill et al. (2021)). However, since this is the first study to use such sudden and high forcing scenarios to study the effect of climate change on atmospheric blocking, I have additionally plotted the proportional change (the relative proportional change between the historic and 4xCO_2) in the models in Fig. 3.2 using red crosses.

In general, the proportional change in the models (indicated by the red crosses) is well correlated with the ESB response. However, UKESM, CanESM5 and CNRM-ESM2-1 show a large increase in blocking proportionally but a small ESB response. In these models there is either an unusually high climate sensitivity (UKESM and CanESM5 have the 2nd and 3rd highest climate sensitivity respectively of the models in this study) and/or a small historic blocking climatology (UKESM, CNRM-ESM2-1 and CanESM5 have the 2nd, 3rd and 5th lowest historical JJA Europe blocking occurrence). For simplicity, across the rest of this thesis I will focus on the ESB response metric for European blocking.

None of the individual trends in Fig. 3.2 are statistically significant. However, statistically significant relationships (p-value <0.01) are observed across the model ensemble when I study how the ESB response relates to the historic climatology for several variables. These variables indicate the role of different mechanisms, which are discussed in sections 3.4.2 - 3.4.5.

3.4.2 The role of Arctic Amplification in the ESB response

Arctic amplification (AA) is a commonly cited possible mechanism to influence NH blocking events (Francis and Vavrus 2012; Hassanzadeh et al. 2014; Overland et al. 2015; Peings et al. 2017; Fabiano et al. 2021). It is argued that the increased surface warming over the Arctic compared to the rest of the Earth (Manabe and Wetherald 1975), associated with rapid sea ice loss (Dai et al. 2019), could impact the Northern Hemisphere jet stream (Francis and Vavrus 2012). It has been hypothesised that by reducing the surface meridional temperature gradient the speed of the jet stream reduces, and therefore Rossby waves are slower and more amplified (Francis and Vavrus 2015; Francis et al. 2018), increasing the likelihood of blocking events. This hypothesis has received criticism, with several studies claiming that there is no convincing evidence that a link between AA and midlatitude extreme weather exists (Barnes 2013; Barnes and Screen 2015; Blackport and Screen 2020; Dai and Song 2020). Further discussion of the possible role of AA can be found in section 1.3.3.

I note that whilst Francis and Vavrus (2012) claim that AA plays a role in increasing midlatitude extreme weather across all seasons, the discussion around the role of AA in midlatitude weather is usually in the context of considering winter (Cohen et al. 2013; Barnes and Screen 2015; Overland et al. 2015), since the peak season for AA is November-January (Liang et al. 2022). Certainly, the role of a stratospheric pathway enabling AA to influence midlatitude summer weather is not relevant, since there is no stratospheric polar vortex in JJA (Kidston et al. 2015). However, Coumou et al. (2015) have shown that AA does have a significant impact on weakening the NH JJA midlatitude circulation. Coumou et al. (2015) found that this reduction in zonal wind speed is associated with reductions both in eddy kinetic energy (EKE) and the amplitude of fast-moving Rossby waves, implying an increase in persistence in JJA NH circulation patterns. Since heat extremes such as the 2010 Russian heatwave are associated with low EKE (Dole et al. 2011), it is possible that AA is working to increase the severity of heat extremes through increasing the persistence of weather and therefore increasing the persistence of JJA blocking events (Schubert et al. 2011). If this is the case for Europe, I should expect to find a correlation between AA and increased ESB.

I studied the relationship between changes in the equator-to-pole temperature gradient at the surface and at 850 hPa between the tropics and polar regions following the method of Harvey et al. (2014). I found no statistically significant correlations across any of the regions discussed in 3.3.3 (not shown). Therefore, there is limited evidence to suggest that AA has a role in influencing the variation in ESB response across the CMIP5/6 model ensemble studied here.

3.4.3 The role of tropical upper-tropospheric warming (UTW) in the ESB response

3.4.3.1 Background

A second mechanism that is frequently discussed in the literature which may have an impact on ESB under climate change is enhanced tropical upper-tropospheric warming (UTW). The temperature gradient between the tropics and mid-latitudes at higher altitudes is strengthening (Allen and Sherwood 2008), which would work to increase jet stream-level winds through the thermal wind relationship (see section 1.2.3). An increased upper-level temperature gradient is expected to shift the jet stream poleward and increase storm track activity (Held 1993). This may work to decrease the persistence and frequency of atmospheric blocking events by reducing the stationarity of circulation patterns (Vries et al. 2013). This process competes with AA which is expected to shift the jet stream equatorward, weaken the jet stream and decrease storm track activity, leading to more blocking events (Barnes and Polvani 2015). This has led to the NH midlatitude jet described as in a “tug-of-war” between the processes of AA and UTW (Barnes and Screen 2015; Screen et al. 2018; Peings et al. 2019). Harvey et al. (2014) found that both mechanisms are important in influencing the storm track response across CMIP5 models, but in JJA the storm track response across the CMIP5 models is dominated by the lower-tropospheric temperature differences. Riboldi et al. (2020) found from studying Rossby

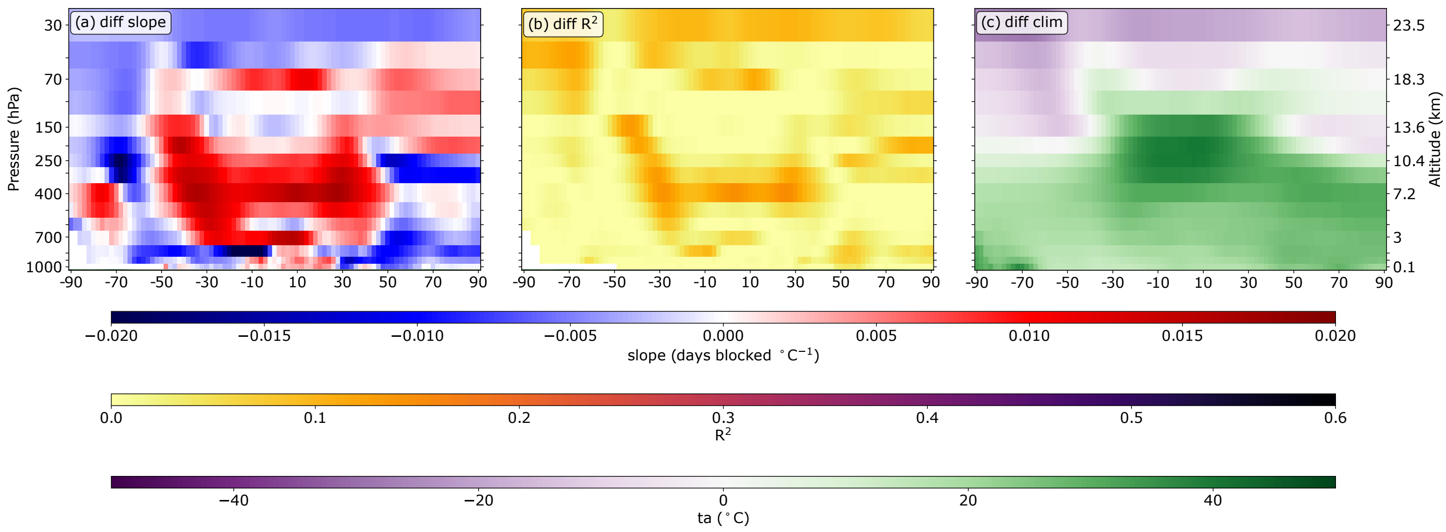

Figure 3.3: Linear regression across 22 models (shown in 3.2) between the change in T (zonally-averaged across all longitudes) and the ESB response, scaled by the change in GMST. For each grid cell, the latitude/longitude point is the dependent variable against the ESB response. The left (middle) panel shows the slope (R^2) for the linear regression in each grid cell. The right panel shows the mean zonally-averaged T change across all models.

phase speeds in reanalysis data that whilst reduced phase speed is associated with midlatitude atmospheric blocking and extreme temperatures, the Rossby phase speed is not associated with AA for either JJA or DJF, reducing the likelihood of an explicit connection between AA and atmospheric blocking but highlighting a potential role for UTW.

3.4.3.2 UTW and its relation to ESB response

In order to assess the role of UTW in influencing the ESB response, the temperature difference is compared to the ESB response across the model ensemble. Figure 3.3 shows the linear regression between the change in zonally-averaged T across all longitudes for each latitude/level grid cell and the ESB response. Similar analyses were performed for zonally-averaged T other longitude bands listed in section 3.3.3 and similar results for the regressions were found (not shown).

Figure 3.3a-b indicates a weak correlation between increased tropical UTW and increased ESB occurrence ($R^2 \approx 0.1$ across 30° S - 30° N and 250 - 400 hPa). Whilst these correlations are not statistically significant, Fig. 3.3g distinctively highlights a pattern of positive slopes across the tropics in the upper troposphere that would be expected if there was a strong positive relationship between UTW and increased ESB. However, since the correlation is very weak, I conclude that there is no substantial evidence to relate UTW to ESB.

3.4.4 The role of changes in the Atlantic midlatitude meridional temperature gradient in the ESB response

In this subsection, I propose a separate physical mechanism that can influence ESB through modifying the Euro-Atlantic midlatitude meridional temperature gradient ($\Delta T_{\text{ML-Atl}}$). From studying U patterns across the models and splitting the models into groups with a positive ESB response (10 models) from those with a negative ESB response (12 models), I identify distinct patterns in U and how U changes across models (Figs. 3.4- 3.5). These changes correlate with changing patterns of baroclinic instability which influence the meridional temperature gradient across the Euro-Atlantic region and atmospheric blocking occurrence (Fig. 3.6).

First, in section 3.4.4.1 I show the relevant correlations which support the existence of this physical mechanism. Then in section 3.4.4.2 I provide a description of the mechanism with an accompanying infographic (Fig. 3.7).

3.4.4.1 Analysis of U and vorticity changes between models

Figures 3.4 and 3.5 show the NH U patterns averaged over all longitudes and the Atlantic, respectively, separated by the period in the columns (historical and 4xCO_2) and the model group (negative and positive ESB response) in the first and second rows and columns. The first two panels in the third column (Figs. 3.4c, 3.5c 3.4f and 3.5f) show the difference between the 4xCO_2 run and historical run U climatologies across the negative (Figs. 3.4c and 3.5c) and positive (Figs. 3.4f and 3.5f) models. The third row (Figs. 3.4g - 3.4i and 3.5g - 3.5i) shows the difference between the positive and negative model groups, with the positive model groups subtracted from the negative model groups. Figures 3.4g and 3.5g (3.4h and 3.5h) show the difference in the historical (4xCO_2) periods. Figures 3.4i and 3.5i shows the difference between the positive and negative model groups in the change in U climatology between the 4xCO_2 and historical periods. Figures 3.4i and 3.5i therefore highlight differences between the positive and negative model groups under climate change.

Analysis of changes in the NH U. Figure 3.4 shows that both model groups show a decrease in the strength of the JJA polar jet in the 4xCO_2 run (note the decrease in U at

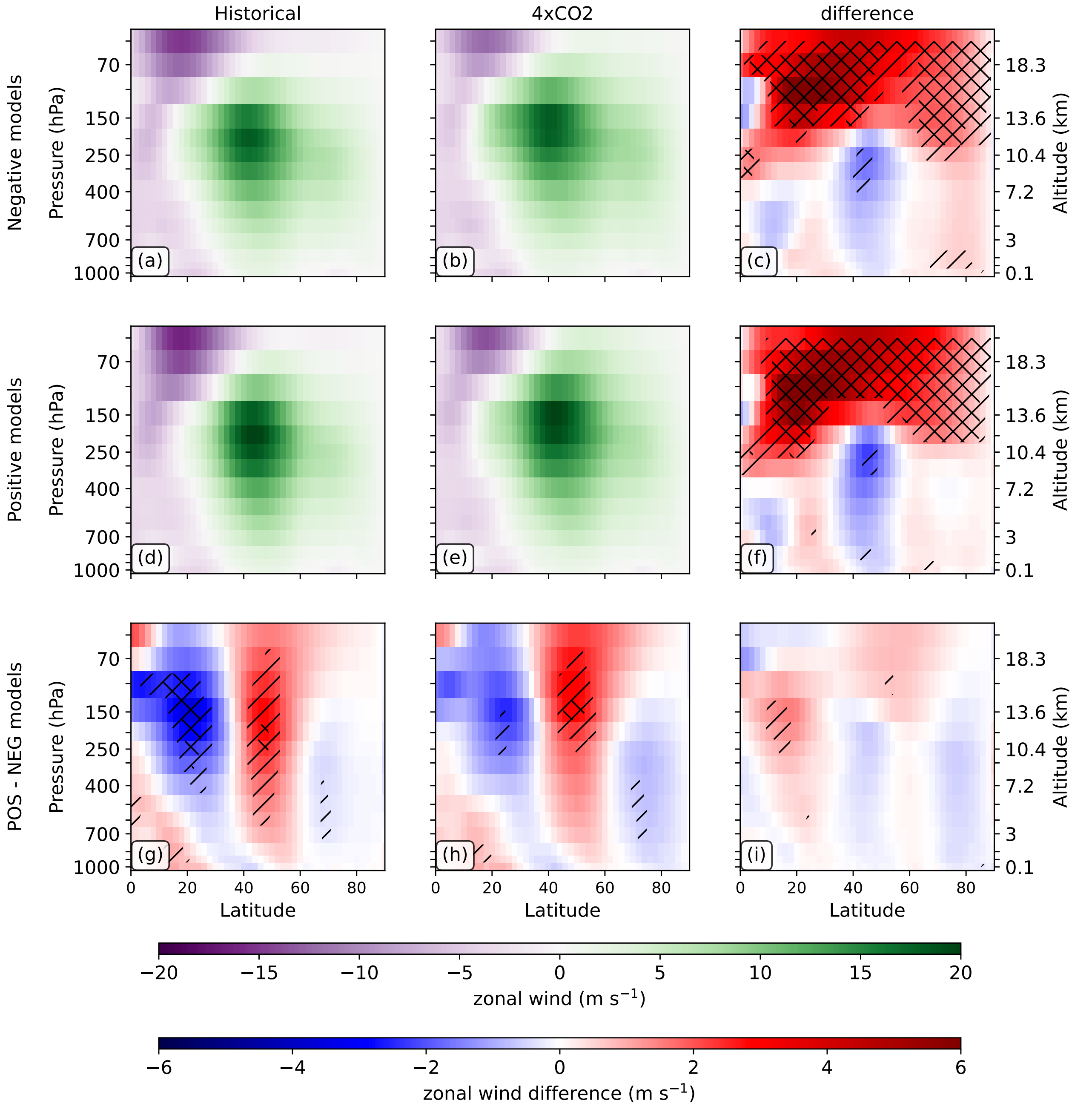

Figure 3.4: The NH zonally-averaged U across the model groups. Averaged across all longitudes. Separated out for the model groups in the rows and the model periods in the columns. The mean U across the negative models is shown in the top row, the positive models in the middle row and the difference between them in the bottom row. The left and middle columns show the mean U for the historical and 4xCO_2 periods, and the rightmost column shows the difference, subtracting the historical run from the 4xCO_2 run. Hatching indicates statistically significant p-values for the two sample independent t-test between the positive and negative model groups. Slashed hatching indicates a p-value < 0.05, and cross hatching indicates a p-value < 0.01, not accounting for multiple hypothesis testing.

200 hPa and 50° N in Figs. 3.4c and 3.4f). As discussed in section 3.4.2, this will tend to decrease the propagation of Rossby waves from tropical diabatic heating since there is less EKE

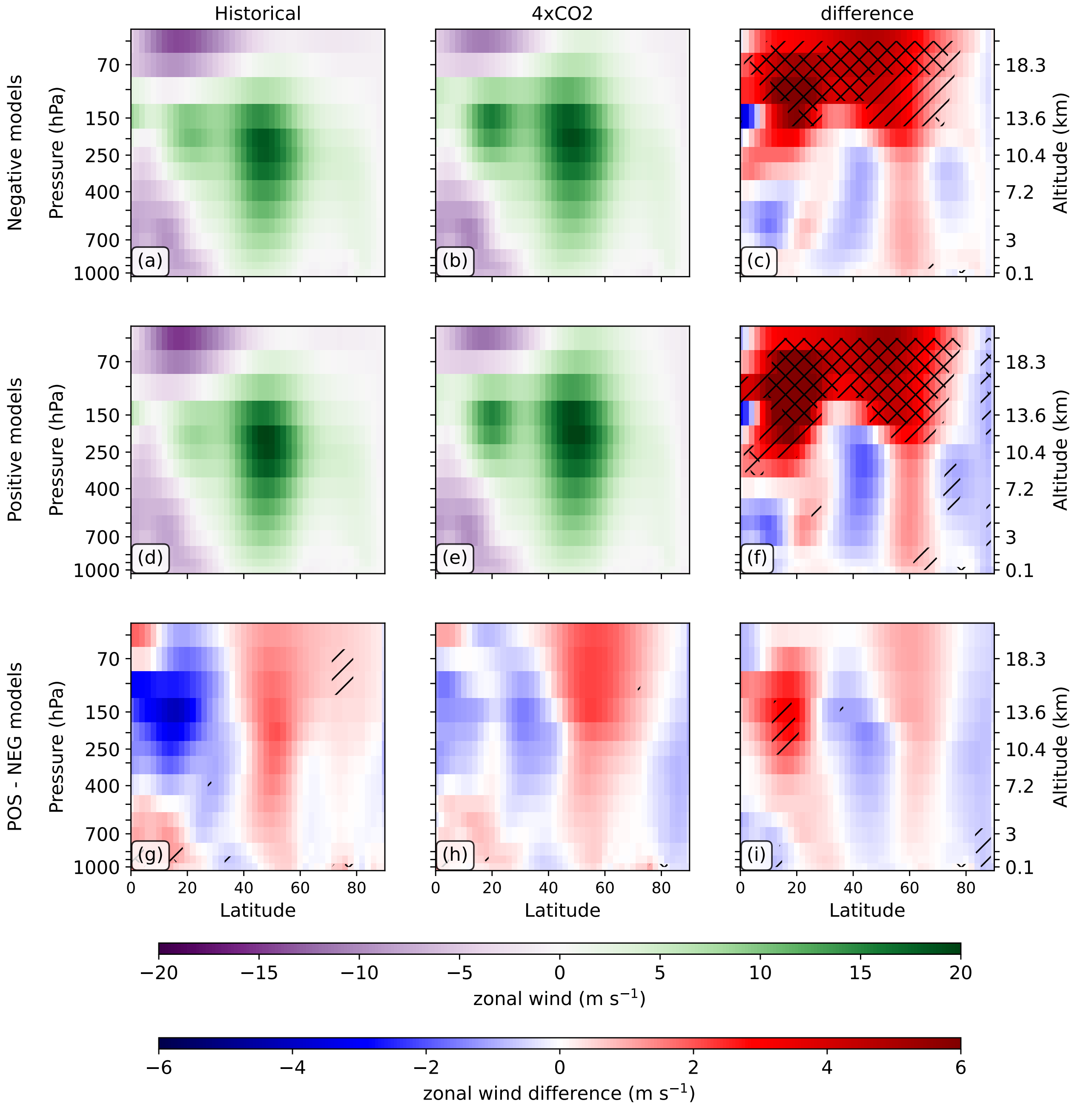

Figure 3.5: As for Fig. 3.4, but averaged across the Atlantic region (80° W - 14° W as defined in section 3.3.3).

in the atmosphere (Coumou et al. 2015).

In addition, the models with a positive ESB response have faster upper tropospheric U than those with a negative ESB response. This can be seen by studying the first column of Fig. 3.4, and noting the positive (negative) U difference in Fig. 3.4g at 200 hPa and 50° N (20° N) where there is a positive (negative) U climatology. This suggests that there is a relationship between the historic climatology and ESB response, which will be further explored in chapter 4.

Analysis of changes in the NH Atlantic U. Figure 3.5 shows the U averaged across the Atlantic for the two model groups, and there are several observations that can be made from Fig. 3.5 to inform the mechanism described in section 3.4.4.2:

1. The models with a positive (negative) ESB response have a weaker (stronger) subtropical Atlantic jet historically. This can be seen by studying the first column of Fig. 3.4, and noting the negative U difference in Fig. 3.4g at 200 hPa and 30° N, the location of the secondary subtropical jet.

2. The models with a positive (negative) ESB response have a stronger (weaker) polar Atlantic jet historically. This can be seen by studying the first column of Fig. 3.4, and noting the positive U difference in Fig. 3.4g at 200 hPa and 50° N.

3. 1. and 2. imply that **models with a positive (negative) ESB response have a stronger (weaker) meridional gradient in the 200 hPa U across 30° N - 50° N historically**. This results from corresponding differences in the meridional temperature gradient shown in Fig. C.4 in Appendix C.2.

4. There is a poleward shift in the Atlantic polar jet across all models (see the negative sign at 45° N and 200 hPa and the positive sign at 60° N and 200 hPa and the positive sign in Figs. 3.5c and 3.5f).

5. There is a greater poleward shift in the Atlantic polar jet across models with a positive ESB response. This can be seen by the hatched region in Fig. 3.5i, indicating a greater increase in the strength of the subtropical North Atlantic jet in the models with a positive climate feedback. This greater increase in the strength of the subtropical North Atlantic jet leads to a greater shift in the Atlantic polar jet, which can be seen in the negative (positive) sign 45° N (60° N) in Fig. 3.5i.

In summary, Fig. 3.4 indicates a general weakening of the strength of the NH circulation and Figs. 3.5c and 3.5f show that both model groups have a general weakening of the strength of the North Atlantic jet. However, Fig. 3.5i indicates a differential strengthening of the North Atlantic subtropical jet, with a stronger response in the positive ESB response model group. This suggests a possible mechanism for the development of Rossby wave-breaking events in the Euro-Atlantic region in the positive model group which will be further discussed in section 3.4.4.2.

Analysis of changes in 200 hPa vorticity. Figure 3.6 shows the pattern of linear regression between 200 hPa vorticity and ESB. Many of the statistically significant features of this graph relate to the tropical forcing mechanism discussed in section 3.4.5. What is most relevant for the Atlantic meridional temperature gradient is the bottom panel (Fig. 3.6g-i) which shows the linear regression between changes in 200 hPa vorticity and changes in ESB.

In Fig. 3.6g, hatched regions that extend NE from the subtropical North Atlantic across the Mediterranean, Scandinavia and the Arctic Ocean north of Russia show a pattern of positive and negative vorticity anomalies. From Fig. 3.6h these have a peak R^2 of 0.55. The pattern is positive/negative/positive/negative across the subtropical Atlantic/Mediterranean/NW Eurasia/Arctic Ocean. I note that this pattern is similar to the pattern of 200 hPa U shifts shown in Fig. C.5i in Appendix C.2, which shows a negative/positive/negative/positive response in the 200 hPa U between the positive and negative model groups across the subtropical Atlantic/Mediterranean/NW Eurasia/Arctic Ocean.

These suggest that models with a positive (negative) model feedback show a greater (reduced) occurrence of this series of vorticity anomalies under climate change, which works to increase (decrease) ESB.

3.4.4.2 Explanation of the physical mechanism

In this subsection I propose a mechanism consistent with the results shown in Figs. 3.4-3.6. This mechanism can be briefly described as having two components:

- A weakening of the JJA NH midlatitude jet that decreases EKE in the atmosphere and enables more atmospheric blocking (Coumou et al. 2015); and
- a poleward shift of the JJA Euro-Atlantic jet as the rest of the jet weakens, leading to more Rossby wave-breaking in the Euro-Atlantic region.

Each of these components work to increase the occurrence of ESB events and they act in both model groups. However, both components occur more (less) in models with a positive (negative)

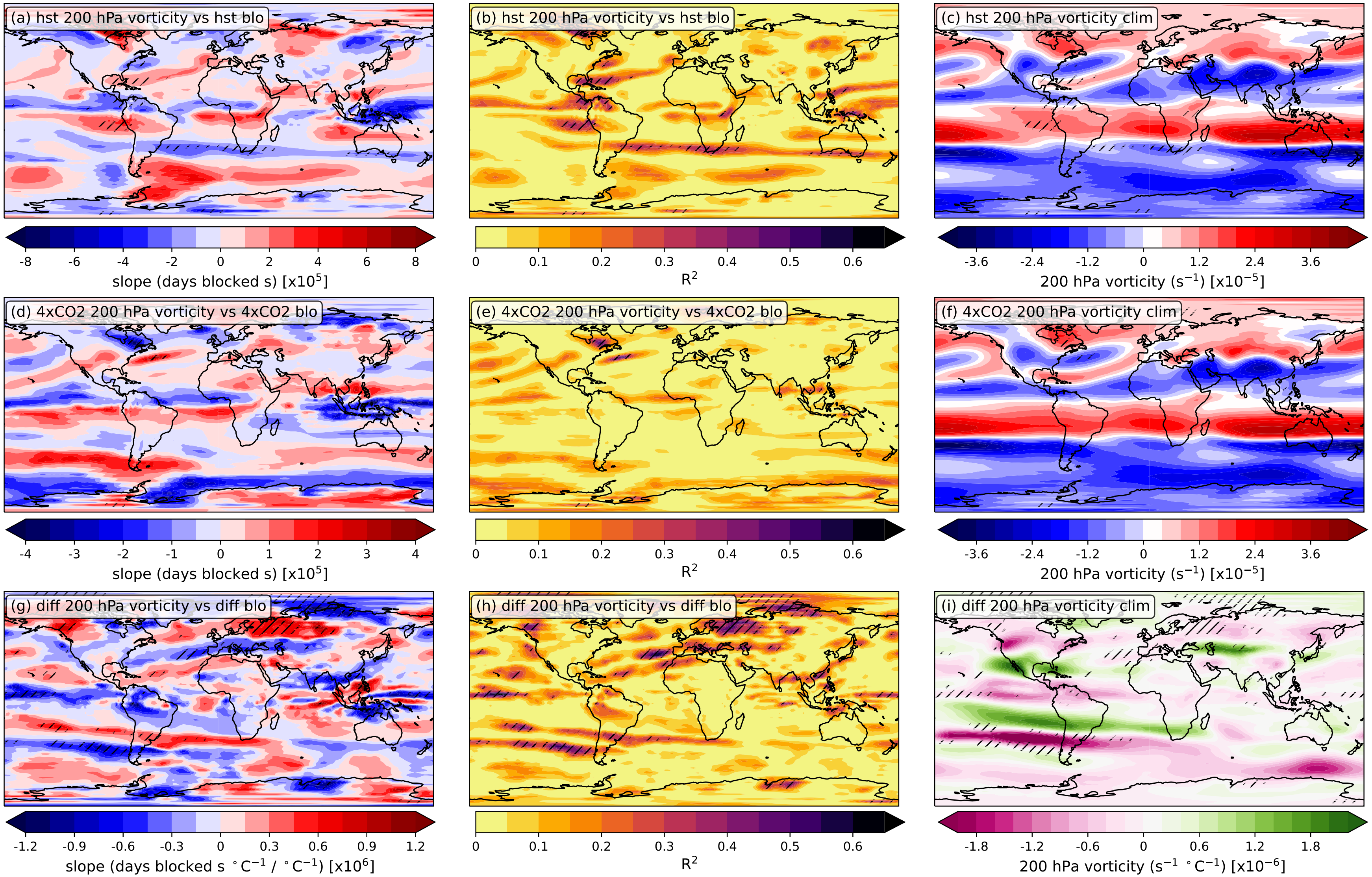

Figure 3.6: Linear regression across 22 models (shown in Fig. 3.2) between 200 hPa vorticity and ESB. For each grid cell, the latitude/longitude point is the dependent variable against ESB. The left (middle) column shows the slope (R^2) for each grid cell. The top (middle) row shows the linear regression for the historical ($4xCO_2$) periods. The bottom row shows the correlation between the change in 200 hPa vorticity and the change in ESB between the historical and the $4xCO_2$ runs, scaled by the change in GMST across all models. The rightmost column shows the historical and $4xCO_2$ mean climatologies (Fig. 3.3c and 3.3f respectively) across all models. Figure 3.3i shows the mean 200 hPa vorticity change across all models, scaled by the change in GMST. Hatching indicates where the p-value < 0.01, not accounting for multiple hypothesis testing. Compare to Fig. 3.3 which has the same layout of panels but for zonally-averaged T.

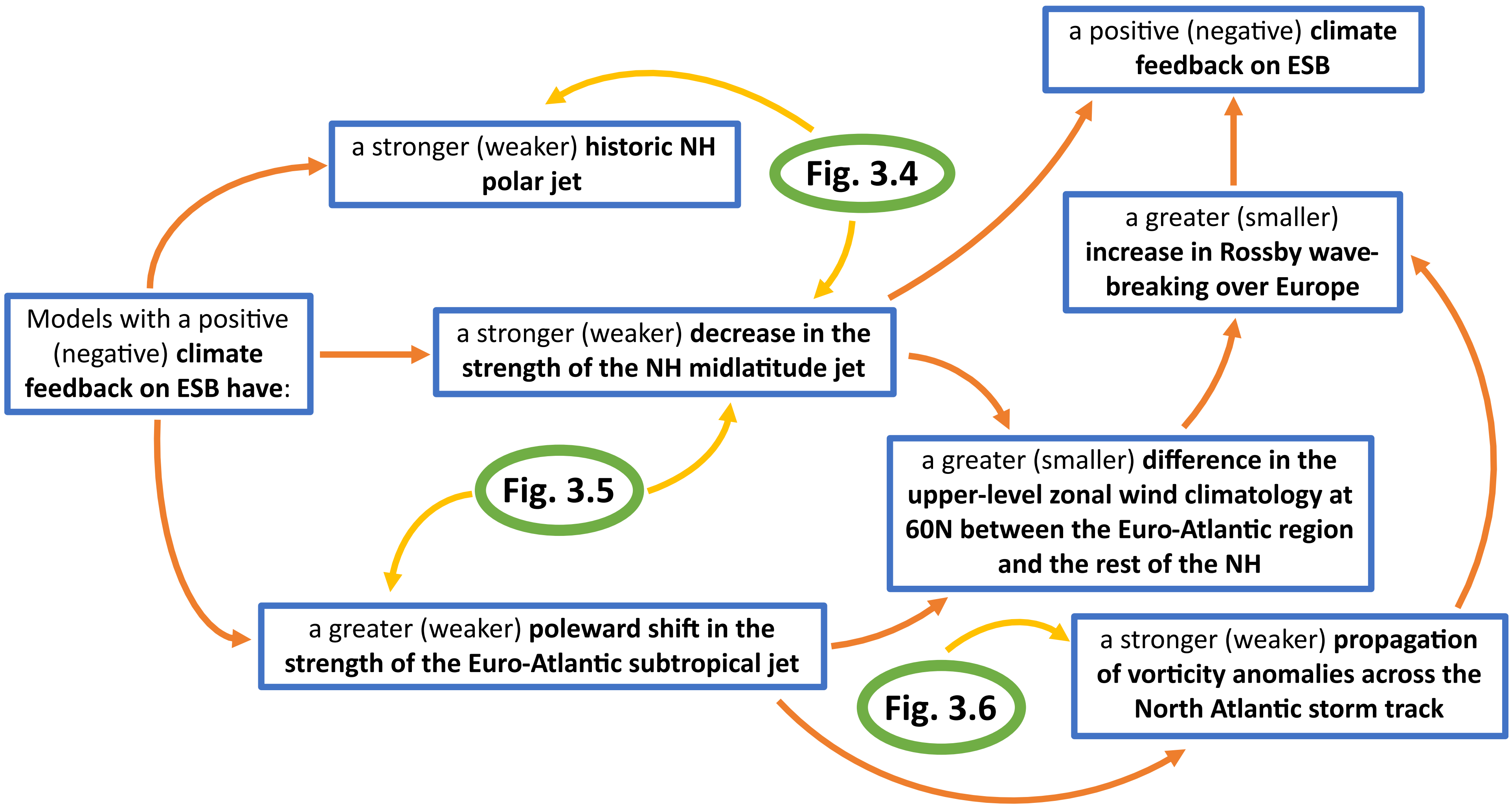

Figure 3.7: A diagram summarizing the suggested mechanism for how changes in North Atlantic U across the model ensemble are causally connected to changes in ESB. The blue text boxes indicate physical changes and orange arrows show causal connections between these changes. Green ovals reference figures which highlight the relevant correlations to justify the causal connections between these physical changes and changes in ESB. Yellow arrows show which figures support which physical changes.

ESB response.

Figure 3.5 shows that models with a positive (negative) ESB response have a greater (weaker) increase in the strength of the subtropical Atlantic jet. This differential change in the subtropical jet results from differences in the heating profile between the models; models with a positive (negative) ESB response have a greater (smaller) increase in the meridional temperature gradient in the NH Atlantic tropical upper troposphere (see Fig. C.4 in Appendix C.2). Figure 3.5i additionally shows that this greater increase in the strength of the Atlantic subtropical jet in models with a positive ESB response is associated with a poleward shift of the Atlantic polar jet. This is supported by Lee and Kim (2003), who have shown through an idealised primitive equation model that baroclinic wave growth occurs when the subtropical jet is sufficiently strong.

The fact that a poleward shift of the Atlantic polar jet is associated with an increase in ESB is contrary to initial expectation, since in general a poleward shift of the jet is associated with increased EKE, faster U and a reduction in the occurrence of blocking anticyclones (Schubert et al. 2011; Coumou et al. 2015; Francis et al. 2018). However, from comparing Fig. 3.5 to Fig. 3.4 and similar zonally-averaged U plots across the other regional averages discussed in section 3.3.3 (not shown), I note that **this poleward shift of the Atlantic jet appears to be a distinct phenomenon in the Euro-Atlantic region** in contrast to the rest of the NH. This creates a differential response of the jet in the Euro-Atlantic with respect to the rest of the NH that is greater in models with a positive ESB response. Figure 3.5 shows that **models with a positive (negative) ESB response have a greater (smaller) difference in the upper-level zonal wind climatology at 60 °N between the Euro-Atlantic region and the rest of the NH**.

This increased shift in the jet position could lead to more frequent discontinuities in the jet stream, and therefore more Rossby wave-breaking events over Europe. Since Rossby-wave breaking is a common way of discussing blocking anticyclones (Pelly and Hoskins 2003; Gabriel and Peters 2008; Hoskins and James 2014a), this provides a possible mechanism for how an increased meridional temperature gradient in the NH Atlantic can lead to more ESB.

This mechanism is reinforced by Fig. 3.6, which shows the correlation between 200 hPa vorticity anomalies and ESB across all models for the historical and 4xCO_2 periods and the difference between them. Figure 3.6i shows how changes in vorticity patterns relate to changes in ESB, and highlights a clear pattern across the Euro-Atlantic region of alternating positive and negative vorticity anomalies that are associated with a more positive ESB response. This shows that models with a positive (negative) ESB response have a distinctive pattern of vorticity anomalies that propagate across the Euro-Atlantic storm track.

Additional evidence has been included in Appendix C. The same pattern of vorticity anomalies in Fig. 3.6i can be seen not only in the 200 hPa vorticity field but in the 200 hPa U field shown in Fig. C.5i in Appendix C.2. Further, by regressing the historical U shear against ESB, Figure C.6 in Appendix C.3 shows that ESB is associated with an increased zonal wind shear in the subtropical Atlantic at 20° N. U shear is associated with baroclinic instability (Vallis 2006a) which can cause the development of cyclones (Houze 2014). This highlights the potential role of baroclinic instability in the subtropical Atlantic influencing ESB in line with the above mechanism.

3.4.5 The role of Rossby waves from diabatic heating in the tropical Pacific in the ESB response

In this section, I introduce a fourth potential mechanism contributing to the historical occurrence of ESB, and therefore (through the negative correlation found in chapter 3 between historical ESB and ESB response) influences the ESB response. The hypothesis behind the mechanism is that the propagation of Rossby waves from diabatic heating in the tropical Pacific (Hoskins and Karoly 1981) can lead to Rossby wave perturbations that extend to the North Pacific. These exert an influence on the NH circulation to lead to increased ESB. These Rossby wave perturbations are expected to decrease as the NH U decreases under climate change.

I first present the relevant data in section 3.4.5.1 through Figures 3.8-3.10. In section 3.4.5.2 provide an explanation of the physical mechanism with reference to an explanatory figure (Fig. 3.11) and relevant literature.

3.4.5.1 Analysis of the physical mechanism

In this section, I provide a detailed discussion of the relevant features from Figs. 3.8, 3.9 and 3.10 to support the physical mechanism which will be described in Fig. 3.11.

Linear regression between ESB and global precipitation patterns Figure 3.8 shows a linear regression across all 22 models in Fig. 3.8 between JJA precipitation and ESB. The top row shows the correlations historically between precipitation and blocking, and it is clear that tropical precipitation is correlated with ESB. The hatching in Fig. 3.8a across the tropical Pacific suggests that models with high levels of precipitation across the central tropical Pacific in the Inter-tropical Convergence Zone (ITCZ) have an increased occurrence of ESB, with peak $R^2 \approx 0.45$ in the central tropical Pacific. This suggests that the ITCZ may play a role across models in producing diabatic heating that generates Rossby waves of relevance for ESB, as discussed in section 3.4.5.2.

The other prominent hatched regions in Figs. 3.8a-c are in the Southern Hemisphere. These are bands that extend across the South Pacific and Southern Indian Ocean, where increased precipitation is correlated with increased ESB. These correlations are unlikely to be causally connected, but since diabatic heating from the tropics will produce Rossby waves in both hemispheres, perturbations to SH circulation patterns (which could themselves lead to precipitation anomalies) are likely to also be correlated with ESB in some regions.

Figures 3.8d - 3.8f show the correlations between precipitation and ESB in the 4xCO_2 runs. Comparing to Figs. 3.8a and 3.8d shows that whilst the sign is the same, the magnitude and significance of the correlations across the tropical Pacific are much weaker (note the factor of two difference in the colourbars), and the prominent hatched regions are no longer present. This suggests that the Rossby wave mechanism decreases with importance under climate change, as discussed in section 3.4.5.2.

Figures 3.8g - 3.8h show the slope and R^2 of the change in precipitation and the change in ESB per degree GMST across the model ensemble. Interestingly, there is a strong ($R^2 \approx 0.55$) correlation between increased precipitation in the tropical Pacific and increased ESB. This shows that whilst diabatic heating from the tropical Pacific is less strongly associated with

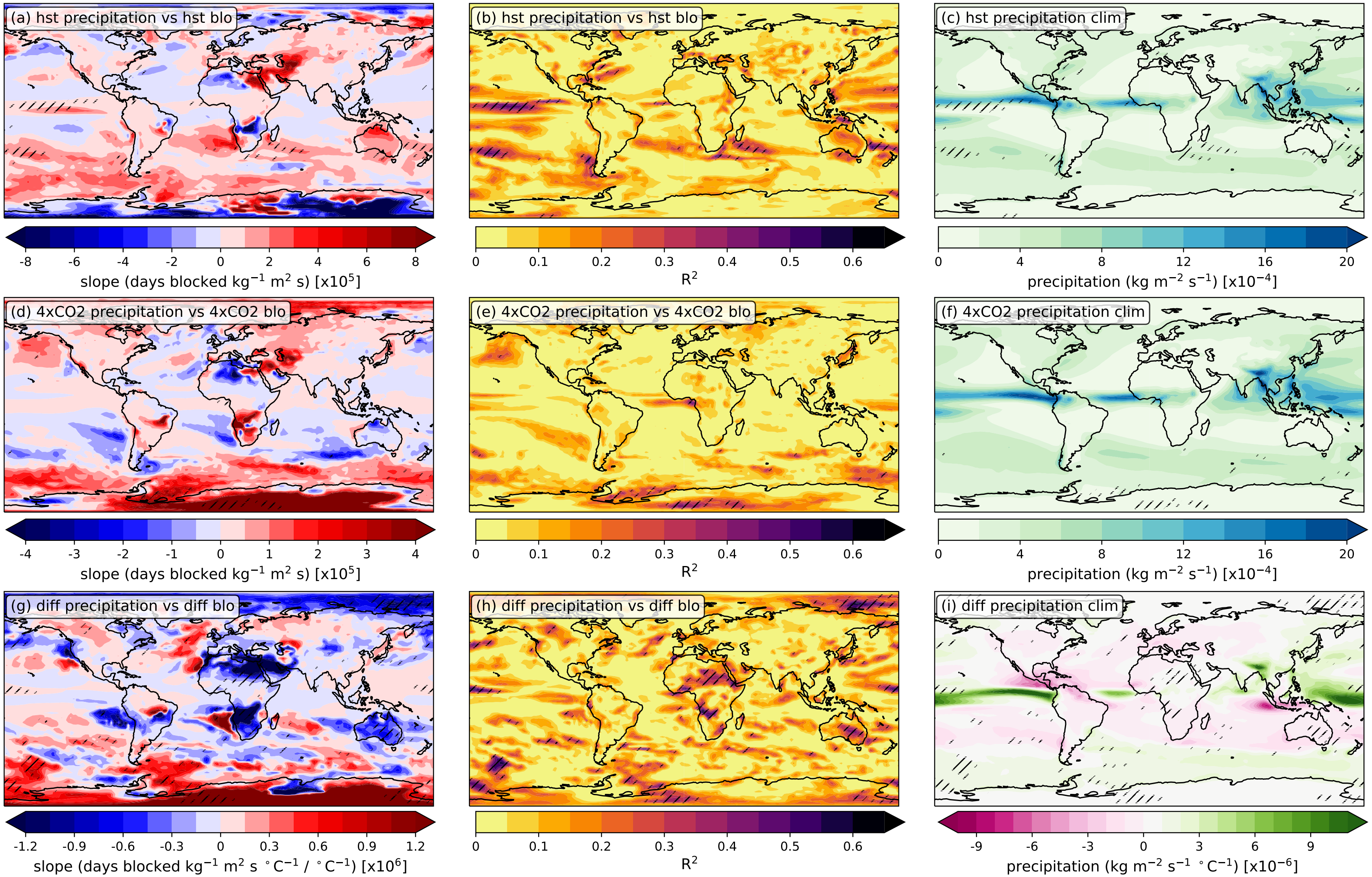

Figure 3.8: Linear regression across 22 models (shown in Fig. 3.8) between precipitation and ESB. For each grid cell, the latitude/longitude point is the dependent variable against ESB. The left (middle) column shows the slope (R^2) for each grid cell. The top (middle) row shows the linear regression for the historical ($4xCO_2$) periods. The bottom row shows the correlation between the change in precipitation and the change in ESB between the historical and the $4xCO_2$ runs, scaled by the change in GMST across all models. The rightmost column shows the historical and $4xCO_2$ mean climatologies (Fig. 3.8c and 3.8f respectively) across all models. Figure 3.8i shows the mean precipitation change across all models, scaled by the change in GMST. Hatching indicates where the p-value < 0.01, not accounting for multiple hypothesis testing.

ESB (due to the weakening circulation discussed in section 3.4.5.2), propagation of Rossby waves from diabatic heating in the tropical Pacific still plays an additional role across models in increasing ESB in the 4xCO_2 run. Therefore this mechanism works to affect the diversity of ESB response across models, providing an additional contribution alongside the previously discussed mechanisms.

Linear regression between ESB and zonally-averaged U. Figure 3.9 shows the correlation between historical U and ESB occurrence across the model ensemble. Each row shows the slope, R^2 and climatology of a different zonally-averaged band, following the region definitions in section 3.3.3. There is a significant positive correlation between the U in the tropics across the IO+PAC region and its subregions. This can be seen in Figs. 3.9d, 3.9g and 3.9m, which all have hatched regions at 15° N - 20° N. Noting that this is a positive correlation and from the climatologies (Figs. 3.9f, 3.9i and 3.9o) there is easterly flow in these regions, it follows that a weaker easterly flow across the tropical Asia-Pacific region at 15° N - 20° N is correlated with increased ESB, with peak $R^2 \approx 0.5$. This will be further discussed in section 3.4.5.2.

I also note that there are some hatched regions in the extatropical SH in the Euro-Atlantic region across 200 hPa - 30 hPa in Figs. 3.9p and 3.9s. There are unlikely to be direct causal connections relating SH weather patterns to ESB, but (as in Fig. 3.8) these correlations reflect how the tropical forcing that is influencing the NH is also influencing the SH.

Linear regression between ESB and 200 hPa streamfunction. Figure 3.10 shows how 200 hPa streamfunction is correlated with the occurrence of ESB events (see definition of streamfunction in section 1.2.4). The arrangement of panels is the same as in the precipitation linear regression plot (Fig. 3.8), where the slope and R^2 of linear regressions for each grid cell across all 22 models are shown in the left and middle columns respectively, and the right column shows the climatology. Hatching indicates where the p-values are less than 0.01, not accounting for multiple hypothesis testing.

The top row of Fig. 3.10 shows that 200 hPa streamfunction has tropical and extratropical correlations associated with Rossby waves produced from diabatic heating in the tropical Asia-Pacific. Figure 3.10a shows significant correlations with increasing streamfunction in both

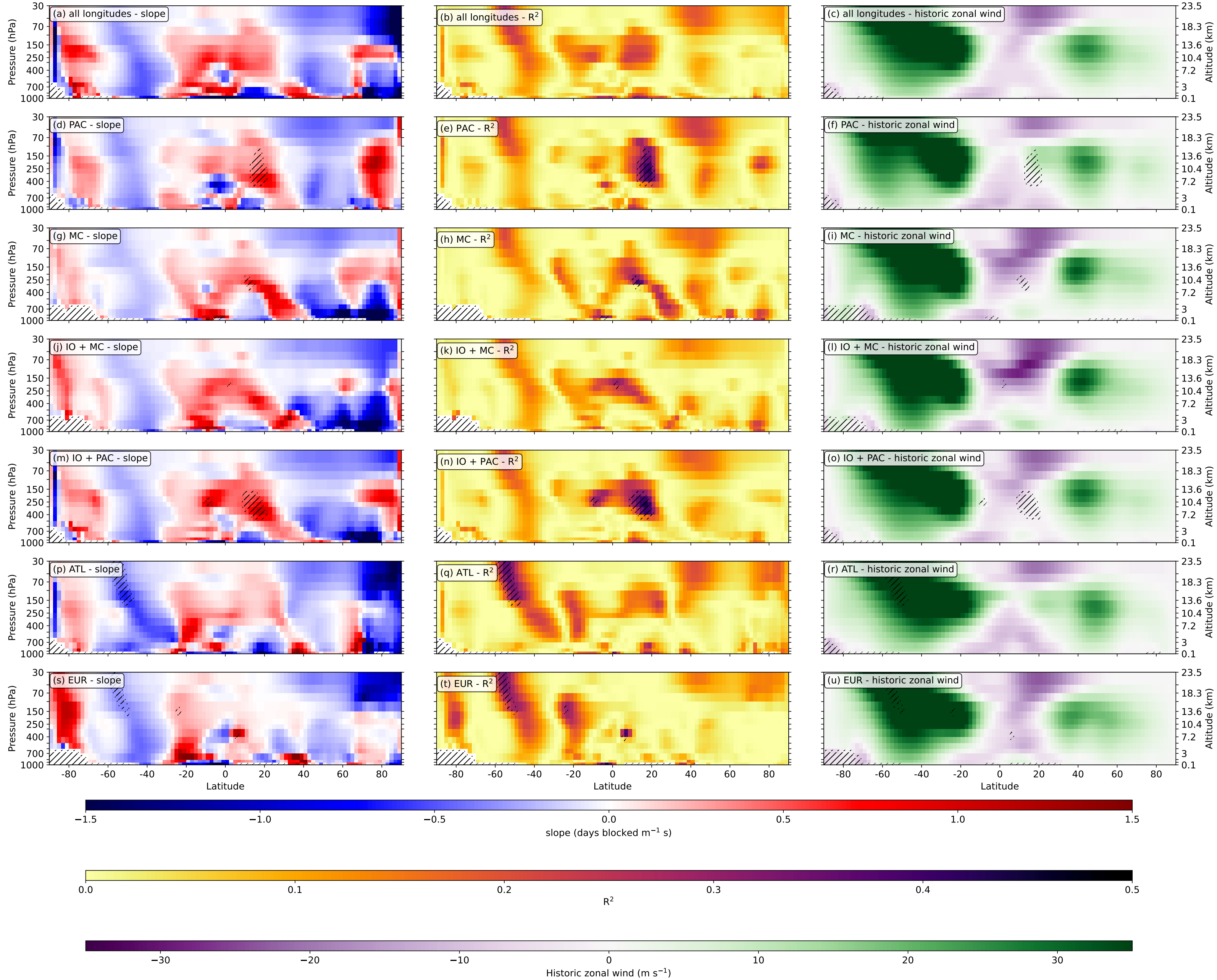

Figure 3.9: The relationship between the blocking occurrence and global patterns of U in the historical (1979-2005) period across the CMIP5/6 model ensemble in Fig. 3.2. The left and central columns show the slope and R^2 for the linear regression respectively, and the rightmost column shows the U climatology. Hatching indicates where the p-value < 0.01, not correcting for multiple hypothesis testing.

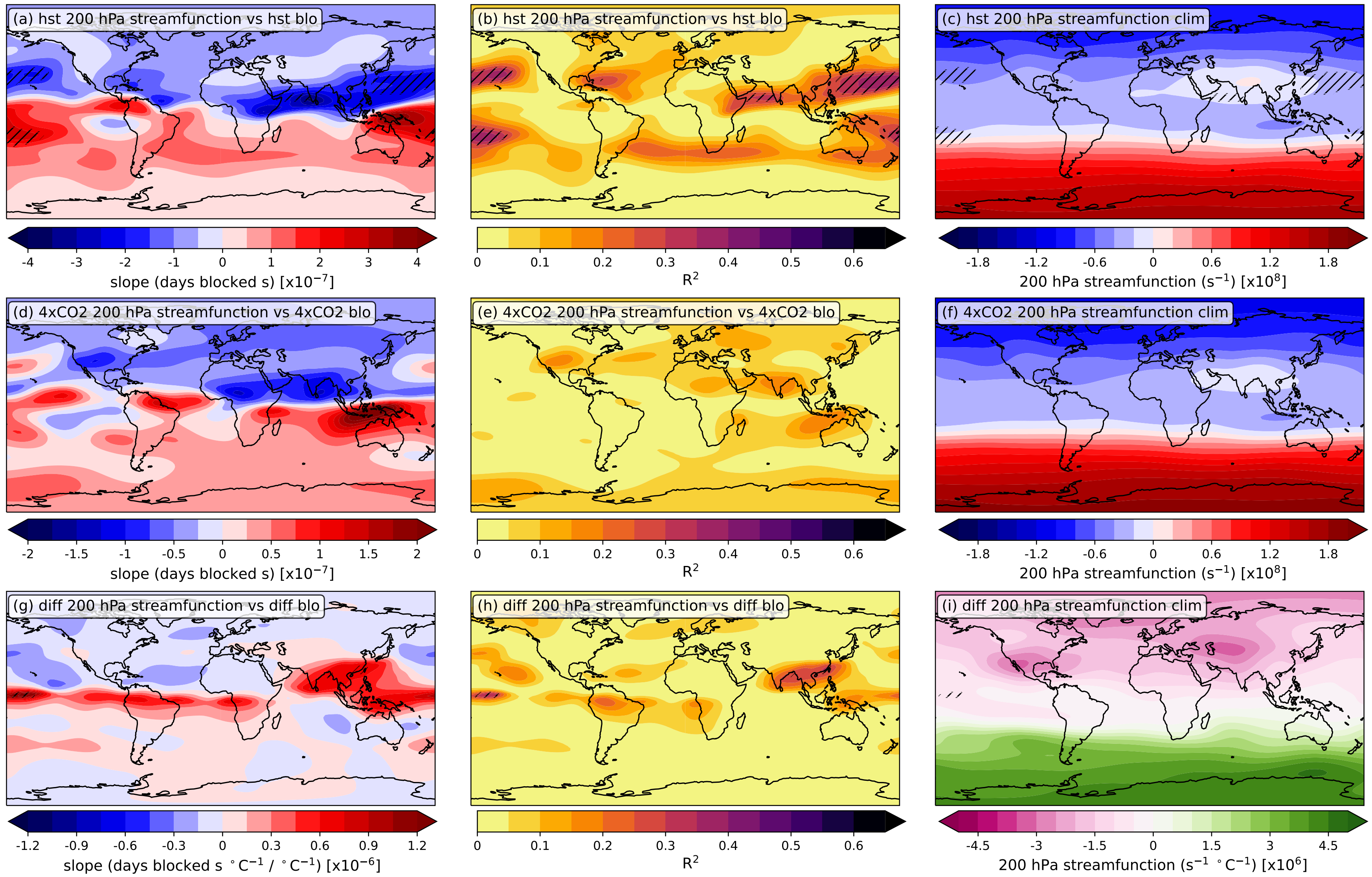

Figure 3.10: Linear regression across 22 models (shown in Fig. 3.8) between 200 hPa streamfunction and ESB. For each grid cell, the latitude/longitude point is the dependent variable against ESB. The left (middle) column shows the slope (R^2) for each grid cell. The top (middle) row shows the linear regression for the historical ($4xCO_2$) periods. The bottom row shows the correlation between the change in precipitation and the change in ESB between the historical and the $4xCO_2$ runs, scaled by the change in GMST across all models. The rightmost column shows the historical and $4xCO_2$ mean climatologies (Fig. 3.8c and 3.8f respectively) across all models. Figure 3.8i shows the mean streamfunction change across all models, scaled by the change in GMST. Hatching indicates where the p-value < 0.01, not accounting for multiple hypothesis testing.

hemispheres (note from Fig. 3.10c that streamfunction has a negative sign in the NH and a positive sign in the SH). The maximum positive and negative slopes are located in the South Asian Monsoon (see Fig. 1 of Ha et al. (2018)) and Maritime Continent (MC) (Ramage 1959) regions respectively, and hatched regions with significant correlations extend in both directions from these regions into the North and South Pacific, respectively. This suggests that both the South Asian Monsoon and MC may act as sources for diabatic heating, leading to Rossby wave perturbations across the Pacific relevant to ESB.

The middle row (Figs. 3.10d, 3.10e, 3.10f) shows the slope, R^2 and climatology of the $4xCO_2$ period, indicating the role of 200 hPa vorticity in influencing ESB in the $4xCO_2$ run.

The clear feature is that whilst the pattern of correlations is similar, the strength of the correlations and magnitude of the slope is significantly smaller. There are few hatched regions across Figs. 3.10d-f, and (noting the colourbar Figs. 3.10d has half the magnitude when compared to Fig. 3.10a) the magnitude of the slope decreases by a factor of two. Comparing Fig. 3.10b to Fig. 3.10e the peak R^2 decreases from $\approx$0.35 to $\approx$0.15, indicating that the effect of Rossby wave propagation from tropical forcing on ESB decreases significantly in the $4xCO_2$ run. Therefore, the mechanism of tropical diabatic heating on ESB through Rossby wave propagation significantly decreases with climate change. This will be discussed in section 3.4.5.2.

Figs. 3.10g and 3.10h show the linear regression coefficients of the difference between the historical and $4xCO_2$ periods against the change in ESB, scaled by GMST. Figure 3.10i show the difference between the historical and $4xCO_2$ climatologies, scaled by GMST. Similar results were found when not using the GMST scaling (not shown). The bottom row in Fig. 3.10 therefore highlights the regions where changes in 200 hPa streamfunction and vorticity relate to changes in ESB.

Figure 3.10g shows a positive correlation between changes in 200 hPa streamfunction across the MC, SAM and equatorial tropical Pacific and changes in ESB. The most prominent part of this trend is in the middle of the equatorial tropical Pacific, with $R^2 \approx 0.30$. From comparison with Figs. 3.10c and 3.10f, this region has a negative background climatology of streamfunction, and from comparison with Fig. 3.10i the models generally show a decrease in the streamfunction across the equatorial Pacific. Therefore the positive correlation in Fig. 3.10g implies that a *greater decrease in the magnitude of equatorial streamfunction is associated with an increase in ESB*. Further, from comparison to the 200 hPa U field in Fig. C.5, this region of positive streamfunction correlation across the tropical Asia-Pacific is associated with easterly flow in the climatology. Since a higher magnitude of streamfunction indicates the flow rate is high, the greater decrease in the magnitude of streamfunction indicates a greater decrease in the easterly flow across the tropical Asia-Pacific. The positive correlation in Fig. 3.10g therefore indicates that tropical diabatic heating still plays a role in increasing the occurrence of ESB events in the 4xCO_2 run. As also shown by Fig. 3.8, this confirms that diabatic heating in the equatorial Pacific still plays a role in influencing the ESB response under climate change.

3.4.5.2 Explanation of the physical mechanism

The tropical Asia-Pacific includes many convectively active regions that have a significant effect on the global atmospheric heating and circulation. One of these is the Inter-tropical Convergence Zone (ITCZ), a region of enhanced precipitation and rainfall across the equatorial Pacific, corresponding to the upward branch of the Hadley circulation. As a region of enhanced diabatic heating from deep convection (Wiel et al. 2016), it plays an important role in the transfer of heat to the extratropics (Waliser and Somerville 1994).

One way in which the tropical Pacific fuels global atmospheric circulation is through producing Rossby wave trains. These are formed from vertical motion and upper-tropospheric divergence, causing anomalous upper-level vorticity (Bjerknes 1966; Fuentes-Franco et al. 2022), which extend eastward and poleward from the tropics to influence weather at higher latitudes (Hoskins and Karoly 1981; Sardeshmukh and Hoskins 1988; Jin and Hoskins 1995) (see section 1.2.8 for an explanation of what Rossby waves are, and section 1.2.8.1 for an explanation of how Rossby waves can be produced by diabatic heating).

Regions of high diabatic heating in the tropical Pacific are frequently coincident with large precipitation anomalies. Yu (2007) calculated the vertically integrated diabatic heating in the tropical Pacific, and found that the precipitation-related term dominates the contribution to diabatic heating in the tropical Pacific. Figure 3.8a shows that precipitation across the equatorial Pacific is positively correlated with ESB. The correlation is strongest across the

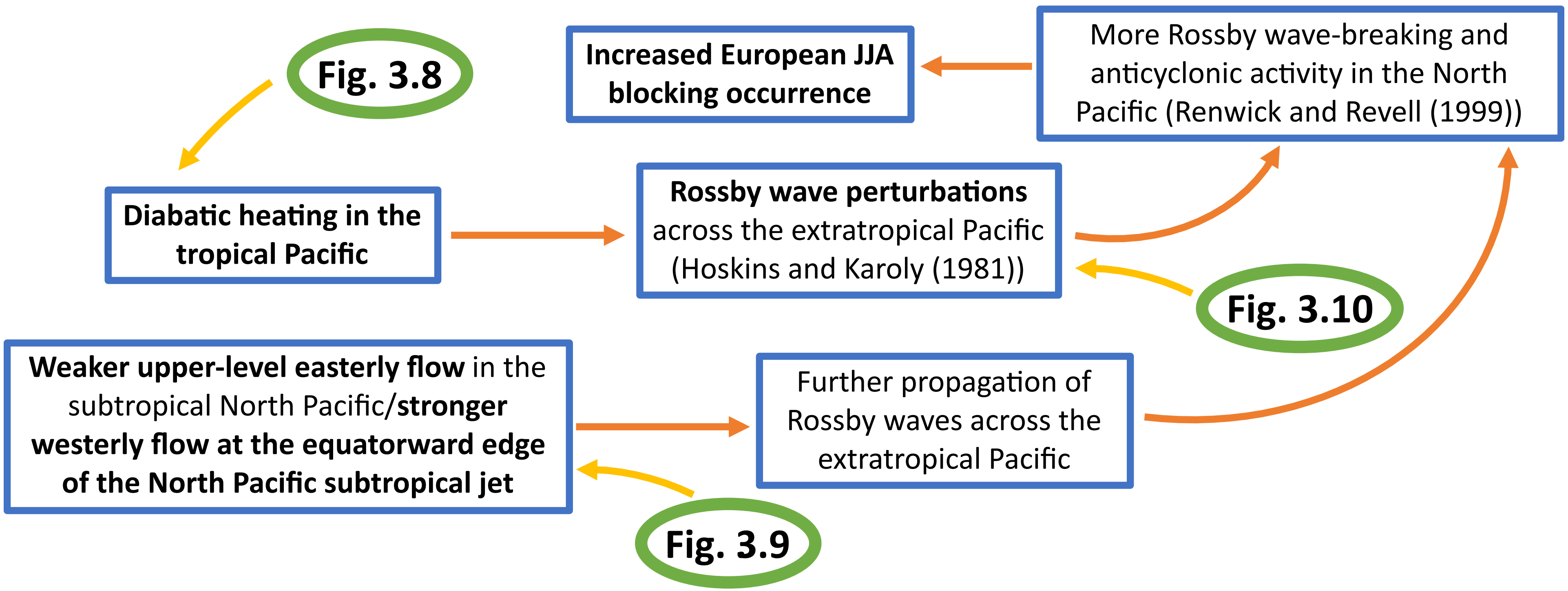

Figure 3.11: A diagram summarizing the suggested mechanism for how diabatic heating in the Pacific is causally connected to ESB. The blue text boxes indicate physical effects and orange arrows show causal connections between these effects. Relevant literature to justify the causal connections is highlighted in the text boxes. Green circles reference figures which highlight correlations between certain physical effects and ESB. Yellow arrows connect the figures to their relevant physical effects.

central Pacific, suggesting that diabatic heating from the ITCZ in particular is associated with increased propagation of Rossby waves into the extratropics and subsequently ESB. Furthermore, the relationship between the propagation of Rossby waves in the North Pacific and ESB is suggested by the correlations in Fig. 3.10a between 200 hPa streamfunction and ESB.

The modelling studies of Ting and Sardeshmukh (1993) and Hoskins and Ambrizzi (1993) both found that diabatic heating in the equatorial Pacific can act as a "Rossby wave source" (Sardeshmukh and Hoskins 1988). What is unusual in this mechanism is that I am hypothesising significant Rossby wave propagation in the North Pacific in JJA. Whilst Hoskins and Ambrizzi (1993) showed propagation of Rossby waves in both hemispheres, the propagation of Rossby waves in the North Pacific is significantly weaker in JJA. This is in line with my analysis, where I find that the correlations between U and ESB in Fig. 3.9 are most significant in the Southern Hemisphere. Since there cannot be a direct causal connection between SH U and ESB, these correlations suggest that there is a common mechanism that causes both shifts in the SH U and ESB. This can be explained by the fact that tropical Pacific diabatic heating in JJA will produce a greater Rossby wave perturbation in the SH, so the signal-to-noise ratio is higher in the SH.

A further related correlation in Fig. 3.9a is between the flow at the equatorward edge of the subtropical N Pacific jet and ESB. This shows that models with a N Pacific subtropical jet that extends further equatorward have a greater occurrence of ESB events. I hypothesise that a more equatorward shift of the N Pacific jet enables further propagation of Rossby waves. Whilst I am not aware of any research that has specifically studied how the background climatology poleward of a region of diabatic heating would affect the propagation of Rossby waves into that hemisphere, the seasonality of Rossby wave propagation (strong in winter) suggests that stronger westerlies will be associated with more Rossby wave propagation (Nie et al. 2019).

Renwick and Revell (1999) showed for the South East Pacific in JJA that there is an increased occurrence of atmospheric blocking resulting from diabatic heating in the tropics. Since Fig. 3.10a shows that there is a similar pattern of streamfunction correlations which propagates into the NH, I hypothesise a similar process of Rossby wave-breaking which affects the synoptic-scale dynamics in the North Pacific. However, it is not clear from my analysis what the precise nature and location of such a disruption would be.

The correlations shown in Figs. 3.8, 3.9 and 3.10 between ESB and the tropical Pacific precipitation, U and streamfunction respectively together suggest that Rossby wave propagation in the North Pacific can increase ESB. However, an additional plausible way to connect the Rossby wave propagation in the North Pacific with ESB needs to be hypothesised. This could occur through Rossby wave propagation in the North Pacific affecting a teleconnection pattern such as the circumglobal teleconnection (CGT). The CGT extends from central Asia across the North Pacific and is the second leading empirical orthogonal function of inter-annual variability of the upper-tropospheric NH JJA circulation (Ding and Wang 2005). Furthermore, Fig. 5 of Ding and Wang (2005) shows that the CGT pattern in August is associated with positive 200 hPa geopotential height anomalies in North-Western Europe and the North Central Pacific. This suggests that increased anticyclonic activity in the North Pacific (which can arise from a tropical Pacific Rossby wave source as discussed in Renwick and Revell (1999)) could reinforce the CGT pattern such that more stationary anticyclonic activity is found in North-western Europe. Such a pathway is not clearly discerned from the linear regression analysis in Figs. 3.8-3.10, since there is a relatively low signal-to-noise ratio between the tropical Pacific and ESB. Therefore, whilst the analysis shown does not provide a clear signal of the CGT pattern, there is at least one possible pathway for how diabatic heating in the tropical Pacific could influence ESB.

An additional feature of the Figs. 3.8 and 3.10 is that the correlations become weaker in the 4xCO_2 runs between ESB and precipitation and streamfunction, respectively (compare the first and second columns in both figures and see extended discussion in 3.4.5.1). This can be understood by the fact that the U across the NH JJA weakens with climate change (Coumou et al. 2015; Shaw 2019). Since the tropical Pacific diabatic heating works to increase ESB, this weakening of the connection provides an additional mechanism which causes a general decrease of ESB under climate change. This could contribute to why certain models have a negative ESB response. However, Fig. 3.8g also shows that models with a greater increase in precipitation in the ITCZ have a positive ESB response. This suggests that whilst there is a general decrease in the strength of the Rossby wave propagation, this mechanism still plays an additional role in contributing to the variety of responses to ESB response (alongside the previous mechanism discussed in section 3.4.4).

3.5 Discussion and Conclusions

From applying the SOM-BI to high forcing scenarios, I have found a divergence of future responses in the ESB response (Fig. 3.2). To explain differences in model projections of ESB, in this chapter I have discussed four physical mechanisms that may have a significant impact on the occurrence of ESB events.

The first two of these mechanisms are Arctic Amplification and tropical upper tropospheric warming. Whilst these are extensively discussed in the literature (Francis and Vavrus 2012; Barnes and Polvani 2015; Barnes and Screen 2015; Fabiano et al. 2021) and both play a role in influencing the ESB circulation, I have found that neither seems to have a distinct directly measurable influence in affecting the diversity of the ESB response. Note that this does not mean that they are irrelevant for changes in the NH JJA circulation, but simply that these processes cannot be considered in isolation from other mechanisms to explain the ESB response.

AA plays a significant role in generally reducing the NH JJA circulation (Coumou et al. 2015; Coumou et al. 2018b; Shaw 2019) and thereby reduces the occurrence of ESB. I find that models with a greater (smaller) reduction in the strength of the NH jet have a positive (negative) ESB response. However, the lack of a significant direct correlation between AA and changes in ESB suggests that other mechanisms need to be considered in addition to this effect.

Two further mechanisms are proposed which can influence ESB occurrence. The first of these considers the midlatitude temperature gradient across the Euro-Atlantic region, and notes that there is a greater poleward shift in the NH Atlantic jet in models with a positive ESB response. This shift can be understood to increase Euro-Atlantic Rossby wave-breaking, since this poleward shift of the jet occurs uniquely in the Euro-Atlantic region, and therefore creates a greater discontinuity between the jet in the Euro-Atlantic and the rest of the NH. Such an effect is not commonly considered, since the poleward shift of the jet is typically considered in DJF (Woollings et al. 2011; Woollings and Blackburn 2012), and is associated with faster winds, more EKE and therefore less atmospheric blocking (Coumou et al. 2015). This mechanism appears to be a distinct feature in the Euro-Atlantic region in the summer.

An additional mechanism is introduced which relates the greater occurrence of ESB to diabatic heating in the tropical Asia-Pacific, which produces Rossby waves that propagate polewards (Hoskins and Karoly 1981) and influences the synoptic conditions in the North Pacific. I suggest that by doing so the CGT is reinforced, leading to an increase in the occurrence of ESB events (Ding and Wang 2005). By studying statistical correlations between ESB and several dynamic variables such as precipitation, U and 200 hPa vorticity and streamfunction, I find that these last two mechanisms seem particularly prominent in how they influence ESB events. This highlights the significant role of the tropics in influencing ESB events (Sun et al. 2022).

A clear limitation from the above analysis is that by studying linear regressions across the model ensemble, I am not able to directly deduce the causal connections between correlations. Such analysis may be possible through a focused modelling study using an intermediate complexity model to investigate these proposed mechanisms and quantify the effect these have on atmospheric blocking (see section 5.2.2 for further discussion on the future work to verify the hypothesis).

From my discussion, it is clear that there are several mechanisms that are important in influencing the response of ESB under climate change. Therefore, if I want to to derive an estimate for the ESB response, I will need to consider a combination of several mechanisms simultaneously. Chapter 4 therefore combines the mechanisms discussed here in a multiple linear regression framework to derive an estimate for the ESB response.

Chapter 4

Estimating the response of European summer blocking to climate change

4.1 Introduction

The research question for this thesis is to investigate the ESB response to climate change. Chapter 2 has developed a new index to identify ESB events, which has been applied to models in high forcing in chapter 3. Figures 3.4 and 3.5 indicate that there is a relationship between the past climatology of a model and its future trend. This creates the possibility of using an emergent constraint to derive a quantitative estimate of the ESB response (see section 1.5.7 for a discussion on emergent constraints). Such emergent constraints have been used in different contexts (Hall and Qu 2006; Cox et al. 2013; Cox et al. 2018), and whilst they have received criticism (Riboldi et al. 2020), a greater confidence can placed on such predictions if they are based on verified mechanisms (Hall et al. 2019).

Chapter 3 has outlined four possible physical mechanisms that relate to the ESB response. In this chapter these same mechanisms are used as the basis for deriving an estimate of the ESB response using a multiple linear regression (MLR). In section 4.2, I discuss the method and the metrics used in the MLR regression. In section 4.3, I show the results from the MLR analysis and derive the estimate of the ESB response, and in section 4.4, I discuss these results.

4.2 Methods

I use the same datasets of 22 CMIP models and the ERA5 reanalysis as discussed in sections 3.2. I use the self-organizing map blocking index (SOM-BI) introduced in chapter 2 to identify blocking events in the historical ("hist") (1979-2005) and 4xCO_2 (120 years after the start of the 4xCO_2) runs, with the normalisation of the SOM-BI index as discussed in section 3.3.

To predict the ESB response from the historical period, I employ a multiple linear regression (MLR) using a variety of metrics. These metrics are all based on monthly data from zonal wind (U) at 400 hPa as well as air temperature (T) at the surface (T_{surf}) and on four pressure levels (850 hPa, 300 hPa, 250 hPa and 150 hPa). The Pacific and Atlantic longitudinal bands are averaged across for several of the metrics. These are the same as those described in section 3.3.3:

- Pacific (PAC): 140 °E - 236 °E; and
- Atlantic (ATL): 80 °W - 14 °W.

4.2.1 Metrics used as proxies for the mechanisms

Chapter 3 discussed four mechanisms that each have a potential role in affecting the historical and projected ESB occurrence under climate change across 22 CMIP models:

1. Arctic amplification (AA);
2. enhanced tropical upper-tropospheric warming (UTW);
3. changes in the Euro-Atlantic midlatitude meridional temperature gradient; and
4. the propagation of Rossby waves from diabatic heating in the equatorial Pacific.

The choice of relevant metrics for each variable follows from the analysis and discussion for each mechanism in sections 3.4.2 - 3.4.5:

1. The equator-to-pole temperature gradient at 850 hPa (ΔT_{850});
2. The equator-to-pole temperature gradient at 250 hPa (ΔT_{250});

3. The 300 hPa temperature difference (ΔT_{300}) between 30 °N and 10 °N averaged across the Atlantic;

4. The surface temperature difference (ΔT_{surf}) between 60 °N and 40 °N averaged across the Atlantic;

5. The 150 hPa temperature difference (ΔT_{150}) between 60 °N and 40 °N averaged across the Atlantic;

6. Precipitation (Pr) averaged across the equatorial Pacific between 2 °S and 2 °N;

7. U_{400} at 20 °N averaged across the Pacific.

Metrics 1 and 2 were chosen because they are the equator-to-pole temperature gradient metrics from Harvey et al. (2014), where lower and upper-level equator-to-pole temperature differences are calculated as the latitudinally area-averaged time-mean temperature difference between the tropical (30 °S - 30 °N) and polar (60 °N - 90 °N) regions. These were studied with reference to the first two mechanisms in sections 3.4.2- 3.4.3.

Metrics 3-7 were all specifically chosen since the historical values of their particular latitudes, levels and regions have the strongest patterns of correlation with the ESB response across models. Metrics 3, 4 and 5 all relate to the midlatitude meridional temperature gradient across the North Atlantic at different levels and in different ways, and so relate to the third mechanism discussed in section 3.4.4.1 (see also Fig. C.4, which shows that the changes in temperature gradients across the Atlantic differentiate the climate models with a positive and negative ESB response). ΔT_{300} between 30 °N and 10 °N averaged across the Atlantic relates to the strength of the North Atlantic subtropical jet, but also the warming of the tropical tropopause, so relates to both the tropical upper tropospheric warming and the midlatitude meridional temperature gradient mechanisms. ΔT_{surf} across the midlatitude Atlantic at 40 - 60 °N at the surface will reflect the difference in the strength and location of the North Atlantic jet stream between models. ΔT_{150} between 40 °N and 60 °N will relate to the location of the jet, but also the difference in the height of the tropopause between models, which relates to the strength of midlatitude baroclinic eddies (Zurita-Gotor and Vallis 2011).

Metrics 6 and 7 both relate to the influence of diabatic heating in the tropical Pacific on ESB (the fourth mechanism discussed in section 3.4.5.2). Metric 6 relates to the precipitation in the tropical Pacific, which is going to be well correlated with diabatic heating of the atmosphere (Yu 2007), and therefore indicates the strength of Rossby wave propagation (Hoskins and Karoly 1981). The choice of averaging across the equatorial Pacific is motivated by Fig. 3.8a (reproduced in Fig. 4.1), which particularly highlights the equatorial Pacific as a region where the level of precipitation is correlated with ESB. The value of U_{400} at 20 °N averaged across the Pacific relates to the average location of the Pacific subtropical jet, such that models with stronger easterly flow at this latitude (and an equatorward subtropical jet) have more ESB historically.

4.3 Results

In this section, I present the results from the MLR analysis. Sections 4.3.1 and 4.3.2 and Tables 4.1 and 4.2 show the results from the 7 variable and 2 variable MLR analysis, respectively. In each case four MLRs are calculated to study:

1. how the historical values of the metrics correlate with the historical ESB (**hist** $\rightarrow$ **hist**);
2. how the historical values of the metrics correlate with the ESB response (**hist** $\rightarrow$ **diff**);
3. how the 4xCO_2 values of the metrics correlate with the 4xCO_2 ESB (**4x$\mathbf{CO_2}$** $\rightarrow$ **4x$\mathbf{CO_2}$**); and
4. how the change in values of the metrics correlate with the ESB response (**diff** $\rightarrow$ **diff**).

I then assume that the correlation between the metrics and ESB may relate to one of the suggested causal mechanisms described in chapter 3.

Figure 4.1 in section 4.3.2 illustrates the two most important physical mechanisms that I have identified from the MLR analysis, with reference to the discussion in chapter 3. Figure 4.1 also geographically shows the two metrics used in the 2 variable MLR analysis in Table 4.2 to capture these physical mechanisms and provide an estimate for the ESB response.

Section 4.3.3 then presents a scatter plot (Fig. 4.2) to graphically compare the **hist** $\rightarrow$ **diff** MLR for three cases: using metrics 1 and 2; using all 7 metrics (Table 4.1); and using 2 metrics

Table 4.1: The coefficients of MLR analysis, using the seven metrics listed in section 4.2 to predict ESB across the 22 model ensemble. The top half of the table shows the mechanisms and linear regression coefficients (in days °C^{-1}) associated with each metric. The 1st column specifies the mechanism from chapter 3 that each metric is associated with and the 2nd column specifies the metric. The 3rd - 6th columns show the coefficients for each MLR using normalised data. Four MLRs are listed across four columns: the MLR between the historical values of each metric and the historical ESB (hist → hist); the MLR between the historical ESB and the ESB response (hist → diff); the MLR between the metrics and ESB in the 4xCO_2 period (4xCO_2 → 4xCO_2); and the MLR between the change in the metrics listed and the ESB response (diff → diff). The bottom half of the table specifies the intercept and skill metrics (three error metrics and the R^2) for each MLR. The bottom row shows the predicted values of the average level of historical ESB (in days) and the ESB response (days °C^{-1}) using the MLR for the real atmosphere. A graphical representation of the **hist → diff** with the ERA5 prediction is shown in Fig. 4.2b.

Mechanism	Metric	hist → hist	hist → diff	4xCO_2 → 4xCO_2	diff → diff
1	ΔT_{850}	-3.01	0.97	-4.31	-0.32
2	ΔT_{250}	-1.70	0.54	1.46	-0.13
2/3	ΔT_{300} (30 °N - 10 °N) Atl avg	-0.85	-0.35	-1.96	1.30
3	ΔT_{surf} (60 °N - 40 °N) Atl avg	-4.39	0.95	6.78	2.37
3	ΔT_{150} (60 °N - 40 °N) Atl avg	8.75	-3.57	-2.15	-1.06
4	Pr (2 °S - 2 °N) Pac avg	0.38	0.88	2.42	0.45
4	U_{400} 20 °N Pac avg	2.69	-1.57	4.41	1.70
	intercept	14.25	2.25	26.08	21.96
	root mean square error	1.13	0.28	0.87	1.21
	R^2	0.66	0.78	0.61	0.25
	ERA5 prediction	21 days	-0.55 ± 0.28 days °C^{-1}		

(Table 4.2). Figure 4.2 therefore graphically represents how I obtain my estimate for the ESB response.

4.3.1 MLR for seven metrics

Table 4.1 shows the results from the seven metric MLR. The top half of Table 4.1 shows the coefficients for all four MLRs in the order specified above. Note that the second of these four result columns (hist → diff), is the one that can be used to estimate the ESB response. The bottom half of Table 4.1 specifies the intercept and two skill metrics (root mean square error and R^2) of the MLR. The bottom row provides a prediction of the historical blocking amount and the ESB response using ERA5 reanalysis data. Note that the coefficients in the top half of Table 4.1 are for the MLR using data for each metric that has been normalised to a value between -1 and 1, using the maximum absolute value for each metric. This enables a comparison of the sign and magnitude of each coefficient between them, and does not affect the R^2 of the regression. The error coefficients are for the MLR that has not been scaled by the metrics, to enable direct comparison to the ERA5 estimate in SI units. The normalisation of the data makes no difference to the skill of the MLR.

By comparing the coefficients in Table 4.1 with one another, the ΔT_{150} metric averaged across the Atlantic has the largest magnitude of its coefficient for both the **hist** $\rightarrow$ **hist** and **hist** $\rightarrow$ **diff** MLRs. The sign indicates that models with a larger ΔT_{150} between 60 °N and 40 °N have more ESB historically.

The ΔT_{150} metric has coefficients significantly larger than all other metrics for the historical comparisons, but for the **4xCO**$_2$ $\rightarrow$ **4xCO**$_2$ and **diff** $\rightarrow$ **diff** studies the dominant term is the ΔT_{surf} term between 60 °N and 40 °N. This means that whilst ΔT_{150} across the midlatitude Atlantic is most important metric historically (and can therefore be used to predict the ESB response), the ΔT_{surf} metric is more important under climate change at influencing ESB. This change in the most significant metric under climate change and reflects the changing dynamics in the North Atlantic jet. As discussed in section 3.4.4.2, the North Atlantic jet both weakens under climate change and shifts poleward, and in models with a positive (negative) ESB response have a greater (smaller) weakening of the jet and a greater (weaker) poleward shift of the jet. Between 60 °N and 40 °N, each of these metrics relate to both aspects of the influence of the midlatitude meridional temperature gradient on ESB, but in different ways. ΔT_{surf} relates to both the strength and position of the North Atlantic midlatitude jet. In addition, ΔT_{150} between 60 °N and 40 °N reflects changes in the height of the tropopause between models, and therefore relates to the strength of baroclinic eddies and the profile of heating in the tropical troposphere. From this analysis, I am not able to determine precisely which changes in the dynamics of the North Atlantic midlatitude jet under climate change are most important in influencing ESB, but the changing magnitude of coefficients for the surface and 150 hPa temperature gradients reflects the importance of the Atlantic midlatitude meridional temperature gradient, both historically and under climate change.

The R^2 of the MLR reflects how predictive the model is. For each of the first three regressions (**hist** $\rightarrow$ **hist**, **hist** $\rightarrow$ **diff** and **4xCO**$_2$ $\rightarrow$ **4xCO**$_2$) the skill score for the MLR is reasonably predictive (0.66, 0.78 and 0.61 respectively). The R^2 of 0.78 for the **hist** $\rightarrow$ **diff** may indicate over-fitting; since seven metrics have been chosen to run a MLR across 22 models, there is a significant risk of over-fitting. To address this, the two most skilful metrics have been identified and a separate MLR run for them (discussed in section 4.3.2 and shown in Table 4.2) to make a trustworthy prediction for the ESB response.

There is a significant decrease in the skill for the **diff** $\rightarrow$ **diff** regression. This suggests that the metrics that are most relevant for developing a historical understanding of ESB are not effective at predicting how the change in the relevant physical mechanisms causes the change in ESB. This suggests that the historical climatology of the physical mechanisms is more relevant than the changes in the physical mechanism in terms of understanding the ESB response. This is consistent with the results from chapter 3; the differences between the models historically are a much higher magnitude than the changes that occur in the model groups. This can be seen in the U field in Figs. 3.4 and 3.5.

4.3.2 MLR for the two most skilful metrics

To reduce the risk of over-fitting, several MLRs were run with different combinations of the seven metrics used in Table 4.1. Two metrics were identified as playing a particularly important role in using their historical value to predict the ESB response: ΔT_{150} between 60 °N and 40 °N, averaged over the Atlantic; and U_{400} at 20 °N, averaged across the Pacific. Table 4.1 indicates the prominence of these variables, since they have the largest coefficients for the **hist** $\rightarrow$ **diff** regression.

These two metrics and their accompanying mechanisms are graphically illustrated in Fig. 4.1. The top half of Fig. 4.1 overlays the graphically illustrations on top of the historical zonal wind climatology at 200 hPa. A stronger North Atlantic midlatitude temperature gradient at 150 hPa between 60 °N and 40 °N indicates more ESB, due to a greater change in the midlatitude tropopause height and changes in baroclinic instability (related to mechanism #3 described in 3.4.4.2). This mechanism is indicated on the right hand side of Fig. 4.1, with gold text boxes and arrows summarising the flow diagram from Fig. 3.7. On the bottom right of Fig. 4.1, I reproduce Figs. 3.5a-f, which indicates that the strengthening of the subtropical

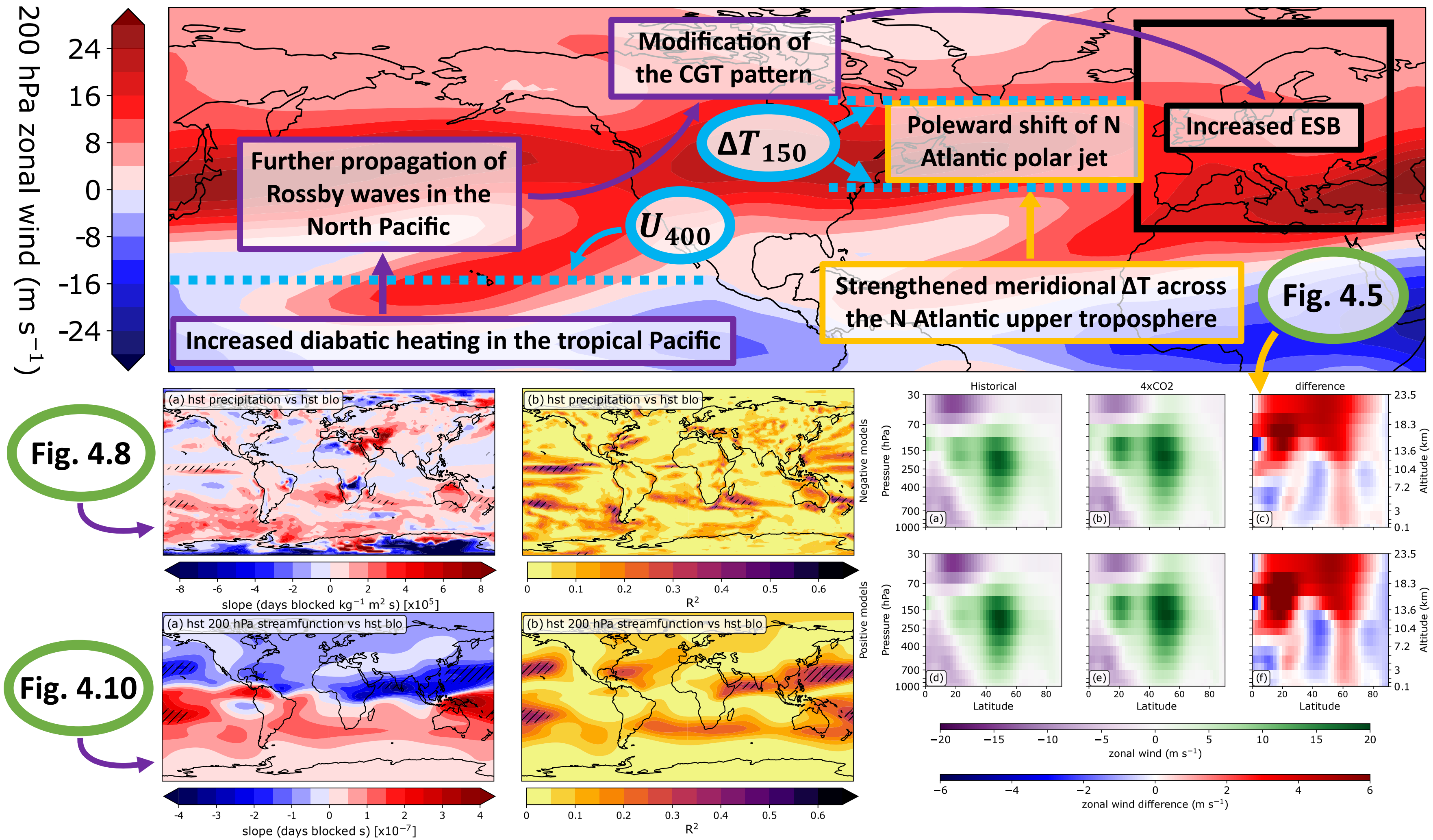

Figure 4.1: An infographic showing the two physical mechanisms identified in this chapter as most important in influencing the ESB response. These are mechanisms #3 and #4 from the list in section 4.1, and are discussed in sections 3.4.3 and 3.4.5 respectively. Mechanisms #3 and #4 are described in yellow and purple text boxes and arrows, respectively. The dotted cyan lines show the latitudes and longitude bands for the two metrics used in the MLR analysis in Table 4.2. The descriptions of the physical mechanisms in the top panel are projected onto the ERA5 historical (1979-2005) JJA zonal wind climatology at 200 hPa. The bottom half shows panels from key figures in sections 3.4.3 and 3.4.5, to highlight the physical basis in my analysis for proposing these two mechanisms. The black box indicates the boundaries for the region of study for SOM-BI as defined in section 2.2.2.

jet (due to an increased upper tropospheric meridional temperature gradient across the North Atlantic) and resultant poleward shift of the polar jet (Lee and Kim 2003) is greater in the models with a positive ESB response. Mechanism #3 suggests that this poleward shift of the North Atlantic jet creates more Rossby wave breaking across the Euro-Atlantic region because it contrasts with the general weakening of the jet in other longitude bands (see Fig. 3.4), such that a larger poleward shift creates a greater meridional displacement of the North Atlantic jet. The dotted cyan lines across the North Atlantic indicate the two longitudinal bands across the North Atlantic which are used to calculate the ΔT_{150} metric. As can be seen from the ERA5 U climatology, these temperature gradients are taken between the maximum speed of the polar jet (at approximately 50 °N). Therefore, the ΔT_{150} metric at this region is an appropriate metric to use to capture the physics of mechanism #3, since it describes differences in the jet location across models and how those jet locations change with climate change.

In addition, a stronger zonal wind at 400 hPa in the Pacific at 20 °N indicates more ESB, due to a North Pacific subtropical jet that is closer to the equator, enabling further propagation of Rossby waves from the tropical Pacific (related to mechanism #4 described in 3.4.5.2). This mechanism is indicated on the left hand side of Fig. 4.1, with purple text boxes and arrows summarising the flow diagram from Fig. 3.11. On the bottom left of Fig. 4.1, I reproduce Figs. 3.8a-b and 3.10a-b, which show important correlations historically between ESB occurrence and precipitation in the tropical Pacific (Figs. 3.8a-b) and ESB occurrence and streamfunction in the North Pacific (Figs. 3.10a-b). The dotted cyan line across the North Pacific lies at 20 °N, indicating the location for the U_{400} metric used in the two variable MLR analysis. From comparing to the U_{200} climatology, this metric lies across the regional of the subtropical jet where in the West Pacific there is easterly flow (in blue) and in the East Pacific there is westerly flow (in red). Therefore the value of the U_{400} metric will indicate how close to the equator the subtropical Pacific jet is and also its strength. Where there is stronger westerly flow in this region, there is more Rossby wave propagation into the North Pacific resulting from diabatic heating. Therefore, the U_{400} metric is an appropriate metric to use to capture the physics of mechanism #4, since it describes differences in the Pacific subtropical jet location and strength across models and how that jet location and strength (and the subsequent Rossby wave propagation in the North Pacific) is affected by climate change.

Table 4.2 shows the MLR for the two most skilful metrics. Both metrics positively correlate with historical ESB. The normalised coefficients indicate that ΔT_{150} is a more important variable for controlling ESB, suggesting that the Atlantic meridional temperature gradient is more important than Pacific Rossby wave propagation. The use of both metrics to predict ESB response from historical data (**hist** $\rightarrow$ **diff**) leads to $R^2 = 0.65$. By comparison, the seven metric MLR in Table 4.1 was $R^2 = 0.78$. There was not another metric from the list of seven metrics provided in Table 4.1 that significantly contributed to the difference between these, indicating that these two metrics provide sufficient skill to the MLR for predicting the ESB response without the risk of over-fitting.

Two predictions can be made from the MLR analysis. First, using the **hist** $\rightarrow$ **hist** regression, the historical values of ΔT_{150} and U_{400} in ERA5 can be used to predict the amount of ESB. The predicted average number of days blocked from the MLR is 22 days, which is 7 days (28%) lower than the average number of blocked days that were manually identified in the Ground Truth Dataset (see section 2.2.2). Both Tables 4.1 and 4.2 also show an under-estimate of historical ESB. This reflects the fact that the models under-estimate the amount of ESB historically, and therefore a derived MLR from the models will under-estimate the amount of historical blocking. The second prediction that can be made from the MLR analysis is that the ESB response can be estimated from **hist** $\rightarrow$ **diff**. I obtain a value of 0.22 ± 0.35 days $°C^{-1}$. I use the root mean square error on the regression as the uncertainty for the prediction of ESB response, since the root mean square error directly reflects the accuracy of forecasts from the linear regression (Wilks 2005). I note that this estimate significantly differs from the estimate in Table 4.1 (-0.55 ± 0.28 days $°C^{-1}$), but I consider this latter estimate to be unreliable since the seven metric MLR is probably over-fitting the data (note that there are only 22 models in the ensemble). I also note that Table 4.1 has several large values for slopes, which further indicates over-fitting. Therefore, the estimate from Table 4.2 for the ESB response is the more reliable estimate.

Table 4.2: As for Table 4.1, but instead showing the MLR analysis from the two metrics that provide the most skill in predicting the ESB response from historical data. A graphical representation of the **hist → diff** with the ERA5 prediction is shown in Fig. 4.2c.

Mechanism	**Metric**	**hist→hist**	**hist→ diff**	**4xCO_2 → 4xCO_2**	**diff → diff**
3	ΔT_{150} (60 °N - 40 °N) Atl avg	8.89	-2.61	-2.99	-0.13
4	U_{400} 20 °N Pac avg	3.41	-1.23	3.34	-0.18
	intercept	14.04	2.59	22.13	-0.09
	root mean square error	1.31	0.35	1.26	0.59
	R^2	0.55	**0.65**	0.19	0.01
	ERA5 prediction	22 days	**0.22 ± 0.35 days °C^{-1}**		

4.3.3 A comparison of the MLR predictions for the ESB response

Figure 4.2 shows the **hist → diff** MLR for three cases: using metrics 1 and 2; using all 7 metrics (Table 4.1); and using 2 metrics (Table 4.2). Figure 4.2 therefore graphically represents how I obtain my estimate for the ESB response.

Figure 4.2a shows the MLR using only metrics 1 and 2. Metrics 1 and 2 are the equator-to-pole temperature gradients at 850 hPa and 250 hPa, respectively, and so relate to the "tug-of-war" of physical processes that are commonly discussed in the literature (see Barnes and Screen (2015) and sections 3.4.2 and 3.4.3 for further discussion). However, I am not able to use these two metrics to predict the ESB response, since no relationship emerges between the historical and future behaviour. Since such a relationship has already been established (see chapter 3), I conclude that the "tug-of-war" is an inadequate description of the physics to describe the processes involved in understanding the ESB response.

Figure 4.2b shows the MLR using the 7 metrics shown in Table 4.1. This produces a strong correlation of $R^2 = 0.78$ between the past and future data. However, since there are only 22 models, using 7 metrics in a MLR is likely over-fitting the data, so whilst a prediction for the cliamte feedback on ESB in the real atmosphere can be obtained, this is unlikely to be accurate.

Figure 4.2c shows the MLR using the 2 metrics shown in Table 4.2 and Fig. 4.1. This still produces a good correlation of $R^2 = 0.65$, and since only two metrics are used there is a low risk of over-fitting. I therefore conclude that the prediction for the ESB response in the real atmosphere obtained from this analysis is the most reliable.

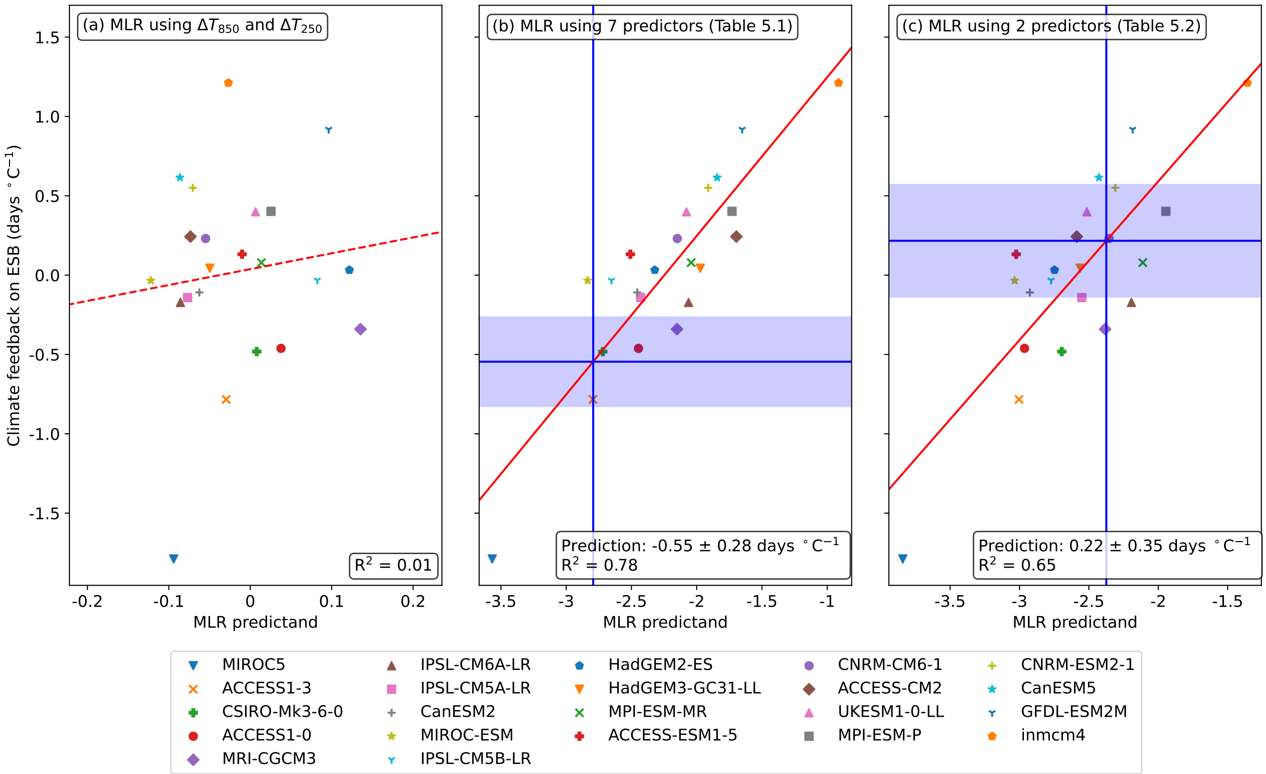

Figure 4.2: A comparison of three MLRs for the **hist** → **diff** comparison, which compares the historical behaviour with the ESB response to produce an estimate for the ESB response in the real atmosphere. The x-axis shows the result from summing the coefficients for each metric multiplied by the historical value in each given climate model, and the y-axis shows the ESB response for each model. The red line indicates the linear regression. The blue lines show the prediction for the ESB response, using the values for the metrics from the ERA5 historical period. The uncertainty on the ERA5 prediction is in blue, and is the root mean square error of the regression. The R^2 for each regression is shown in the bottom left, alongside the value for the ERA5 prediction where appropriate. (a) shows the case for the two metric MLR using the first two metrics listed in table 4.1, using the equator-to-pole temperature gradients at 850 hPa and 250 hPa. (b) shows the case for the seven metric MLR described in 4.3.1 and shown in Table 4.1. (c) shows the case for the two metric MLR described in 4.3.2 and shown in Table 4.2.

4.4 Discussion and Conclusions

In agreement with conclusions from chapter 3, my analysis suggests that the two most important mechanisms to influence ESB historically (and therefore to influence the ESB response from chapter 3) are:

- the North Atlantic meridional temperature gradient; and
- Rossby wave propagation in the North Pacific.

From identifying the most relevant metrics that correspond to these physical mechanisms, I have used MLR to estimate the ESB response. I have identified two relevant metrics which I have used to predict the ESB response and obtained a value of 0.22 ± 0.35 days °C^{-1}. This value is relatively small, and the uncertainty on the value (the root mean square error of the regression) is larger than the value itself. However, given that the SOM-BI probably provides a conservative estimate for the change resulting from blocking, the data evidence points towards a small positive feedback (this will be discussed further in section 5.1.3). One implication is that models which show very significant changes in ESB in the future reflect significant over- and under-representations of the mechanisms which impact ESB. In particular, they will most likely mis-represent either or both of the two mechanisms described above, or - equivalently - other mechanisms that might drive these correlations but that are not considered in my analysis. In section 5.2.3, I discuss what future work could be undertaken to further refine this estimate.

However, an untested assumption is made with the above analysis. I note that by simply using the correlation between the historical bias and future trend of ESB, I obtain an estimated ESB response of -2.04 ± 0.32 days °C^{-1} (not shown). I assume that this result is unreliable. To make this assumption, I assume that the reason that all the models have a significantly lower blocking occurrence than the ERA5 reanalysis is to do with systematic issues of the representation of blocking in global climate models (see section 1.3.4), and therefore the intercept in the correlation between the historical bias and future trend of ESB is too low. In any case, given that the actual occurrence of ESB is significantly higher than found in all models, extrapolation beyond the model ensemble is needed to derive an estimate for the ESB response, so any method of estimating the ESB response from the historical bias of ESB events in the model ensemble alone cannot be made with confidence.

Another possible explanation for the strong relationship between the past bias and future trend of ESB is that there may be additional systematic issues with the application of the SOM-BI that cause the occurrence of model biases that have not been addressed by the normalization. Whilst the normalisation of the SOM-BI (see section 3.3.2) has been shown to significantly reduce the biases between the historical climatology and the change in the occurrence of SOM node groups, this problem may still persist through biases in the variability of the MSLP climatology between each model and the historical data. Since the definition of blocking events from the SOM-BI is fundamentally tied to the occurrence of certain SOM nodes in ERA5 (even after applying normalisation), and since these SOM nodes are defined from the ERA5 climatology, there is still a potential that the blocking events in a given model will be sensitive to the differences in the climatological differences between ERA5 and the given model. Given that the results from the normalised SOM-BI can be physically interpreted in a way consistent with the occurrence of ESB events, it seems likely that blocking events are being adequately described. However, to test this assumption an alternative blocking index such as the AGP index (introduced and applied in chapter 2) should be used to confirm that a relationship exists between the past bias and future trend of ESB events, that can be independently verified from the SOM-BI index (an important requirement specified by Woollings et al. (2018)). However, there is a lack of daily geopotential height data for the 4xCO_2 scenarios. Of the 22 models studied in this chapter, only five models (UKESM1-0-LL, HadGEM3-GC31-LL, GFDL-ESM2M, IPSL-CM5A-LR, MIROC5) have daily 4xCO_2 geopotential height data available. Whilst I am not able to do a direct comparison of the results, these models could be studied and the AGP index compared to the SOM-BI index. This and other possible avenues for future work will be further discussed in section 5.2.3).

Finally, I note that these mechanisms are clearly co-dependent and interact with one another in potentially complex ways, and the metrics that I use do not fully quantify the strength of these mechanisms. In addition, there is a risk with this analysis that the correlations that I identify are driven by additional mechanisms that have not been suggested here. However, this initial analysis provides a discussion of some of the most important mechanisms involved in influencing the ESB response in models across the CMIP archive.

Chapter 5

Conclusions and future work

5.1 Conclusions

5.1.1 The self-organising map blocking index (SOM-BI)

This thesis has examined the ESB response on European summer blocking (ESB) occurrence. In order to study this problem, I have developed a new blocking index using a combination of supervised and unsupervised machine learning. This is based on the self-organizing map (SOM) clustering algorithm, and the training of the selection of node groups associated with ESB from the SOM. Such an algorithm is a significant advance over the literature, where typically either blocking indices (BIs) are used or machine learning methods are employed to study more generic changes in circulation patterns. By developing a BI that is based on common machine learning methods in the literature, I have advanced a unique method which brings together both approaches and yields several advantages:

1. **Improved skill of the algorithm, particularly in application to climate models**. Table 2.1 in section 2.3.2 compares the skill of different algorithms in identifying ESB by comparing the classification skill of each algorithm to the objectively labelled ground truth dataset (GTD, defined in section 2.2.2). It was found that the SOM-BI has a similar skill to the most effective BI studied (the DG83 index) for the ERA5 reanalysis period, but a significant improvement in skill over the BIs when comparing the SOM-BI to the

climate model output. This is particularly important since some of the indices such as the AGP index had a surprisingly low detection skill for ESB events in the climate model.

2. **The use and comparison of a variety of variables used to study atmospheric blocking**. Whilst BIs are typically defined on one variable and level (500 hPa geopotential height (Z_{500} for Dole and Gordon (1983); vertically averaged potential vorticity for Schwierz et al. (2004) and potential temperature on the dynamic tropopause for Pelly and Hoskins (2003)), the SOM-BI can be used with a variety of variables, and the skill of different methods has been compared (see Fig. 2.6). Of the variables studied, Z_{500} was found to be the most effective variable at classifying atmospheric blocking events.

3. **A spatio-temporal identification of types of blocking events over Europe**. Since groups of SOM nodes that exist across time are used to identify blocked nodes, blocking events can be classified in new ways through the application of such groups. The application of these different blocked node groups to classifying categories of blocking event over Europe was described in section 2.3.7 and shown in Fig. 2.10, and involves the use of K-means clustering to specify the number of blocking events one is interested in. This is unique in that other BIs generally do not provide categories of blocking events over particular regions. Whilst other BIs could be used to study the changing persistence of blocking events over particular regions, identifying a shift of types of blocking events that have been both spatially and temporally defined (as shown in Fig. 2.10 between Eastern and Western European blocking events) is enabled by the SOM-BI. This regional identification and trend analysis of blocking events enables a more finely-tuned study of blocking events over Europe beyond the typical study of Scandinavian blocking events.

5.1.2 Physical mechanisms influencing the historic and future occurrence of ESB events

Points 1 and 2 above have enabled the study of atmospheric blocking events in the 4xCO_2 runs. This is useful because such a high forcing scenario ensures a high signal-to-noise ratio; these runs are also conceptually simple since there are no changes in other atmospheric components such as aerosols. Such runs do not typically have daily Z_{500} data available, but they do have frequently archived daily mean sea level pressure (MSLP) output. Whilst this variable has a slightly lower skill than Z_{500} in identifying blocking events, the lack of a need to detrend MSLP (see section 3.3.1 and Appendix B.3) is a key advantage and has enabled the straightforward use of the SOM-BI to study atmospheric blocking in 4xCO_2 runs. By comparing the results of such analyses across 22 CMIP5/6 climate models, the ESB response was determined in each model. A range of positive and negative ESB responses was identified across all models (see Fig. 3.2).

In addition, chapter 3 showed that there is a relationship between the historic U climatology and the ESB response (Figs. 3.4 and 3.5). This relationship between the historic climate and future ESB response enables the possibility of developing a prediction of the ESB response. This could provide observational constraint on the model uncertainty (see section 1.5.7).

To develop this estimate for the ESB response, an understanding of the relevant physical mechanisms which cause ESB is necessary (Hall et al. 2019). I have discussed four mechanisms that can play a role in influencing the ESB response, motivated by the existing literature and augmented by correlations I identified across the CMIP5/6 ensembles:

1. Arctic amplification (AA);
2. increased tropical upper-tropospheric warming (UTW);
3. changes in the midlatitude Euro-Atlantic meridional temperature gradient; and
4. the propagation of Rossby waves from diabatic heating in the equatorial Pacific.

AA and UTW are commonly discussed in the literature as a "tug-of-war" in the midlatitudes (Screen et al. 2018; Peings et al. 2019). AA is hypothesised to increase midlatitude blocking through reducing the temperature gradient in the lower troposphere, leading to a weaker NH jet with a shift equatorward, which is associated with more stationary weather and Rossby wave-breaking (Barnes and Screen 2015). Increased warming in the tropical upper troposphere (compared to equivalent altitudes at higher latitudes) is hypothesised to decrease atmospheric blocking through increasing the NH meridional temperature gradient in the upper troposphere (Barnes and Screen 2015), leading to a stronger NH jet with a shift poleward, which is associated with more storm track activity and fewer persistent anticyclones (Held 1993).

By studying the relation between relevant metrics for these mechanisms and ESB, no significant relationship was found across the model ensemble between the ESB response and AA, or between the ESB response and enhanced UTW. This is a surprising result, as it indicates that there is additional physics driving the changes in ESB that is not usually explicitly considered. Note that this does not suggest that AA or UTW are unimportant, since they may have a significant effect through affecting other mechanisms that more directly impact the ESB response.

From studying the correlations with changes in ESB across several dynamical variables, two additional mechanisms (3 and 4 in the list above) have been hypothesised which influence both the historic ESB occurrence and the ESB response. The third mechanism involves changes in the Euro-Atlantic meridional temperature gradient. This mechanism has two related components:

1. AA decreases the lower-tropospheric Euro-Atlantic meridional temperature gradient, leading to a weaker NH polar jet; and

2. UTW in the Atlantic causes a significant increase in the strength of the North Atlantic subtropical jet, causing a poleward shift of the Euro-Atlantic polar jet.

Both of these features occur across all models and work to increase ESB. These changes in the jet strength and position occur to a greater extent in models with a positive ESB response. The weaker NH jet could lead to more ESB since it tends to increase the waviness of the jet, as is commonly discussed (Francis and Vavrus 2012; Hassanzadeh et al. 2014; Coumou et al. 2015; Overland et al. 2015; Peings et al. 2017; Fabiano et al. 2021). Additionally, the concurrent poleward shift of the NH Atlantic polar jet seems to be correlated with increased Rossby wave-breaking in the Euro-Atlantic region. This can be seen from the greater (smaller) increase in the strength of the Euro-Atlantic subtropical jet in models with a positive (negative) ESB response.

I propose that this increased strength of the Euro-Atlantic subtropical jet creates a poleward shift of the Euro-Atlantic polar jet. However, rather than this decreasing the occurrence of ESB (as would be typically expected from a poleward shift of the jet (Barnes and Screen 2015)), this poleward shift of the Atlantic jet works to increase ESB since it occurs alongside a general equatorward shift of the NH polar jet. I hypothesise that this creates a greater meridional displacement between the North Atlantic jet and the rest of the NH polar jet, which increases Rossby wave propagation.

The fourth mechanism relates to the propagation of Rossby waves in the North Pacific from the tropical Pacific, arising from diabatic heating (Hoskins and Karoly 1981). This is not a mechanism that has been causally connected to atmospheric blocking in Europe before. Additionally, the presence of such a connection is also unusual in JJA, because the Rossby wave propagation is much weaker in the NH summer (Hoskins and Ambrizzi 1993; Ting and Sardeshmukh 1993).

From distinct correlations with precipitation in the tropical Pacific and ESB in the historic period, I hypothesise that diabatic heating is causally connected to ESB. From studying the zonal wind correlations, I also hypothesise that models with a more equatorward North Pacific subtropical jet enables further propagation of these Rossby waves across the North Pacific. Whilst it is not clear precisely how the propagation of Rossby waves in the JJA North Pacific affects the NH JJA circulation and influences the occurrence of ESB events, the presence of remote influences on the JJA Euro-Atlantic circulation such as the circumglobal teleconnection (CGT) provides a plausible mechanism by which tropical Pacific diabatic heating can modulate ESB (Ding and Wang 2005).

Both of these mechanisms (3 and 4) relate to the commonly discussed AA and UTW, but add additional physics that has not been previously discussed in the context of ESB. These mechanisms also underscore the importance of tropical influences on ESB (Sun et al. 2022), and involve complex dynamics that have not yet been adequately studied. This motivates future work to understand how mechanisms 3 and 4 relate to ESB.

5.1.3 Estimating the ESB response

Chapter 4 showed that there is a significant negative correlation between the historic occurrence of ESB and the ESB response across the model ensemble. This motivates the possibility of using the bias of the historic climatology to influence future ESB events. Chapter 3 discussed four physical mechanisms that can play a role in influencing ESB occurrence historically. Two mechanisms (weakening and poleward shift of the Euro-Atlantic jet, and Rossby wave propagation in the North Pacific) were particularly highlighted as having important roles in influencing ESB both historically and under climate change. Therefore, to provide an estimate of the ESB response based on these mechanisms, in chapter 4 I use multiple linear regression (MLR) across several metrics that are related to the four mechanisms discussed above and relate the historic ESB to future ESB.

First I use a seven metric MLR which covers all four mechanisms and obtain a R^2 skill of 0.78. This is a very high skill, but since I am only using 22 models in the regression it is likely over-fitting the data. From comparing the coefficients associated with each metric, the MLR highlights two metrics that significantly contribute to the overall skill of the prediction of the ESB response (change in T_{150} between 60 °N and 40 °N average across the Atlantic; and U_{400} at 20 °N, averaged across the Pacific). These two metrics relate to the two prominent mechanisms discussed in chapter 3, which provides further implications for the importance of these two metrics in understanding ESB and its response to climate change.

From using these two metrics in a MLR, I obtain an R^2 skill of 0.65; this is also high which indicates good predictive skill, but since only two metrics are used in this regression there is a much lower risk of over-fitting. Therefore I use this regression to obtain a best estimate for the ESB response, and get a result of 0.22 ± 0.35 days $°C^{-1}$.

Note that in section 3.3.2.2, I discuss the normalisation of the SOM-BI that was used to calculate ESB. As part of the normalisation process I define the MSLP anomaly in each model differently between the historic and 4xCO_2 runs. This was necessary to reduce direct dependence of trends in atmospheric blocking on changes in the mean state of MSLP. However, since these changes in MSLP will also reflect coupled thermodynamic-dynamic shifts under climate change, the normalised SOM-BI will tend to under-estimate the magnitude of the changes to ESB. This means that the resulting estimate for the ESB response is likely a lower bound estimate of the actual feedback. Note that Figs. B.1a and B.1b compare the results for the non-normalised and normalised data, respectively. The non-normalised trends in Fig. B.1a uses the MSLP anomalies with respect to the historical data for both the historical and 4xCO_2 periods, and the normalised trends in Fig. B.1b take the anomaly and dividing by the standard deviation of the historical and 4xCO_2 periods separately for the historical and 4xCO_2 data (as discussed in section 3.3.2). The magnitude of the trends is an over-estimate of the dynamic changes in climate in the case Fig. B.1a (ranging from -2.5 to 3.5 days $°C^{-1}$) and an under-estimate in B.1b (ranging from -2 to 1.5 days $°C^{-1}$). I therefore conclude from my analysis that it is most likely that the occurrence of ESB will modestly increase with climate change.

5.2 Future work

5.2.1 Future analysis with the SOM-BI

In this analysis the SOM-BI has been created and used to study changes in four categories of ESB events, distinguished by their location (shown in Fig. 2.10 in section 2.3.7). Four metrics were considered across the ERA5 1979-2019 period to study trends in blocking events: occurrence (number of blocked days), persistence (average duration of a blocking events), maximum duration of a blocking event and number of blocking events. This detailed approach to studying trends in ESB was not carried throughout my thesis and the comparison across the climate models in chapters 3 - 4. This is because to compare the historic and 4xCO_2 scenarios, mean sea level pressure (MSLP) was used, due to complexities with detrending other variables after a nonlinear climate forcing and due to a lack of other available data. One reason for this is that I found that MSLP could not as sharply distinguish between different categories of ESB events, so the different categories of blocking event were not studied. In addition, the other metrics (persistence, maximum duration and event number) were not studied across the 4xCO_2 run comparison, because in previous applications of blocking indices to the climate models persistence and maximum duration were found to be significantly correlated with the occurrence metric (not shown).

However, studying the separate metrics alongside a range of blocking categories across the CMIP5 and CMIP6 models could yield several interesting results. Such study could identify shifts in the domain between Eastern and Western European blocking events, which may indicate the increased prevalence of certain Rossby wavenumbers with particular phase positions (Kornhuber et al. 2019; Kornhuber et al. 2020). The changing persistence of either Eastern or Western European blocking events could further indicate increases in the persistence of such patterns (Rousi et al. 2022). To extend the study of blocking categories in this way I would need to use geopotential height. The RCP and SSP scenarios could be used in this regard with the SOM-BI, assuming that geopotential height can be sufficiently well detrended to remove the thermodynamic effect of troposphere expansion.

Further quantities such as the Rossby wave breaking properties or the nature of blocking onset and decay can also be studied, both in ERA5 data (which has now been extended back to 1950 (Bell et al. 2021)) and across CMIP5 and CMIP6. This analysis could be done by studying particular dynamical quantities on the blocked days identified by the SOM-BI, and extended by contrasting the dynamical quantities across different categories of blocking pattern identified by the SOM-BI node groups. I have also made the GTDs available for both ERA5 and UKESM, which have wider application in understanding historic blocking events, how they interact with other meteorological phenomena (such as heatwaves and droughts) and comparing blocking patterns and their occurrences between reanalyses and CMIP6 models (cf. process-based climate model evaluation, Nowack et al. (2020)). I encourage similar ground truth datasets to be created for other world regions and seasons, and the SOM-BI method could then be trained for and applied to those regions.

5.2.2 Exploration of the physical mechanisms influencing the ESB response

The analysis from chapters 3 and 4 highlighted two mechanisms that are particularly important in influencing the ESB response:

1. changes in the midlatitude Euro-Atlantic meridional temperature gradient; and

2. the propagation of Rossby waves from diabatic heating in the equatorial Pacific.

The first of these involves two elements: a decreased strength of the NH polar jet arising from AA and an increase in the strength of the subtropical North Atlantic jet, causing a poleward shift of the Euro-Atlantic polar jet. Whilst the first of these mechanisms is commonly discussed in the literature (Francis and Vavrus 2012; Barnes and Screen 2015; Woollings et al. 2018) and has a relatively simple mechanism with well understood physics, the second of these elements is dynamically complex. I hypothesise that a poleward shift of the Atlantic polar jet increases ESB. Since this shift is a unique regional feature of the Euro-Atlantic (and is a more prominent shift in models with a positive ESB response), a poleward shift of the Atlantic polar jet may increase the likelihood of Rossby wave-breaking events through a greater latitudinal gradient in the zonal wind between the Euro-Atlantic and adjacent regions. Whilst such a mechanism is plausible and consistent with physical understanding and the correlations in the data between positive and negative model groups, my analysis has not developed a detailed physical understanding of precisely how this poleward shift of the Euro-Atlantic polar jet can increase ESB.

In addition, whilst the propagation of Rossby waves in the North Pacific arising from diabatic heating in the tropical Pacific is well understood (Hoskins and Karoly 1981; Hoskins and Ambrizzi 1993; Ting and Sardeshmukh 1993), the physics of how Rossby wave propagation in the North Pacific may influence ESB is not well understood. Whilst such a correlation is plausible given physical connections between the North Pacific and Europe such as the circumglobal teleconnection (Ding and Wang 2005), a detailed physical understanding of this has not been explored.

To explore this, an intermediate complexity model could be used with which simplified experiments could be run. By changing the Euro-Atlantic meridional temperature gradient, the strength of the subtropical Atlantic jet could be increased from thermal wind balance. The effects that this has on the position of the Atlantic polar jet and on subsequent Rossby wave-breaking could then be investigated. A further experiment using an intermediate complexity model could be run to study how teleconnections in the NH boreal summer can be influenced by Rossby wave propagation in the North Pacific, given a source of diabatic heating in the tropical Pacific.

This would shed light on the physical connection between diabatic heating in the tropical Pacific and ESB.

Finally, the prominence of these mechanisms in the real atmosphere could be further investigated from reanalysis data. Whilst chapters 3 and 4 show that the two mechanisms above are important in affecting ESB historically, the two mechanisms themselves have not been directly explored with reanalysis data. Figure C.1 shows the relationship between annual historic ESB occurrence and the annual JJA zonal wind climatology for ERA5. The same region of zonal wind correlations at the equatorward edge of the North Pacific subtropical jet (400 hPa and 20° N in Fig. C.1k) is correlated with ESB, with $R^2 \approx 0.2$. This suggests that the Rossby wave propagation in the North Pacific may influence ESB in the real atmosphere. Other variables such as streamfunction, vorticity and precipitation could be investigated here. Particular cases could be identified for particular years or blocking events where the tropical Pacific has had the greatest influence on ESB. Such analysis could confirm the influence of Rossby waves in the North Pacific on ESB, and case studies could inform our understanding of the physics behind this mechanism.

5.2.3 Improving the prediction of the ESB response

In chapter 4, an estimate for the ESB response is provided, derived from the relationship between the tropical zonal wind bias and the ESB response across the model ensemble. An estimate of 0.22 ± 0.35 days $°C^{-1}$ was obtained. As discussed in section 5.1.3, this estimate for the ESB response is probably an underestimate, given that the normalisation of the SOM-BI will tend to remove part of the dynamic climate change signal. To develop a more accurate estimate for the ESB response, several further investigations could be conducted:

1. Investigate the SOM-BI and other BIs (such as AGP or DG83 as discussed and applied in chapter 2) in the RCP8.5 and SSP5-8.5 transient scenarios, and investigate if there is a relationship between the historic occurrence of ESB and future occurrence of ESB. The transient scenarios do not have the data limitations of the $4xCO_2$ runs, so from daily geopotential height data the AGP, DG83 and SOM-BI indices can all be directly compared. However, there will be a weaker signal-to-noise ratio than in the $4xCO_2$ run, which would

affect the statistical significance of the results. In addition, using this transient scenarios produces a more complex picture, since the transient climate response between the models is different (Meehl et al. 2020), and there are also changes to other forcing agents such as aerosols across these runs. The transience, smaller forcing and presence of other forcing agents limit the ability for using the transient scenarios to derive an accurate ESB response.

2. The AGP index could be used in the 4xCO_2 run for the models which have available data. This would ensure a strong signal-to-noise ratio and provide a comparative estimate of the ESB response across these models. From comparing the magnitude of change in ESB between the AGP and SOM-BI methods, the ESB response estimate could be appropriately scaled to correct for the conservative estimate provided by the SOM-BI method. However, only five of the 22 climate models studied (UKESM1-0-LL, HadGEM3-GC31-LL, GFDL-ESM2M, IPSL-CM5A-LR, MIROC5) have daily 4xCO_2 geopotential height data available, so this comparison would provide limited data.

Each of the above approaches has limitations. The transient scenarios have many models to compare and both the AGP and DG83 indices can be used, but there is a relatively weak signal-to-noise ratio. However, using the 4xCO_2 scenario run has a strong signal-to-noise ratio but fewer models available. Additionally, apart from the SOM-BI only the AGP index can be used in the 4xCO_2 run, since the DG83 index requires detrended geopotential height data, and sensible detrending is particularly challenging with a nonlinear climate forcing (see section 2.2.1 and Malik et al. (2020) for an example). Therefore, both of the above approaches could be used in tandem to provide a more robust prediction of the ESB response.

References

Agel, L., Barlow, M., Skinner, C., Colby, F., and Cohen, J. (2021), Four distinct Northeast US heat wave circulation patterns and associated mechanisms, trends, and electric usage, *npj Climate and Atmospheric Science* 4.1, 31. DOI: 10.1038/s41612-021-00186-7.

Ali, H. and Mishra, V. (2018), Contributions of Dynamic and Thermodynamic Scaling in Subdaily Precipitation Extremes in India, *Geophysical Research Letters* 45.5, 2352–2361. DOI: 10.1002/2018GL077065.

Allen, M. R. and Ingram, W. J. (2002), Constraints on future changes in climate and the hydrologic cycle, *Nature* 419.6903, 228–232. DOI: 10.1038/nature01092.

Allen, R. J. and Sherwood, S. C. (2008), Warming maximum in the tropical upper troposphere deduced from thermal winds, *Nature Geoscience* 1.6, 399–403. DOI: 10.1038/ngeo208.

Altenhoff, A. M., Martius, O., Croci-Maspoli, M., Schwierz, C. B., and Davies, H. C. (2008), Linkage of atmospheric blocks and synoptic-scale Rossby waves: a climatological analysis, *Tellus A: Dynamic Meteorology and Oceanography* 60, 1053–1063.

Bacmeister, J. T., Hannay, C., Medeiros, B., Gettelman, A., Neale, R., Fredriksen, H. B., Lipscomb, W. H., Simpson, I., Bailey, D. A., Holland, M., Lindsay, K., and Otto-Bliesner, B. (2020), CO2 Increase Experiments Using the CESM: Relationship to Climate Sensitivity and Comparison of CESM1 to CESM2, *Journal of Advances in Modeling Earth Systems* 12.11. DOI: https://doi.org/10.1029/2020MS002120.

Barnes, E. A. and Screen, J. A. (2015), The impact of Arctic warming on the midlatitude jet-stream: Can it? Has it? Will it?, *WIREs Climate Change* 6.3, 277–286. DOI: 10.1002/wcc.337.

Barnes, E. A. (2013), Revisiting the evidence linking Arctic amplification to extreme weather in midlatitudes, *Geophysical Research Letters* 40.17, 4734–4739. DOI: 10.1002/grl.50880.

Barnes, E. A., Dunn-Sigouin, E., Masato, G., and Woollings, T. (2014), Exploring recent trends in Northern Hemisphere blocking, *Geophysical Research Letters* 41.2, 638–644. DOI: 10.1002/2013GL058745.

Barnes, E. A. and Polvani, L. M. (2015), CMIP5 Projections of Arctic Amplification, of the North American/North Atlantic Circulation, and of Their Relationship, *Journal of Climate* 28.13, 5254–5271. DOI: 10.1175/JCLI-D-14-00589.1.

Barnes, E. A., Slingo, J., and Woollings, T. (2012a), A methodology for the comparison of blocking climatologies across indices, models and climate scenarios, *Climate Dynamics* 38.11, 2467–2481. DOI: 10.1007/s00382-011-1243-6.

Barnes, E. A., Slingo, J., and Woollings, T. (2012b), A methodology for the comparison of blocking climatologies across indices, models and climate scenarios, *Climate Dynamics* 38.11, 2467–2481. DOI: 10.1007/s00382-011-1243-6.

Barriopedro, D., García-Herrera, R., Lupo, A. R., and Hernández, E. (2006), A Climatology of Northern Hemisphere Blocking, *Journal of Climate* 19.6, 1042–1063. DOI: 10.1175/JCLI3678.1.

Barriopedro, D., García-Herrera, R., and Trigo, R. (2010), Application of blocking diagnosis methods to General Circulation Models. Part I: A novel detection scheme, *Climate Dynamics* 35, 1373–1391. DOI: 10.1007/s00382-010-0767-5.

Bell, B., Hersbach, H., Simmons, A., Berrisford, P., Dahlgren, P., Horányi, A., Muñoz-Sabater, J., Nicolas, J., Radu, R., Schepers, D., Soci, C., Villaume, S., Bidlot, J.-R., Haimberger, L., Woollen, J., Buontempo, C., and Thépaut, J.-N. (2021), The ERA5 global reanalysis: Preliminary extension to 1950, *Quarterly Journal of the Royal Meteorological Society* 147.741, 4186–4227. DOI: https://doi.org/10.1002/qj.4174.

Benjamini, Y. and Hochberg, Y. (1995), Controlling the False Discovery Rate: A Practical and Powerful Approach to Multiple Testing, *Journal of the Royal Statistical Society: Series B (Methodological)* 57.1, 289–300. DOI: 10.1111/j.2517-6161.1995.tb02031.x.

Berckmans, J., Woollings, T., Demory, M.-E., Vidale, P.-L., and Roberts, M. (2013a), Atmospheric blocking in a high resolution climate model: influences of mean state, orography and eddy forcing, *Atmospheric Science Letters* 14.1, 34–40. DOI: `https://doi.org/10.1002/asl2.412`.

Berckmans, J., Woollings, T., Demory, M.-E., Vidale, P.-L., and Roberts, M. (2013b), Atmospheric blocking in a high resolution climate model: influences of mean state, orography and eddy forcing, *Atmospheric Science Letters* 14.1, 34–40.

Berggren, R., Bolin, B., and Rossby, C.-G. (1949), An Aerological Study of Zonal Motion, its Perturbations and Break-down, *Tellus A* 1, 14–37.

Bjerknes, J. (1966), A possible response of the atmospheric Hadley circulation to equatorial anomalies of ocean temperature, *Tellus* 18.4, 820–829. DOI: `https://doi.org/10.1111/j.2153-3490.1966.tb00303.x`.

Bjerknes, V. (1898), Über einen hydrodynamischen Fundamentalsatz und seine Anwendung besonders auf die Mechanik der Atmosphäre und des Weltmeeres, *Kongl. Sven. Vetensk. Akad. Handlingar* 31, 1–35.

Black, E., Blackburn, M., Harrison, G., Hoskins, B., and Methven, J. (2004), Factors contributing to the summer 2003 European heatwave, *Weather* 59.8, 217–223. DOI: `10.1256/wea.74.04`.

Blackport, R. and Screen, J. A. (2020), Insignificant effect of Arctic amplification on the amplitude of midlatitude atmospheric waves, *Science Advances* 6.8. DOI: `10.1126/sciadv.aay2880`.

Brayshaw, D. J., Hoskins, B., and Blackburn, M. (2009), The basic ingredients of the North Atlantic storm track. Part I: Land–sea contrast and orography, *Journal of the Atmospheric Sciences* 66.9, 2539–2558.

Brunner, L., Hegerl, G. C., and Steiner, A. K. (2017), Connecting Atmospheric Blocking to European Temperature Extremes in Spring, *Journal of Climate* 30.2, 585–594. DOI: `10.1175/JCLI-D-16-0518.1`.

Cassano, J. J., Uotila, P., Lynch, A. H., and Cassano, E. N. (2007), Predicted changes in synoptic forcing of net precipitation in large Arctic river basins during the 21st century, *Journal of Geophysical Research: Biogeosciences* 112.G4. DOI: `10.1029/2006JG000332`.

Cassou, C. (2008), Intraseasonal interaction between the Madden–Julian Oscillation and the North Atlantic Oscillation, *Nature* 455.7212, 523–527. DOI: `10.1038/nature07286`.

Cattiaux, J., Vautard, R., Cassou, C., Yiou, P., Masson-Delmotte, V., and Codron, F. (2010), Winter 2010 in Europe: A cold extreme in a warming climate, *Geophysical Research Letters* 37.20. DOI: 10.1029/2010GL044613.

Cattiaux, J., Douville, H., and Peings, Y. (2013), European temperatures in CMIP5: origins of present-day biases and future uncertainties, *Climate Dynamics* 41.11, 2889–2907. DOI: 10.1007/s00382-013-1731-y.

Ceppi, P. and Nowack, P. (2021), Observational evidence that cloud feedback amplifies global warming, *Proceedings of the National Academy of Sciences* 118.30. DOI: 10.1073/pnas.2026290118.

Charney, J. G. (1947), THE DYNAMICS OF LONG WAVES IN A BAROCLINIC WESTERLY CURRENT, *Journal of Atmospheric Sciences* 4.5, 136–162. DOI: 10.1175/1520-0469(1947)004<0136:TDOLWI>2.0.CO;2.

Charney, J. G. (1963), A Note on Large-Scale Motions in the Tropics, *Journal of Atmospheric Sciences* 20.6, 607–609. DOI: 10.1175/1520-0469(1963)020<0607:ANOLSM>2.0.CO;2.

Chen, G., Lu, J., Burrows, D. A., and Leung, L. R. (2015), Local finite-amplitude wave activity as an objective diagnostic of midlatitude extreme weather, *Geophysical Research Letters* 42.24, 10, 952–10, 960. DOI: 10.1002/2015GL066959.

Chen, Y., Moufouma-Okia, W., Masson-Delmotte, V., Zhai, P., and Pirani, A. (2018), Recent Progress and Emerging Topics on Weather and Climate Extremes Since the Fifth Assessment Report of the Intergovernmental Panel on Climate Change, *Annual Review of Environment and Resources* 43.1, 35–59. DOI: 10.1146/annurev-environ-102017-030052.

Chou, C., Wu, T.-C., and Tan, P.-H. (2013), Changes in gross moist stability in the tropics under global warming, *Climate Dynamics* 41.9, 2481–2496. DOI: 10.1007/s00382-013-1703-2.

Christidis, N., Jones, G., and Stott, P. (2014), Dramatically increasing chance of extremely hot summers since the 2003 European heatwave, *Nature Climate Change* 5, 46–50. DOI: 10.1038/nclimate2468.

Ciais, P., Reichstein, M., Viovy, N., Granier, A., Ogée, J., Allard, V., Aubinet, M., Buchmann, N., Bernhofer, C., Carrara, A., Chevallier, F., De Noblet, N., Friend, A. D., Friedlingstein, P., Grünwald, T., Heinesch, B., Keronen, P., Knohl, A., Krinner, G., Loustau, D., Manca, G., Matteucci, G., Miglietta, F., Ourcival, J. M., Papale, D., Pilegaard, K., Rambal, S., Seufert, G., Soussana, J. F., Sanz, M. J., Schulze, E. D., Vesala, T., and Valentini, R. (2005), Europe-wide reduction in primary productivity caused by the heat and drought in 2003, *Nature* 437.7058, 529–533. DOI: 10.1038/nature03972.

Cloutier-Bisbee, S. R., Raghavendra, A., and Milrad, S. M. (2019), Heat Waves in Florida: Climatology, Trends, and Related Precipitation Events, *Journal of Applied Meteorology and Climatology* 58.3, 447–466. DOI: 10.1175/JAMC-D-18-0165.1.

Cohen, J., Zhang, X., Francis, J., Jung, T., Kwok, R., Overland, J., Ballinger, T. J., Bhatt, U. S., Chen, H. W., Coumou, D., Feldstein, S., Gu, H., Handorf, D., Henderson, G., Ionita, M., Kretschmer, M., Laliberte, F., Lee, S., Linderholm, H. W., Maslowski, W., Peings, Y., Pfeiffer, K., Rigor, I., Semmler, T., Stroeve, J., Taylor, P. C., Vavrus, S., Vihma, T., Wang, S., Wendisch, M., Wu, Y., and Yoon, J. (2020), Divergent consensuses on Arctic amplification influence on midlatitude severe winter weather, *Nature Climate Change* 10.1, 20–29. DOI: 10.1038/s41558-019-0662-y.

Cohen, J. and Barlow, M. (2005), The NAO, the AO, and global warming: how closely related?, *Journal of Climate* 18.21, 4498–4513.

Cohen, J., Jones, J., Furtado, J. C., and Tziperman, E. (2013), Warm Arctic, cold continents: A common pattern related to Arctic sea ice melt, snow advance, and extreme winter weather, *Oceanography* 26.4, 150–160.

Coumou, D., Di Capua, G., Vavrus, S., Wang, L., and Wang, S. (2018a), The influence of Arctic amplification on mid-latitude summer circulation, *Nature Communications* 9.1, 2959. DOI: 10.1038/s41467-018-05256-8.

Coumou, D., Di Capua, G., Vavrus, S., Wang, L., and Wang, S. (2018b), The influence of Arctic amplification on mid-latitude summer circulation, *Nature Communications* 9.1, 2959. DOI: 10.1038/s41467-018-05256-8.

Coumou, D., Lehmann, J., and Beckmann, J. (2015), The weakening summer circulation in the Northern Hemisphere mid-latitudes, *Science* 348.6232, 324–327. DOI: 10.1126/science.1261768.

Coumou, D., Petoukhov, V., Rahmstorf, S., Petri, S., and Schellnhuber, H. J. (2014), Quasi-resonant circulation regimes and hemispheric synchronization of extreme weather in boreal summer, *Proceedings of the National Academy of Sciences* 111.34, 12331–12336. DOI: 10.1073/pnas.1412797111.

Coumou, D., Robinson, A., and Rahmstorf, S. (2013), Global increase in record-breaking monthly-mean temperatures, *Climatic Change* 118.3, 771–782. DOI: 10.1007/s10584-012-0668-1.

Cox, P. M., Huntingford, C., and Williamson, M. S. (2018), Emergent constraint on equilibrium climate sensitivity from global temperature variability, *Nature* 553.7688, 319–322. DOI: 10.1038/nature25450.

Cox, P. M., Pearson, D., Booth, B. B., Friedlingstein, P., Huntingford, C., Jones, C. D., and Luke, C. M. (2013), Sensitivity of tropical carbon to climate change constrained by carbon dioxide variability, *Nature* 494.7437, 341–344. DOI: 10.1038/nature11882.

Croci-Maspoli, M., Schwierz, C., and Davies, H. C. (2007), A Multifaceted Climatology of Atmospheric Blocking and Its Recent Linear Trend, *Journal of Climate* 20.4, 633–649. DOI: 10.1175/JCLI4029.1.

Crum, F. X. and Stevens, D. F. (1988), A Case Study of Atmospheric Blocking Using Isentropic Analysis, *Monthly Weather Review* 116.1, 223–241. DOI: 10.1175/1520-0493(1988)116<0223:ACSOAB>2.0.CO;2.

Cutter, S., Osman-Elasha, B., Campbell, J., Cheong, S. M., McCormick, S., Pulwarty, R., Supratid, S., Ziervogel, G., Calvo, E., Mutabazi, K., Arnall, A., Arnold, M., Bayer, J. L., Bohle, H. G., Emrich, C., Hallegatte, S., Koelle, B., Oettle, N., Polack, E., Ranger, N., and Rist, S. (2012), Managing the Risks from Climate Extremes at the Local Level. In: *Managing the Risks of Extreme Events and Disasters to Advance Climate Change Adaptation*. Special Report of the Intergovernmental Panel on Climate Change. Cambridge: Cambridge University Press, 291–338.

Dai, A., Luo, D., Song, M., and Liu, J. (2019), Arctic amplification is caused by sea-ice loss under increasing CO2, *Nature Communications* 10.1, 121. DOI: 10.1038/s41467-018-07954-9.

Dai, A. and Song, M. (2020), Little influence of Arctic amplification on mid-latitude climate, *Nature Climate Change* 10.3, 231–237. DOI: 10.1038/s41558-020-0694-3.

Davini, P., Cagnazzo, C., Gualdi, S., and Navarra, A. (2012), Bidimensional Diagnostics, Variability, and Trends of Northern Hemisphere Blocking, *Journal of Climate* 25.19, 6496–6509. DOI: 10.1175/JCLI-D-12-00032.1.

Davini, P. and D'Andrea, F. (2016), Northern Hemisphere Atmospheric Blocking Representation in Global Climate Models: Twenty Years of Improvements?, *Journal of Climate* 29.24, 8823–8840. DOI: 10.1175/JCLI-D-16-0242.1.

Davini, P. and D'Andrea, F. (2020), From CMIP3 to CMIP6: Northern Hemisphere Atmospheric Blocking Simulation in Present and Future Climate, *Journal of Climate* 33.23, 10021–10038. DOI: 10.1175/JCLI-D-19-0862.1.

Dawson, A., Palmer, T. N., and Corti, S. (2012), Simulating regime structures in weather and climate prediction models, *Geophysical Research Letters* 39.21. DOI: https://doi.org/10.1029/2012GL053284.

Day, J. J., Sandu, I., Magnusson, L., Rodwell, M. J., Lawrence, H., Bormann, N., and Jung, T. (2019), Increased Arctic influence on the midlatitude flow during Scandinavian Blocking episodes, *Quarterly Journal of the Royal Meteorological Society* 145.725, 3846–3862. DOI: https://doi.org/10.1002/qj.3673.

Delhasse, A., Hanna, E., Kittel, C., and Fettweis, X. (2021), Brief communication: CMIP6 does not suggest any atmospheric blocking increase in summer over Greenland by 2100, *International Journal of Climatology* 41.4, 2589–2596. DOI: 10.1002/joc.6977.

Deser, C., Magnusdottir, G., Saravanan, R., and Phillips, A. (2004), The effects of North Atlantic SST and sea ice anomalies on the winter circulation in CCM3. Part II: Direct and indirect components of the response, *Journal of Climate* 17.5, 877–889.

Deser, C., Phillips, A., Bourdette, V., and Teng, H. (2012), Uncertainty in climate change projections: the role of internal variability, *Climate Dynamics* 38.3, 527–546. DOI: 10.1007/s00382-010-0977-x.

Diday, E. and Simon, J. C. (1980), Clustering Analysis. In: *Digital Pattern Recognition*. Ed. by K. S. Fu. Berlin, Heidelberg: Springer Berlin Heidelberg, 47–94. DOI: 10.1007/978-3-642-67740-3_3.

Diffenbaugh, N. S., Singh, D., Mankin, J. S., Horton, D. E., Swain, D. L., Touma, D., Charland, A., Liu, Y., Haugen, M., Tsiang, M., and Rajaratnam, B. (2017), Quantifying the influence of global warming on unprecedented extreme climate events, *Proceedings of the National Academy of Sciences* 114.19, 4881–4886. DOI: 10.1073/pnas.1618082114.

Ding, Q. and Wang, B. (2005), Circumglobal Teleconnection in the Northern Hemisphere Summer, *Journal of Climate* 18.17, 3483–3505. DOI: 10.1175/JCLI3473.1.

Dole, R. M. and Gordon, N. D. (1983), Persistent Anomalies of the Extratropical Northern Hemisphere Wintertime Circulation: Geographical Distribution and Regional Persistence Characteristics, *Monthly Weather Review* 111.8, 1567–1586.

Dole, R. M., Hoerling, M. P., Perlwitz, J., Eischeid, J. K., Pegion, P. J., Zhang, T., Quan, X., Xu, T., and Murray, D. (2011), Was there a basis for anticipating the 2010 Russian heat wave?, *Geophysical Research Letters* 38.

Drouard, M. and Woollings, T. (2018), Contrasting Mechanisms of Summer Blocking Over Western Eurasia, *Geophysical Research Letters* 45.21, 12, 040–12, 048. DOI: https://doi.org/10.1029/2018GL079894.

Dunn-Sigouin, E., Son, S.-W., and Lin, H. (2013), Evaluation of Northern Hemisphere Blocking Climatology in the Global Environment Multiscale Model, *Monthly Weather Review* 141.2, 707–727. DOI: 10.1175/MWR-D-12-00134.1.

E., O. J., R., W. K., and Muyin, W. (2011), Warm Arctic - cold continents: climate impacts of the newly open Arctic Sea, *Polar Research*. DOI: 10.3402/polar.v30i0.15787.

Eady, E. T. (1949), Long Waves and Cyclone Waves, *Tellus* 1.3, 33–52. DOI: https://doi.org/10.1111/j.2153-3490.1949.tb01265.x.

Elliot, R. and Smith, T. (1949), A study of the effect of large blocking highs on the general circulation in the northern hemisphere westerlies, *J Meteor* 6, 67–85.

Ertel, H. (1942), Ein neuer hydrodynamischer Wirbelsatz, *Meteorol. Z.* 59.9, 277–281.

Eyring, V., Bony, S., Meehl, G. A., Senior, C. A., Stevens, B., Stouffer, R. J., and Taylor, K. E. (2016), Overview of the Coupled Model Intercomparison Project Phase 6 (CMIP6) experimental design and organization, *Geoscientific Model Development* 9.5, 1937–1958. DOI: 10.5194/gmd-9-1937-2016.

Fabiano, F., Christensen, H. M., Strommen, K., Athanasiadis, P., Baker, A., Schiemann, R., and Corti, S. (2020), Euro-Atlantic weather Regimes in the PRIMAVERA coupled climate simulations: impact of resolution and mean state biases on model performance, *Climate Dynamics* 54.11, 5031–5048. DOI: 10.1007/s00382-020-05271-w.

Fabiano, F., Meccia, V., Davini, P., Ghinassi, P., and Corti, S. (2021), A regime view of future atmospheric circulation changes in northern mid-latitudes, *Weather and Climate Dynamics* 2, 163–180. DOI: 10.5194/wcd-2-163-2021.

Fereday, D., Chadwick, R., Knight, J., and Scaife, A. A. (2018), Atmospheric Dynamics is the Largest Source of Uncertainty in Future Winter European Rainfall, *Journal of Climate* 31.3, 963–977. DOI: 10.1175/JCLI-D-17-0048.1.

Fernandez-Granja, J. A., Casanueva, A., Bedia, J., and Fernandez, J. (2021), Improved atmospheric circulation over Europe by the new generation of CMIP6 earth system models, *Climate Dynamics* 56.11, 3527–3540. DOI: 10.1007/s00382-021-05652-9.

Ferranti, L., Corti, S., and Janousek, M. (2015), Flow-dependent verification of the ECMWF ensemble over the Euro-Atlantic sector, *Quarterly Journal of the Royal Meteorological Society* 141.688, 916–924. DOI: https://doi.org/10.1002/qj.2411.

Fischer, E. M. and Knutti, R. (2015), Anthropogenic contribution to global occurrence of heavy-precipitation and high-temperature extremes, *Nature Climate Change* 5, 560–564.

Fogt, R. L. and Marshall, G. J. (2020), The Southern Annular Mode: Variability, trends, and climate impacts across the Southern Hemisphere, *WIREs Climate Change* 11.4, e652. DOI: https://doi.org/10.1002/wcc.652.

Folland, C. K., Boucher, O., Colman, A., and Parker, D. E. (2018), Causes of irregularities in trends of global mean surface temperature since the late 19th century, *Science Advances* 4.6. DOI: 10.1126/sciadv.aao5297.

Francis, J. A., Skific, N., and Vavrus, S. J. (2018), North American Weather Regimes Are Becoming More Persistent: Is Arctic Amplification a Factor?, *Geophysical Research Letters* 45.20, 11, 414–11, 422. DOI: https://doi.org/10.1029/2018GL080252.

Francis, J. A. and Vavrus, S. J. (2012), Evidence linking Arctic amplification to extreme weather in mid-latitudes, *Geophysical Research Letters* 39.6. DOI: 10.1029/2012GL051000.

Francis and Vavrus (2015), Evidence for a wavier jet stream in response to rapid Arctic warming, *Environmental Research Letters* 10.1, 014005. DOI: 10.1088/1748-9326/10/1/014005.

Fuentes-Franco, R., Koenigk, T., Docquier, D., Graef, F., and Wyser, K. (2022), Exploring the influence of the North Pacific Rossby wave sources on the variability of summer atmospheric circulation and precipitation over the Northern Hemisphere, *Climate Dynamics*. DOI: 10.1007/s00382-022-06194-4.

Gabriel, A. and Peters, D. H. W. (2008), A Diagnostic Study of Different Types of Rossby Wave Breaking Events in the Northern Extratropics, *Journal of the Meteorological Society of Japan* 86, 613–631.

García-Herrera, R., Díaz, J., Trigo, R. M., Luterbacher, J., and Fischer, E. M. (2010), A Review of the European Summer Heat Wave of 2003, *Critical Reviews in Environmental Science and Technology* 40.4, 267–306. DOI: 10.1080/10643380802238137.

García-León, D., Casanueva, A., Standardi, G., Burgstall, A., Flouris, A. D., and Nybo, L. (2021), Current and projected regional economic impacts of heatwaves in Europe, *Nature Communications* 12.1, 5807. DOI: 10.1038/s41467-021-26050-z.

Garfinkel, C. I., Son, S.-W., Song, K., Aquila, V., and Oman, L. D. (2017), Stratospheric variability contributed to and sustained the recent hiatus in Eurasian winter warming, *Geophysical Research Letters* 44.1, 374–382. DOI: https://doi.org/10.1002/2016GL072035.

Garriott, E. (1904), Long range forecasts, *US Weather Bureau Bulletin* 35.

Gibson, P., Pitman, A., Lorenz, R., and Perkins-Kirkpatrick, S. (2017a), The Role of Circulation and Land Surface Conditions in Current and Future Australian Heat Waves, *Journal of Climate* 30. DOI: 10.1175/JCLI-D-17-0265.1.

Gibson, P. B., Pitman, A. J., Lorenz, R., and Perkins-Kirkpatrick, S. E. (2017b), The Role of Circulation and Land Surface Conditions in Current and Future Australian Heat Waves, *Journal of Climate* 30.24, 9933–9948. DOI: 10.1175/JCLI-D-17-0265.1.

Gil, Y., Pierce, S. A., Babaie, H., Banerjee, A., Borne, K., Bust, G., Cheatham, M., Ebert-Uphoff, I., Gomes, C., Hill, M., et al. (2018), Intelligent systems for geosciences: an essential research agenda, *Communications of the ACM* 62.1, 76–84.

Glickman, T. S. and Zenk, W. (2000), *Glossary of meteorology.* AMS (American Meteorological Society).

Gregory, J. M., Ingram, W. J., Palmer, M. A., Jones, G. S., Stott, P. A., Thorpe, R. B., Lowe, J. A., Johns, T. C., and Williams, K. D. (2004), A new method for diagnosing radiative forcing and climate sensitivity, *Geophysical Research Letters* 31.3. DOI: https://doi.org/10.1029/2003GL018747.

Grotjahn, R. and Zhang, R. (2017), Synoptic Analysis of Cold Air Outbreaks over the California Central Valley, *Journal of Climate* 30.23, 9417–9433. DOI: 10.1175/JCLI-D-17-0167.1.

Ha, K.-J., Seo, Y.-W., Lee, J.-Y., Kripalani, R. H., and Yun, K.-S. (2018), Linkages between the South and East Asian summer monsoons: a review and revisit, *Climate Dynamics* 51.11, 4207–4227. DOI: 10.1007/s00382-017-3773-z.

Hall, A., Cox, P., Huntingford, C., and Klein, S. (2019), Progressing emergent constraints on future climate change, *Nature Climate Change* 9.4, 269–278. DOI: 10.1038/s41558-019-0436-6.

Hall, A. and Qu, X. (2006), Using the current seasonal cycle to constrain snow albedo feedback in future climate change, *Geophysical Research Letters* 33.3. DOI: https://doi.org/10.1029/2005GL025127.

Hannachi, A., Straus, D. M., Franzke, C. L. E., Corti, S., and Woollings, T. (2017), Low-frequency nonlinearity and regime behavior in the Northern Hemisphere extratropical atmosphere, *Reviews of Geophysics* 55.1, 199–234. DOI: https://doi.org/10.1002/2015RG000509.

Hartigan, J. A. and Wong, M. A. (1979), Algorithm AS 136: A K-Means Clustering Algorithm, *Journal of the Royal Statistical Society. Series C (Applied Statistics)* 28.1, 100–108. DOI: 10.2307/2346830.

Harvey, B. J., Shaffrey, L. C., and Woollings, T. J. (2014), Equator-to-pole temperature differences and the extra-tropical storm track responses of the CMIP5 climate models, *Climate Dynamics* 43.5, 1171–1182. DOI: 10.1007/s00382-013-1883-9.

Hassanzadeh, P., Kuang, Z., and Farrell, B. F. (2014), Responses of midlatitude blocks and wave amplitude to changes in the meridional temperature gradient in an idealized dry

GCM, *Geophysical Research Letters* 41.14, 5223–5232. DOI: https://doi.org/10.1002/2014GL060764.

Hauser, S., Teubler, F., Riemer, M., Knippertz, P., and Grams, C. (2022), Towards a diagnostic framework unifying different perspectives on blocking dynamics: insight into a major blocking in the North Atlantic-European region. DOI: 10.5194/wcd-2022-44.

Hawkins, E. and Sutton, R. (2009), The Potential to Narrow Uncertainty in Regional Climate Predictions, *Bulletin of the American Meteorological Society* 90.8, 1095–1108. DOI: 10.1175/2009BAMS2607.1.

Held, I. M. (1993), Large-Scale Dynamics and Global Warming, *Bulletin of the American Meteorological Society* 74.2, 228–242. DOI: 10.1175/1520-0477(1993)074<0228:LSDAGW>2.0.CO;2.

Held, I. M. and Soden, B. J. (2006), Robust Responses of the Hydrological Cycle to Global Warming, *Journal of Climate* 19.21, 5686–5699. DOI: 10.1175/JCLI3990.1.

Hersbach, H., Bell, B., Berrisford, P., Hirahara, S., Horányi, A., Muñoz-Sabater, J., Nicolas, J., Peubey, C., Radu, R., Schepers, D., Simmons, A., Soci, C., Abdalla, S., Abellan, X., Balsamo, G., Bechtold, P., Biavati, G., Bidlot, J., Bonavita, M., De Chiara, G., Dahlgren, P., Dee, D., Diamantakis, M., Dragani, R., Flemming, J., Forbes, R., Fuentes, M., Geer, A., Haimberger, L., Healy, S., Hogan, R. J., Hólm, E., Janisková, M., Keeley, S., Laloyaux, P., Lopez, P., Lupu, C., Radnoti, G., Rosnay, P. de, Rozum, I., Vamborg, F., Villaume, S., and Thépaut, J.-N. (2020), The ERA5 global reanalysis, *Quarterly Journal of the Royal Meteorological Society* 146.730, 1999–2049. DOI: https://doi.org/10.1002/qj.3803.

Hewitson, B. and Crane, R. (2002), Self-Organizing Maps: Applications to synoptic climatology, *Climate Research* 22, 13–26. DOI: 10.3354/cr022013.

Higgins, M. E. and Cassano, J. J. (2009), Impacts of reduced sea ice on winter Arctic atmospheric circulation, precipitation, and temperature, *Journal of Geophysical Research: Atmospheres* 114.D16. DOI: https://doi.org/10.1029/2009JD011884.

Honda, M., Inoue, J., and Yamane, S. (2009), Influence of low Arctic sea-ice minima on anomalously cold Eurasian winters, *Geophysical Research Letters* 36.8. DOI: https://doi.org/10.1029/2008GL037079.

Hopsch, S., Cohen, J., and Dethloff, K. (2012), Analysis of a link between fall Arctic sea ice concentration and atmospheric patterns in the following winter, *Tellus A: Dynamic Meteorology and Oceanography*. DOI: 10.3402/tellusa.v64i0.18624.

Horton, D. E., Johnson, N. C., Singh, D., Swain, D. L., Rajaratnam, B., and Diffenbaugh, N. S. (2015), Contribution of changes in atmospheric circulation patterns to extreme temperature trends, *Nature* 522, 465–468. DOI: 10.1038/nature14550.

Hoskins, B. J., McIntyre, M. E., and Robertson, A. W. (1985), On the use and significance of isentropic potential vorticity maps, *Quarterly Journal of the Royal Meteorological Society* 111.470, 877–946. DOI: 10.1002/qj.49711147002.

Hoskins, B. J. and James, I. N. (2014a), *Fluid dynamics of the mid-latitude atmosphere*. John Wiley & Sons. Chap. 17.5.

Hoskins, B. J. and Ambrizzi, T. (1993), Rossby Wave Propagation on a Realistic Longitudinally Varying Flow, *Journal of Atmospheric Sciences* 50.12, 1661–1671. DOI: 10.1175/1520-0469(1993)050<1661:RWPOAR>2.0.CO;2.

Hoskins, B. J. and James, I. N. (2014b), Potential vorticity. In: *Fluid Dynamics of the Midlatitude Atmosphere*. John Wiley & Sons, Ltd. Chap. 10, 177–186. DOI: https://doi.org/10.1002/9781118526002.ch18.

Hoskins, B. J. and Karoly, D. J. (1981), The Steady Linear Response of a Spherical Atmosphere to Thermal and Orographic Forcing, *Journal of the Atmospheric Sciences* 38, 1179–1196.

Houze, R. A. (2014), Chapter 11 - Clouds and Precipitation in Extratropical Cyclones. In: *Cloud Dynamics*. Ed. by R. A. Houze. Vol. 104. International Geophysics. Academic Press, 329–367. DOI: https://doi.org/10.1016/B978-0-12-374266-7.00011-1.

Huang, C. S. Y. and Nakamura, N. (2015), Local Finite-Amplitude Wave Activity as a Diagnostic of Anomalous Weather Events, *Journal of the Atmospheric Sciences* 73.1, 211–229. DOI: 10.1175/JAS-D-15-0194.1.

Huguenin, M. F., Fischer, E. M., Kotlarski, S., Scherrer, S. C., Schwierz, C., and Knutti, R. (2020), Lack of Change in the Projected Frequency and Persistence of Atmospheric Circulation Types Over Central Europe, *Geophysical Research Letters* 47.9. e2019GL086132 2019GL086132, e2019GL086132. DOI: https://doi.org/10.1029/2019GL086132.

Huth, R., Beck, C., Philipp, A., Demuzere, M., Ustrnul, Z., Cahynová, M., Kyselý, J., and Tveito, O. E. (2008), Classifications of atmospheric circulation patterns: recent advances and applications. *Annals of the New York Academy of Sciences* 1146, 105–52.

Illari, L. (1984), A diagnostic study of the potential vorticity in a warm blocking anticyclone, *J. Atmos. Sci.* 41, 3518–3526.

Inoue, J., Hori, M. E., and Takaya, K. (2012), The Role of Barents Sea Ice in the Wintertime Cyclone Track and Emergence of a Warm-Arctic Cold-Siberian Anomaly, *Journal of Climate* 25.7, 2561–2568. DOI: https://doi.org/10.1175/JCLI-D-11-00449.1.

Jézéquel, A., Cattiaux, J., Naveau, P., Radanovics, S., Ribes, A., Vautard, R., Vrac, M., and Yiou, P. (2018), Trends of atmospheric circulation during singular hot days in Europe, *Environmental Research Letters* 13.5, 054007. DOI: 10.1088/1748-9326/aab5da.

Jézéquel, A., Yiou, P., and Radanovics, S. (2017), Role of circulation in European heatwaves using flow analogues, *Climate Dynamics*. DOI: 10.1007/s00382-017-3667-0.

Jin, F. and Hoskins, B. J. (1995), The Direct Response to Tropical Heating in a Baroclinic Atmosphere, *Journal of Atmospheric Sciences* 52.3, 307–319. DOI: 10.1175/1520-0469(1995)052<0307:TDRTTH>2.0.CO;2.

Johnson, N. (2013), How many ENSO flavors can we distinguish?, *Journal of Climate* 26, 4816–4827. DOI: 10.1175/JCLI-D-12-00649.1.

Juliano, T. W. and Lebo, Z. J. (2020), Linking large-scale circulation patterns to low-cloud properties, *Atmospheric Chemistry and Physics* 20.12, 7125–7138. DOI: 10.5194/acp-20-7125-2020.

Jung, T. (2012), High-resolution global climate simulations with the ECMWF model in Project Athena: Experimental design, model climate, and seasonal forecast skill, *J. Climate* 25, 3155–3172.

Kageyama, M., D'Andrea, F., Ramstein, G., Valdes, P. J., and Vautard, R. (1999), Weather regimes in past climate atmospheric general circulation model simulations, *Climate Dynamics* 15.10, 773–793. DOI: 10.1007/s003820050315.

Kanamitsu, M., Ebisuzaki, W., Woollen, J., Yang, S.-K., Hnilo, J. J., Fiorino, M., and Potter, G. L. (2002), NCEP–DOE AMIP-II Reanalysis (R-2), *Bulletin of the American Meteorological Society* 83.11, 1631–1644. DOI: 10.1175/BAMS-83-11-1631.

Karpatne, A., Ebert-Uphoff, I., Ravela, S., Babaie, H. A., and Kumar, V. (2018), Machine learning for the geosciences: Challenges and opportunities, *IEEE Transactions on Knowledge and Data Engineering* 31.8, 1544–1554.

Kennedy, D., Parker, T., Woollings, T., Harvey, B., and Shaffrey, L. (2016), The response of high-impact blocking weather systems to climate change, *Geophysical Research Letters* 43.13, 7250–7258.

Kidston, J., Scaife, A. A., Hardiman, S. C., Mitchell, D. M., Butchart, N., Baldwin, M. P., and Gray, L. J. (2015), Stratospheric influence on tropospheric jet streams, storm tracks and surface weather, *Nature Geoscience* 8.6, 433–440.

Kim, B.-M., Son, S.-W., Min, S.-K., Jeong, J.-H., Kim, S.-J., Zhang, X., Shim, T., and Yoon, J.-H. (2014), Weakening of the stratospheric polar vortex by Arctic sea-ice loss, *Nature Communications* 5.1, 4646. DOI: 10.1038/ncomms5646.

King, D., Schrag, D., Dadi, Z., Ye, Q., Ghosh, A., Hynard, J., and Rodger, T. (2015), *Climate change: a risk assessment.*

Knox, J. L. and Hay, J. E. (1984), Blocking signatures in the Northern Hemisphere: Rationale and identification, *Journal of Climatology* 22, 36–47.

Knutti, R., Furrer, R., Tebaldi, C., Cermak, J., and Meehl, G. A. (2010), Challenges in Combining Projections from Multiple Climate Models, *Journal of Climate* 23.10, 2739–2758. DOI: 10.1175/2009JCLI3361.1.

Kohonen, T. (1982), Self-organized formation of topologically correct feature maps, *Biological Cybernetics* 43.1, 59–69. DOI: 10.1007/BF00337288.

Kornhuber, K., Coumou, D., Vogel, E., Lesk, C., Donges, J. F., Lehmann, J., and Horton, R. M. (2020), Amplified Rossby waves enhance risk of concurrent heatwaves in major breadbasket regions, *Nature Climate Change* 10.1, 48–53. DOI: 10.1038/s41558-019-0637-z.

Kornhuber, K., Osprey, S., Coumou, D., Petri, S., Petoukhov, V., Rahmstorf, S., and Gray, L. (2019), Extreme weather events in early summer 2018 connected by a recurrent hemispheric wave-7 pattern, *Environmental Research Letters* 14.5, 054002. DOI: 10.1088/1748-9326/ab13bf.

Kueh, M.-T. and Lin, C.-Y. (2020), The 2018 summer heatwaves over northwestern Europe and its extended-range prediction, *Scientific Reports* 10.1, 19283. DOI: 10.1038/s41598-020-76181-4.

Lary, D. J., Alavi, A. H., Gandomi, A. H., and Walker, A. L. (2016), Machine learning in geosciences and remote sensing, *Geoscience Frontiers* 7.1. Special Issue: Progress of Machine Learning in Geosciences, 3–10. DOI: https://doi.org/10.1016/j.gsf.2015.07.003.

Lee, S. and Kim, H.-K. (2003), The Dynamical Relationship between Subtropical and Eddy-Driven Jets, *Journal of the Atmospheric Sciences* 60.12, 1490–1503. DOI: 10.1175/1520-0469(2003)060<1490:TDRBSA>2.0.CO;2.

Lejenäs, H. and Økland, H. (1983), Characteristics of northern hemisphere blocking as determined from a long time series of observational data, *Tellus A* 35A.5, 350–362. DOI: 10.1111/j.1600-0870.1983.tb00210.x.

Lester, H., Gallagher, J., and Kell, G. (1984), NBS/NRC steam tables: thermodynamic and transport properties and computer programs for vapor and liquid states of water in SI units.

Levine, X. and Schneider, T. (2015), Baroclinic Eddies and the Extent of the Hadley Circulation: An Idealized GCM Study, *Journal of the Atmospheric Sciences* 72, 2741–2761. DOI: 10.1175/JAS-D-14-0152.1.

Li, C., Storch, J.-S. von, and Marotzke, J. (2013), Deep-ocean heat uptake and equilibrium climate response, *Climate Dynamics* 40.5, 1071–1086. DOI: 10.1007/s00382-012-1350-z.

Liang, Y.-C., Polvani, L. M., and Mitevski, I. (2022), Arctic amplification, and its seasonal migration, over a wide range of abrupt CO2 forcing, *npj Climate and Atmospheric Science* 5.1, 14. DOI: 10.1038/s41612-022-00228-8.

Liniger, M. A. and Davies, H. C. (2004), Seasonal differences in extratropical potential vorticity variability at tropopause levels, *Journal of Geophysical Research: Atmospheres* 109.D17. DOI: https://doi.org/10.1029/2004JD004639.

Liu, J., Curry, J. A., Wang, H., Song, M., and Horton, R. M. (2012), Impact of declining Arctic sea ice on winter snowfall, *Proceedings of the National Academy of Sciences* 109.11, 4074–4079. DOI: 10.1073/pnas.1114910109.

Liu, Q. (1994), On the definition and persistence of blocking, *Tellus A* 46.3, 286–298. DOI: https://doi.org/10.1034/j.1600-0870.1994.t01-2-00004.x.

Liu, Y. and Weisberg, R. H. (2005), Patterns of ocean current variability on the West Florida Shelf using the self-organizing map, *Journal of Geophysical Research: Oceans* 110.C6. DOI: 10.1029/2004JC002786.

Lloyd, S. (1982), Least squares quantization in PCM, *IEEE Transactions on Information Theory* 28.2, 129–137. DOI: 10.1109/TIT.1982.1056489.

Loikith, P. C., Lintner, B. R., and Sweeney, A. (2017), Characterizing Large-Scale Meteorological Patterns and Associated Temperature and Precipitation Extremes over the Northwestern United States Using Self-Organizing Maps, *Journal of Climate* 30, 2829–2847.

Lupo, A. R. (2021), Atmospheric blocking events: a review, *Annals of the New York Academy of Sciences* 1504.1, 5–24. DOI: https://doi.org/10.1111/nyas.14557.

Ma, J., Chadwick, R., Seo, K.-H., Dong, C., Huang, G., Foltz, G. R., and Jiang, J. H. (2018), Responses of the Tropical Atmospheric Circulation to Climate Change and Connection to the Hydrological Cycle, *Annual Review of Earth and Planetary Sciences* 46.1, 549–580. DOI: 10.1146/annurev-earth-082517-010102.

Madsen, M. S., Langen, P. L., Boberg, F., and Christensen, J. H. (2017), Inflated Uncertainty in Multimodel-Based Regional Climate Projections, *Geophysical Research Letters* 44.22, 11, 606–11, 613. DOI: 10.1002/2017GL075627.

Malik, A., Nowack, P. J., Haigh, J. D., Cao, L., Atique, L., and Plancherel, Y. (2020), Tropical Pacific climate variability under solar geoengineering: impacts on ENSO extremes, *Atmospheric Chemistry and Physics* 20.23, 15461–15485. DOI: 10.5194/acp-20-15461-2020.

Manabe, S. and Wetherald, R. T. (1975), The Effects of Doubling the CO2 Concentration on the climate of a General Circulation Model, *Journal of Atmospheric Sciences* 32.1, 3–15. DOI: 10.1175/1520-0469(1975)032<0003:TEODTC>2.0.CO;2.

Mann, M. E., Rahmstorf, S., Kornhuber, K., Steinman, B. A., Miller, S. K., Petri, S., and Coumou, D. (2018), Projected changes in persistent extreme summer weather events: The role of quasi-resonant amplification, *Science Advances* 4.10. DOI: 10.1126/sciadv.aat3272.

Mansfield, D. (2007), The use of potential vorticity as an operational forecast tool, *Meteorological Applications* 3, 195–210. DOI: 10.1002/met.5060030301.

Mansfield, L. A., Nowack, P. J., Kasoar, M., Everitt, R. G., Collins, W. J., and Voulgarakis, A. (2020), Predicting global patterns of long-term climate change from short-term simulations using machine learning, *npj Climate and Atmospheric Science* 3.1, 44. DOI: 10.1038/s41612-020-00148-5.

Masato, G., Woollings, T., and Hoskins, B. (2014), Structure and impact of atmospheric blocking over the Euro-Atlantic region in present-day and future simulations, *Geophysical Research Letters* 41.3, 1051–1058. DOI: 10.1002/2013GL058570.

Masato, G., Hoskins, B. J., and Woollings, T. (2013), Winter and Summer Northern Hemisphere Blocking in CMIP5 Models, *Journal of Climate* 26.18, 7044–7059. DOI: 10.1175/JCLI-D-12-00466.1.

Matsueda, M. (2011), Predictability of Euro-Russian blocking in summer of 2010, *Geophysical Research Letters* 38.6. DOI: 10.1029/2010GL046557.

Matsueda, M., Mizuta, R., and Kusunoki, S. (2009), Future change in wintertime atmospheric blocking simulated using a 20-km-mesh atmospheric global circulation model, *Journal of Geophysical Research: Atmospheres* 114.D12. DOI: 10.1029/2009JD011919.

McCusker, K. E., Fyfe, J. C., and Sigmond, M. (2016), Twenty-five winters of unexpected Eurasian cooling unlikely due to Arctic sea-ice loss, *Nature Geoscience* 9.11, 838–842. DOI: 10.1038/ngeo2820.

Meehl, G. A., Senior, C. A., Eyring, V., Flato, G., Lamarque, J.-F., Stouffer, R. J., Taylor, K. E., and Schlund, M. (2020), Context for interpreting equilibrium climate sensitivity and transient climate response from the CMIP6 Earth system models, *Science Advances* 6.26. DOI: 10.1126/sciadv.aba1981.

Michelangeli, P.-A., Vautard, R., and Legras, B. (1995), Weather Regimes: Recurrence and Quasi Stationarity, *Journal of Atmospheric Sciences* 52.8, 1237–1256. DOI: 10.1175/1520-0469(1995)052<1237:WRRAQS>2.0.CO;2.

Mioduszewski, J. R., Rennermalm, A. K., Hammann, A., Tedesco, M., Noble, E. U., Stroeve, J. C., and Mote, T. L. (2016), Atmospheric drivers of Greenland surface melt revealed by self-organizing maps, *Journal of Geophysical Research: Atmospheres* 121.10, 5095–5114. DOI: https://doi.org/10.1002/2015JD024550.

Miralles, D., Teuling, A., Heerwaarden, C. van, and Arellano, J. (2014), Mega-heatwave temperatures due to combined soil desiccation and atmospheric heat accumulation, *Nature Geoscience* 7. DOI: 10.1038/ngeo2141.

Mitchell, D., Kornhuber, K., Huntingford, C., and Uhe, P. (2019), The day the 2003 European heatwave record was broken, *The Lancet Planetary Health* 3.7, e290–e292. DOI: 10.1016/s2542-5196(19)30106-8.

Mullen, S. L. (1987), Transient Eddy Forcing of Blocking Flows. *Journal of the Atmospheric Sciences* 44, 3–22.

Nakamura, H. and Wallace, J. M. (1993), Synoptic Behavior of Baroclinic Eddies during the Blocking Onset, *Monthly Weather Review* 121.7, 1892–1903. DOI: 10.1175/1520-0493(1993)121<1892:SBOBED>2.0.CO;2.

Nakamura, N. and Huang, C. S. Y. (2018), Atmospheric blocking as a traffic jam in the jet stream, *Science* 361.6397, 42–47. DOI: 10.1126/science.aat0721.

Nie, Y., Zhang, Y., Yang, X.-Q., and Ren, H.-L. (2019), Winter and Summer Rossby Wave Sources in the CMIP5 Models, *Earth and Space Science* 6.10, 1831–1846. DOI: https://doi.org/10.1029/2019EA000674.

Norris, J., Chen, G., and Neelin, J. D. (2019), Thermodynamic versus Dynamic Controls on Extreme Precipitation in a Warming Climate from the Community Earth System Model Large Ensemble, *Journal of Climate* 32.4, 1025–1045. DOI: 10.1175/JCLI-D-18-0302.1.

Nowack, P., Runge, J., Eyring, V., and Haigh, J. D. (2020), Causal networks for climate model evaluation and constrained projections, *Nature Communications* 11.1, 1415. DOI: 10.1038/s41467-020-15195-y.

Nowack, P. J., Abraham, N. L., Braesicke, P., and Pyle, J. A. (2018a), The Impact of Stratospheric Ozone Feedbacks on Climate Sensitivity Estimates, *Journal of Geophysical Research: Atmospheres* 123.9, 4630–4641. DOI: `https://doi.org/10.1002/2017JD027943`.

Nowack, P. J., Braesicke, P., Luke Abraham, N., and Pyle, J. A. (2017), On the role of ozone feedback in the ENSO amplitude response under global warming, *Geophysical Research Letters* 44.8, 3858–3866. DOI: `https://doi.org/10.1002/2016GL072418`.

Nowack, P., Braesicke, P., Haigh, J., Abraham, N., Pyle, J., and Voulgarakis, A. (2018b), Using machine learning to build temperature-based ozone parameterizations for climate sensitivity simulations, *Environmental Research Letters* 13.10, 104016. DOI: 10.1088/1748-9326/aae2be.

Orlanski, I. and Gross, B. (2000), The Life Cycle of Baroclinic Eddies in a Storm Track Environment, *Journal of the Atmospheric Sciences* 57.21, 3498–3513. DOI: 10.1175/1520-0469(2000)057<3498:TLCOBE>2.0.CO;2.

Oueslati, B., Yiou, P., and Jézéquel, A. (2019), Revisiting the dynamic and thermodynamic processes driving the record-breaking January 2014 precipitation in the southern UK, *Scientific Reports* 9.1, 2859. DOI: 10.1038/s41598-019-39306-y.

Overland, J., Francis, J. A., Hall, R., Hanna, E., Kim, S.-J., and Vihma, T. (2015), The Melting Arctic and Midlatitude Weather Patterns: Are They Connected?, *Journal of Climate* 28.20, 7917–7932. DOI: 10.1175/JCLI-D-14-00822.1.

Palmer, T. N. (1999), A Nonlinear Dynamical Perspective on Climate Prediction, *Journal of Climate* 12.2, 575–591. DOI: 10.1175/1520-0442(1999)012<0575:ANDPOC>2.0.CO;2.

Peings, Y., Cattiaux, J., Vavrus, S., and Magnusdottir, G. (2017), Late Twenty-First-Century Changes in the Midlatitude Atmospheric Circulation in the CESM Large Ensemble, *Journal of Climate* 30.15, 5943–5960. DOI: 10.1175/JCLI-D-16-0340.1.

Peings, Y., Cattiaux, J., and Magnusdottir, G. (2019), The Polar Stratosphere as an Arbiter of the Projected Tropical Versus Polar Tug of War, *Geophysical Research Letters* 46.15, 9261–9270. DOI: `https://doi.org/10.1029/2019GL082463`.

Pelly, J. L. and Hoskins, B. J. (2003), A New Perspective on Blocking, *Journal of the Atmospheric Sciences* 60.5, 743–755. DOI: 10.1175/1520-0469(2003)060<0743:ANPOB>2.0.CO;2.

Petoukhov, V., Rahmstorf, S., Petri, S., and Schellnhuber, H. (2013), Quasiresonant amplification of planetary waves and recent Northern Hemisphere weather extremes, *Proceedings of the National Academy of Sciences of the United States of America* 110. DOI: 10.1073/pnas.1222000110.

Petoukhov, V. and Semenov, V. A. (2010), A link between reduced Barents-Kara sea ice and cold winter extremes over northern continents, *Journal of Geophysical Research: Atmospheres* 115.D21. DOI: https://doi.org/10.1029/2009JD013568.

Philip, S., Kew, S., Van Oldenborgh, G. J., Anslow, F., Seneviratne, S., Vautard, R., Coumou, D., Ebi, K., Arrighi, J., Singh, R., Aalst, M., Pereira Marghidan, C., Wehner, M., Yang, W., Li, S., Schumacher, D., Hauser, M., Bonnet, R., Luu, L., and Otto, F. (2021), Rapid attribution analysis of the extraordinary heatwave on the Pacific Coast of the US and Canada June 2021. DOI: 10.5194/esd-2021-90.

Pierrehumbert, R. and Swanson, K. (1995), Baroclinic instability, *Annual review of fluid mechanics* 27.1, 419–467.

Pinheiro, M. C., Ullrich, P. A., and Grotjahn, R. (2019), Atmospheric blocking and intercomparison of objective detection methods: flow field characteristics, *Climate Dynamics*. DOI: 10.1007/s00382-019-04782-5.

Qu, X., Hall, A., DeAngelis, A. M., Zelinka, M. D., Klein, S. A., Su, H., Tian, B., and Zhai, C. (2018), On the Emergent Constraints of Climate Sensitivity, *Journal of Climate* 31.2, 863–875. DOI: 10.1175/JCLI-D-17-0482.1.

Quandt, L.-A., Keller, J. H., Martius, O., and Jones, S. C. (2017), Forecast Variability of the Blocking System over Russia in Summer 2010 and Its Impact on Surface Conditions, *Weather and Forecasting* 32.1, 61–82. DOI: 10.1175/WAF-D-16-0065.1.

Ramage, C. S. (1959), Hurricane Development, *Journal of Atmospheric Sciences* 16.3, 227–237. DOI: 10.1175/1520-0469(1959)016<0227:HD>2.0.CO;2.

Renwick, J. A. and Revell, M. J. (1999), Blocking over the South Pacific and Rossby Wave Propagation, *Monthly Weather Review* 127.10, 2233–2247. DOI: 10.1175/1520-0493(1999)127<2233:BOTSPA>2.0.CO;2.

Rex, D. F. (1950), Blocking Action in the Middle Troposphere and its Effect upon Regional Climate, *Tellus* 2.4, 275–301. DOI: 10.1111/j.2153-3490.1950.tb00339.x.

Riboldi, J., Lott, F., D'Andrea, F., and Rivière, G. (2020), On the Linkage Between Rossby Wave Phase Speed, Atmospheric Blocking, and Arctic Amplification, *Geophysical Research Letters* 47.19. DOI: https://doi.org/10.1029/2020GL087796.

Robine, J.-M., Cheung, S. L. K., Roy, S. L., Oyen, H. V., Griffiths, C., Michel, J.-P., and Herrmann, F. R. (2008), Death toll exceeded 70,000 in Europe during the summer of 2003, *Comptes Rendus Biologies* 331.2. Dossier : Nouveautés en cancérogenèse / New developments in carcinogenesis, 171–178. DOI: https://doi.org/10.1016/j.crvi.2007.12.001.

Robinson, W. A. (1989), On the structure of potential vorticity in baroclinic instability, *Tellus A: Dynamic Meteorology and Oceanography* 41.4, 275–284. DOI: 10.3402/tellusa.v41i4.11840.

Roebber, P. J. (2009), Visualizing Multiple Measures of Forecast Quality, *Weather and Forecasting* 24.2, 601–608. DOI: https://doi.org/10.1175/2008WAF2222159.1.

Rossby, C. G. (1940), Planetary flow patterns in the atmosphere, *Q. J. R. Meteorol. Soc.* 66, 68–87.

Rousi, E., Kornhuber, K., Beobide-Arsuaga, G., Luo, F., and Coumou, D. (2022), Accelerated western European heatwave trends linked to more-persistent double jets over Eurasia, *Nature Communications* 13.1, 3851. DOI: 10.1038/s41467-022-31432-y.

Rugenstein, M., Bloch-Johnson, J., Abe-Ouchi, A., Andrews, T., Beyerle, U., Cao, L., Chadha, T., Danabasoglu, G., Dufresne, J.-L., Duan, L., Foujols, M.-A., Frölicher, T., Geoffroy, O., Gregory, J., Knutti, R., Li, C., Marzocchi, A., Mauritsen, T., Menary, M., Moyer, E., Nazarenko, L., Paynter, D., Saint-Martin, D., Schmidt, G. A., Yamamoto, A., and Yang, S. (2019), LongRunMIP: Motivation and Design for a Large Collection of Millennial-Length AOGCM Simulations, *Bulletin of the American Meteorological Society* 100.12, 2551–2570. DOI: 10.1175/BAMS-D-19-0068.1.

Rypdal, M., Fredriksen, H.-B., Rypdal, K., and Steene, R. J. (2018), Emergent constraints on climate sensitivity, *Nature* 563.7729, E4–E5. DOI: 10.1038/s41586-018-0639-4.

Saffioti, C., Fischer, E. M., and Knutti, R. (2017), Improved Consistency of Climate Projections over Europe after Accounting for Atmospheric Circulation Variability, *Journal of Climate* 30.18, 7271–7291. DOI: 10.1175/JCLI-D-16-0695.1.

Sánchez-Benítez, A., Barriopedro, D., and García-Herrera, R. (2019), Tracking Iberian heatwaves from a new perspective, *Weather and Climate Extremes* 28, 100238. DOI: 10.1016/j.wace.2019.100238.

Sardeshmukh, P. D. and Hoskins, B. J. (1988), The Generation of Global Rotational Flow by Steady Idealized Tropical Divergence, *Journal of Atmospheric Sciences* 45.7, 1228–1251. DOI: 10.1175/1520-0469(1988)045<1228:TGOGRF>2.0.CO;2.

Scaife, A. and Knight, J. (2008), Ensemble simulations of the cold European winter of 2005-2006, *Quarterly Journal of the Royal Meteorological Society* 134.636, 1647–1659.

Scaife, A. A., Woollings, T., Knight, J., Martin, G., and Hinton, T. (2010), Atmospheric Blocking and Mean Biases in Climate Models, *Journal of Climate* 23.23, 6143–6152. DOI: 10.1175/2010JCLI3728.1.

Schalge, B., Blender, R., and Fraedrich, K. (2011), Blocking Detection Based on Synoptic Filters, *Advances in Meteorology* 2011, 717812. DOI: 10.1155/2011/717812.

Schaller, N., Sillmann, J., Anstey, J., Fischer, E. M., Grams, C. M., and Russo, S. (2018), Influence of blocking on Northern European and Western Russian heatwaves in large climate model ensembles, *Environmental Research Letters* 13.5, 054015. DOI: 10.1088/1748-9326/aaba55.

Scherrer, S., Croci-Maspoli, M., Schwierz, C., and Appenzeller, C. (2006), Two-dimensional indices of atmospheric blocking and their statistical relationship with winter climate patterns in the Euro-Atlantic region, *International Journal of Climatology* 26, 233–249. DOI: 10.1002/joc.1250.

Schiemann, R., Athanasiadis, P., Barriopedro, D., Doblas-Reyes, F., Lohmann, K., Roberts, M. J., Sein, D. V., Roberts, C. D., Terray, L., and Vidale, P. L. (2020), Northern Hemisphere blocking simulation in current climate models: evaluating progress from the Climate Model Intercomparison Project Phase 5 to 6 and sensitivity to resolution, *Weather and Climate Dynamics* 1.1, 277–292. DOI: 10.5194/wcd-1-277-2020.

Schlef, K. E., Moradkhani, H., and Lall, U. (2019), Atmospheric Circulation Patterns Associated with Extreme United States Floods Identified via Machine Learning, *Scientific Reports* 9.1, 7171. DOI: 10.1038/s41598-019-43496-w.

Schneidereit, A., Schubert, S., Vargin, P., Lunkeit, F., Zhu, X., Peters, D. H. W., and Fraedrich, K. (2012), Large-Scale Flow and the Long-Lasting Blocking High over Russia: Summer 2010, *Monthly Weather Review* 140.9, 2967–2981. DOI: 10.1175/MWR-D-11-00249.1.

Schubert, S., Wang, H., and Suárez, M. J. (2011), Warm Season Subseasonal Variability and Climate Extremes in the Northern Hemisphere: The Role of Stationary Rossby Waves, *Journal of Climate* 24, 4773–4792. DOI: 10.1175/JCLI-D-10-05035.1.

Schwierz, C., Croci-Maspoli, M., and Davies, H. C. (2004), Perspicacious indicators of atmospheric blocking, *Geophysical Research Letters* 31.6. DOI: https://doi.org/10.1029/2003GL019341.

Screen, J. A., Deser, C., Smith, D. M., Zhang, X., Blackport, R., Kushner, P. J., Oudar, T., McCusker, K. E., and Sun, L. (2018), Consistency and discrepancy in the atmospheric response toArctic sea-ice loss across climate models, *Nature Geoscience* 11.3, 155–163. DOI: 10.1038/s41561-018-0059-y.

Screen, J. A. and Simmonds, I. (2013), Exploring links between Arctic amplification and mid-latitude weather, *Geophysical Research Letters* 40.5, 959–964. DOI: https://doi.org/10.1002/grl.50174.

Sejas, S. A., Albert, O. S., Cai, M., and Deng, Y. (2014), Feedback attribution of the land-sea warming contrast in a global warming simulation of the NCAR CCSM4, *Environmental Research Letters* 9.12, 124005. DOI: 10.1088/1748-9326/9/12/124005.

Sellar, A. A., Jones, C. G., Mulcahy, J. P., Tang, Y., Yool, A., Wiltshire, A., O'Connor, F. M., Stringer, M., Hill, R., Palmieri, J., Woodward, S., Mora, L. de, Kuhlbrodt, T., Rumbold, S. T., Kelley, D. I., Ellis, R., Johnson, C. E., Walton, J., Abraham, N. L., Andrews, M. B., Andrews, T., Archibald, A. T., Berthou, S., Burke, E., Blockley, E., Carslaw, K., Dalvi, M., Edwards, J., Folberth, G. A., Gedney, N., Griffiths, P. T., Harper, A. B., Hendry, M. A., Hewitt, A. J., Johnson, B., Jones, A., Jones, C. D., Keeble, J., Liddicoat, S., Morgenstern, O., Parker, R. J., Predoi, V., Robertson, E., Siahaan, A., Smith, R. S., Swaminathan, R., Woodhouse, M. T., Zeng, G., and Zerroukat, M. (2019), UKESM1: Description and Evaluation of the U.K. Earth System Model, *Journal of Advances in Modeling Earth Systems* 11.12, 4513–4558. DOI: 10.1029/2019MS001739.

Shaw, T. A. (2019), Mechanisms of Future Predicted Changes in the Zonal Mean Mid-Latitude Circulation, *Current Climate Change Reports* 5.4, 345–357. DOI: 10.1007/s40641-019-00145-8.

Shepherd, T. G. (2014), Atmospheric circulation as a source of uncertainty in climate change projections, *Nature Geoscience* 7, 703–708.

Sheridan, S. C. and Lee, C. C. (2011), The self-organizing map in synoptic climatological research, *Progress in Physical Geography: Earth and Environment* 35.1, 109–119. DOI: 10.1177/0309133310397582.

Shukla, J. and Mo, K. C. (1983), Seasonal and Geographical Variation of Blocking, *Monthly Weather Review* 111.2, 388–402. DOI: 10.1175/1520-0493(1983)111<0388:SAGVOB>2.0.CO;2.

Shutts, G. J. (1983), The propagation of eddies in diffluent jetstreams: Eddy vorticity forcing of 'blocking' flow fields, *Quarterly Journal of the Royal Meteorological Society* 109.462, 737–761. DOI: https://doi.org/10.1002/qj.49710946204.

Simpson, I. R., Blackburn, M., and Haigh, J. D. (2009), The role of eddies in driving the tropospheric response to stratospheric heating perturbations, *Journal of the Atmospheric Sciences* 66.5, 1347–1365.

Singh, D., Swain, D. L., Mankin, J. S., Horton, D. E., Thomas, L. N., Rajaratnam, B., and Diffenbaugh, N. S. (2016), Recent amplification of the North American winter temperature dipole, *Journal of Geophysical Research: Atmospheres* 121.17, 9911–9928. DOI: 10.1002/2016JD025116.

Skific, N. and Francis, J. (2012), Self-Organizing Maps: A Powerful Tool for the Atmospheric Sciences. In: DOI: 10.5772/54299.

Skific, N., Francis, J. A., and Cassano, J. J. (2009), Attribution of Projected Changes in Atmospheric Moisture Transport in the Arctic: A Self-Organizing Map Perspective, *Journal of Climate* 22.15, 4135–4153. DOI: 10.1175/2009JCLI2645.1.

Small, D., Atallah, E., and Gyakum, J. R. (2013), An Objectively Determined Blocking Index and its Northern Hemisphere Climatology, *Journal of Climate* 27.8, 2948–2970. DOI: 10.1175/JCLI-D-13-00374.1.

Sousa, P. M., Barriopedro, D., García-Herrera, R., Woollings, T., and Trigo, R. M. (2021), A New Combined Detection Algorithm for Blocking and Subtropical Ridges, *Journal of Climate* 34.18, 7735–7758. DOI: 10.1175/JCLI-D-20-0658.1.

Starr, V. P. and Neiburger, M. (1940), Potential vorticity as a conservative property, *J. Marine Res.* 3, 202–210.

Stephens, G. L. and Ellis, T. D. (2008), Controls of Global-Mean Precipitation Increases in Global Warming GCM Experiments, *Journal of Climate* 21.23, 6141–6155. DOI: 10.1175/2008JCLI2144.1.

IPCC, 2013: Climate Change 2013: The Physical Science Basis. Contribution of Working Group I to the Fifth Assessment Report of the Intergovernmental Panel on Climate Change. (2013). In: ed. by T. Stocker, D. Qin, G.-K. Plattner, M. Tignor, S. Allen, J. Boschung, A. Nauels, Y. Xia, V. Bex, and P. Midgley.

Stott, P. A., Stone, D. A., and Allen, M. R. (2004), Human contribution to the European heatwave of 2003, *Nature* 432.7017, 610–614. DOI: 10.1038/nature03089.

Strommen, K., Mavilia, I., Corti, S., Matsueda, M., Davini, P., Hardenberg, J. von, Vidale, P.-L., and Mizuta, R. (2019), The Sensitivity of Euro-Atlantic Regimes to Model Horizontal Resolution, *Geophysical Research Letters* 46.13, 7810–7818. DOI: https://doi.org/10.1029/2019GL082843.

Suarez-Gutierrez, L., Müller, W. A., Li, C., and Marotzke, J. (2020), Dynamical and thermodynamical drivers of variability in European summer heat extremes, *Climate Dynamics* 54.9, 4351–4366. DOI: 10.1007/s00382-020-05233-2.

Sumner, E. J. (1954), A study of blocking in the Atlantic-European of the northern hemisphere, *Quarterly Journal of the Royal Meteorological Society* 80.345, 402–416. DOI: https://doi.org/10.1002/qj.49708034510.

Sun, X., Ding, Q., Wang, S.-Y. S., Topál, D., Li, Q., Castro, C., Teng, H., Luo, R., and Ding, Y. (2022), Enhanced jet stream waviness induced by suppressed tropical Pacific convection during boreal summer, *Nature Communications* 13.1, 1288. DOI: 10.1038/s41467-022-28911-7.

Swain, D. L., Horton, D. E., Singh, D., and Diffenbaugh, N. S. (2016), Trends in atmospheric patterns conducive to seasonal precipitation and temperature extremes in California. eng, *Science advances* 2.4. 1501344[PII]. DOI: 10.1126/sciadv.1501344.

Swanson, K. L., Kushner, P. J., and Held, I. M. (1997), Dynamics of Barotropic Storm Tracks, *Journal of the Atmospheric Sciences* 54, 791–810.

Tamarin-Brodsky, T., Hodges, K., Hoskins, B. J., and Shepherd, T. G. (2020), Changes in Northern Hemisphere temperature variability shaped by regional warming patterns, *Nature Geoscience* 13.6, 414–421. DOI: 10.1038/s41561-020-0576-3.

Taylor, K. E., Stouffer, R. J., and Meehl, G. A. (2012), An Overview of CMIP5 and the Experiment Design, *Bulletin of the American Meteorological Society* 93.4, 485–498.

Thomas, C., Voulgarakis, A., Lim, G., Haigh, J., and Nowack, P. (2021), An unsupervised learning approach to identifying blocking events: the case of European summer, *Weather and Climate Dynamics* 2.3, 581–608. DOI: 10.5194/wcd-2-581-2021.

Thornhill, G., Collins, W., Olivié, D., Skeie, R. B., Archibald, A., Bauer, S., Checa-Garcia, R., Fiedler, S., Folberth, G., Gjermundsen, A., Horowitz, L., Lamarque, J.-F., Michou, M., Mulcahy, J., Nabat, P., Naik, V., O'Connor, F. M., Paulot, F., Schulz, M., Scott, C. E., Séférian, R., Smith, C., Takemura, T., Tilmes, S., Tsigaridis, K., and Weber, J. (2021), Climate-driven chemistry and aerosol feedbacks in CMIP6 Earth system models, *Atmospheric Chemistry and Physics* 21.2, 1105–1126. DOI: 10.5194/acp-21-1105-2021.

Thorpe, A. J. (1985), Diagnosis of Balanced Vortex Structure Using Potential Vorticity, *Journal of Atmospheric Sciences* 42.4, 397–406. DOI: 10.1175/1520-0469(1985)042<0397:DOBVSU>2.0.CO;2.

Tibaldi, S. and Molteni, F. (1990), On the operational predictability of blocking, *Tellus A* 42.3, 343–365. DOI: https://doi.org/10.1034/j.1600-0870.1990.t01-2-00003.x.

Ting, M. and Sardeshmukh, P. D. (1993), Factors Determining the Extratropical Response to Equatorial Diabatic Heating Anomalies, *Journal of Atmospheric Sciences* 50.6, 907–918. DOI: 10.1175/1520-0469(1993)050<0907:FDTERT>2.0.CO;2.

Trenberth, K. E., Dai, A., Rasmussen, R. M., and Parsons, D. B. (2003), The Changing Character of Precipitation, *Bulletin of the American Meteorological Society* 84.9, 1205–1218. DOI: 10.1175/BAMS-84-9-1205.

Trenberth, K. E. and Guillemot, C. J. (1994), The total mass of the atmosphere, *Journal of Geophysical Research: Atmospheres* 99.D11, 23079–23088. DOI: https://doi.org/10.1029/94JD02043.

Twardosz, R., Walanus, A., and Guzik, I. (2021), Warming in Europe: Recent Trends in Annual and Seasonal temperatures, *Pure and Applied Geophysics* 178.10, 4021–4032. DOI: 10.1007/s00024-021-02860-6.

Ullmann, A., Fontaine, B., and Roucou, P. (2014), Euro-Atlantic weather regimes and Mediterranean rainfall patterns: Present-day variability and expected changes under CMIP5 projections, *International Journal of Climatology* 34. DOI: 10.1002/joc.3864.

Vallis, G. K. (2006a), Atmospheric and Oceanic Fluid Dynamics: Fundamentals and Large-scale Circulation. In: Cambridge University Press. Chap. 2: Effects of Rotation and Stratification. DOI: 10.1017/CBO9780511790447.

Vallis, G. K. (2006b), Atmospheric and Oceanic Fluid Dynamics: Fundamentals and Large-scale Circulation. In: Cambridge University Press. Chap. 9: Barotropic and Baroclinic Instability. DOI: 10.1017/CBO9780511790447.

Vallis, G. K. (2006c), Atmospheric and Oceanic Fluid Dynamics: Fundamentals and Large-scale Circulation. In: Cambridge University Press. Chap. 1: Equations of Motion. DOI: 10.1017/CBO9780511790447.

Vallis, G. K. (2006d), Atmospheric and Oceanic Fluid Dynamics: Fundamentals and Large-scale Circulation. In: Cambridge University Press. Chap. 5: Geostrophic Theory. DOI: 10.1017/CBO9780511790447.

Vallis, G. K. (2006e), Atmospheric and Oceanic Fluid Dynamics: Fundamentals and Large-scale Circulation. In: Cambridge University Press. Chap. 6: Wave Fundamentals. DOI: 10.1017/CBO9780511790447.

Vallis, G. K. (2006f), Atmospheric and Oceanic Fluid Dynamics: Fundamentals and Large-scale Circulation. In: Cambridge University Press. Chap. 12: Geostrophic Turbulence and Baroclinic Eddies. DOI: 10.1017/CBO9780511790447.

Vautard, R. (1990), Multiple Weather Regimes over the North Atlantic: Analysis of Precursors and Successors, *Monthly Weather Review* 118.10, 2056–2081. DOI: 10.1175/1520-0493(1990)118<2056:MWROTN>2.0.CO;2.

Vautard, R., Yiou, P., Otto, F., Stott, P., Christidis, N., Van Oldenborgh, G. J., and Schaller, N. (2016), Attribution of human-induced dynamical and thermodynamical contributions in extreme weather events, *Environmental Research Letters* 11. DOI: 10.1088/1748-9326/11/11/114009.

Vecchi, G. A. and Soden, B. J. (2007), Global Warming and the Weakening of the Tropical Circulation, *Journal of Climate* 20.17, 4316–4340. DOI: 10.1175/JCLI4258.1.

Verdecchia, M., Visconti, G., D'Andrea, F., and Tibaldi, S. (1996), A Neural Network Approach for blocking recognition, *Geophysical Research Letters* 23, 2081–2084. DOI: 10.1029/96GL01810.

Visbeck, M. H., Hurrell, J. W., Polvani, L., and Cullen, H. M. (2001), The North Atlantic Oscillation: Past, present, and future, *Proceedings of the National Academy of Sciences* 98.23, 12876–12877. DOI: 10.1073/pnas.231391598.

Vries, H. de, Woollings, T., Anstey, J., Haarsma, R. J., and Hazeleger, W. (2013), Atmospheric blocking and its relation to jet changes in a future climate, *Climate Dynamics* 41.9, 2643–2654. DOI: 10.1007/s00382-013-1699-7.

Waliser, D. E. and Somerville, R. C. J. (1994), Preferred Latitudes of the Intertropical Convergence Zone, *Journal of Atmospheric Sciences* 51.12, 1619–1639. DOI: 10.1175/1520-0469(1994)051<1619:PLOTIC>2.0.CO;2.

Wang, X., Han, Y., Xue, W., Yang, G., and Zhang, G. J. (2022), Stable climate simulations using a realistic general circulation model with neural network parameterizations for atmospheric moist physics and radiation processes, *Geoscientific Model Development* 15.9, 3923–3940. DOI: 10.5194/gmd-15-3923-2022.

Wiel, K. van der, Matthews, A. J., Joshi, M. M., and Stevens, D. P. (2016), The influence of diabatic heating in the South Pacific Convergence Zone on Rossby wave propagation and the mean flow, *Quarterly Journal of the Royal Meteorological Society* 142.695, 901–910. DOI: https://doi.org/10.1002/qj.2692.

Wilks, D. (2005), Statistical Methods in the Atmospheric Sciences, Volume 91, Second Edition (International Geophysics), 179–198.

Wittek, P., Gao, S. C., Lim, I. S., and Zhao, L. (2017), somoclu: An Efficient Parallel Library for Self-Organizing Maps, *Journal of Statistical Software* 78.9. DOI: 10.18637/jss.v078.i09.

Woollings, T., Barriopedro, D., Methven, J., Son, S.-W., Martius, O., Harvey, B., Sillmann, J., Lupo, A. R., and Seneviratne, S. (2018), Blocking and its Response to Climate Change, *Current Climate Change Reports* 4.3, 287–300. DOI: 10.1007/s40641-018-0108-z.

Woollings, T. and Blackburn, M. (2012), The North Atlantic Jet Stream under Climate Change and Its Relation to the NAO and EA Patterns, *Journal of Climate* 25.3, 886–902.

Woollings, T., Hannachi, A., and Hoskins, B. (2010), Variability of the North Atlantic eddy-driven jet stream, *Quarterly Journal of the Royal Meteorological Society* 136.649, 856–868. DOI: https://doi.org/10.1002/qj.625.

Woollings, T., Pinto, J., and Santos, J. (2011), Dynamical Evolution of North Atlantic Ridges and Poleward Jet Stream Displacements, *Journal of the Atmospheric Sciences* 68, 954–963. DOI: 10.1175/2011jas3661.1.

Wu, Y., Miao, C., Fan, X., Gou, J., Zhang, Q., and Zheng, H. (2022), Quantifying the Uncertainty Sources of Future Climate Projections and Narrowing Uncertainties With Bias Correction Techniques, *Earth's Future* 10.11. e2022EF002963 2022EF002963, e2022EF002963. DOI: https://doi.org/10.1029/2022EF002963.

Xie, S.-P., Deser, C., Vecchi, G. A., Collins, M., Delworth, T. L., Hall, A., Hawkins, E., Johnson, N. C., Cassou, C., Giannini, A., and Watanabe, M. (2015), Towards predictive understanding of regional climate change, *Nature Climate Change* 5.10, 921–930. DOI: 10.1038/nclimate2689.

Xu, G., Osborn, T. J., Matthews, A. J., and Joshi, M. M. (2016), Different atmospheric moisture divergence responses to extreme and moderate El Niños, *Climate Dynamics* 47.1, 393–410. DOI: 10.1007/s00382-015-2844-2.

Yu, B. (2007), The Pacific–North American pattern associated diabatic heating and its relationship to ENSO, *Atmospheric Science Letters* 8.4, 107–112. DOI: https://doi.org/10.1002/asl.160.

Yu, B., Wei, Y.-M., Gomi, K., and Matsuoka, Y. (2018), Future scenarios for energy consumption and carbon emissions due to demographic transitions in Chinese households, *Nature Energy* 3.2, 109–118. DOI: 10.1038/s41560-017-0053-4.

Zurita-Gotor, P. and Vallis, G. K. (2011), Dynamics of Midlatitude Tropopause Height in an Idealized Model, *Journal of the Atmospheric Sciences* 68.4, 823–838. DOI: 10.1175/2010JAS3631.1.

Zwiers, F. W. and Storch, H. von (1995), Taking Serial Correlation into Account in Tests of the Mean, *Journal of Climate* 8.2, 336–351. DOI: 10.1175/1520-0442(1995)008<0336:TSCIAI>2.0.CO;2.

Appendix A

Appendix A1

A.1 UKESM case studies

In the UKESM pre-industrial run, we show in Fig. A.2 part of a heatwave in the (arbitrary) year 2014. This year shows the largest spatial extent of heat extremes, where the number of grid cells exceeding the 90th (99th) temperature percentile peaks at 66% (24%) on 19 (20) July 2014. To complement this extreme case, we also show in Fig. A.3 a period from the 2030 summer, which shows the edge of a blocking pattern in Eastern Europe on the 19 July and an anticyclone shifting across Europe over 20-27 July.

Since VPV is not available as a variable, the S04 blocking index cannot be calculated, and we have instead shown MSLP in Figs. A.2b and A.3b.

Many of the same features are observed. Extreme heat is associated with persistent high pressure and stationary surface winds. The MSLP field is broadly correlated with the Z_{500} anomalies, but frequently the Z_{500} anomaly doesn't represent the MSLP anomalies well, such as on the 25th July 2014 shown in Fig. A.2, where low MSLP is contrasted with high Z_{500}. The AGP index in general performs worse than in ERA5, since the zonal Z_{500} gradients are not as prominent. The DG83 index is still able to describe blocking patterns from the Z_{500} anomalies. The SOM-BI labelling is generally consistent with the ground truth dataset in both cases.

The MSLP field is broadly correlated with the Z_{500} anomalies, but frequently the Z_{500} anomaly does not represent the MSLP anomalies well, such as on the 25th July 2014

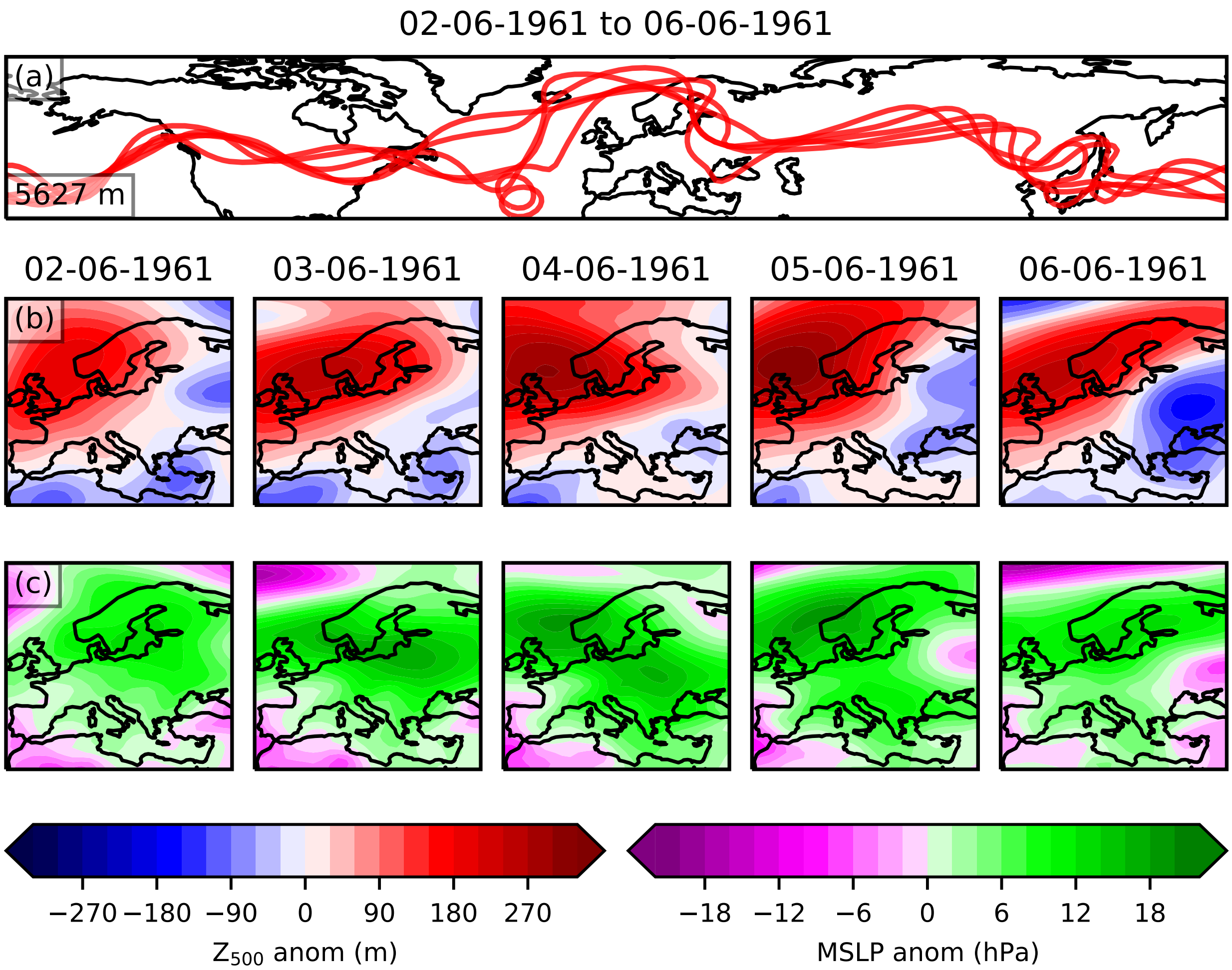

Figure A.1: The information used to classify blocks in the UKESM GTD. (a) shows the daily Z_{500} contour for the averaged value across 30-70 °N, indicated in the bottom left of the panel. (b) and (c) show the Z_{500} time detrended anomaly and MSLP anomaly for each day.

shown in Fig. A.2, where low MSLP is contrasted with high Z_{500}. The surface wind fields in UKESM similarly show the easterly wind direction associated with high pressure and vice versa, particularly when the MSLP anomalies are also strong such as on the 20-21 July 2030 in Fig. A.3.

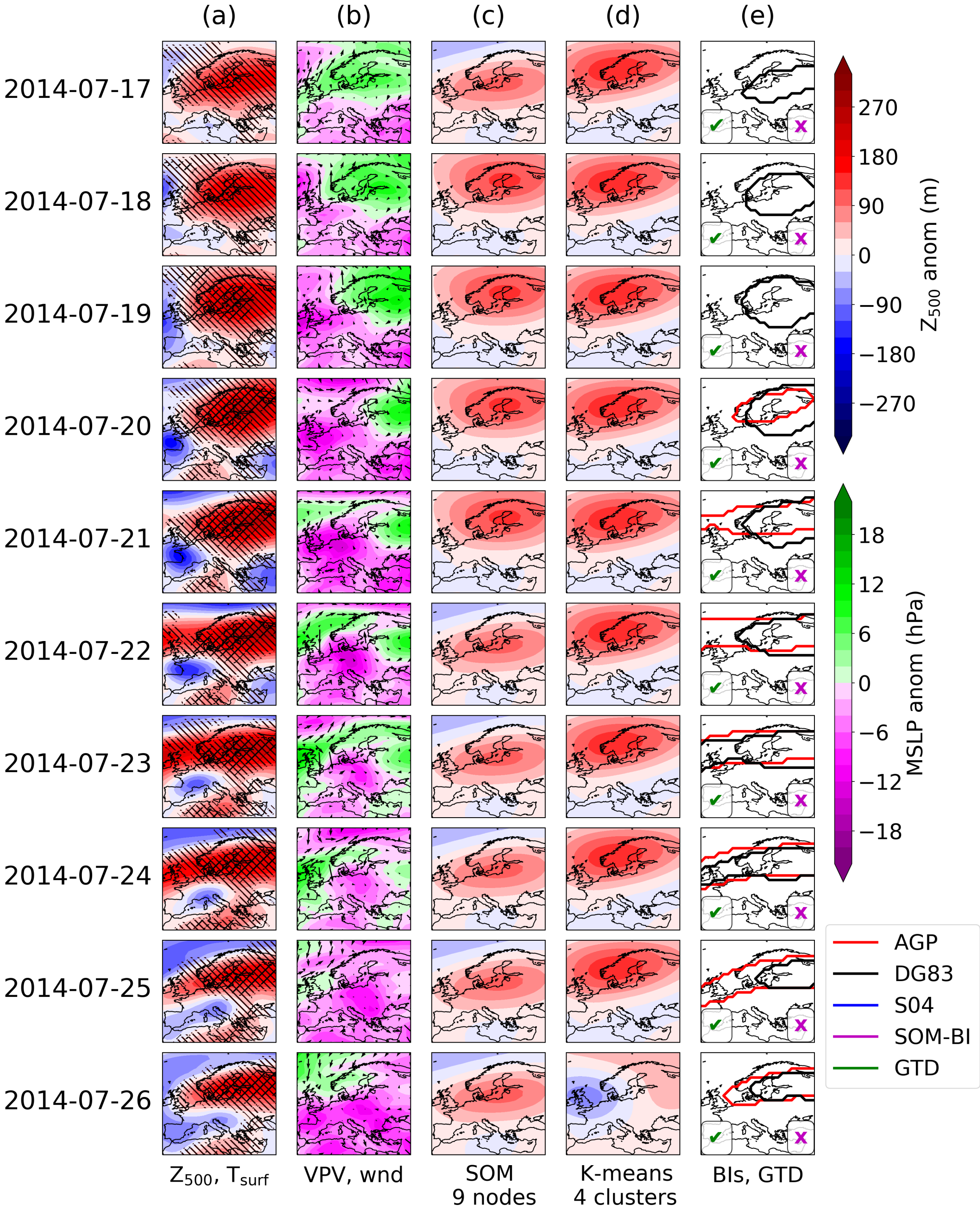

Figure A.2: As with the case studies shown in figures 2.4 and 2.5, but for a heatwave in UKESM.

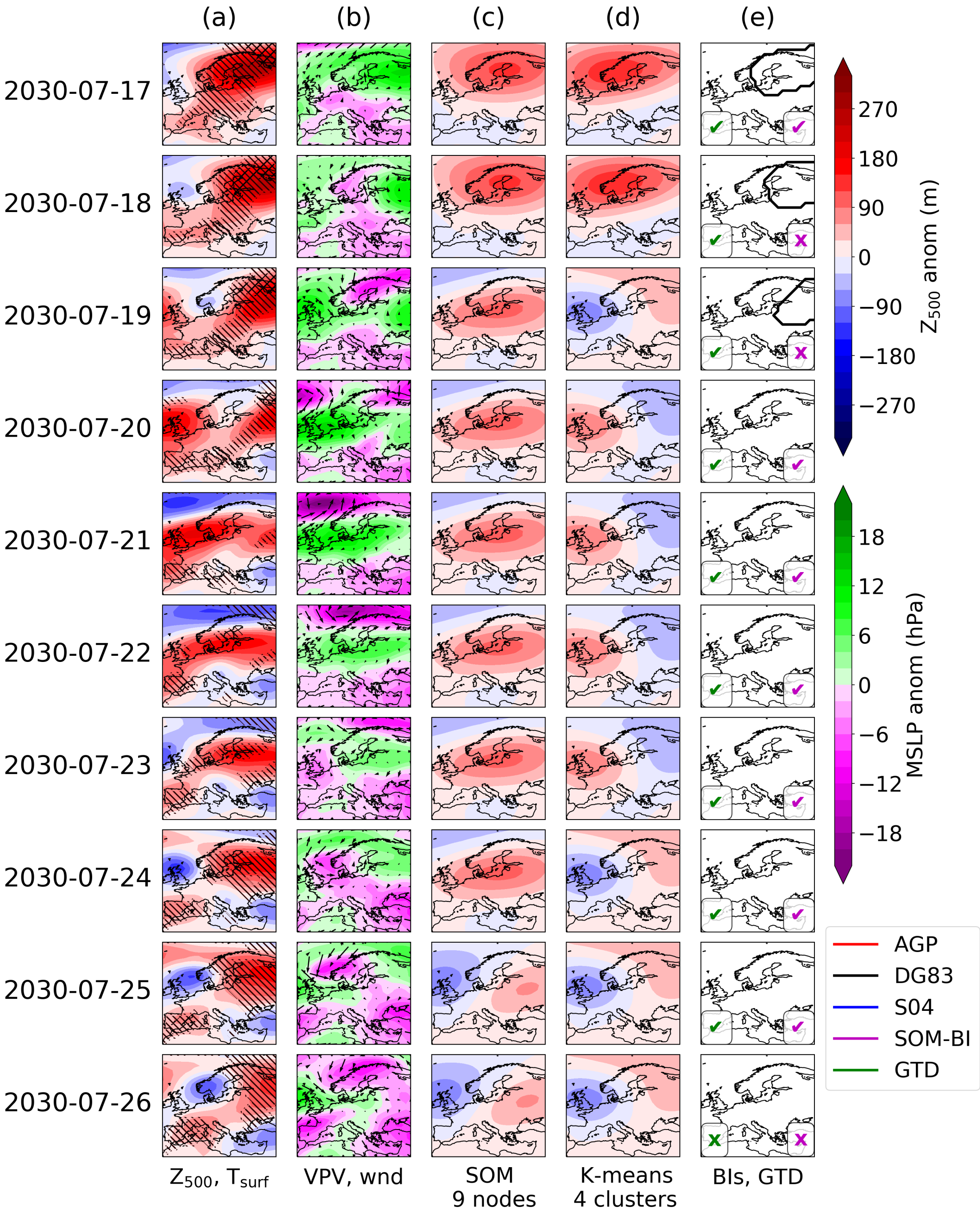

Figure A.3: As above, but for a transient period in UKESM.

A.2 Blocking climatologies

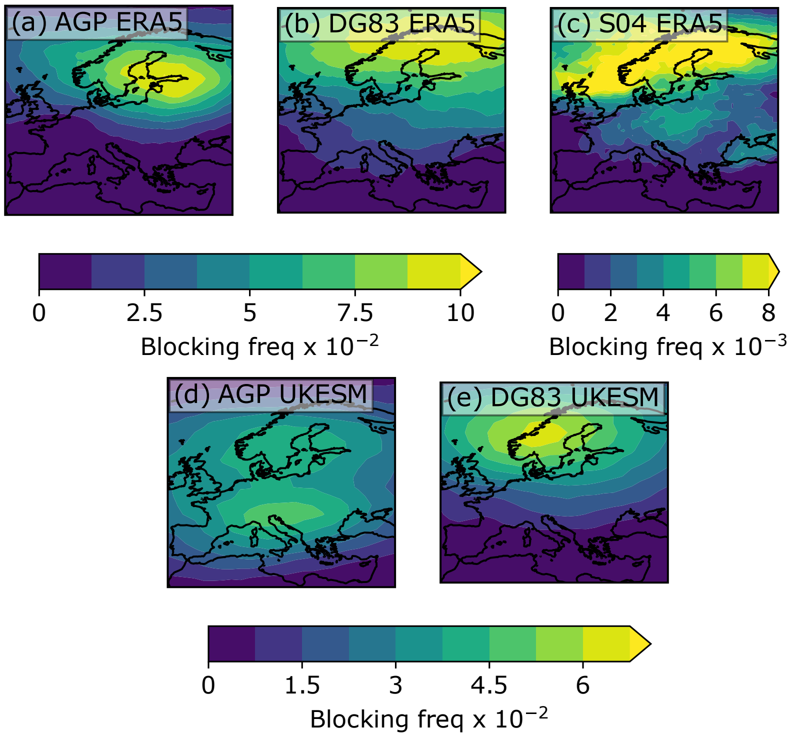

Figure A.4: Occurrence of blocking events per grid cell across JJA Europe for three BIs in ERA5 1979-2019 and two BIs in UKESM JJA 1960-2060.

A.3 Difference between the SOM and K-means analysis

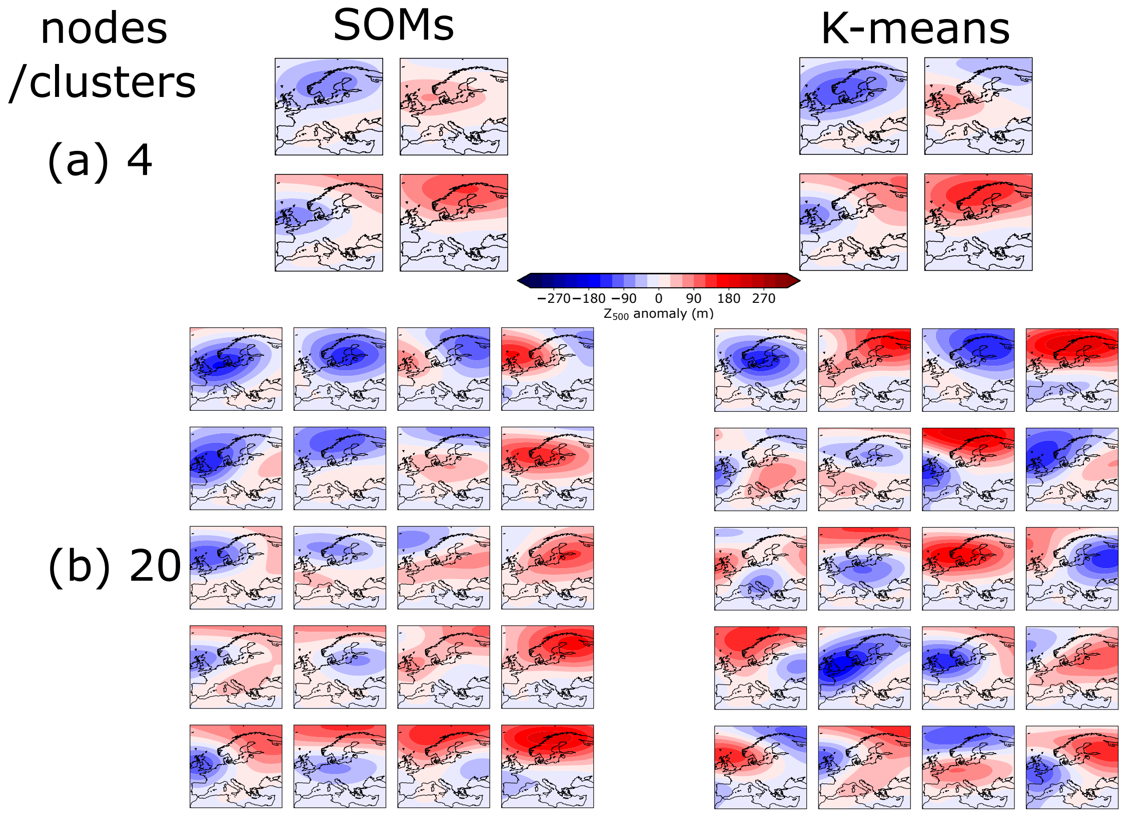

Figure A.5: Comparison of the SOM analysis and K-means clustering for (a) 4 and (b) 20 nodes/clusters. Whilst the K-means and SOM analysis produce a similar set of patterns for smaller node numbers, their behaviour diverges for larger node numbers. Since the neighbourhood function ensures that several nodes are updated at once, the SOM produces a continuum of weather patterns. However, since the K-means clustering updates each centroid independently, it will seek to maximise the differences between each cluster. This causes some centroids for high cluster numbers to represent mixed weather regimes that are less realistic than the SOM continuum of weather regimes. The data used for above is ERA5 Z_{500} across JJA 1979-2019.

A.4 Code and data availability

The scripts used for the self-organizing map blocking index, the plots for this chapter and the ground truth datasets for labelling of blocking events in JJA Europe (in both ERA5 1979-2019 and UKESM pre-industrial control 1960-2060) can be accessed in `github.com/carlmagnusthomas/SOM-BI`. ERA5 data is available from `confluence.ecmwf.int` and UKESM data is available from `esgf-node.llnl.gov`.

Appendix B

Appendix A2

B.1 The model bias of the SOM-BI using MSLP anomalies that have not been normalised

This section describes the model bias that is evident in the SOM-BI index using the MSLP anomalies in the 4xCO2 runs, extending the discussion in 3.3.2. There are two differences between the non-normalised MSLP data and the normalised MSLP anomalies:

1. Definition of anomalies: in the non-normalised case, the MSLP anomalies in the 4xCO2 period are defined with respect to the anomalies of the historic period. This will overemphasise the dynamic shifts in the MSLP climatology over this time period, since the 4xCO2 anomalies are projected onto a shifted background state. In the normalised case, the anomalies are defined with respect to each climatological period.

2. Normalising by standard deviation: in the normalised case, the anomalies in each grid cell are divided by the standard deviation of MSLP for each period, such that such that (MSLP_{norm}) are calculated:

$$MSLP_{norm} = \frac{MSLP - \mu_{MSLP}}{\sigma_{MSLP}} \tag{B.1}$$

Figure B.1 shows the ESB response across 20 global climate models across CMIP5 and CMIP6.

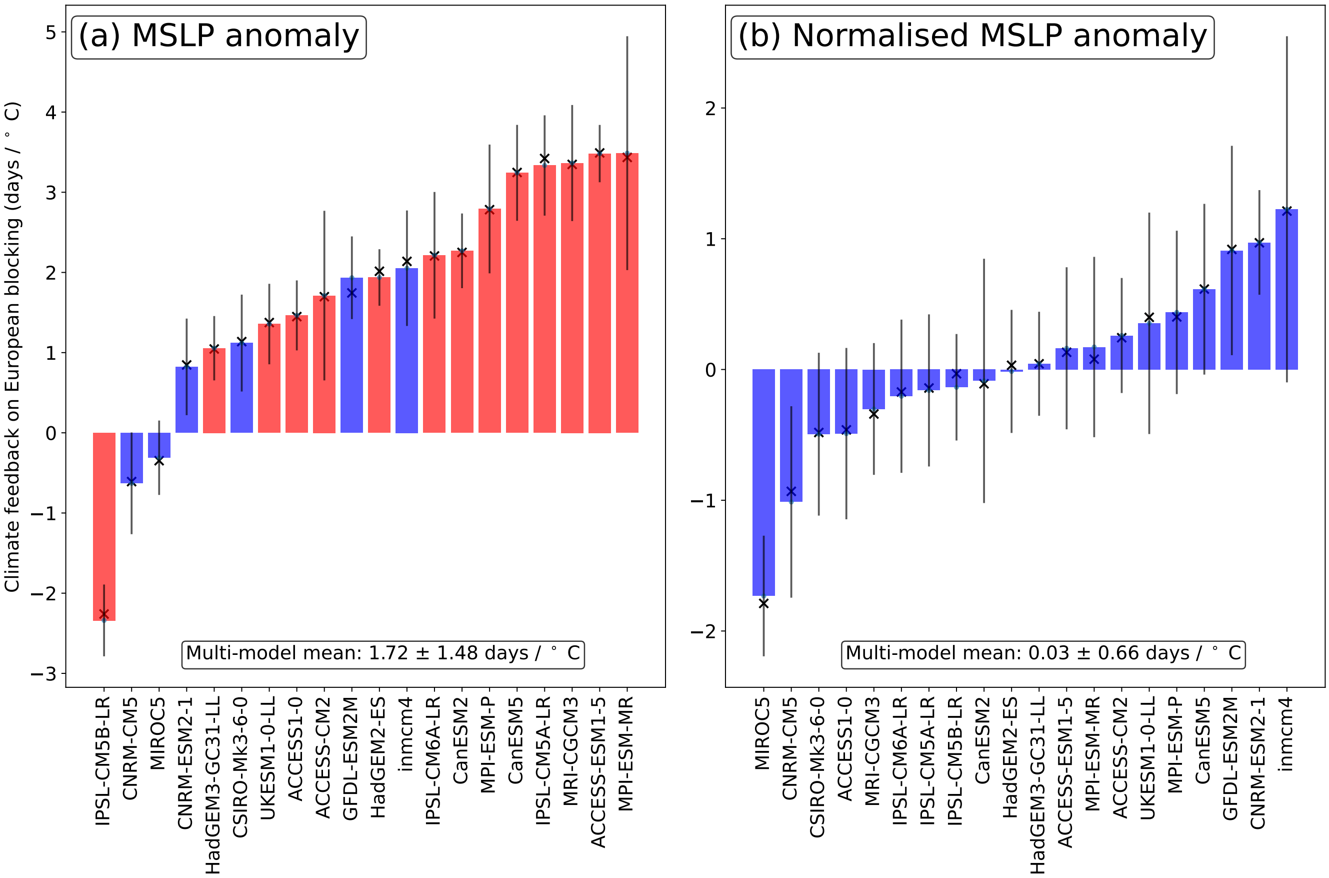

Figure B.1: The response of ESB to climate change across 20 global climate models. Derived by combining the 4xCO2 and historical periods of JJA global mean surface temperature and mean JJA blocking over Europe and calculating a linear regression. Red bars show statistically significant trends (p-value < 0.05, corrected for multiple hypothesis testing). The lines show the error bars on the trend. Blocking occurrence is calculated using the SOM-BI for (a) the MSLP anomaly and (b) the MSLP normalised anomaly. Crosses indicate the mean change in blocking occurrence divided by the GMST change between the 4xCO2 and historical periods.

The trends are derived by combining the 4xCO2 and historical periods of JJA global mean surface temperature and mean JJA blocking over Europe and calculating a linear regression, averaged over each year, as in Fig. 3.2. Red bars show statistically significant trends, and the lines show the standard error on the trend. Figures B.1 (a) and B.1 (b) show the ESB response calculated using the MSLP anomaly and normalized MSLP anomaly respectively. The MSLP anomaly calculation shows across several models a statistically significant ESB response, with 85% of models showing a positive trend. The multi-model mean is an increase of 1.7 ± 1.5 days blocked over European summer per degree of GMST increase. Therefore, whilst there is a wide divergence of model responses in the ESB response, an increase is generally reported.

However, in Fig. B.1 (b) no model shows a statistically significant trend. The magnitude of the trends across all models is significantly lower than those of Fig. B.1 (a), and 7 of the 20 models have a change in the sign of the ESB response between Fig. B.1 (a) and B.1 (b). Figure B.1 (b) also shows a more consistent model response across different model groups, which would be expected to have similar physical features. In particular, the IPSL models (IPSL-CM5B-LR, IPSL-CM5A-LR and IPSL-CM6A-LR) all have a very similar slightly negative ESB response in Fig. B.1 (b), but in Fig. B.1 (a) IPSL-CM5B-LR and IPSL-CM5A-LR show opposite trends.

These differences between the normalised and non-normalised data are striking, and they result from model biases in the historic MSLP distribution (see 3.3.2 and Fig. 3.1). These model biases can be seen in how the future change in the models is sensitive to the past occurrence of certain SOM nodes for the non-normalised MSLP data.

Figures B.2 and B.3 show the optimised SOM for each index and the statistically significant (p-value < 0.05) trends between the occurrence of each SOM node and the future trend in that model. In each case the occurrence of the SOM nodes is shown as the difference between the occurrence of that SOM node in the historic climatology in the model and the occurrence of that SOM node in the ERA5 climatology. These are therefore measures of model skill.

Figure B.2 shows clear decreases in the occurrence of the SOM nodes with negative anomalies in MSLP over Scandinavia (nodes 3, 4, 5, 7 and 9), and clear increases in those nodes with positive anomalies over Scandinavian MSLP (nodes 17, 18, 19 and 20). This suggests that the changes in the occurrence of certain blocking patterns are dependent on how much the model deviates from the past occurrence of SOM nodes. Since all models use an SOM trained on ERA5 data, this suggests that the differences between the MSLP climatology historically lead to a greater occurrence of blocking in the future. This could be due to difference in the physics, or simply because if the model is incorrect in its MSLP climatology, the effect of changes in the 4xCO2 run is going to be significantly magnified, since the positive SOM nodes that occur historically infrequently suddenly occur much more frequently in the 4xCO2 models. This does not necessarily reflect interesting physics, but an error in the application of the algorithm.

However, Fig, B.3 does not show such trends. Whilst both models have statistically significant trends, there are many more (9 out of 20) in the non-normalised data than in the normalised data (4 out of 16). Additionally, after correcting for multiple-hypothesis testing the trends in Fig. B.3 are no longer significant, but most of the trends in Fig. B.2 remain significant after applying this correction. The SOM nodes that occur more or less frequently historically in Fig. B.3 do not map on to clear parts of the European domain where there would be biases in the $MSLP_{norm}$ climatology. For example, the occurrence of nodes 6 and 2 (which have a slight positive relationship with future trend) shows a pattern of positive MSLP anomalies over Scandinavia, but the occurrence of node 11 (which also has a slight positive trend) shows a negative $MSLP_{norm}$ anomaly over Scandinavia. This shows that there are no clear biases that relate the past skill of the $MSLP_{norm}$ climatology to the future trend in the SOM-BI index. Therefore, using the normalised MSLP anomalies corrects for the model biases in the historic MSLP climatology.

This correction is also shown in Fig. B.4, which shows slope and R^2 for a linear regression between the historic MSLP climatology and the future trend in European summer blocking for (a) the MSLP SOM-BI and (b) the $MSLP_{norm}$ SOM-BI trends, The hatching shows statistical significance, and there is a clear relationship between the negative MSLP over Scandinavia and peak R^2 0.45 in the climatology and a positive future trend in the MSLP SOM-BI, but in (b) there are no statistically significant trends, with peak R^2 0.15. The lack of any statistically significant correction between the MSLP climatology and the $MSLP_{norm}$ SOM-BI trends shows that the normalisation has removed the model bias. Therefore, the normalised MSLP anomaly is an effective way of calculating future trends in SOM-BI in the 4xCO2 runs.

B.2 Applying the SOM-BI to normalized MSLP data

This section describes the optimization of the SOM-BI index using normalized MSLP anomalies discussed and motivated in section 3.3 and B.1. Since $MSLP_{norm}$ is effectively a new variable with a new SOM (see Fig. B.3), the SOM-BI needs to be optimised again to identify the optimal set of node groups associated with blocking. This requires an optimization of the SOM node number, and then an identification of the best blocked node group within that set, calculated through cross-validation (see section 2.3.3 and the skill score comparison in Fig. 2.6). Figure B.5 shows the optimization of this node group. The optimisation follows a similar pattern to

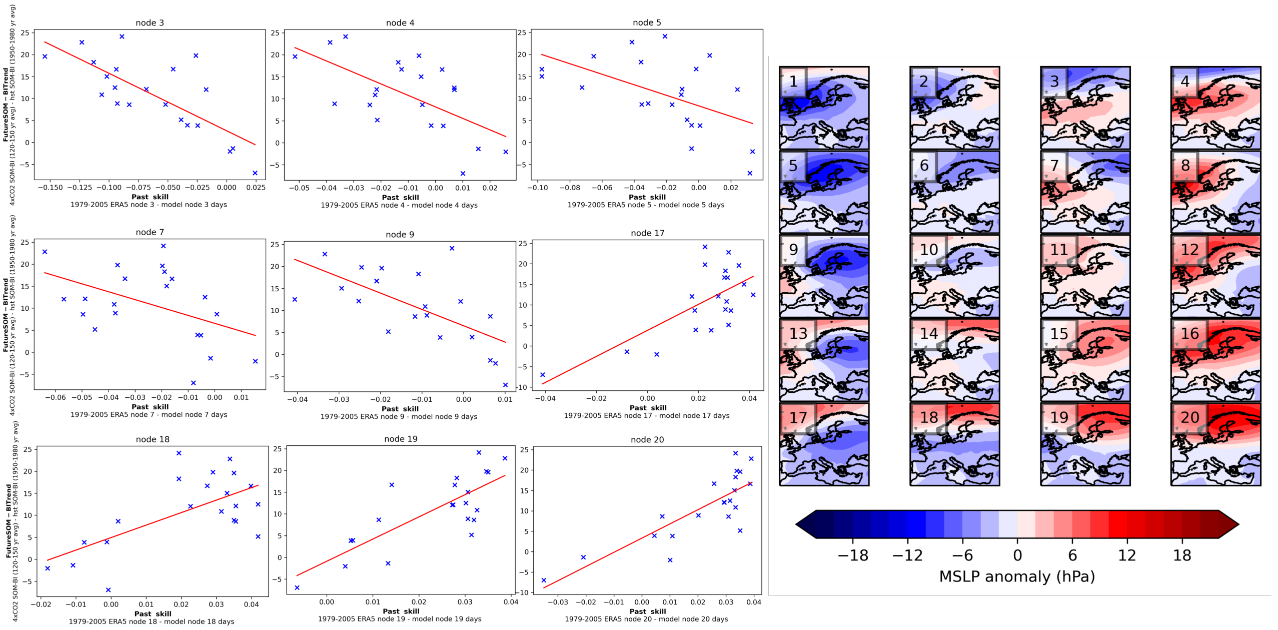

Figure B.2: The optimised self-organising maps used for calculating blocking using the MSLP anomaly (right), alongside the statistically significant trends in relating the SOM node occurrence to the model skill (left). These trends remain statistically significant after accounting for multiple hypothesis testing.

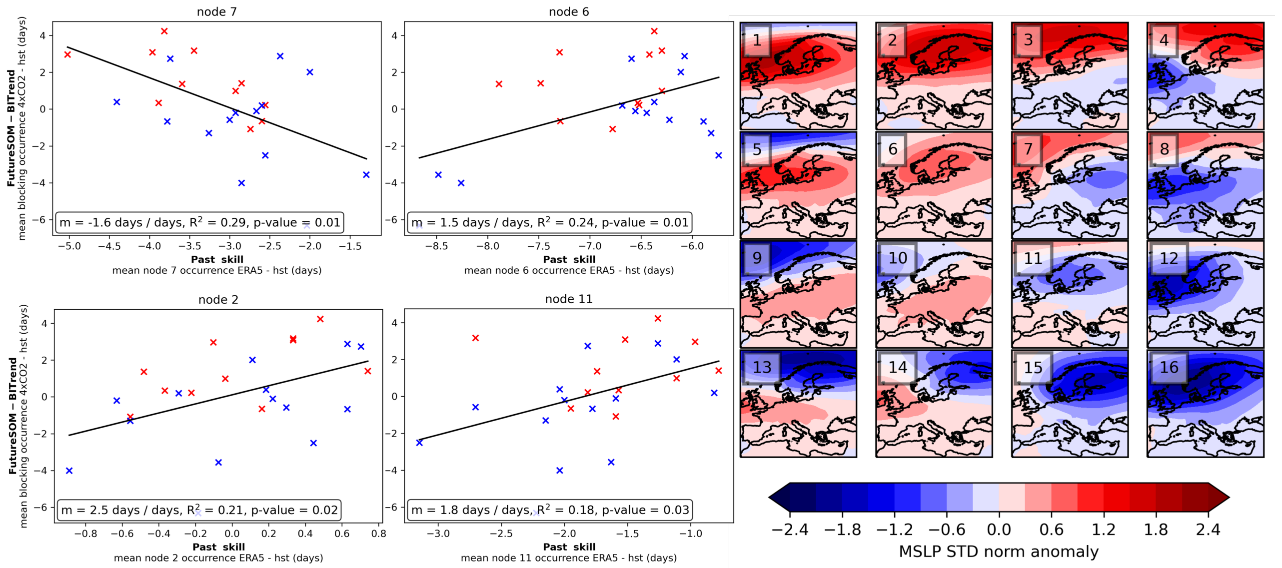

Figure B.3: As in figure B.2 but for the normalised MSLP anomalies. After accounting for multiple hypothesis testing, none of these trends are statistically significant.

the MSLP optimization in Fig 2.6 (b), where the recall decreases whilst precision increases with an increasing node number. The difference between precision and recall is smallest at node number 16 (arranged in a 4x4 SOM arrangement), so this has been chose for optimization. The cross-validation F1 score in 0.65, which is very similar to the cross-validation F1 score of 0.66

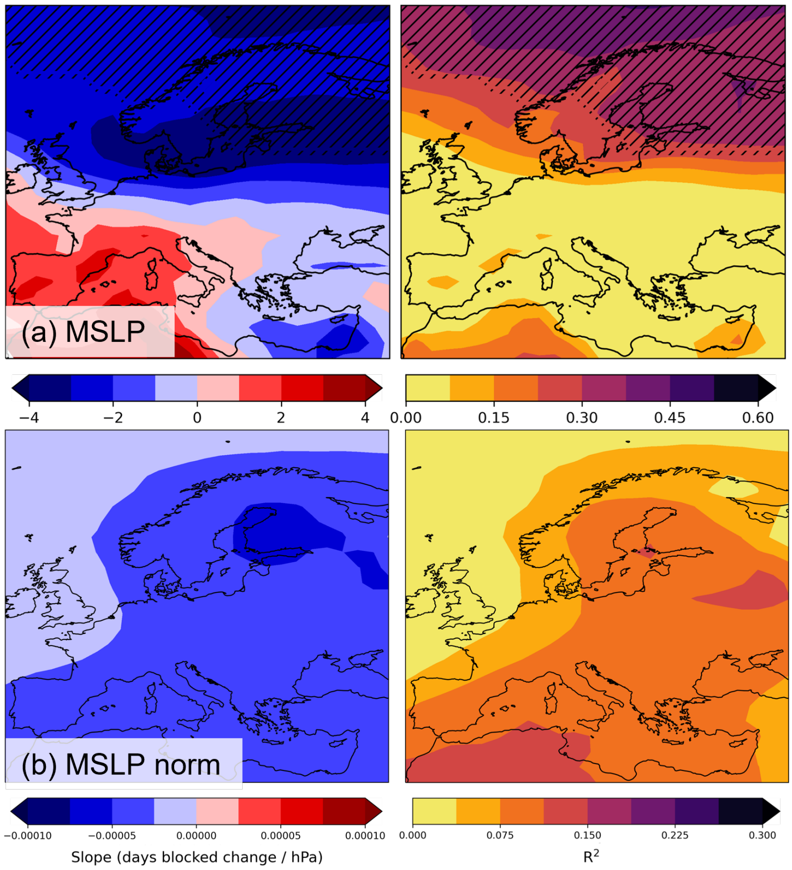

Figure B.4: The slope (left) and R^2 (right) of a linear regression between the mean historic JJA MSLP climatology (1979-2005) and the change in blocking across 26 CMIP5/CMIP6 models. Hatching shows where the p-value is statistically significant (p-value ¡ 0.05). The top row shows the relationship for the MSLP anomaly plots and the bottom row shows the same for the normalised MSLP anomalies.

for the non-normalised MSLP anomalies. In order to derive the optimal set of SOM blocked node groups, a slightly different method was used to that described in section 2.3.3. Since the cross-validation produces 10 different sets of blocked node groups with a widely varying F1 score, the blocked node group with the smallest number of blocked node groups was chosen, which also had a higher F1 score (0.70) and a smaller difference between the precision and recall (0.01). This is different to taking the blocked node group set that would be obtained without cross-validation, which was the method employed with the other indices, which led to a larger number of blocked node groups associated with blocking, and a higher F1 score overall, but introduces a potential error in overfitting the dataset (albeit generally with combinations of blocked node groups that are rarer). This modification in the choice of optimal node groups was motivated by the fact that smaller node groups generally show better F1 scores when applied across different datasets (see table 2.2 in section 2.3.5). This minor modification is likely to

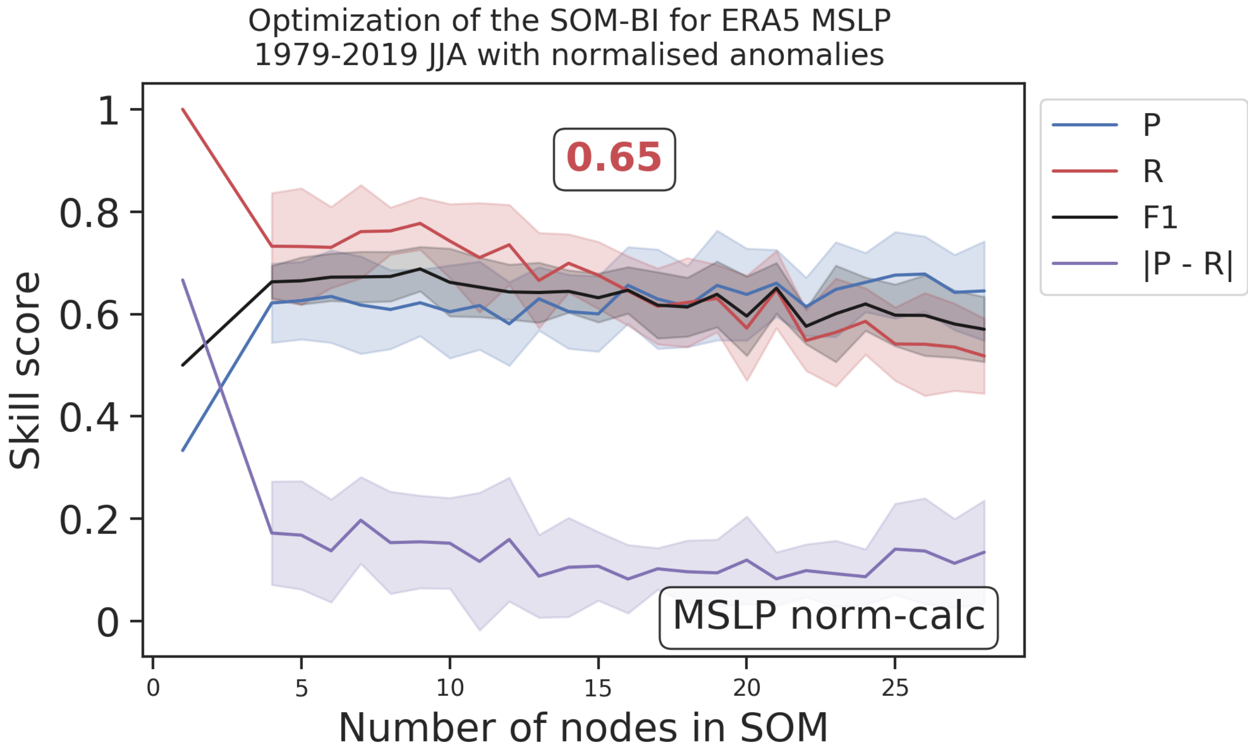

Figure B.5: The optimization of the node number for the normalized MSLP anomalies using 10-fold cross validation in the ERA5 dataset. See Figure 2.6 for the optimization across other variables and section 2.3.3 for a further discussion and comparison with other variables.

slightly improve the classification of blocking with the $MSLP_{norm}$ variable.

B.3 Using MSLP as a variable to investigate dynamic climate change

Figure B.5 shows the relationship between MSLP and surface temperature for 150 years in the UKESM1-0-LL abrupt-4xCO2 simulation for JJA. Figure B.6 (a) shows the trend globally, which increases with the increase in GMST. This demonstrates that the thermodynamic effect clearly dominates the MSLP distribution globally. However, there is no discernible relationship between surface temperature and MSLP when averaged over the European domain. This demonstrates that on the regional scale which this thesis is concerned with, the dynamic changes in MSLP dominate. Therefore climatic changes in MSLP at the regional scale reflect dynamic mechanism of climate change rather than thermodynamics.

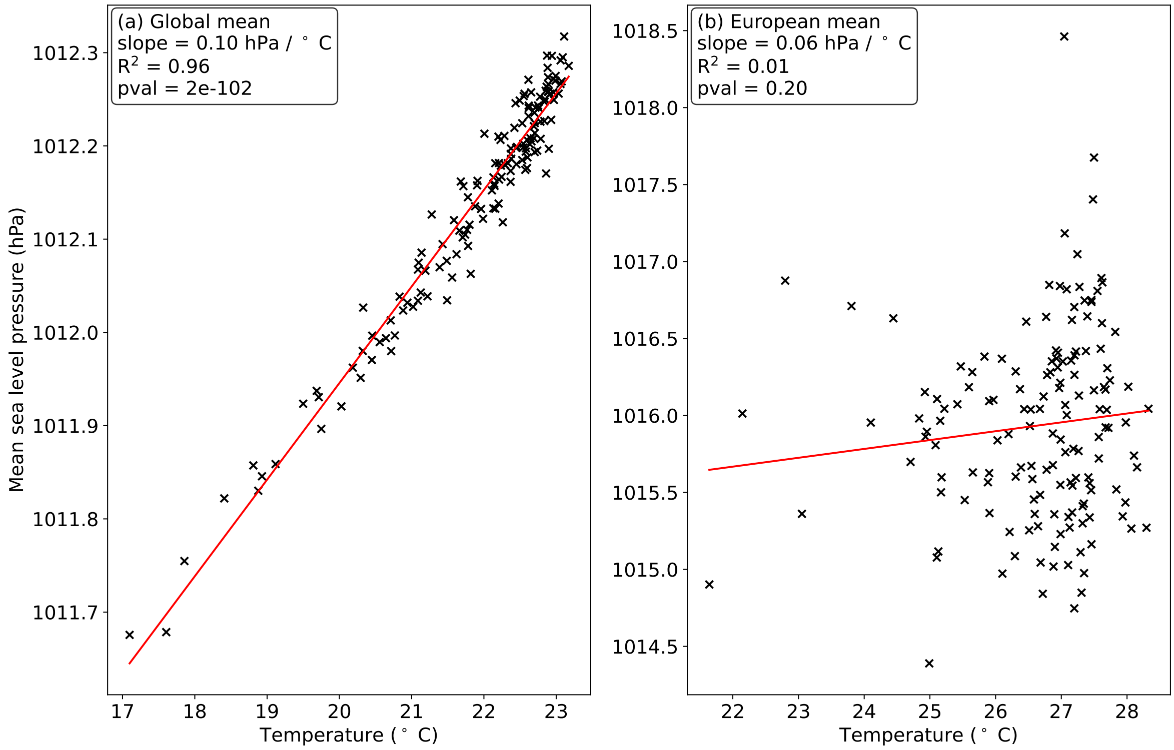

Figure B.6: The relationship between mean sea level pressure and surface temperature using 150 years from in the UKESM 4xCO2 run. Taking the annual JJA average (a) globally and (b) over Europe. The linear regression statistics are shown in each figure.

Appendix C

Appendix A3

C.1 Historic zonal wind and historic JJA European blocking occurrence in ERA5 and CMIP models

Figure C.1 shows the relationship between historic blocking occurrence and U for ERA5. The ground truth dataset (GTD) is used to define the seasonal occurrence of blocking (see section 2.2.2).

The most notable feature is that there is a strong correlation between negative U anomalies over Europe and the seasons which have more atmospheric blocking over Europe. This can be seen by the negative hatched region in Figs. C.1s - u at 40 ° N - 60 ° N, which extends across all pressure levels, with $R^2 > 0.5$. There is also a hatched positive region across 66 - 78 ° N, which is situated at the top of the European domain, indicating a poleward diversion of flow that would be typical for omega blocks. The diversion of flow around a blocked region across the atmosphere is a trivial feature of atmospheric blocking events. However, the fact that the occurrence of blocking events over a season can be correlated with the seasonal climatology of U is significant, since this demonstrates that atmospheric blocking events can impact the seasonal climatology of U over a region.

Similar correlations in hatched regions occur at similar latitudes in other longitude bands, including over the Pacific in Fig. C.1b ($R^2 \approx 0.2$) and in the global average in Fig. C.1a ($R^2 \approx 0.25$). This indicates the greater prevalence of higher hemispheric Rossby wavenumbers

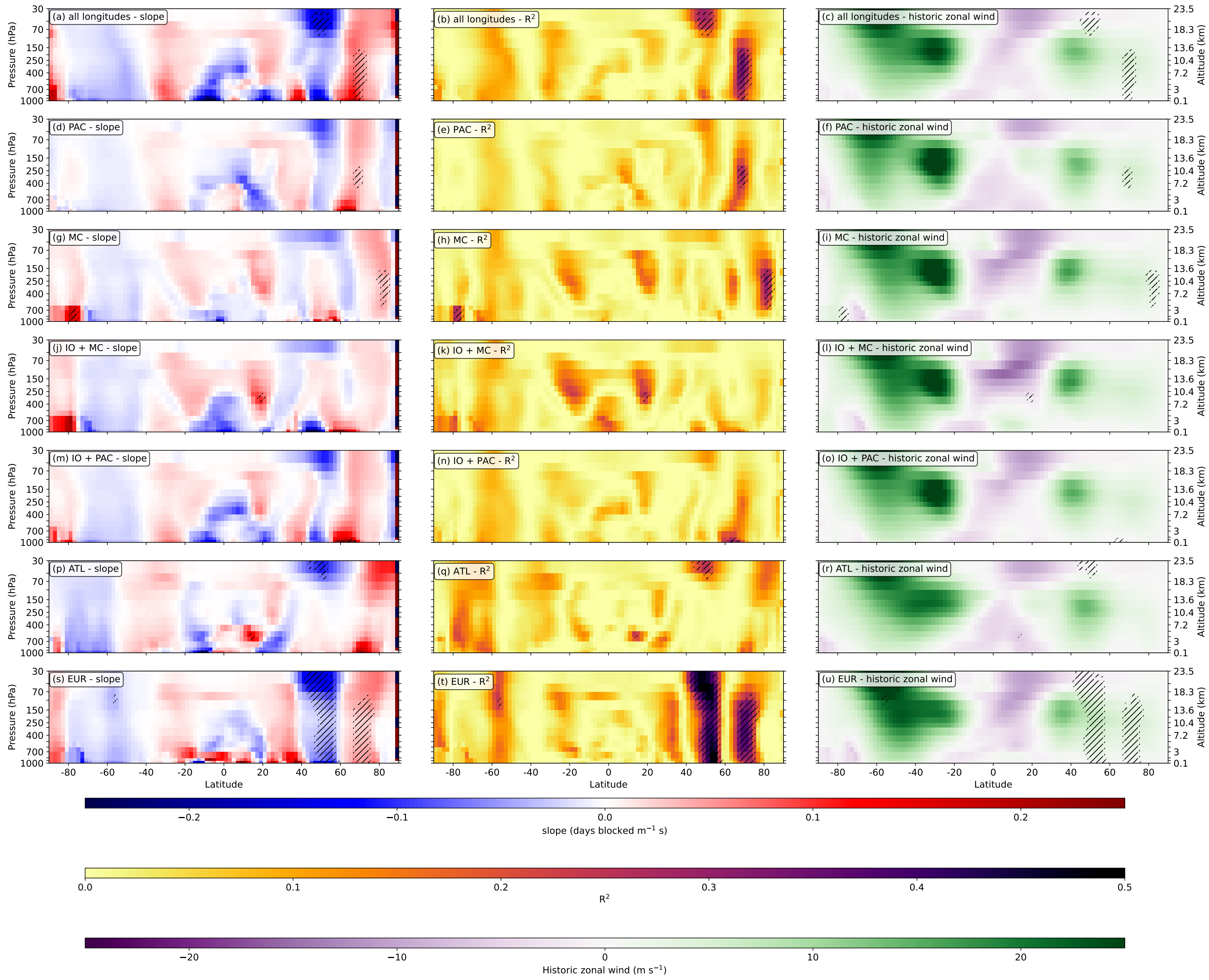

Figure C.1: The relationship between ESB and global patterns of U for the ERA5 reanalysis across the historic (1979-2005) period. The left and central columns show the slope and R^2 for the linear regression respectively, and the rightmost column shows the U climatology. Hatching indicates where the p-value < 0.01, not correcting for multiple hypothesis testing.

associated with blocking events, a well-known result in the literature (e.g. Kornhuber et al. (2019)).

Another noteworthy feature of Fig. C.1 is that there are correlations in the tropical Asia-Pacific region associated with increased blocking. This is strongest for the IO+MC longitude band, in the hatched region at 400 hPa and 20° N in Fig. C.1k, with $R^2 \approx 0.2$, This longitude band, latitude and level is also the region in the tropics where there is the strongest correlation across the CMIP5/6 model ensemble between past model skill and future trend (not shown). This region represents the equatorward edge of the Noth Pacific subtropical jet, and (as illustrated in Fig. 3.11) a more equatorward North Pacific subtropical jet can be connected to ESB through enabling further Rossby wave propagation across the Pacific. The fact that a similar (but weaker) correlation can be identified in the same region in ERA5 suggests that the Rossby wave physical mechanism has played a role historically in the development of future blocking events. This will be further discussed in section 5.2.2.

Figures C.2 and C.3 show the same correlations for two models from the model ensemble (ACCESS-CM2 and GFDL-ESM2M respectively). These two models are shown because they show strongly contrasting correlations between the tropical U and ESB between each other and the ERA5 reanalysis. Whilst the ERA5 reanalysis shows some correlations with tropical forcing, ACCESS-CM2 has no significant correlation with the tropics or correlation outside of the region of Europe and GFDL-ESM2M has strong correlations (highest $R^2 \approx 0.5$) between the U and ESB in the tropics and across both hemispheres. Both models have a relatively low historic blocking occurrence and a positive ESB response (not shown). This suggests that models have strong differences in the relationship between U and ESB individually. However, significant features emerge when studying trends across the model ensemble.

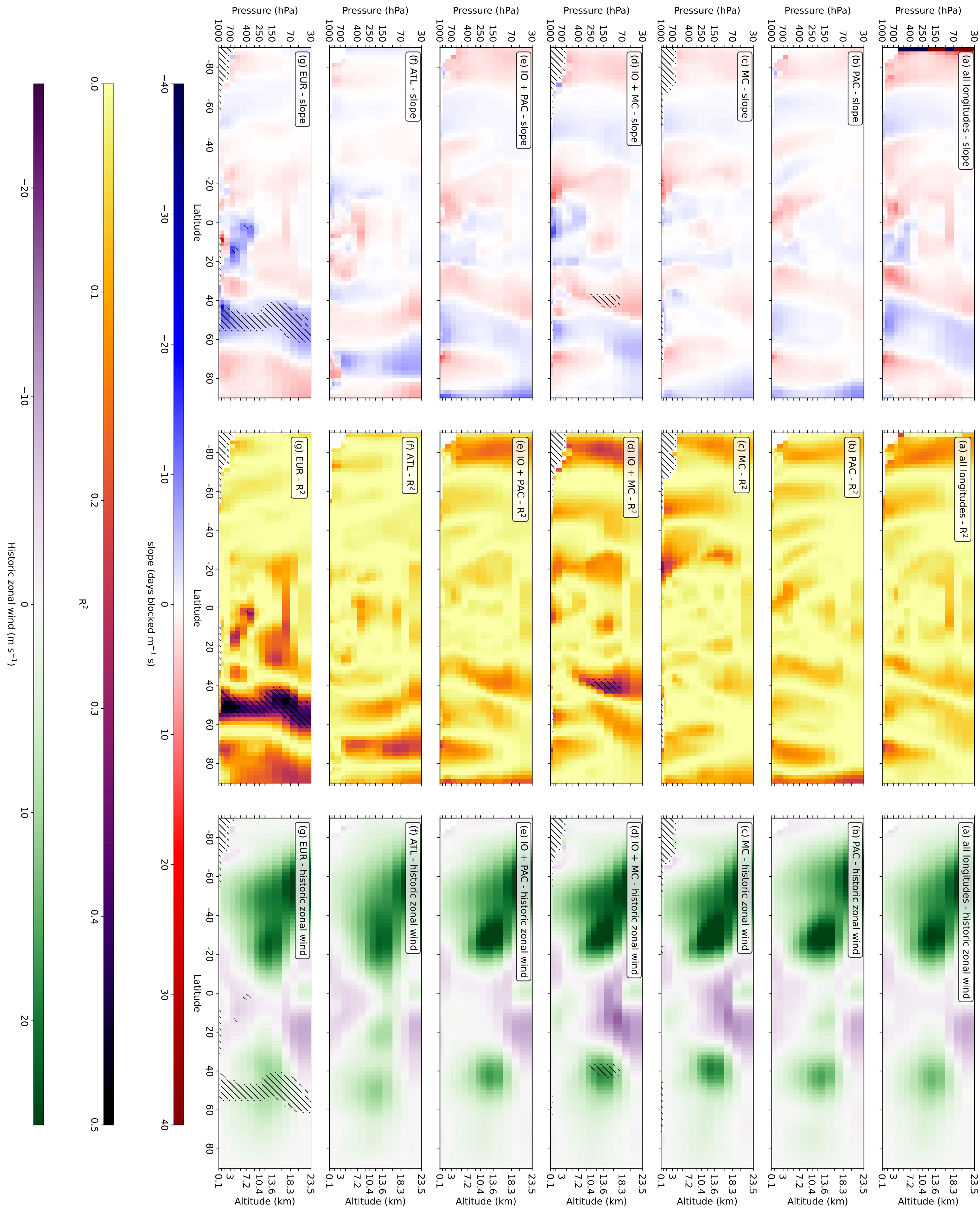

Figure C.2: As in Fig. C.1 but for the ACCESS-CM2 climate model.

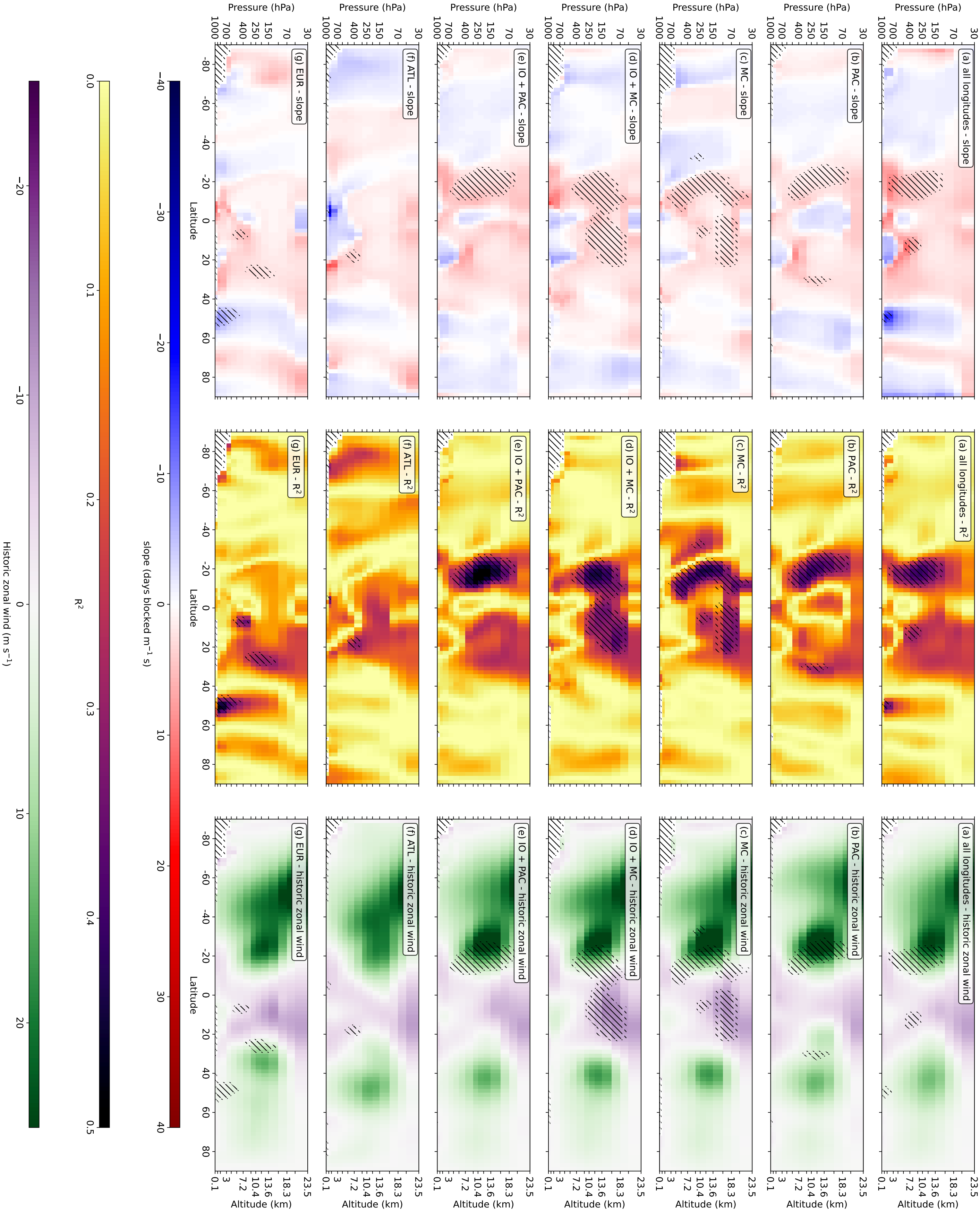

Figure C.3: As in Fig. C.1 but for the GFDL-ESM2M climate model.

C.2 Change in the Atlantic temperature profile and 200 hPa U between models

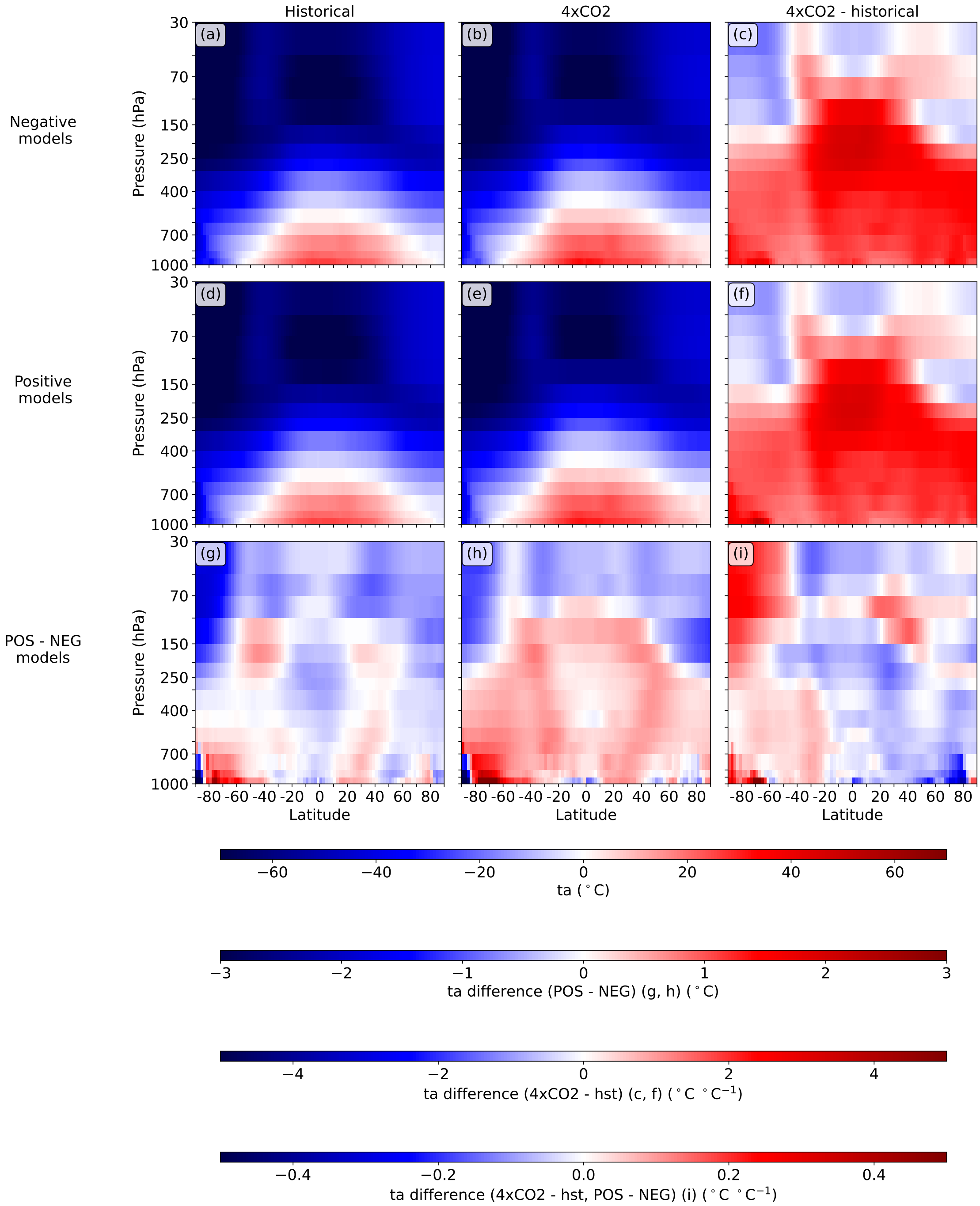

Figure C.4: The difference between the T zonally averaged across the Atlantic. Separated across the positive and negative model groups. Fig. C.4i shows that there is a greater (smaller) increase in the meridional temperature gradient for the positive (negative) model groups.

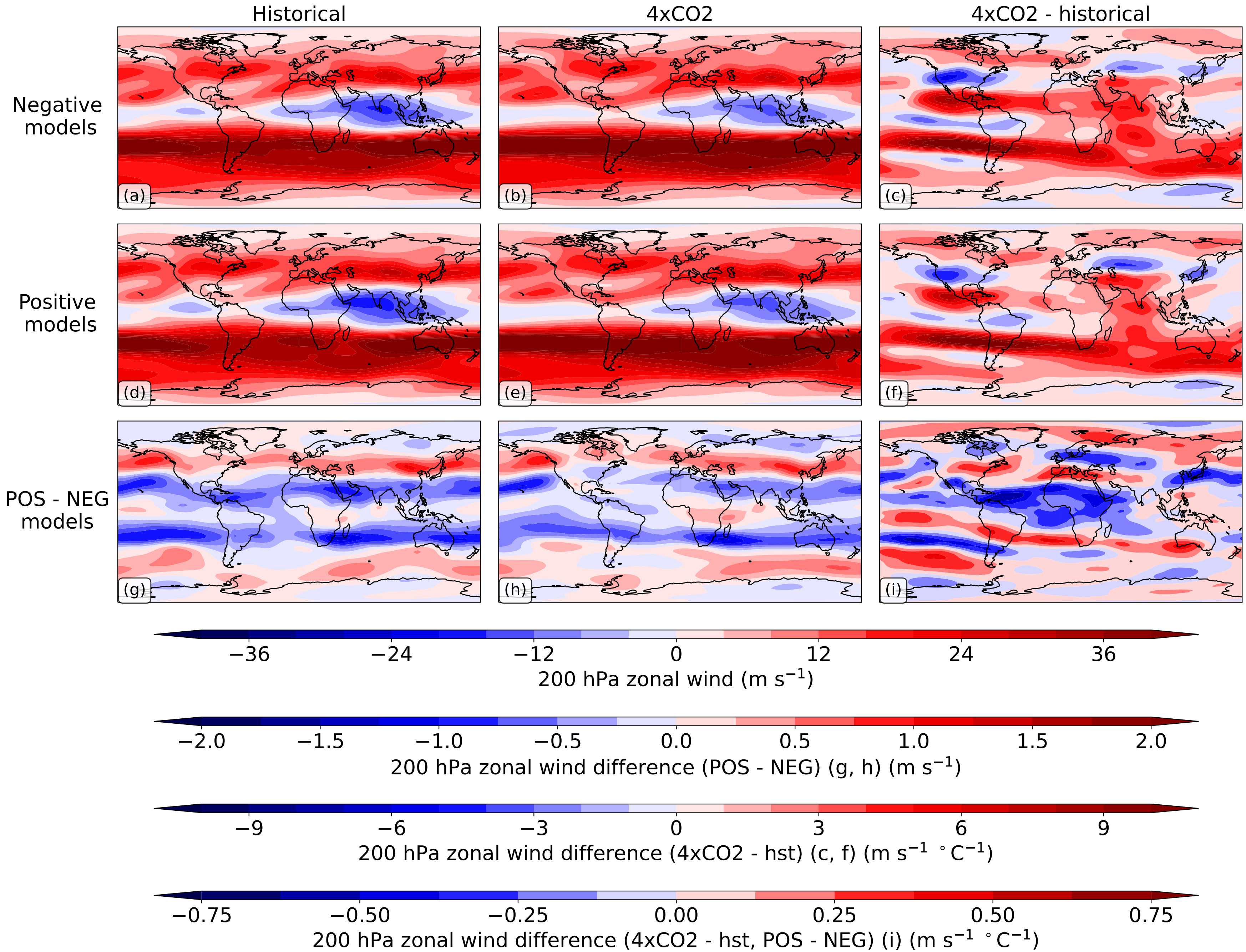

Figure C.5: As in Fig. 3.4, but instead of showing the zonally averaged U across the NH, the 200 hPa U is shown across all grid points.

C.3 Historic relationship between U shear and blocking

Figure C.6 shows the correlations of linear regressions between the JJA U shear and ESB. Here U shear is defined as the partial derivative of U with respect to the decreasing pressure level ($-\frac{\partial u}{\partial p}$). I define the vertical wind shear here using a partial derivative to provide a two-dimensional picture of the flow across latitude and pressure level, and because such a definition follows more closely the physical connection between vertical wind shear and baroclinic instability. Baroclinic instability occurs in the midlatitude atmosphere, and arises from the existence of a meridional temperature gradient that causes a vertical shear of the mean flow (Charney 1947; Eady 1949). Baroclinic instability generates large-scale eddies which grow by taking energy from the mean flow (Pierrehumbert and Swanson 1995) and are the cause for all midlatitude cyclones.

As in Fig. 3.8, the strongest correlations for changes to the U shear are in the SH. Across all panels in the left column of Fig. C.6, a pattern of positive (negative) correlations of U shear at 200 hPa exists at 30° S (55° S). Across the total longitudinal average in Fig. 3.8b, the R^2 exceeds 0.50. This change in U gradient indicates a shift in the location of baroclinic eddies in the SH, associated with the propagation of Rossby waves from the tropics (Hoskins and Karoly 1981). Therefore these are not causal correlations but reflect the role of tropical forcing in increasing ESB.

In the NH extratropics, the most significant correlation is in the Atlantic region (Figs. C.6p - C.6r), with a pattern of positive (negative) correlations at 300 hPa and 25° N (35 ° N), with $R^2 \approx 0.4$. Comparison to the Atlantic U climatology in Fig. 3.9r shows that this series of correlations exist in the Atlantic subtropical jet, and at the edge of the easterly flow in the tropical Atlantic.

The increased (decreased) U shear at 25° N (35 ° N) in the Atlantic upper-troposphere may be associated with the second mechanism described in 3.4.4.2, which proposed that the propagation of positive and negative vorticity anomalies along the North Atlantic storm track is associated with increased ESB. Baroclinic instability can be understood as interacting potential vorticity anomalies at different levels in the atmosphere (Robinson 1989), so vorticity anomalies are likely to be associated with increasing and decreasing patterns of U shear.

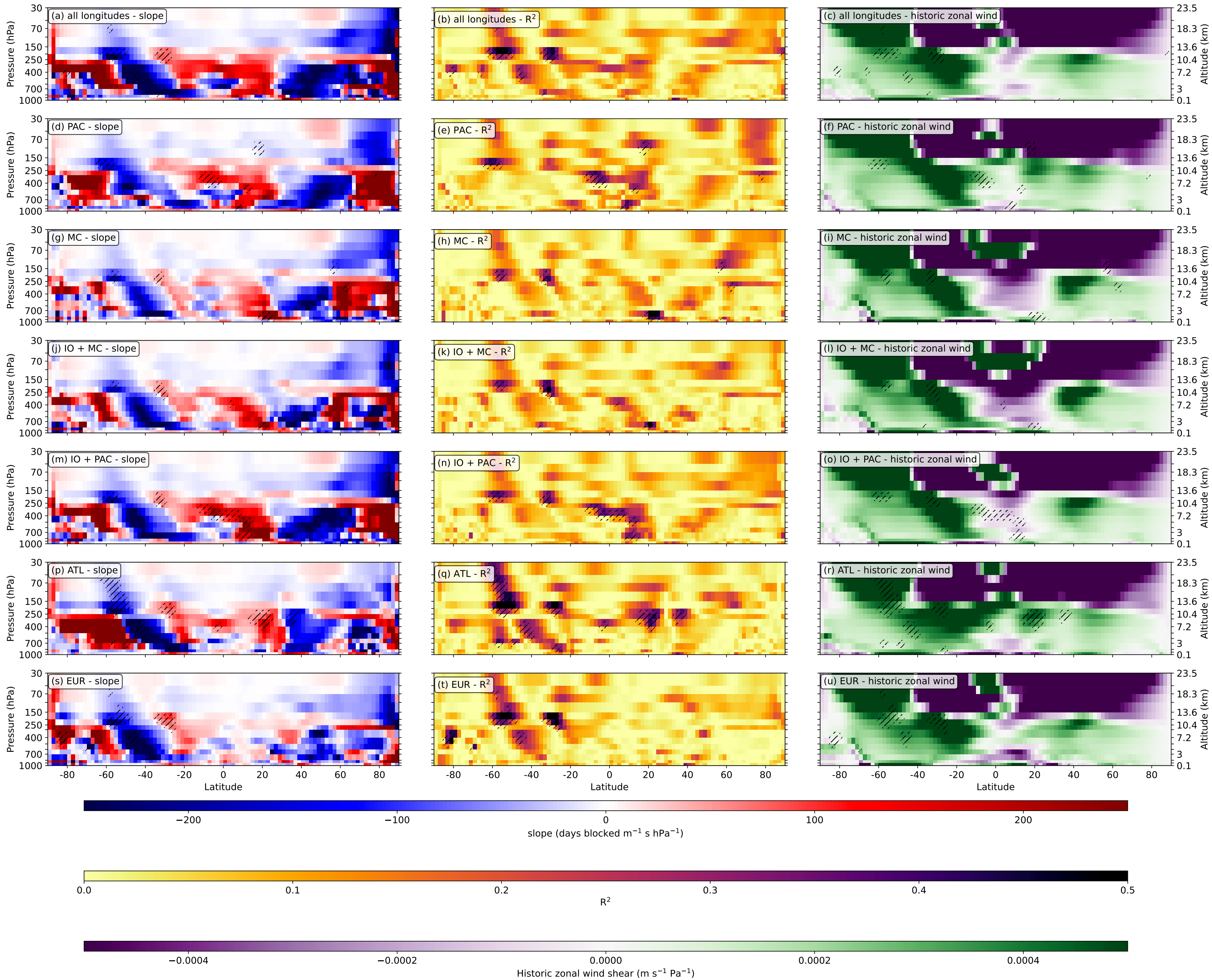

Figure C.6: As in Fig. 3.9, but showing the relationship between the historic U shear (defined here as the partial derivative of U and pressure level) and the historic ESB across the CMIP5/6 model ensemble in Fig. 3.2.

I note that 25° N is a relatively low latitude to consider baroclinic instability, since the Coriolis parameter is much smaller at this latitude, However, Charney (1963) has shown through scale analysis that the quasi-barotropic assumption of synoptic-scale motion is not valid at 20° N. Therefore it is reasonable to consider that baroclinic instability is important at 25° N.